CARBON DIOXIDE SEQUESTRATION AND ENHANCED COALBED METHANE RECOVERY IN UNMINEABLE COALBEDS OF THE POWDER RIVER BASIN, WYOMING

A DISSERTATION

SUBMITTED TO THE DEPARTMENT OF GEOPHYSICS

AND THE COMMITTEE ON GRADUATE STUDIES

OF STANFORD UNIVERSITY

IN PARTIAL FULFILLMENT OF THE REQUIREMENTS

FOR THE DEGREE OF

DOCTOR OF PHILOSOPHY

Hannah Elizabeth Ross

August 2007

I certify that I have read this dissertation and that, in my opinion, it is fully adequate in scope and quality as dissertation for the degree of Doctor of Philosophy.

_____
(Mark D. Zoback) Principal Advisor

I certify that I have read this dissertation and that, in my opinion, it is fully adequate in scope and quality as dissertation for the degree of Doctor of Philosophy.

_____
(Franklin M. Orr, Jr.)

I certify that I have read this dissertation and that, in my opinion, it is fully adequate in scope and quality as dissertation for the degree of Doctor of Philosophy.

_____
(Jerry M. Harris)

I certify that I have read this dissertation and that, in my opinion, it is fully adequate in scope and quality as dissertation for the degree of Doctor of Philosophy.

_____
(Anthony R. Kovscek)

Approved for the University Committee on Graduate Studies.

ABSTRACT

This thesis presents contributions to the challenges of global warming, coalbed methane water disposal and the determination of crustal thermal structure in areas with sparse heat-flow measurements.

The first problem addressed in this thesis is global warming, where it has been shown that the amount of carbon dioxide (CO_2) in the atmosphere has risen from pre-industrial levels of 280 ppm to present levels of ~380 ppm. This increase in atmospheric CO_2 is attributed to the world's expanding use of fossil fuels and is believed to be one of the primary causes of global warming. As a means for reducing greenhouse gas emissions it has been proposed that CO_2 be sequestered in geologic formations. Coalbeds are an attractive geological environment for CO_2 sequestration because CO_2 is retained in the coal as an adsorbed phase and the cost of sequestration can be offset by enhanced coalbed methane recovery (ECBM). In order to examine the feasibility of sequestering CO_2 in unmineable coalbeds of the Powder River Basin (PRB), Wyoming, a reservoir characterization study and fluid flow simulations have been carried out. The results suggest that CO_2 sequestration and ECBM are feasible in the PRB and it is estimated that unmineable coalbeds in the PRB can sequester a total of 1.3 to 1.8 billion tonnes of CO_2 (assuming all coalbeds in the basin are overlain by impermeable caprocks). Therefore, at Wyoming's current CO_2 emissions rate, the coal resources of the PRB could sequester Wyoming's annual emissions for the next 20 to 30 years.

The second issue addressed in this thesis is the disposal of coalbed methane (CBM) water, which is co-produced with CBM in the PRB. CBM water poses a serious environmental hazard to the PRB because in some areas the water has high saline and sodium contents, making it unsuitable for agricultural use and potentially damaging to wildlife habitats if discharged at the surface. One option for the disposal of CBM water is injection into aquifers, but for injection to be feasible the porosity and permeability of the sands needs to be high, the pore pressure would ideally be sub-hydrostatic, and the aquifer cannot be in hydraulic communication with coalbeds or aquifers used for irrigation or domestic use. In order to determine if pore pressures in aquifers are low enough to allow for significant CBM water injection and to determine whether the coals and sands are in communication with each other, pore pressures in 250 wells that monitor water levels in coalbeds and adjacent sands within the PRB have been calculated. The analysis indicates that both the sands and coalbeds have sub-hydrostatic pore pressures and that at present all sand aquifers that are in hydraulic communication with a producing coalbed are within ~200 ft of the coalbed. Therefore, in order to be sure that disposed CBM water does not migrate back into producing coalbeds over time, CBM water disposal should be undertaken in sand aquifers with sub-hydrostatic pore pressures further than ~200 ft from coalbeds. In addition, fluid flow simulations estimate that the water injection rate into deep sands (~1000 ft) will be four times greater than the average water production rate per CBM well in the PRB.

The final challenge addressed in this thesis is the determination of crustal thermal structures in areas with sparse heat-flow data. Curie-isotherm depths can be used as a proxy for temperature in mid- to lower crust and in order to test if Curie depths can be used to map the thermal structure of the crust, Curie depths across California were calculated. This study is the first to determine the Curie-temperature isotherm for California. Using an improved methodology to estimate the depth to the Curie-isotherm, an inverse relationship between estimated Curie depths and heat-flow measurements across California is shown. Specifically, the Great Valley has low heat flow (less than 50 mW/m^2) and deep Curie depths (30-45 km), whereas the Coast

Ranges of California are characterized by high heat flow (80-85 mW/m^2) and shallower Curie depths (20-30 km). However, the spatial resolution of the spectral analysis method is not high enough to use Curie depth as a crustal thermal indicator in areas that lack heat-flow and earthquake data to validate the estimated depths to Curie-temperature isotherm.

ACKNOWLEDGMENTS

To my advisor, Prof. Mark Zoback, thank you for all your enthusiasm, scientific knowledge, insights, patience and time. You have not only shaped this thesis, but you have shaped me into a better scientist and for that I am extremely thankful. Thank you also for caring not only about my research, but about my life outside of the lab – Kevin, my future, homesickness, seeing the world. I am truly grateful for all the time and energy you have put into me over these past six years. Thank you!

Thank you to my committee, Prof. Lynn Orr, Prof. Jerry Harris and Prof. Tony Kovscek, for all your guidance and for our many discussions. I have really enjoyed working with you all and sincerely appreciate the time you have spent with me.

To Dr. Richard Blakely, thank you for the many hours spent helping me understand the spectral analysis method and editing our paper. Thank you also for your encouragement and continued interest in my research and life. I do wish that this pilot study had worked out, as I would have loved to have kept working with you.

Many, many thanks to Paul, for all the time you spent helping me with my simulator, discussing my research and reading my thesis. I really appreciate all your help and know that you are going to make an amazing advisor some day soon. You rock!

To Susan, thank you for looking after me and the group. I'm so happy Mark took on such a caring and lovely person!

Thank you to all the many students who have helped me with my research and class work. Without you I would not be here. Special thanks to Carolyn, Herve and Christian, for helping me set up my simulations and working through early problems. To Lourdes, for passing on all your knowledge about coalbed methane in the PRB. I've also been lucky enough to be part of the Stanford Global Climate and Energy Project and have worked with many fantastic PIs and students. Thank you for all the stimulating discussions.

To my brilliant research group, Ellen, Amie, Laura, Amy, Pijush, John V., Hiroki, Nai, Lourdes, Alvin, Paul and John T., thank you for keeping me sane through it all; for the many coffee breaks, research insights, code help, poster and talk help, fun ski trips and dinners. I've loved working with you all! Thank you to my other Geophysics buddies, Katie, Emily, James, Dave S., Dave W. and Jess, for helping make Mitchell a brighter place.

I've also been blessed with wonderful, wonderful friends outside of Geophysics, whom I've met mostly through IVGrad and church. You have all made this time here at Stanford so much fun and have filled my life with much joy! To Kirsty, Jacob, Katie, Ted, Steve, Caleb, Clint, Mike, Liane, Walter, Erik, Rachel, Greg, Diane, Pete, Maria, Hanna, Derek, Meagin, Jess, Jeremiah and the Kovacics, thank you for all the dinners, Thanksgivings, Christmases, Easters, Hullabaloos, game nights, beds, trips, movies, retreats, chats, prayers…

Finally, a great, big, huge thank you to my amazing husband, Kevin, loving parents, Michael and Frances, and wonderful brothers, Nathanael and David. Thank you for reminding me to be the little red caboose, for your love, patience, prayers and continual support. Especially to Kevin for walking beside me through all of this! I love you.

"Trust in the Lord with all your heart and lean not on your own understanding; in all your ways acknowledge him, and he will make your paths straight." Proverbs 3:5-6.

TABLE OF CONTENTS

LIST OF TABLES

Number *Page*

LIST OF FIGURES

Number *Page*

Chapter 1

INTRODUCTION

1.1 Overview and motivation

This thesis is composed of three separate studies: the first looks at the feasibility of carbon dioxide (CO_2) sequestration and enhanced coalbed methane recovery in unmineable coalbeds of the Powder River Basin, Wyoming, the second is focused on coalbed methane water disposal and wellbore completion methods in the Powder River Basin, and the last involves calculating Curie-isotherm depths across California. Although distinct in focus and methodology, these studies all demonstrate the value of detailed geologic and geophysical modeling as an aid to the important global human challenges of hazard mitigation and global warming.

For the first study I was interested in whether it was feasible to sequester CO_2 in unmineable coalbeds of the Powder River Basin, Wyoming, and whether enhanced coalbed methane recovery could be achieved through CO_2 injection. Since the industrial age, the amount of CO_2 in the atmosphere has risen from pre-industrial levels of 280 ppm to present levels of ~380 ppm (Tans, 2007) and this increase in atmospheric CO_2 is attributed to the world's expanding use of fossil fuels and is believed to be the primary cause of global warming (Mann et al., 1998; Energy Information Administration, 2006; Intergovernmental Panel on Climate Change,

2007). In order to reduce greenhouse gas emissions it has been proposed that CO_2 be sequestered in geologic formations, and unmineable coalbeds have been put forward as one of the geologic storage options for CO_2.

The motivating questions behind this study were:

- Is it feasible to sequester CO_2 in unmineable coalbeds?
- Does CO_2 injection result in significant improvements in methane (CH_4) recovery (enhanced coalbed methane)?
- What are the volumes of CO_2 that can be sequestered and CH_4 that can be produced?
- Will horizontal hydraulic fractures mitigate the negative effect of matrix swelling on injectivity?
- What are the most sensitive parameters controlling the CO_2 sequestration and enhanced coalbed methane potential in unmineable coalbeds?

The second study looked at coalbed methane water disposal in the Powder River Basin, where coalbed methane production in the basin is associated with very large volumes of water production (~590 million barrels in 2006; Wyoming Oil and Gas Conservation Commission, 2006). In many places of the basin the water has high saline and sodium contents, making it unsuitable for agricultural use because the water degrades the soil quality leading to soil erosion and damage to wildlife habitats. One option for the disposal of coalbed methane water is injection into aquifers and I have investigated this option by calculating coalbed and sand pore pressures in the Powder River Basin and running simulations to look at the feasibility of injecting coalbed methane water into those sands. In addition, I have extended the study of Colmenares and Zoback (2007), evaluating coalbed methane wellbore completion methods in the Powder River Basin to determine if there are ways to produce less coalbed methane

water, while still achieving adequate coal depressurization for coalbed methane production.

The last study involved the determination of Curie-isotherm depths across California, estimated from magnetic anomalies, in order to test the resolution of the spectral analysis method used to calculate Curie depths. I was interested in whether Curie depths were an appropriate proxy for lithospheric thermal structure in intraplate regions, where heat-flow data is sparse. California was chosen as a test area because of its large number of well-documented surface heat-flow measurements and statewide aeromagnetic coverage of adequate quality. In this study I introduced an improved methodology for calculating Curie depths, where sub-region dimensions are increased in a stepwise manner until long-wavelength anomalies are appropriately sampled and each sub-region spectrum determined from the magnetic anomalies is manually fit with a theoretical expression that directly yields the depth to the bottom of the magnetic layer.

1.2 Thesis outline

In addition to this Introduction, this thesis contains five chapters. Chapters 2 and 3 cover the CO_2 sequestration and enhanced coalbed methane study, chapters 4 and 5 are focused on the coalbed methane water disposal and mitigation research and chapter 6 covers the Curie-isotherm depth study. Chapter 6 has been published in its entirety.

1.2.1 Chapter 2 - CO_2 sequestration and enhanced coalbed methane recovery: Reservoir characterization and fluid flow simulations of the Powder River Basin, Wyoming

Chapter 2 describes the construction of a 3D stochastic reservoir model and fluid flow simulations used to determine the feasibility of sequestering CO_2 in unmineable coalbeds of the Powder River Basin, Wyoming. I was also interested in the enhanced coalbed methane potential of CO_2 sequestration. The reservoir characterization

required to build the 3D model is described in detail, where I used geostatistical techniques and history-matching to populate my model with permeability and porosity values. In addition, I outline the fluid flow simulation set-up and report on the volumes of CO_2 sequestered and CH_4 produced that I obtain through modeling CO_2 injection into unmineable coalbeds. Results from the fluid flow simulations suggest that CO_2 sequestration is feasible in unmineable coalbeds of the Powder River Basin and that enhanced coalbed methane recovery will yield 5-8 times more CH_4 than conventional coalbed methane production practices.

Furthermore, I discuss the effects of gas buoyancy, one layer reservoir models and homogenous permeability fields on sequestration and enhanced coalbed methane estimates, and show that unmineable coalbeds need to be overlain by impermeable caprocks or the CO_2 will migrate into overlying units and eventually to the surface.

1.2.2 Chapter 3 - CO_2 sequestration and enhanced coalbed methane recovery: Fluid flow simulation sensitivity analysis of the Powder River Basin, Wyoming

Chapter 3 is a continuation of the CO_2 sequestration study detailed in Chapter 2 and involves a sensitivity analysis on the coal properties and simulation parameters used in the fluid flow simulations carried out for the study. The sensitivity analysis reveals that the CO_2 sequestration and enhanced coalbed methane potential of unmineable coalbeds in the Powder River Basin are sensitive to cleat permeability, the injection bottom hole pressure (BHP) constraint, slow diffusion times, coal thickness, high cleat compressibility, large volumetric strains for CO_2, adsorption isotherms, relative permeability and injection well orientation. In addition, the enhanced coalbed methane recovery volume is also sensitive to cleat porosity, well spacing, the initial reservoir pressure and the injected gas composition.

1.2.3 Chapter 4 - Sub-hydrostatic pore pressure in coalbed and sand aquifers of the Powder River Basin, Wyoming, and implications for disposal of coalbed methane water through injection

Large quantities of water are associated with the production of coalbed methane in the Powder River Basin and in some areas this water has high saline and sodium contents, making it unsuitable for agricultural use and potentially environmentally damaging if discharged at the surface. In Chapter 4, I determine if pore pressures in Powder River Basin aquifers are low enough to allow for significant coalbed methane water injection into the aquifers and whether the coals and sands are in hydraulic communication with each other. In order to do this I calculated pore pressures in wells that monitor water levels in coalbeds and adjacent sands in the Powder River Basin and analyzed pore pressure changes with time for both the coals and their overlying sands. I find that all sands and coalbeds analyzed have sub-hydrostatic pore pressures and that at present; all the sands that appear to be in hydraulic communication with producing coalbeds are less than ~200 ft from the coalbed. In addition, I used fluid flow simulations to look at the feasibility of injecting coalbed methane water into sub-hydrostatic sand aquifers and the results suggest that injection rates will be higher than the average water production rate per well in the basin.

1.2.4 Chapter 5 - Hydraulic fracture growth from coalbed methane operations in the Powder River Basin, Wyoming: Implications for coalbed methane water management

Coalbed methane operators in the Powder River Basin routinely carry out water-enhancement on their wells. Water-enhancement procedures are used to connect the coal cleats to the wellbore to increase gas production and as it turns out, coalbed methane operators in the Powder River Basin routinely fracture the coal through this practice (Colmenares and Zoback, 2007). Chapter 5 involves the analysis of ~200 water-enhancement tests from coalbed methane wells in the Powder River Basin in order to determine the magnitude of the least principal stress and the orientation of hydraulic fracture growth. Like Colmenares and Zoback (2007), I find that both

horizontal and vertical hydraulic fractures are created and that some wells with vertical hydraulic fractures produce excessive volumes of coalbed methane water. In this Chapter I investigate why both vertical and horizontal hydraulic fractures form throughout the basin and why some wells with vertical hydraulic fractures produce excessive volumes of water. In addition, it appears that vertical hydraulic fractures in some of the wells with excessive water production could be in communication with active normal faults, where the faults may act as conduits for water migration into the coalbed.

1.2.5 Chapter 6 - Testing the use of aeromagnetic data for the determination of Curie depth in California

In chapter 6 I present a spectral analysis method applied to magnetic anomalies from the state of California in order to estimate the depth to the Curie-isotherm throughout the state. I selected California as the study area because of its statewide aeromagnetic coverage of adequate quality and large number of well-documented surface heat-flow measurements. California also has distinct zones of low (Great Valley and Sierra Nevada) and high (Coast Ranges and Mojave Desert) heat flow that correspond with geologic provinces. These aspects make California a good region to test whether the spectral analysis method can be transported to other regions with fewer heat-flow measurements, such as intraplate regions of the conterminous United States, in order to resolve areas with anomalously high temperatures in the lower crust.

This study is the first to determine the Curie-temperature isotherm for California. Using an improved methodology to estimate the depth to the Curie-isotherm, I find an inverse relationship between estimated Curie depths and heat-flow measurements across California, as expected. Specifically, the Great Valley has low heat flow (less than 50 mW/m^2) and deep Curie depths (30-45 km), whereas the Coast Ranges of California are characterized by high heat flow (80-85 mW/m^2) and shallower Curie depths (20-30 km).

Chapter 2

CO_2 SEQUESTRATION AND ENHANCED COALBED METHANE RECOVERY: RESERVOIR CHARACTERIZATION AND FLUID FLOW SIMULATIONS OF THE POWDER RIVER BASIN, WYOMING

2.1 Abstract

Coalbeds are an attractive geological environment for carbon dioxide (CO_2) sequestration because CO_2 is retained in the coal as an adsorbed phase and the cost of sequestration can be offset by enhanced coalbed methane recovery (ECBM). In order to examine the feasibility of sequestering CO_2 in unmineable coalbeds of the Powder River Basin (PRB), Wyoming, we have carried out a reservoir characterization study and fluid flow simulations. We have focused our study on the Big George coal, part of the Wyodak-Anderson coal zone. Our 3D model of the Big George coal was built

in an area of the PRB where the least principal stress is equal to the overburden stress, resulting in horizontal fracture propagation if hydraulic fracturing was utilized to enhance injectivity and recovery. We populated our 3D grid with cleat and matrix permeability and porosity data from the literature using geostatistical techniques and constrained the cleat permeability and porosity values through history-matching the production data from coalbed methane wells in our model.

Simulations were run with pure CO_2 injection, with and without coal matrix shrinkage and swelling, and it was assumed that the coal was overlain by an impermeable caprock. We found that gravity and buoyancy are the major driving forces behind gas flow within water saturated coal and that coal matrix swelling results in a slight reduction (10%) in injectivity. However, hydraulically fracturing the coal close to its base helped mitigate the negative effect of permeability reduction on injection rate. Our simulations predict that after 13 years of CO_2 injection, ~99% of the total CO_2 injected into the Big George coal would be sequestered and that methane (CH_4) production would be ~5-8 times greater with CO_2 injection than without. We found that one injection well was able to sequester ~9 kt of CO_2 a year. Based on this injection rate, it would take ~7,000 injection wells (each with a lifetime of ~13 years) to sequester the current CO_2 emissions for the State of Wyoming (~63 million tonnes/yr). Since there have already been ~17,000 CBM wells drilled in the PRB and ~34,000 more projected to be drilled in the next decade, utilization of 7,000 wells for CO_2 sequestration is feasible, especially in light of the potential for significant cost recovery through enhanced methane production. Based on the volume of coal in the PRB (at depths greater than 300 m), we estimate that unmineable coalbeds in the PRB can sequester a total of 1.3 to 1.8 billion tonnes of CO_2 and therefore, at Wyoming's current CO_2 emissions rate, the coal resources of the PRB could sequester Wyoming's annual emissions for the next 20 to 30 years.

Finally, we find that simulation models of water saturated coalbeds need to contain more than one layer in the vertical direction to account for the buoyancy effects between the gas and resident water, and that the heterogeneous nature of coal

permeabilities and porosities need to be captured so the sequestration potential of coal-bearing basins are not over-estimated. It is also imperative that coalbeds are overlain by impermeable cap rocks or the CO_2 will migrate into overlying units.

2.2 Introduction

The amount of carbon dioxide (CO_2) in the atmosphere has risen from pre-industrial levels of 280 ppm to present levels of ~380 ppm (Tans, 2007). This increase in atmospheric CO_2 is attributed to the world's expanding use of fossil fuels and is believed to be the primary cause of global warming (Mann et al., 1998; Energy Information Administration (EIA), 2006; Intergovernmental Panel on Climate Change (IPCC), 2007). Based on current emissions projections, world anthropogenic CO_2 emissions are expected to increase from 25,028 million metric tons in 2003 to 43,676 million metric tons in 2030 - growing by 2.1 percent per year (EIA, 2006). In order to stabilize CO_2 concentrations in the atmosphere at 550 ppm, Wigley et al. (1996) (2007) show that the cumulative CO_2 emissions over the 21st century need to decrease from ~5400 $GtCO_2$ to 3240 $GtCO_2$. This means that we need to cut CO_2 emissions by 2160 $GtCO_2$ over the remaining century. IPCC (2007) climate change models suggest that to stabilize CO_2 concentrations between 450 ppm and 1000 ppm, CO_2 emission rates "need to be reduced well below year 2000 values in all scenarios". Additionally, the IPCC (2007) models estimate that cumulative emissions required to stabilize CO_2 concentrations in the atmosphere at 450 ppm will need to be on the order of 2145 $GtCO_2$. Using the Wigley et al. (1996) prediction that emissions could reach 5400 $GtCO_2$ by the end of the century with no mitigation, to stabilize concentrations at 450 ppm would require a decrease in CO_2 emissions of ~3255 $GtCO_2$ or greater.

As a means for reducing greenhouse gas emissions, it has been proposed that CO_2 be sequestered in geological formations, including mature oil and gas fields, deep saline aquifers and unmineable coal seams. Estimates of the world's CO_2 storage capacity in geological formations ranges from 300 to 3200 $GtCO_2$ (U.S. Department of Energy (DOE), 2007). If the upper limit is correct, then the sequestration capacity

of geological formations is large enough to store the 2160 $GtCO_2$ that cannot be emitted to the atmosphere in order to stabilize atmospheric CO_2 concentrations at 550 ppm. Of the three geological storage options, coalbeds are an attractive geological environment for CO_2 sequestration because CO_2 is retained in the coal as an adsorbed phase and the cost of sequestration can be offset by enhanced coalbed methane recovery (ECBM).

We have examined the feasibility of sequestering CO_2 in unmineable coalbeds by conducting a reservoir characterization study and fluid flow simulations on unmineable coalbeds in the Powder River Basin (PRB), Wyoming (Figure 2.1). In particular, we were interested in the ECBM potential of CO_2 sequestration and modeling the effects of horizontal hydraulic fractures on CO_2 injectivity. Our study focused on the sub-bituminous Big George coal, part of the Wyodak-Anderson coal zone of the Tertiary Fort Union Formation. A 3D stochastic reservoir model of the Big George coal was constructed in an area of the PRB where the least principal stress is vertical, thereby guaranteeing horizontal hydraulic fractures. We built our model using well logs from coalbed methane (CBM) wells, and populated the model with permeability and porosity values using geostatistical techniques and history-matching.

The PRB was chosen for several reasons:

- The basin is the location of the fastest growing natural gas play in the USA, mostly from the development of CBM from coalbeds in the Fort Union Formation (Figure 2.1) (DOE/National Energy Technology Laboratory (NETL), 2003). The USGS Powder River Basin Province Assessment Team (2004) has estimated the total CBM resource in the PRB to be 14.3 trillion cubic feet (TCF).

- The state of Wyoming contains point sources for the capture of CO_2, including several coal-fired power plants in the southwestern, eastern and northeastern parts of the state that emit 47 million tonnes of CO_2 per year (EIA, 2007).

- The state of Wyoming has a CO_2 pipeline network, with a proposed extension to the edge of the PRB (Figure 2.1) (Nummedal et al., 2003).

- The PRB meets most of the criteria set out in Gale and Freund (2001) for identifying potential CO_2 sequestration sites: Many of the coalbeds are laterally extensive and isolated from surrounding strata by confining units; the basin is not strongly faulted or folded; permeability in the coals is high enough for CBM production; the coals fall within the optimal depth range (~305-1500 m); and many of the coals are thick.

- We collaborate with several research groups in the Geophysics and Energy Resources Engineering departments at Stanford University, who have ongoing projects in the PRB. The projects involve laboratory studies on coal samples from the PRB, monitoring CO_2 migration in PRB coals, and categorizing fracture growth from water-enhancement practices in PRB coals by CBM operators.

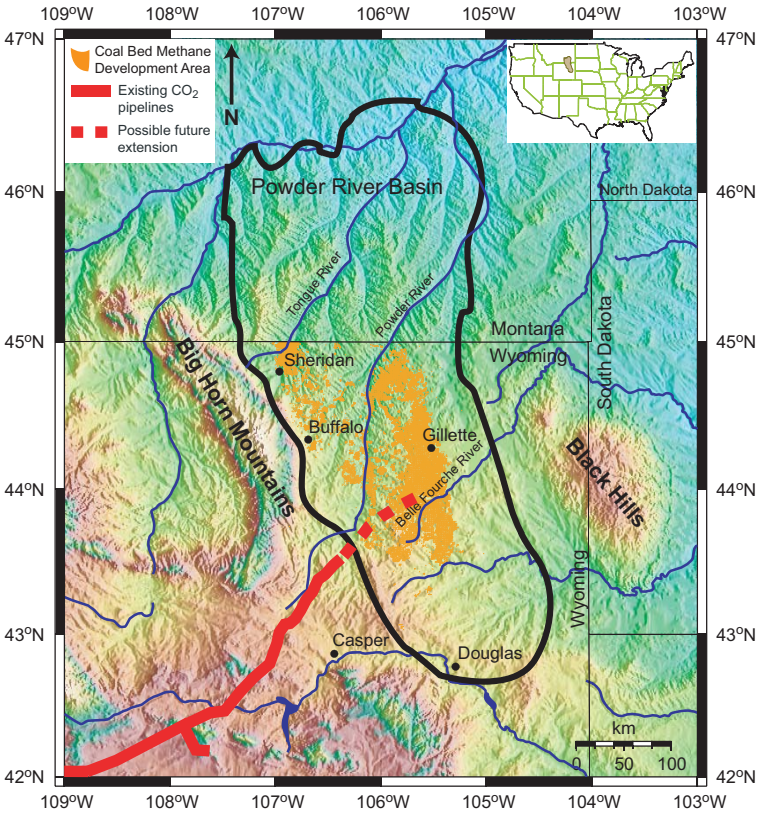

Figure 2.1: Location map of the Powder River Basin, Wyoming (modified from Colmenares and Zoback, 2007). Orange dots correspond to CBM wells. The location of the CO_2 pipeline is from Nummedal et al. (2003).

In this chapter we begin by summarizing the geology of coal, the storage and production of CBM in coal, and the process of ECBM, which are key elements that should be understood before proceeding with modeling and simulations of CO_2 sequestration in unmineable coalbeds (section 2.3). We also give an overview of previous CO_2 sequestration simulation and pilot field studies that have been undertaken in unmineable coalbeds around the world. In section 2.4 we describe the geology and structure of the PRB and discuss the geology of the Big George coal in more detail. We then go on to outline the reservoir characterization we undertook to construct our 3D stochastic reservoir model of the Big George coal and our fluid flow simulation set-up (section 2.5). In section 2.6 we discuss our fluid flow simulation results in relation to the feasibility of CO_2 sequestration and ECBM in the PRB and go on to describe some of the complicating factors that need to be taken into account when running CO_2 sequestration simulation studies for unmineable coal (section 2.7).

Finally, in section 2.8, we discuss CO_2 leakage scenarios due to gas buoyancy and cap rock seal. In the following chapter (Chapter 3) we show results from a sensitivity analysis carried out on the coal parameters and properties used in this chapter to build our 3D stochastic coal model and run our fluid flow simulations.

2.3 Coalbed methane and enhanced coalbed methane

2.3.1 Coal geology

Coal is both a source rock and a reservoir. During coalification (conversion of peat to coal through biochemical decay and metamorphic alteration of the organic matter) large quantities of methane-rich gas and water are produced as by-products. The methane (CH_4) can be either biogenic or thermogenic in origin, depending on the temperature at which the CH_4 is generated (<50ºC for biogenic and >50ºC for thermogenic). Most of the CH_4-rich gas escapes into the atmosphere during this process but some is retained within the coal, where it is either adsorbed onto the coal surface or dispersed in the pores. With burial of coal, water and gas continue to be produced and the coal increases in rank, which is a measure of coal maturity (Anderson et al., 2003). Higher rank coals typically contain more CH_4 (Gale and Freund, 2001) and the various coal ranks in increasing order are: lignite, sub-bituminous, high volatile bituminous, medium volatile bituminous, low volatile bituminous, semi-anthracite and anthracite (Jones et al., 1988). Because large quantities of water are released during the maturation process, coals are typically water saturated. In addition, fractures, known as cleats, form perpendicular to bedding during the coalification process and these are the primary permeability mechanism within coal (Gale and Freund, 2001). The more continuous, primary cleats are called face cleats and the secondary cleats, orientated orthogonal to the face cleats, are called butt cleats. Cleats are considered to be opening-mode fractures that open in the direction of the least principal stress (S_3) (Laubach et al., 1998). It has been suggested that coal cleats form either by contraction of the coalbed due to compaction, from

regional tectonic stresses, from high pore pressures or during exhumation (Laubach et al., 1998).

Coal is composed of both organic and inorganic material. The organic constituents of coal are called macerals, which are sub-divided into three main petrographic groups: inertinite, liptinite and vitrinite (Jones et al., 1988). The reflectance of individual macerals, particularly that of the vitrinites, is a measure of the degree of maturation a coal has undergone (Jones et al., 1988). Vitrinite reflectance ranges from approximately 0.23 for lignites to 5.0 for anthracites.

2.3.2 Coalbed methane

CBM reservoirs can contain up to six to seven times the volume of methane found in conventional gas reservoirs (Nuccio, 2000). In conventional gas reservoirs, gas is stored in the porosity system, whereas in coalbeds the CH_4 is stored by adsorption to coal matrix surfaces (De Bruin and Lyman, 1999). Coalbeds contain both primary (coal matrix) and secondary porosity systems (cleats) (Law et al., 2003), where the primary porosity is dominated by adsorption and this system contains most of the gas-in-place volume. Within the primary porosity system, mass transfer is governed by diffusion due to concentration gradients. In contrast, Darcy flow dominates the secondary porosity system and the fluid flow rate is related to the cleat permeability and pressure gradient (Law et al., 2003). Reeves and Pekot (2001) have suggested a third porosity system, where free gas and water are also stored within the coal matrix.

In order to produce CBM, most coalbeds are depressurized through the removal of water from the coal cleats. This lowers the pressure around the well so that gas and water start to flow through the cleats to the production well. This in turn reduces the pressure at the matrix-cleat interface and CH_4 desorbs from the cleat surface into the secondary porosity system and flows to the production well. As a result, a concentration gradient is set up within the coal matrix and CH_4 desorbs and diffuses through the matrix to the cleats (Law et al., 2003). Initial production is dominated by

water, but once the pore pressure within the coals has been reduced to the point that CH_4 will desorb, CBM is produced (Figure 2.2) (Nuccio, 2000).

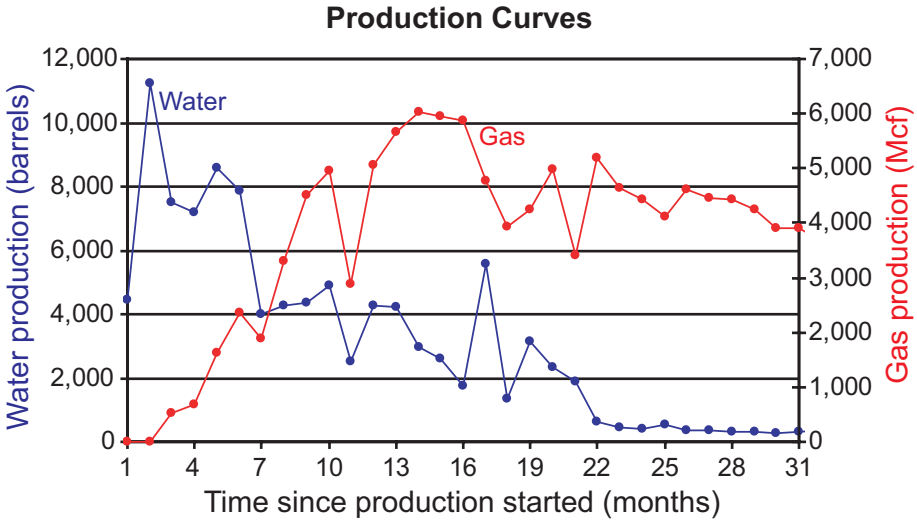

Figure 2.2: Typical water (blue line and symbols) and gas production (red line and symbols) curves for CBM wells in the Powder River Basin, Wyoming (WOGCC, 2004). Modified from Colmenares and Zoback (2007).

A typical composition of CBM is 88-98% CH_4, with lesser amounts of the higher hydrocarbons and CO_2 (Diamond et al., 1986). The estimated amount of CBM in the major coal-bearing basins of the U.S. is 700 TCF, with 150 TCF economically recoverable using today's technology (Rice, 1997).

2.3.3 Enhanced coalbed methane

In ECBM recovery, coal preferentially adsorbs CO_2 over CH_4, displacing the CH_4 from the coal matrix into the cleat system. In laboratory studies of the adsorption behavior of coals it has been shown that high rank coals will adsorb two moles of CO_2 for every one of CH_4, whereas low rank coals, such as sub-bituminous and lignite, can adsorb six to eighteen times more CO_2 than CH_4 (Gluskoter et al., 2002). ECBM utilizes coal's affinity for CO_2, and CH_4 is produced by "displacement desorption" (Gale and Freund, 2001). Initially production of CH_4 will be slow as adsorption of CO_2 only occurs close to the injection well. With time CO_2 will be adsorbed further away from the well, displacing more and more CH_4 until enough free gas is present in

the cleats for mass flow toward the production well, increasing CH_4 productivity (Gale and Freund, 2001).

2.3.4 Coal characteristics under CBM and ECBM conditions

2.3.4.1 Adsorption isotherms

The adsorption isotherms for CO_2 and CH_4 on coal are generally interpreted as type I isotherms, referred to as the Langmuir-type isotherm (White et al., 2005). This type of isotherm is produced when a monolayer of adsorbing molecules is adsorbed onto a non-porous solid, or when micropore filling is the dominant adsorption process (White et al., 2005). The adsorption capacity of coal for CH_4 and CO_2 is a function of both temperature and pressure. Increased temperatures will decrease the coal's storage capacity, while increased pressure will result in increased storage (Meissner, 1984; Wyman, 1984). However, with increasing pressure CO_2 undergoes a phase change to a liquid or supercritical fluid, as shown on the CO_2 phase diagram (depending on the reservoir temperature) (Figure 2.3). With time it is possible that the pressure in the coals will increase and this could lead to a CO_2 conversion from the gas state to a liquid or supercritical liquid, which may have adverse effects on sequestration. In our simulations we are injecting pure CO_2 gas, as the reservoir pressure and temperature of the Big George coal are ~23 atm (~2300 kPa) and ~22ºC respectively (Figure 2.3).

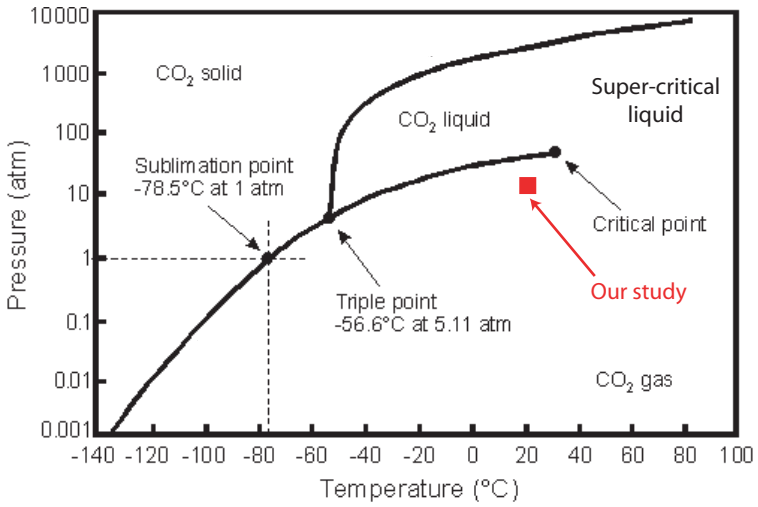

Figure 2.3: CO_2 phase diagram (http://scifun.chem.wisc.edu/chemweek/CO2/CO2.html). For this study the physical properties of the Big George coal fall within the red box.

2.3.4.2 Matrix shrinkage and swelling

Harpalani and Schraufnagel (1990) showed that coal will shrink on desorption of gas and expand on readsorption, and that matrix shrinkage leads to an increase in permeability. Palmer and Vaziri (2004) note significant increases in absolute permeability with CBM depletion in coals from the San Juan basin (10 to 100 times). Harpalani and Chen (1997) found that the increase in permeability due to matrix shrinkage is a linear function of the amount of desorbing gas. In contrast, Harpalani (2005) observed that for Illinois coals permeability actually decreased with desorption of CH_4, from approximately 25 mD to 5 mD. This decrease in permeability is attributed to stress-dependent permeability which leads to a permeability decrease as cleats and fractures close because of an increase in the effective horizontal stress through desorption of the gas (Harpalani, 2005).

Adsorption of CO_2 also potentially results in a reduction in permeability. Harpalani (2005) conducted experiments on cores from Illinois coals and found that at pressures of 745 psi the coal volume increased by 0.65% with CH_4 adsorption and 1.2% for CO_2. During the adsorption of CH_4, Harpalani observed a linear relationship between the amount of adsorbed methane and the induced volumetric strain. This

linear relationship was not observed for CO_2, where the volumetric strain was much higher during initial adsorption, but flattened as the pressure increased. Field evidence from the Allison ECBM pilot in the San Juan basin shows that before injection of CO_2 the coal permeability close to the injection wells was between 100 and 130 mD. However, after injecting CO_2 for just over a year the permeability dropped to less than 1 mD and this reduction in permeability is attributed to matrix swelling from the adsorption of CO_2 (Pekot and Reeves, 2002).

2.3.5 Previous CO_2 sequestration simulation and pilot field studies in unmineable coalbeds

Stevens and Spector (1998) carried out a global assessment of CO_2 sequestration potential in unmineable coalbeds for the International Energy Agency Greenhouse Gas R&D Programme. They estimated the world coalbed CO_2 sequestration capacity to be 225 Gt. Their estimate was based on the assumption that total CH_4 in-place would be replaced by CO_2 at a ratio of 2:1. Parson and Keith (1998) carried out a similar study and estimated that the total sequestration capacity of unmineable coalbeds was ~366-1100 $GtCO_2$, whereas Gale (2003) estimated the capacity to be 40 $GtCO_2$.

In October 2000, the DOE launched a multi-year research and development collaboration called the Coal-Seq project. The purpose of the project was to investigate the feasibility of sequestering CO_2 in deep, unmineable coal seams through two ECBM field projects in the San Juan basin. The two sites were the Allison Unit, where CO_2 was injected, and the Tiffany Unit, where N_2 was injected. The purposes of the field studies were to understand the mechanisms that occur in coalseams during CO_2 and N_2 injection, to demonstrate the value of ECBM, and to evaluate the economics of sequestration. The results from these field studies have been used in a number of simulations, including history-matching the field data by incorporating coal matrix shrinkage and swelling (Pekot and Reeves, 2002; Shi and Durucan, 2004), and in screening models for ECBM recovery and CO_2 sequestration in coal (Taillefret and Reeves, 2003; Reeves et al., 2004).

In 2003, Reeves conducted an assessment of the ECBM and CO_2 sequestration potential of 17 U.S. coal-bearing basins. In each basin Reeves (2003) determined the distribution of in-place and recoverable CH_4 resources by coal rank and used CO_2:CH_4 replacement ratios based on coal rank to assess the amount of CO_2 that could be stored in each basin. In total, it was estimated that U.S. coalbeds could potentially store 90 Gt of CO_2.

Also in 2003, Taillefret and Reeves (2003) developed a screening model to assist industry in project consideration and screening. This screening model is used to predict the performance of ECBM projects under a number of reservoir conditions and operating assumptions. Their model assumes that there is an existing CBM field that is being converted for ECBM recovery and CO_2 sequestration. The model consists of a database of nearly 2000 reservoir simulation cases, which users can retrieve and compare. Users can choose between three values for each of the seven input parameters, including permeability, coal rank, depth, well spacing, injection rate, injection gas and injection timing. In addition, any coal thickness can be specified; although this only means that the model results are scaled up or down (the initial simulations were run with a coal thickness of 3 m). The coals are flat lying and there is no option to change the porosity or fracture spacing. In 2004, Reeves et al. integrated a more robust ECBM and sequestration economic prediction module to Taillefret and Reeves' (2003) screening model. They conducted a number of sensitivity analyses on permeability (using constant values for the entire reservoir), injected gas composition, well spacing, coal depth, injection rates and injection timing. Reeves et al. (2004) also carried out an economic sensitivity analysis. Their major findings were:

- N_2-ECBM appears to be more economically beneficial than CO_2-ECBM.
- ECBM operations are more favorable in low permeability, high rank coals (assuming no matrix shrinkage and swelling) because less CH_4 has been recovered by the initial de-watering stage.

In contrast, Jackson (2006) found that ECBM was more dramatic in under-saturated, low rank, high permeability coals than in fully saturated coals because the presence of CO_2 caused CH_4 that normally would not desorb during de-pressurization in under-saturated coals, to desorb and be produced. Jackson argues that low rank, high permeability coals are good candidates for sequestration because the initial high permeability means that permeability reduction from matrix swelling will be less severe than in low permeability coals and therefore continued stimulation techniques will not be required for injection, reducing cost and time.

In addition to the DOE Allison Unit pilot study in the San Juan basin (2000), a number of small scale pilot studies have been carried out around the world. The Alberta Research Council (ARC), Canada, began a multiwell CO_2 sequestration pilot study in the Medicine River coal in Alberta (Mavor et al., 2004). The project is ongoing, but so far they have injected both pure CO_2 and flue gases to help determine the CO_2 sequestration and ECBM potential of coalbeds in Alberta. Unlike the Allison pilot project where injectivity was reduced by matrix swelling, ARC observed no reduction in injection rates when injecting CO_2. However, it should be noted that the coal was hydraulically fractured before CO_2 injection and this may have helped keep injection rates high.

In 2002, a six year sequestration pilot study was started in Japan called the Japan CO_2 Geosequestration in Coal Seams Project (JCOP) (Yamaguchi et al., 2006). At present the project consists of an injection well and production well. In 2004 they injected CO_2, with no CBM production, at a constant rate of ~2.3 tonne/day using a bottom hole constraint of 15 MPa, set slightly below the fracture pressure. In 2005 they began ECBM and saw a steady increase in CO_2 injectivity from 1.6 tonnes/day to 3.5 tonnes/day. This increase in injectivity was a surprise, as matrix swelling was expected to occur during CO_2 injection, which would reduce permeability and therefore the injection rate. Perhaps the coalbed was mistakenly hydraulically fractured in 2005, helping to maintain injectivity despite the occurrence of matrix

swelling, or production helped reduce reservoir pressures and allowed the injection rate to increase.

In China, a small scale pilot project was carried out in anthracitic coals in South Qinshui (Wong et al., 2006). The target coalbed is 6 m thick and at a depth of 500 m. In April 2004, 192 tonnes of CO_2 were injected into the coal. The measurements from this initial injection were used to validate a simulation model and then the model was used to predict the results from a 5-spot, 150-acre full field sequestration study. The fluid flow simulations show that ECBM would be 2.8 to 15 times greater than primary production (depending on the production well).

Finally, a pilot study has been carried out in Poland, called RECOPOL (Reduction of CO_2 emission by means of CO_2 storage in coal seams in the Silesian Coal Basin of Poland) (van Bergen et al., 2006). In July 2004, CO_2 was injected into three coal seams that range in thickness from 1.3-3.3 m and are at depths of 900-1200 m. A production well was drilled ~150 m away from the injection well and the objective of the study was to see breakthrough at the production well. Initially injection was very low, at 1 tonne/day, but in April 2005 they fractured the coal and were able to achieve injection rates of 12-15 tonnes/day, injecting a total of 760 tonnes of CO_2 and sequestering 690 tonnes. Injection was finally terminated in June 2005. Prior to the start of the field study, simulations were carried out to determine the best well placement for CO_2 breakthrough to occur within the timeframe of the field study. It was found that breakthrough actually occurred earlier than predicted by the modeling and this discrepancy is attributed to the initial simulation model containing only one layer in the vertical direction and therefore not capturing the buoyancy effects between CO_2 and water (van Wageningen, 2006).

2.4 Powder River Basin geology

The PRB is part of southeast Montana and northeast Wyoming, and is an asymmetrical syncline enclosed by the Bighorn Mountains in the west, the Miles City

Arch in the northeast, the Black Hills in the east, the Hartville Uplift in the southeast, and the Casper-Arch-Laramie Range in the southwest (Figure 2.4). The axis of the basin is close to its western side (NW-SE), with the eastern flank dipping gently to the west at 2-5° and the western flank dipping to the east at 20-25° (Flores and Bader, 1999) (Figure 2.5). The basin is composed of Upper Cretaceous barrier shoreface-marine sandstones and shales, and overlying Upper Cretaceous and Tertiary marine and fluvial deposits (Flores, 2004). The Tertiary units contain the coal-bearing Fort Union (Paleocene age) and Wasatch (Eocene age) formations, which were deposited in mires connected to fluvial systems that were fed from highland plateaus (Flores, 2004). The Tongue River Member of the Fort Union Formation is the primary coal-bearing unit of the PRB and is composed of interbedded sandstone, conglomerate, siltstone, limestone and coal (Advanced Resources International, Inc., 2002; Flores and Bader, 1999) (Figure 2.6). The coalbeds range in thickness from a few centimeters to 61 m, are elongate to lenticular in shape, and hundreds of meters to tens of kilometers in lateral extent (Flores and Bader, 1999; Flores, 2004). In addition, the coalbeds serve as aquifers and are recharged at outcrops on the eastern margin of the basin (Flores, 2004).

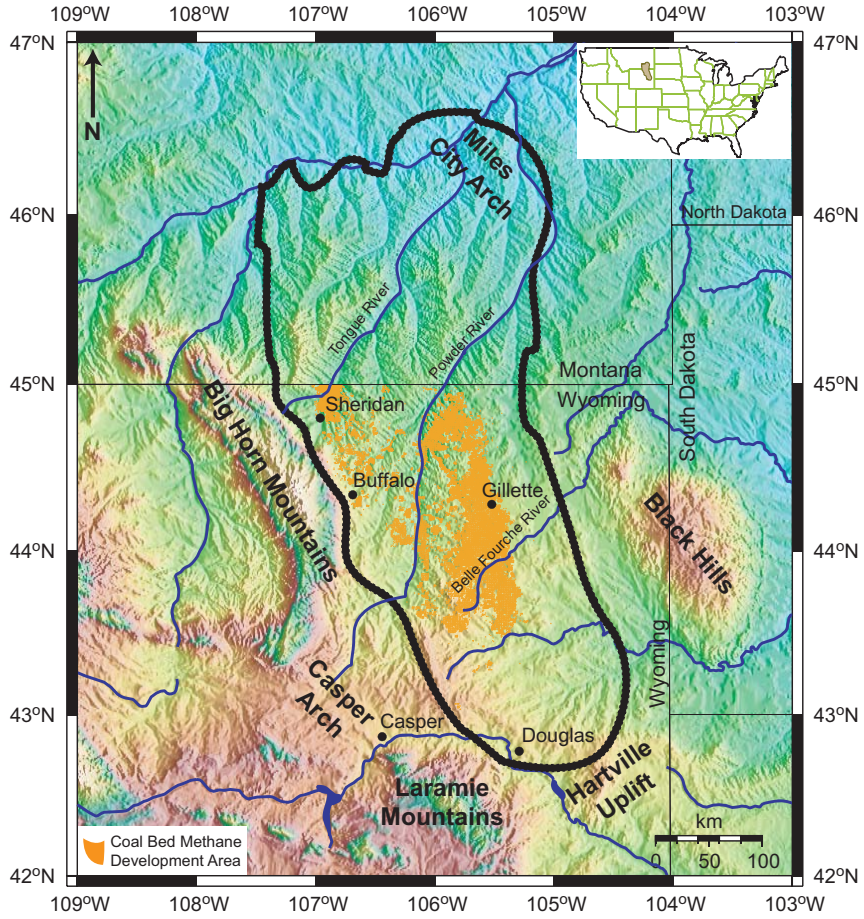

Figure 2.4: Map of surrounding geology to the PRB (modified from Colmenares and Zoback, 2007).

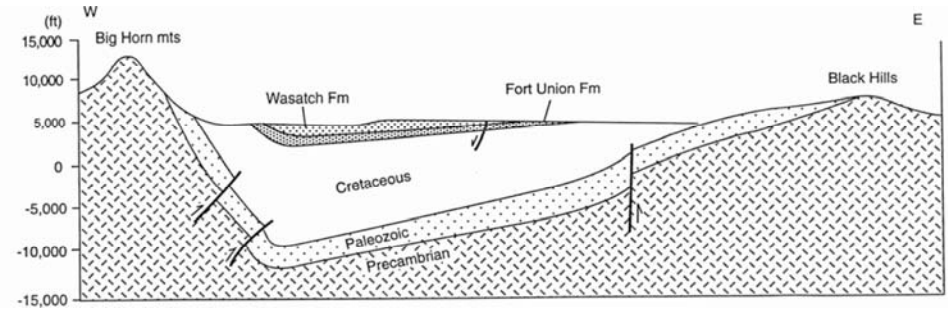

Figure 2.5: Cross section through the PRB (Advanced Resources International, Inc., 2002).

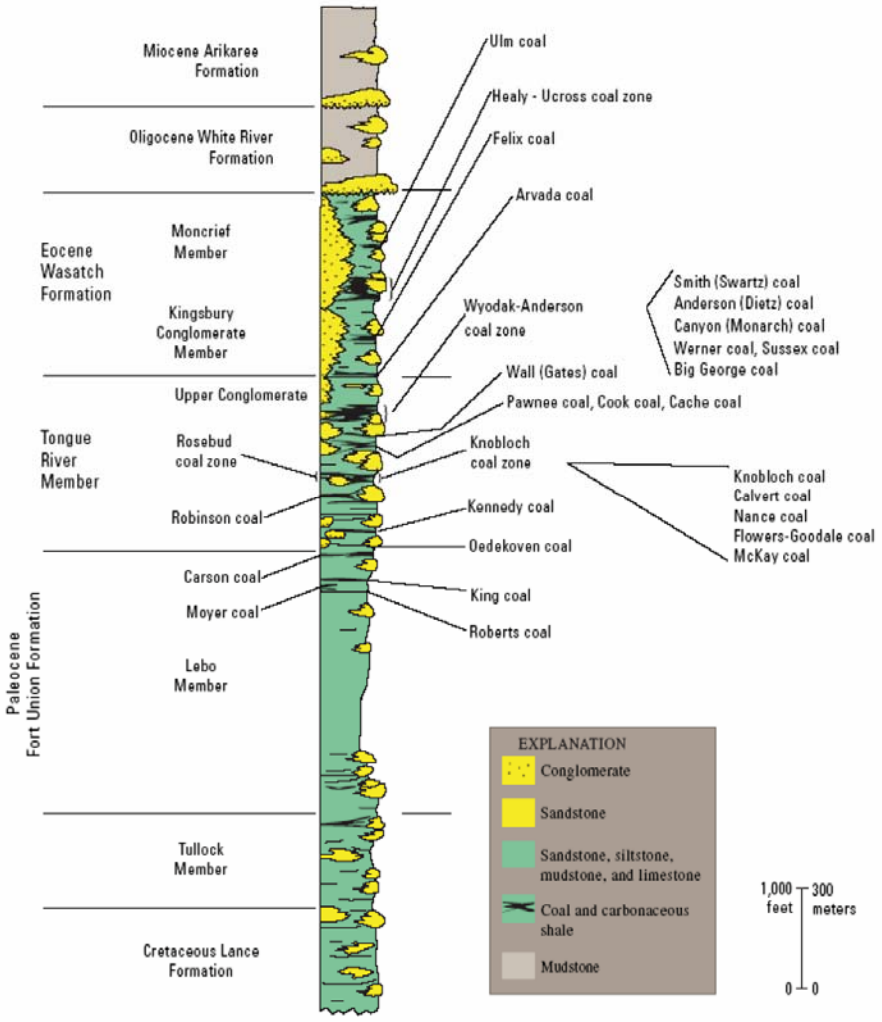

Figure 2.6: Generalized stratigraphic column of the PRB (Flores, 2004).

2.4.1 Big George coal

We have focused our study on the sub-bituminous Big George coal, which is located in the central part of the PRB, is an amalgamation of five coalbeds and is part of the Wyodak-Anderson coal zone of the Tongue River Member (Flores and Bader, 1999) (Figure 2.6). The average depth of the Big George coal is 335 m and it varies in thickness from 14 to 62 m. CBM generated by the Big George coal is composed of 87-94% CH_4, 4-12% CO_2 and trace amounts of hydrocarbons, and the CBM is biogenic in origin (Flores, 2004). However, the average composition of CBM

throughout the PRB is 73% CH_4, 5% CO_2, 22% N_2 and trace amounts of ethane (Flores, 2004). Cleat spacing in the Wyodak-Anderson coal zone ranges from less than a cm to 12 cm and face cleat orientations vary from NE to NW (Flores, 2004). It is believed that the face cleat orientations are due to tectonic stresses, as the face cleats are orientated parallel to NW and NE trending lineaments in the Bighorn Mountains (Flores, 2004) (Figure 2.4).

2.5 Reservoir characterization

2.5.1 Constructing the 3D structural model

We used gamma ray logs and water-enhancement tests to characterize the Big George coal in our study area. Gamma ray logs from CBM wells gave us the depth and thickness of the coal (Figure 2.7) and water-enhancement tests were analyzed to determine the direction of hydraulic fracture propagation in the coal if hydraulic fractures were to be created.

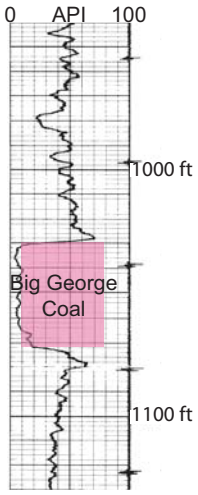

Figure 2.7: Gamma ray log from a CBM well producing from the Big George coal, PRB (WOGCC, 2007).

Water-enhancement tests are used by CBM operators in the PRB to connect the CBM wells to the natural coalbed fracture network. Water-enhancement involves pumping water down the CBM wells at a rate of ~60 barrels per minute (bpm) for ~15

minutes. During these tests it has been found that the operators are successfully hydraulically fracturing the coal and in some areas the hydraulic fractures propagate vertically, whereas in others they grow horizontally (Colmenares and Zoback, 2007). Knowing where vertical hydraulic fractures will form in the coal is especially important when choosing a site for CO_2 sequestration because hydraulic fractures that propagate vertically may penetrate the overlying strata, creating potential leakage conduits for CO_2, and are therefore areas undesirable for injecting CO_2. If we know that we are in an area where horizontal hydraulic fractures will form, then the risk of leakage from accidentally creating hydraulic fractures is less than in areas where vertical hydraulic fractures will grow.

Since hydraulic fractures open against the least principal stress (S_3) (Hubbert and Willis, 1957), we constructed a 3D model of the Big George coal in an area of the PRB where S_3 is the overburden stress (vertical), which means that hydraulic fractures will propagate horizontally in this area (Figure 2.8) (Colmenares and Zoback, 2007). Figure 2.9 shows the location of our study area in the PRB, corresponding to where we have built the 3D model.

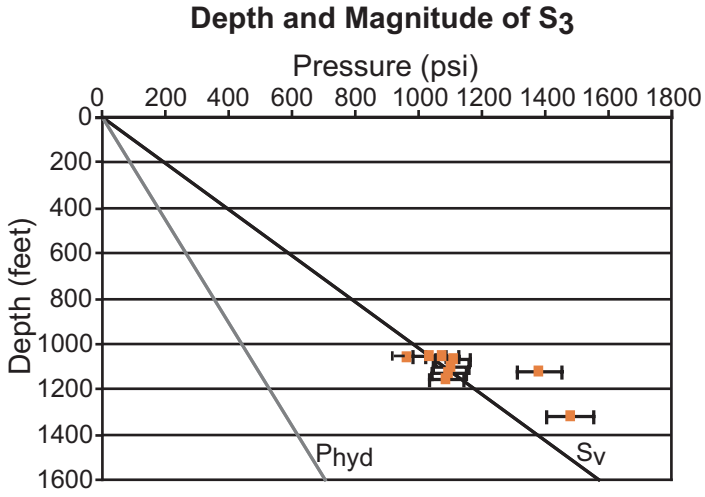

Figure 2.8: Depth versus pressure plot showing the magnitude of S_3 (orange squares) for the Big George coal in our study area. Note that S_3 is equal to the overburden stress (S_v) implying that hydraulic fractures created through water-enhancement are horizontal. P_{hyd} stands for hydrostatic pressure. Modified from Colmenares and Zoback (2007).

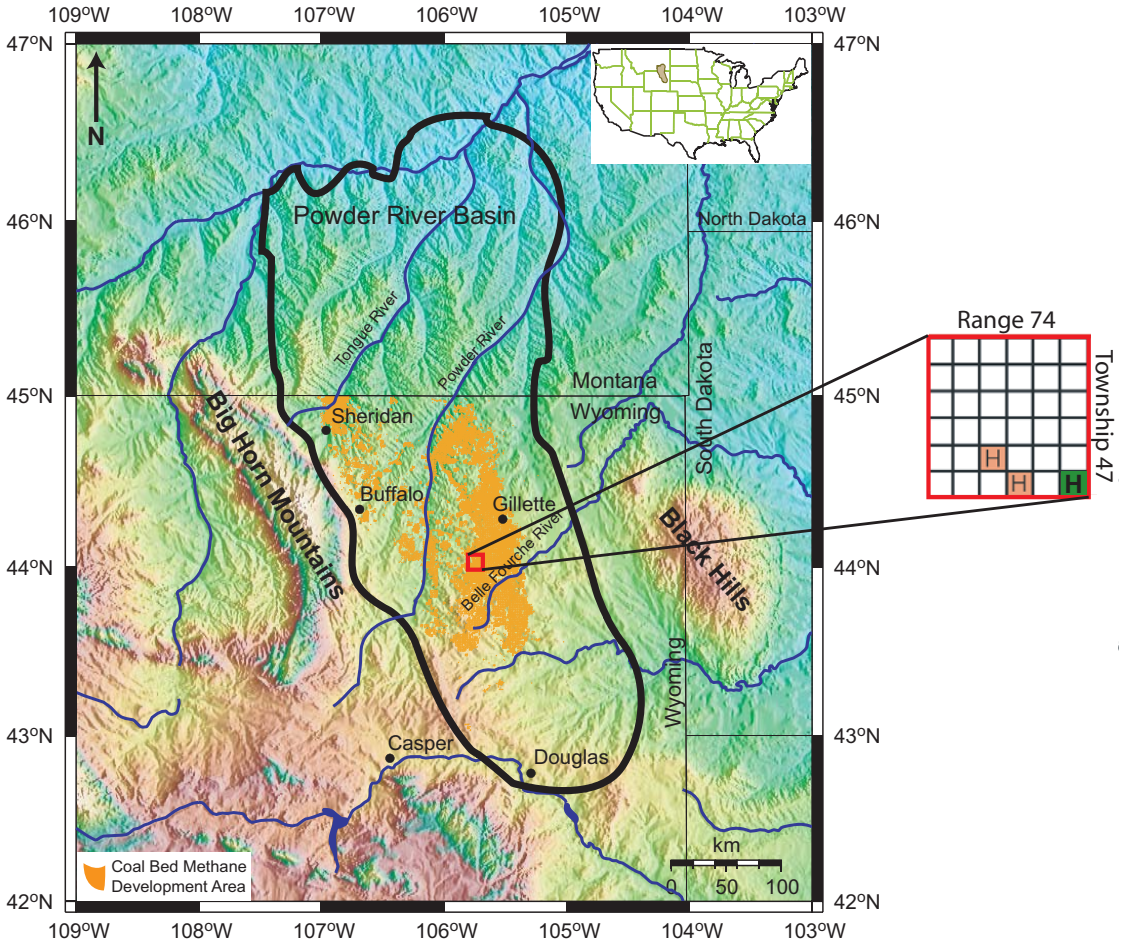

Figure 2.9: Location map of our study area. The red box corresponds to the township and range location of our study area. The green square corresponds to the section in which our 3D stochastic reservoir model was built and is in a section where Colmenares and Zoback (2007) identified horizontal fracture growth from water-enhancement (H stand for horizontal hydraulic fracture).

Our 3D model of the Big George coal is approximately 16 m thick and ranges in depth (to the top) from 315-361 m, with a slight dip to the west (Figure 2.10). The number of grid blocks in our model is 10332 (42 x 41 x 6) (Table 2.1). The grid spacing outlined in Table 2.1 was chosen because it optimizes running time and helps maintain numerical stability with a minimal loss of detail. The model was built using gamma ray logs from five active CBM wells in our study area (Figure 2.7).

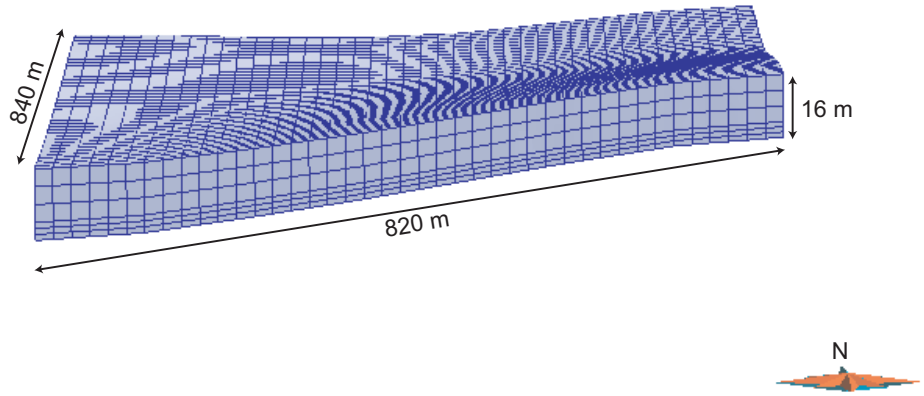

Figure 2.10: 3D simulation grid of the Big George coal. The bottom three layers are at a finer scale so that we can model a horizontal hydraulic fracture at the base of the injection well.

Table 2.1: The dimensions of our 3D simulation grid.

nx	42	dx	20 m
ny	41	dy	20 m
nz	6	dz	Top 3 layers at 4 m Bottom 3 layers at 1.3 m

2.5.2 Hydraulic fractures in coalbeds

We are interested in determining whether horizontal hydraulic fractures could be used to overcome the reduction in injectivity from matrix swelling, which was observed in both the RECOPOL (van Bergen et al., 2006) and Allison Unit pilot (Pekot and Reeves, 2002) studies. Productivity and injectivity is greatly improved by hydraulically fracturing coal (Holditch et al., 1988; Abass, et al., 1990; Puri et al., 1991), as this stimulation technique is used to connect the production and/or injection well to the coal cleats, which are the main conduits for fluid flow to the well. The mechanical properties of coal are significantly different to sands, which typically have values of Young's modulus between 20 GPa and 40 GPa (Holditch et al., 1988). In contrast, the Young's modulus for coal ranges from 0.7 GPa to 7 GPa. This low value of Young's modulus leads to wide hydraulic fractures, but because coals are not very stiff the fractures are unable to grow more than 60 m to 150 m in length (Holditch et

al., 1988; Abass et al., 1990). In our simulations we have used a length of 100 m, a porosity of 30% and a permeability of 1000 mD when modeling a hydraulic fracture and have placed it at the base of the injection well.

2.5.3 Employing geostatistics to populate the 3D model with petrophysical properties

A fundamental part of reservoir engineering is having a 3D model that honors all available data types and provides a quantitative and visual measure of the uncertainty in the properties being modeled (Journel, 1994; Deutsch, 2002). Stochastic reservoir modeling creates such a model by producing multiple realizations that are all plausible, in that they honor both the hard (reference data measured in the field or from well logs) and soft (data calibrated against the hard data) data, and are equally probable (Journel, 1994). These realizations all have a realistic level of heterogeneity, enabling reservoir engineers to move away from layer-cake, homogeneous models (Srivastava, 1994). By processing any number of these realizations through the same fluid flow simulator, the uncertainty in the reservoir model is transferred to the reservoir forecast, yielding a distribution of forecasts that are equally likely (Journel, 1994). This provides a quantitative measure of uncertainty in the simulation results.

The development of 3D stochastic reservoir models is of primary importance when carrying out a CO_2 sequestration project. All of the data collected during the reservoir characterization stage can be incorporated into the 3D model to visualize the reservoir and its characteristics. Geostatistical techniques can then be employed to populate the 3D grid with petrophyiscal properties using spatial correlation that is conditional to data at discrete sampling locations (hard data) (Journel, 1994). The stochastic modeling and geostatistics allows heterogeneity to be introduced in both the vertical and horizontal directions, while still honoring the hard data exactly, and the soft data within a tolerance, thereby creating a representational geologic model. Uncertainty can then be introduced through the generation of hundreds to thousands of realizations.

In the PRB there are no relevant seismic surveys and only minimal well log data is accessible (natural gamma logs). With no hard data available we used history-matching to constrain our permeability and porosity distributions created from literature values and generated multiple realizations to capture the uncertainty in those property fields. We used triangular distributions, simple kriging and sequential Gaussian simulation (SGS) to populate our 3D model with equally probable cleat and matrix permeability and porosity realizations (to capture the heterogeneity of the coal and to model the uncertainty in the cleat and matrix permeability and porosity distribution) (Deutsch, 2002) (see Appendix 1 for details). In total, we generated 15 realizations for both cleat and matrix permeability and porosity.

Our initial permeability and porosity values came from literature on PRB coal (Flores, 2004; Twombly, et al., 2004; Mavor et al., 2003; Ayers, 2002; USGS, 1995). We used triangular distributions for the cleat and matrix permeability and porosity distributions because the published reports gave only minimum and maximum values for these properties. We compared the different ranges given in each report for both cleat and matrix permeability and porosity, and chose end points and modes for each triangular distribution that encompassed all the ranges given for each property (Table 2.2). In addition, Laubach et al. (1998) conducted a study on coal cleat properties and observed that face cleat permeabilities can be three to ten times greater than butt cleat or vertical permeabilities. To capture this anisotropy in cleat permeability we forced the butt cleat and vertical permeabilities to be less than the horizontal face cleat permeability (Table 2.2).

For the total cleat porosity per grid block we used constant values, initially set at 0.02, because the selected simulator does not allow matrix shrinkage and swelling modeling with a variable cleat porosity field.

Table 2.2: Triangular distribution values for matrix and cleat permeability and porosity.

Property	Minimum and Maximum Value	Mode
Horizontal face cleat permeability	100-500 mD	300 mD
Horizontal butt cleat permeability	10-160 mD	100 mD
Vertical face cleat permeability	10-160 mD	100 mD
Matrix permeability	0.04-0.7 mD	0.5 mD
Matrix porosity	0.011-0.1	0.05

We constrained the cleat permeability and porosity values further through history-matching water production data from the active CBM wells used to build our 3D model (keeping gas production fixed) (WOGCC, 2006) (further details in appendix 2). The results of our history-match are detailed in Table 2.3 and the final cleat permeability values are outlined in Table 2.4 and illustrated in Figure 2.11.

Table 2.3: Results from history-matching water production data from active CBM wells used to build our 3D model.

Production Wells	True Water Production per Month (bbl/month) (WOGCC, 2006)	History-matched Water Production per Month (bbl/month)
Well 1	1768	1699
Well 2	2844	2750
Well 3	1696	1683
Well 4	3153	3198
Well 5	937	1111

Table 2.4: Final cleat permeability and porosity distributions derived from history-matching water production.

Property	Minimum and Maximum Value
Horizontal face cleat permeability	4-55 mD
Horizontal butt cleat permeability	0.5-18 mD
Vertical face cleat permeability	0.5-18 mD
Total cleat porosity per grid cell	0.017-0.63

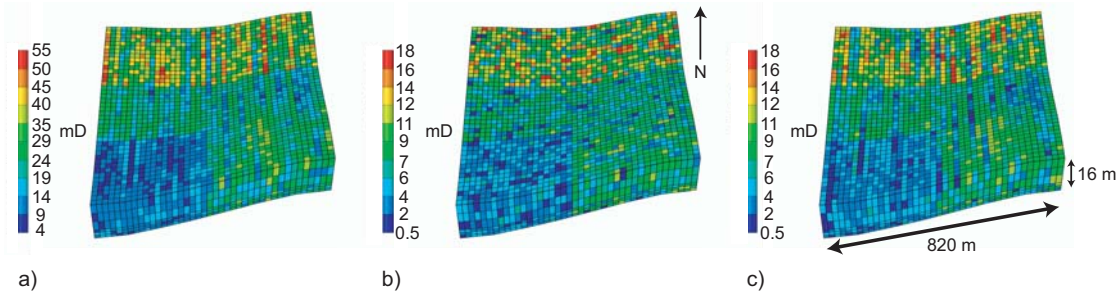

Figure 2.11: Final stochastic 3D reservoir model. a) Horizontal face cleat permeability. b) Horizontal butt cleat permeability. c) Vertical face cleat permeability. This figure shows our 3D model populated with cleat permeability values for one realization. The heterogeneity and anisotropy in coal cleat permeability is modeled using geostatistical techniques. The horizontal face cleat permeability is higher than in the butt cleat and vertical directions (Laubach et al., 1998).

2.5.4 Selecting an ECBM simulator

To properly model transport and adsorption of CO_2 in coalbeds Law et al. (2002; 2003; 2004) proposed that numerical simulators should have the ability to simulate dual porosity, multiple gas components, multiphase Darcy flow in the cleats, pure and mixed gas diffusion between the coal matrix and cleats, pure and mixed gas adsorption in the matrix, adsorption and desorption of pure and mixed gas at the coal surface, coal matrix shrinkage and swelling due to gas desorption and adsorption, dilation and compaction of the cleats due to stress changes, non-isothermal effects with gas injection and movement of water between the matrix and cleats. Law et al. (2002; 2003; 2004) carried out a comparison study of numerical CBM simulators to test whether they incorporated the features required to model gas fluid flow and adsorption and to identify areas needing improvement for modeling ECBM (Law et al., 2002). Eight numerical simulators participated in the study, including GEM, ECLIPSE, COMET, SIMED II, GCOMP, METSIM 2, MoReS and COALCOMP. Table 2.5 outlines the features available for five of the numerical simulators involved in this study.

Table 2.5: Numerical simulator features for CBM and ECBM (Law et al., 2002). A tick means that the simulator has the specified feature and a cross means that it does not.

CBM Simulators	GEM	ECLIPSE	COMET	SIMED II	GCOMP
Mutliple Gas Components (3 or more: CH_4, CO_2 & N_2)	√	×	√	√	√
Dual Porosity Approach	√	√	√	√	×
Mixed Gas Diffusion (Different Diffusion Rates)	√	√	√	√	×
Mixed Gas Adsorption (Extended Langmuir Model)	√	×	√	√	√
Stress Dependent Permeability and Porosity	√	√	√	√	√
Coal Shrinkage/Swelling	√	×	√	√	√

There were four parts to the study, the first focused on a single well test and pure CO_2 injection into a five-spot pattern model. The second was an extension of the first, but with CO_2-enriched flue gas injection. The third was more complex, testing diffusion between the coal matrix and cleats and the effect of matrix shrinkage and swelling on gas adsorption. The final part involved history matching field-test data collected by the ARC during injection of pure CO_2 and flue gas into coalbeds in Alberta, Canada (ECLIPSE did not participate in this part). In general there was very good agreement between the results (production well BHP, injection well BHP, gas production rates, gas production compositions and gas saturation maps) from the different simulators for all four parts (Law et al., 2002; 2003; 2004).

For our fluid flow simulations we chose to use the Computer Modeling Group's Generalized Equation-of-State Model Compositional Reservoir Simulator (GEM), which was built to simulate ECBM scenarios. GEM is a compositional simulator with the ability to simulate dual porosity, multiple gas components, mixed gas diffusion, mixed gas adsorption, stress dependent porosity and permeability, and coal shrinkage and swelling (Law et al., 2002). As shown above, many commercial simulators capable of modeling CBM processes are available (e.g., Eclipse100, COMET, etc.), but GEM was chosen because of its compositional functionality and ability to

incorporate key physical mechanisms involved in ECBM, most notably matrix shrinkage and swelling.

2.5.4.1 Features and limitations of GEM

As noted above, GEM has the ability to simulate all the features stipulated by Law et al. (2002; 2003; 2004), except for adsorption at the coal cleat surface, movement of water between the matrix and cleats, and non-isothermal effects with gas injection if there is a phase change. Specifically, GEM does not allow water in the coal matrix or adsorption in the cleats. In addition, there is some debate over whether the current matrix shrinkage and swelling models incorporated in ECBM simulators are able to simulate correctly these observed mechanisms (Pekot and Reeves, 2002; Palmer, 2004; Palmer et al., 2006). GEM 2005 uses an extended Palmer and Mansoori equation (Palmer and Mansoori, 1996; 1998; GEM, 2005) and all other ECBM simulators that are currently available use some form of the Palmer and Mansoori equation. In section 2.7.1 we will discuss some of the problems associated with the Palmer and Mansoori equation (GEM, 2005) and in Chapter 3 we report on a sensitivity analysis we ran on each of the terms in the equation.

GEM uses both the Langmuir and extended multicomponent Langmuir models to model adsorption in coalbeds. The SUPRI-A group, from the Department of Energy Resources Engineering, Stanford University, have conducted lab experiments on crushed coal samples from the PRB, looking at adsorption/desorption for dry and moist coal, using pure and mixed gases. They found that the Langmuir and extended Langmuir isotherms could be used to fit their observed adsorption/desorption curves (Figure 2.12) (Kovscek and Orr, 2004). In addition, they noted that once a coal contained over 5% moisture, the adsorption curve did not change (Kovscek and Orr, 2004). Since GEM does not allow water/moisture in the coal matrix we used the SUPRI-A group's adsorption laboratory results for a moist coal (PRB coals have 30% moisture (Ellis, 2002)) to incorporate the effects of moisture on gas adsorption and partly overcome GEM's limitation of not allowing water in the coal matrix (Figure 2.13). GEM can also calculate the effect the presence of water would have on gas

diffusion through the matrix, as well as the effect the presence of water in the cleats would have on reducing the contact area for gas trying to flow from the cleats to the matrix. To minimize simulation time and maintain numerical stability, we have only modeled the second water effect (the default choice in GEM 2005).

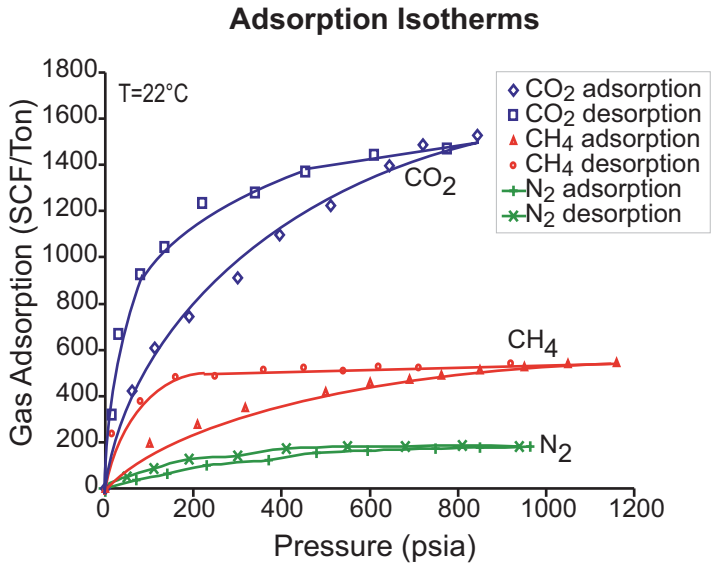

Figure 2.12: Adsorption and desorption isotherms for CO_2, CH_4 and N_2 from dry, crushed, PRB coal samples. Symbols correspond to measured data and lines correspond to the Langmuir model fit to the data, which is used by GEM to model adsorption in coalbeds. Modified from Kovscek and Orr (2004).

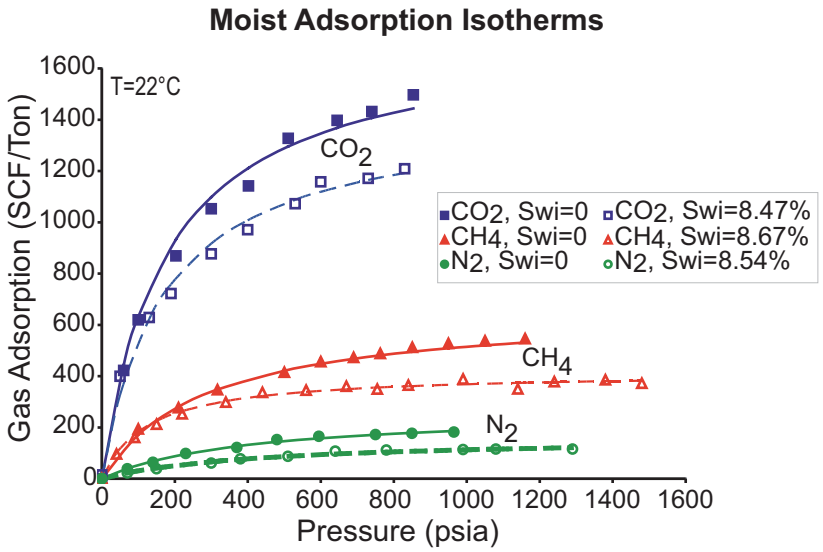

Figure 2.13: Moist and dry adsorption isotherms for crushed, PRB coal samples. Closed symbols correspond to dry adsorption isotherms and open symbols correspond to moist adsorption isotherms. Note that the moist adsorption isotherms are lower than the dry adsorption isotherms. Modified from Tang et al. (2005).

GEM also does not account for gas adsorption in the cleats which means that we cannot model a permeability decrease due to CO_2 molecules lining the cleat surface. However, since the matrix is the primary porosity system, this may not affect the overall mass balance (A. Kovscek, personal communication, 2005). In regards to matrix shrinkage and swelling modeling, GEM 2005 uses an extended Palmer and Mansoori equation (Palmer and Mansoori, 1996; 1998; GEM, 2005), which allows for more than one gas species in the equation and is able to model permeability loss due to matrix swelling from the adsorption of CO_2 (equation 1). The extended equation incorporates the generalized multi component Langmuir model,

$$\frac{\Phi}{\Phi_{ref}} = 1 + c_f (p - p_{ref}) + \frac{1}{\Phi_{ref}} \left(1 - \frac{K}{M}\right) \left(\sum_{j=1}^{j=n} \frac{\varepsilon_{Lj} y_{ref,j} \, p_{ref} / p_{Lj}}{1 + p_{ref} \sum_{k=1}^{k=n} y_{ref,k} / p_{Lk}} - \sum_{j=1}^{j=n} \frac{\varepsilon_{Lj} y_j \, p / p_{Lj}}{1 + p \sum_{k=1}^{k=n} y_k / p_{Lk}} \right), \quad (1)$$

where Φ_{ref} is the reference state (initial) natural fracture porosity, Φ is the fracture porosity at pressure p, c_f is the fracture pore volume compressibility (1/kPa), p_{ref} is the reference state (initial) pressure (kPa), p is pressure (kPa), ε_{Lj} and ε_{Lk} are the volumetric strains at infinite pressure for components j and k, p_{Lj} and p_{Lk} are the Langmuir pressures for the volumetric strain at infinite pressure for components j and k, K is the bulk modulus, M is the axial modulus, $y_{ref,j}$ and $y_{ref,k}$ are the composition of components j and k at reference state (initial) and y_j and y_k are the compositions of components j and k at pressure p. In contrast, the original Palmer and Mansoori equation (Palmer and Mansoori, 1996; 1998) only allowed for one gas species in the model,

$$\frac{\Phi}{\Phi_i} = 1 + c_f (p - p_i) + \frac{\varepsilon_L}{\Phi_i}\left(1 - \frac{K}{M}\right)\left(\frac{p_i}{p_i - p_L} - \frac{p}{p + p_L}\right), \tag{2}$$

where Φ_i is the initial fracture porosity, Φ is the fracture porosity at pressure p, c_f is the fracture pore volume compressibility (1/kPa), p_i is the initial pressure (kPa), p is pressure (kPa), ε_L is volumetric strain at infinite pressure, p_L is the Langmuir pressure for the volumetric strain at infinite pressure, K is the bulk modulus and M is the axial modulus.

2.5.5 Fluid flow simulation set-up

The reservoir fluid flow simulations were run on a 5-spot well pattern (four production wells at each corner and one injection well in the center) with 80-acre well spacing using the Computer Modelling Group's ECBM simulator GEM. Our model and simulation input parameters are listed in Table 2.6. We have run our base case simulations with pure CO_2 gas injection, with and without coal matrix shrinkage and swelling, and with and without a horizontal hydraulic fracture placed at the base of the injection well. The horizontal hydraulic fracture was modeled as a square fracture with dimensions 100 m x 100 m, porosity of 30%, and permeability of 1000 mD. To

prevent accidental hydraulic fracturing of the coal near the injection well, we set the maximum value of the bottom hole pressure (BHP) to be less than 6200 kPa (900 psi), the fracture pressure in this area (Colmenares and Zoback, 2007). We assume that the coalbed is overlain by a thick confining unit by using no-flow boundaries in our simulations. The coal is modeled as water saturated and coal matrix shrinkage and swelling was modeled by the extended Palmer and Mansoori equation (equation 1) (1996; 1998; GEM 2005) included in GEM 2005. Finally, the coals in the PRB are under-pressured, so we have used the regional pressure gradient reported by Advanced Resources International, Inc. (2002) of 7.12 kPa/m (0.315 psi/ft).

Table 2.6: Input parameters for our base case fluid flow simulations.

Input Parameters	Values	References
Initial temperature, °C	22	Tang et al. (2005)
Reservoir pressure gradient, kPa/m	7.12 (0.315 psi/ft)	Advanced Resources International, Inc. (2002)
Coal gas composition	90% CH_4, 0% CO_2, 10% N_2	
Water saturation	99% in cleats, 0% in matrix	Advanced Resources International, Inc. (2002)
Injector BHP constraint, kPa	4000	Less than the fracture pressure in study area, 6200 kPa (Colmenares and Zoback, 2007)
Producer BHP constraint, kPa	1700	History-matching
Cleat spacing, cm	10	Flores (2004), Ayers (2002)
Matrix permeability, mD	0.04-0.7	Flores (2004)
Matrix porosity	0.011-0.1	Advanced Resources International, Inc. (2002)
Cleat permeability, mD	Horizontal face cleat direction, 4-55, horizontal butt cleat direction, 0.5-18 and vertical direction, 0.5-18	Literature (Flores, 2004; Twombly, et al., 2004; Mavor et al., 2003; Ayers, 2002; Laubach et al., 1998; USGS, 1995), and history-matching
Total cleat porosity per grid cell	0.017-0.63	Literature (Twombly, et al., 2004; Mavor et al., 2003; Advanced Resources International, Inc., 2002; USGS, 1995) and history-matching

Adsorption/desorption parameters for PRB coal samples (dry coal desorption for CH_4 and N_2 and moist coal adsorption for CO_2)	Langmuir volume: 0.577 gmole/kg for CH_4, 1.67 gmole/kg for CO_2 and 0.262 gmole/kg for N_2	Tang et al. (2005)
	Inverse Langmuir pressure, 1.7E-3/kPa for CH_4, 8.5E-4/kPa for CO_2 and 8.3E-4/kPa for N_2	
Diffusion coefficient, cm^2/s	0.000001 (100 days) for CH_4, CO_2 and N_2	Seto in Kovscek and Orr (2004)
Rock compressibility	Rock compressibility, 1.45E-7/kPa for matrix and 2.9E-5/kPa for cleats	Law et al. (2003) for matrix and USGS (1995) for cleats
	Reference pressure, 2246 kPa for matrix and cleats	
Shrinkage/swelling for modified Palmer and Mansoori equation in GEM 2005	Strain Langmuir pressure for CH_4, 2069 kPa, CO_2, 345 kPa and N_2, 344 kPa	Harpalani (2005),
	Young's modulus, 0.413E7 kPa	Jones et al. (1988),
	Poisson's ratio, 0.39	Jones et al. (1988),
	Strain at infinite pressure for CH_4, 0.007, CO_2, 0.013 and N_2, 0.004	Harpalani (2005),
	Exponent, 3	Palmer and Mansoori (1996; 1998)
S_3, kPa	6200	Colmenares and Zoback (2007)

For relative permeability curves, we used curves obtained from San Juan coal samples by Gash (1991) (Figure 2.14). Mavor et al. (2003) also used these curves in simulations to history-match CBM production from PRB coal and obtained a good match with the production data. These curves have also been used in simulation studies on Alberta coal (Mavor et al., 2004; Gu and Chalaturnyk, 2005) and in the Law et al. (2002; 2003; 2004) simulation comparison exercises.

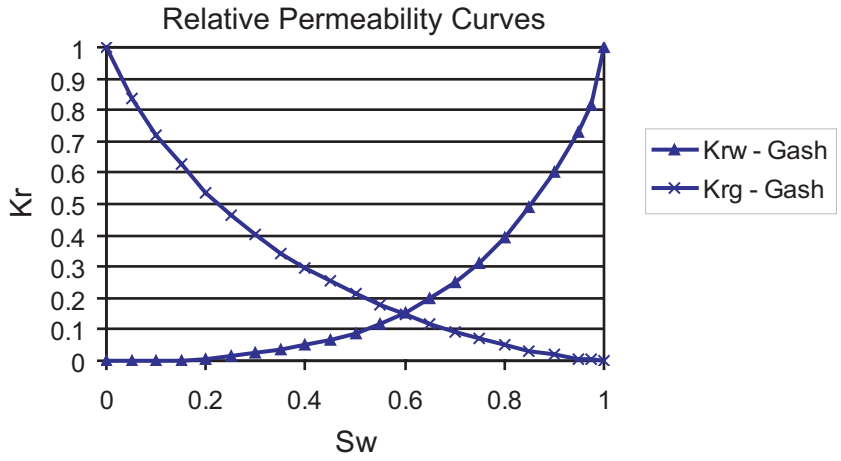

Figure 2.14: Relative permeability curves used in our simulations from Gash (1991). Kr stands for relative permeability, Sw for water saturation, Krw for relative permeability with respect to water and Krg for relative permeability with respect to gas.

In addition, we used gas adsorption/desorption isotherms specific to PRB coal, where coal samples were obtained from a similar depth as our model depth (Tang et al., 2005). For our CO_2 adsorption isotherm we used Tang et al.'s (2005) CO_2 adsorption isotherm derived from laboratory experiments on moist PRB coal, as mentioned earlier, since PRB coals contain 30% moisture (Ellis, 2002) (Figure 2.13). For our CH_4 and N_2 isotherms we used desorption isotherms derived from dry coal (at present there are no desorption curves for moist coal) since N_2 and CH_4 are desorbing throughout our simulations (Tang et al., 2005). Tang et al. (2005) observed hysteresis with desorption and noted that the desorption curves followed different paths depending on the pressure at which desorption was initiated (Figure 2.15). We therefore used Tang et al.'s (2005) desorption curves for CH_4 and N_2 that start at 3275 kPa (475 psi), as this is close to the reservoir pressure of the Big George coal (Figure 2.15).

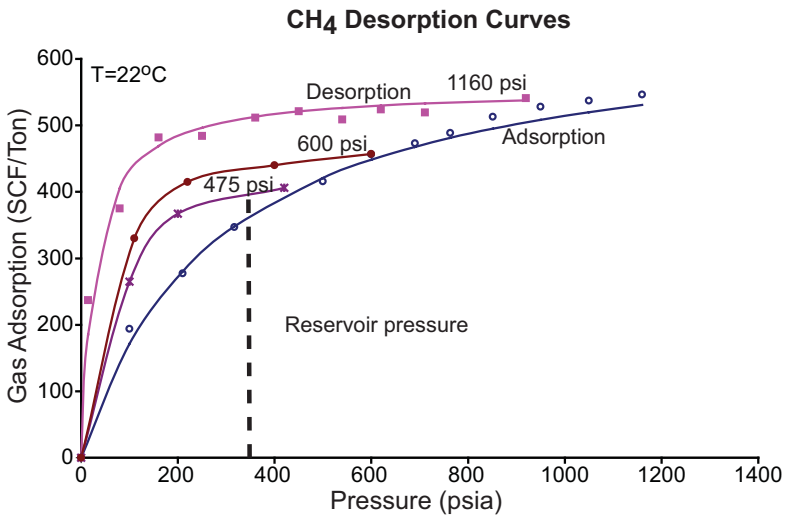

Figure 2.15: Desorption isotherms for CH_4 from dry, crushed, PRB coal samples. The reservoir pressure line marks the reservoir pressure used in our fluid flow simulations (Table 2.6). Modified from Tang et al. (2005).

2.6 Feasibility of CO_2 sequestration and ECBM in the PRB

Our first base case simulation is of primary production for 18 years (6720 days) with no CO_2 injection, whereas subsequent base case simulations include CO_2 injection after 5 years of CBM production, with a total simulation time of 18 years. The additional base cases include 1) pure CO_2 injection after 5 years of primary production with no matrix shrinkage and swelling modeling and no hydraulic fracture, 2) pure CO_2 injection after 5 years of primary production with no matrix shrinkage and swelling modeling but with a horizontal hydraulic fracture placed at the base of the injection well, 3) pure CO_2 injection after 5 years of primary production with matrix shrinkage and swelling modeling but no hydraulic fracture, and 4) pure CO_2 injection after 5 years of primary production with matrix shrinkage and swelling modeling and with a horizontal hydraulic fracture placed at the base of the injection well. In the following chapter (Chapter 3) we will investigate the sensitivity of our base case results to the input parameters used in our simulations, comparing the sensitivity results to base case three above.

2.6.1 Primary production results

Results from our primary production simulation suggest that over an 18 year period ~68,000 MSCF of CH_4 could be produced without the use of enhanced coalbed methane recovery, assuming that the well life can reach ~18 years. This corresponds to a recovery factor of only ~2%.

Figure 2.16 shows CH_4 adsorption before production and after 18 years of primary production in the coal matrix. As can be seen from Figure 2.16, not much CH_4 desorption has occurred over the 18 year time period, which is why the recovery factor is so low. The average adsorption per m^3 has gone from 542 gmole before production to 531 gmole after 18 years of production. This suggests that primary production with vertical wells is actually a very inefficient way of producing CBM. Figure 2.17 is of the water saturation in the cleats before and after production and it appears that most of the water produced over the 18 year time period has come from the upper part of the coalbed.

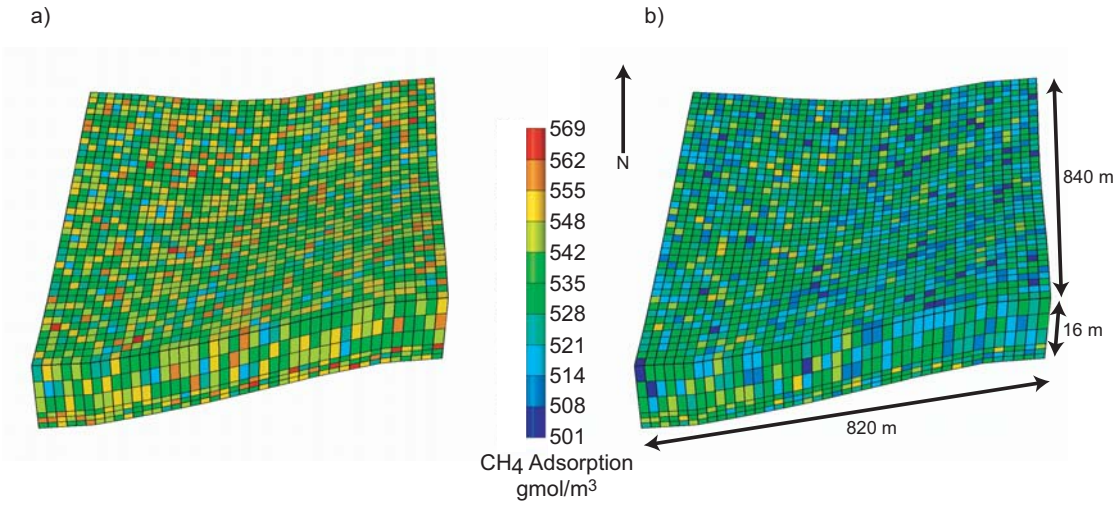

Figure 2.16: CH_4 adsorption in the coal matrix a) before primary production and b) after 18 years of primary production.

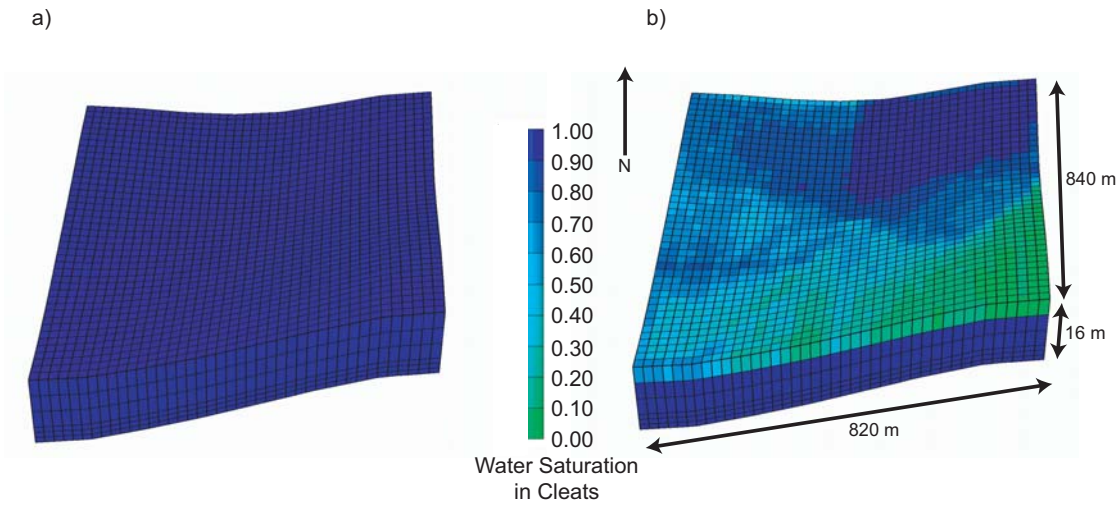

Figure 2.17: Water saturation in the cleats a) before primary production and b) after 18 years of primary production.

2.6.2 CO_2 sequestration and enhanced coalbed methane recovery results

Our fluid flow simulations of CO_2 injection into the Big George coal of the PRB suggest that gravity and buoyancy are the major driving forces behind gas migration within the coal, that coal matrix swelling results in a reduction in CO_2 injectivity, that we can sequester 99% of the total CO_2 injected into the coal, and that ECBM results in a significant increase in CH_4 production.

Fluid flow maps reveal that the injected CO_2 migrates upwards at first and then along the top of the coal (Figure 2.18a). The upward migration of gas is caused by buoyancy forces, owing to the density difference between injected CO_2 and resident water that create gravity override between the gas and water - the gas is less dense than the water, so the gas rises relative to the water. Placing a hydraulic fracture at the base of the injection well assisted in greater penetration of gas into the base of the reservoir and created a more uniform vertical gas sweep, but the gas still rises to the top of the coal rather than migrating laterally from the hydraulic fracture (Figure 2.18b). (We note that the 6 layer model is unable to resolve the gravity gas tongue, so we have run a simulation with 24 layers in the vertical direction to try and capture the gas migration in more detail. The 6 layer model is able to give us a broad scale CO_2 breakthrough prediction, but a more refined gird in the vertical direction will give a

more accurate prediction. The results from the 24 layer simulation are reported in section 2.7.2.)

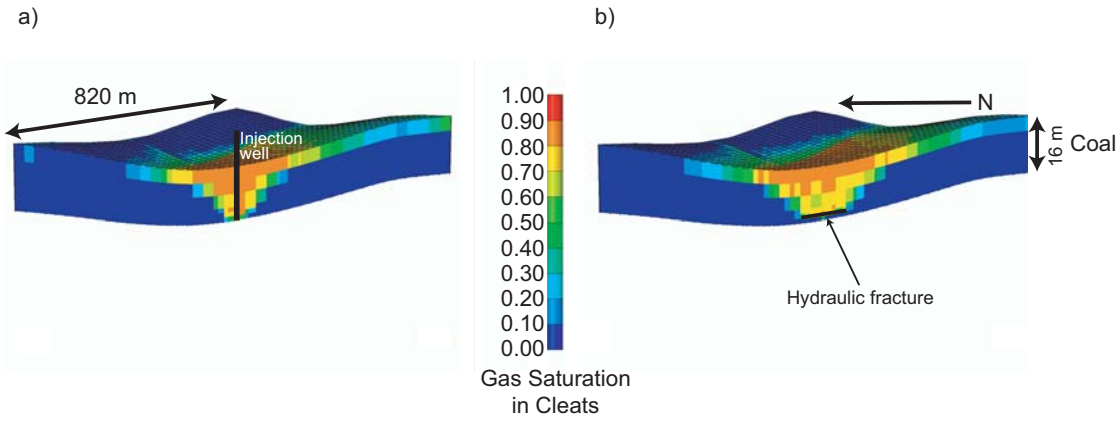

Figure 2.18: Cross section through our simulation model showing gas saturation in the cleats after 13 years of CO_2 injection a) without the presence of a horizontal hydraulic fracture and b) with the placement of a horizontal hydraulic fracture at the base of the injection well (cross section is from the SE to NW corners of the model). Note that the gas rises to the top of the coal before migrating laterally. We are showing results from our base case simulations that include matrix shrinkage and swelling modeling.

We also observe that the CO_2 sweeps the water within the cleats ahead of the gas front so that more water is produced during the ECBM process than during primary production only (Figure 2.19). The average daily water production associated with primary production in our study area is ~77 bbl/day compared with ~150 bbl/day estimated by our simulations incorporating ECBM recovery.

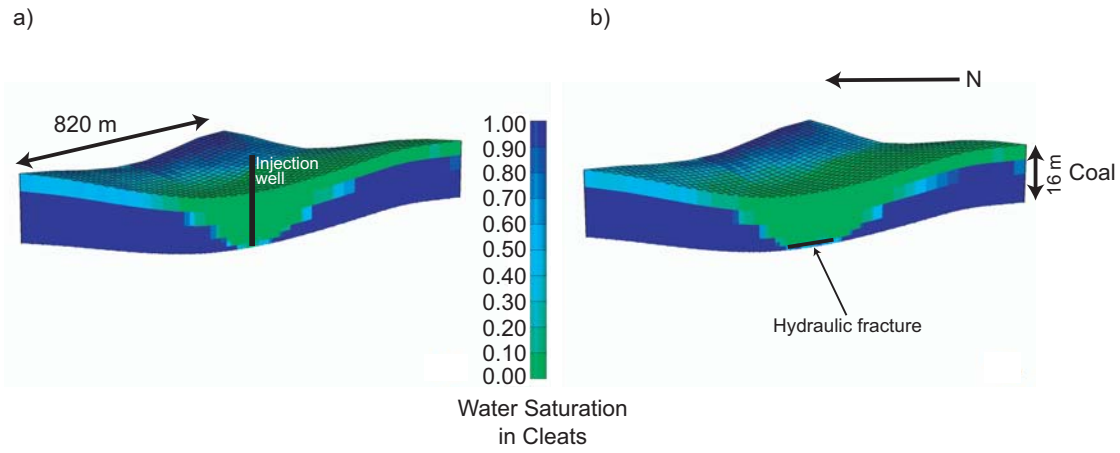

Figure 2.19: Cross section through our simulation model showing water saturation in the cleats after 13 years of CO_2 injection a) without the presence of a horizontal hydraulic fracture and b) with the placement of a horizontal hydraulic fracture at the base of the injection well (cross section is from the SE to NW corners of the model). We are showing results from our base case simulations that include matrix shrinkage and swelling modeling.

The adsorption maps in Figure 2.20 illustrate the area at the top of the coalbed where CH_4 has desorbed and CO_2 has adsorbed after 13 years of CO_2 injection. We observe that where CO_2 has been adsorbed the CH_4 in place has desorbed, which is what we would expect with ECBM recovery. Furthermore, we note that the CO_2 gas has preferentially migrated toward the SE corner of the model, which is the highest point in the model. This preferential flow path implies that gravity and buoyancy are the major forces behind gas migration and that coal cleat permeability is a secondary factor (cleat permeabilities in the NE and NW corners are slightly higher than those in the SE corner (Figure 2.20)).

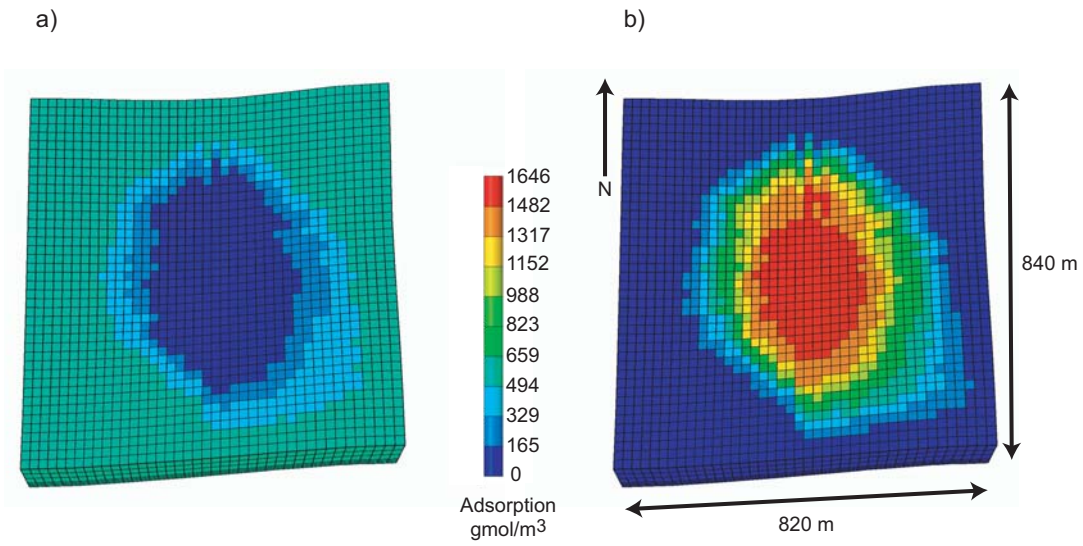

Figure 2.20: Adsorption maps for a) CH_4 and b) CO_2 at the top of the coalbed after 13 years of CO_2 injection. We are showing results from our base case simulation that includes matrix shrinkage and swelling modeling but no hydraulic fracture.

The total volumes of CO_2 that can be sequestered and CH_4 that can be produced after 5 years of primary production and 13 years of CO_2 injection into a 160 acre area of the Big George coal are shown in Figure 2.21. We estimate that the total volume of CO_2 that can be sequestered within 160 acres is ~118,000 tonnes and the ECBM recovery from this same area is ~440,000 MSCF. This actually corresponds to a CH_4 recovery factor of only ~10% due to the gas buoyancy effect which causes the CO_2 to immediately rise to the top of the coal and only contact a small percent of the total coal volume - the remaining CH_4 is still locked in the coal matrix. Re-configuring (optimizing) the well placement so that additional areas of the coal are contacted by CO_2 would help increase this recovery factor.

In addition, our simulations suggest that after 13 years of CO_2 injection we can sequester ~99% of the total CO_2 injected into the Big George coal, assuming the coalbed is overlain by an impermeable caprock, and that CH_4 production will be ~5-8 times greater with CO_2 injection than without (depending on the base case scenarios; Figure 2.21).

Our simulations also show that coal matrix swelling will reduce CO_2 injectivity (~10% reduction in injectivity), but that hydraulically fracturing the coal close to its

base will mitigate the negative effect of permeability reduction on injection rate (Figure 2.21). Placement of a hydraulic fracture at the base of the injection well increased the total volume of CO_2 injected into the coal by ~40% (Figure 2.21). However, the addition of a hydraulic fracture also led to an increase in the total volume of CO_2 produced at 6720 days; from ~270 to 1350 tonnes (~500% increase) (total simulation time was 6720 days). Breakthrough[1] occurred at 6720 days for the case with a hydraulic fracture and no matrix shrinkage and swelling modeling, but no breakthrough was observed for the case with a hydraulic fracture and with matrix shrinkage and swelling modeling (at the time simulations were stopped there was also no breakthrough in the base cases without hydraulic fractures).

Therefore, it appears that for the high permeability coals of the PRB, matrix swelling will not significantly affect CO_2 sequestration volumes, but where swelling is observed, hydraulic fractures can increase the total volumes sequestered and produced. In addition, the swelling acts to slow the rate of gas migration which helps to increase the time until breakthrough when hydraulic fractures are used for stimulation.

[1] We define CO_2 breakthrough as the time at which 1% of the total CO_2 injected is produced. We are interested in maximizing CO_2 sequestration, so do not allow recycling of the produced CO_2. However, recycling of CO_2 could be used with different well configurations so that more of the coal volume is contacted with CO_2, increasing CH_4 recovery and sequestration.

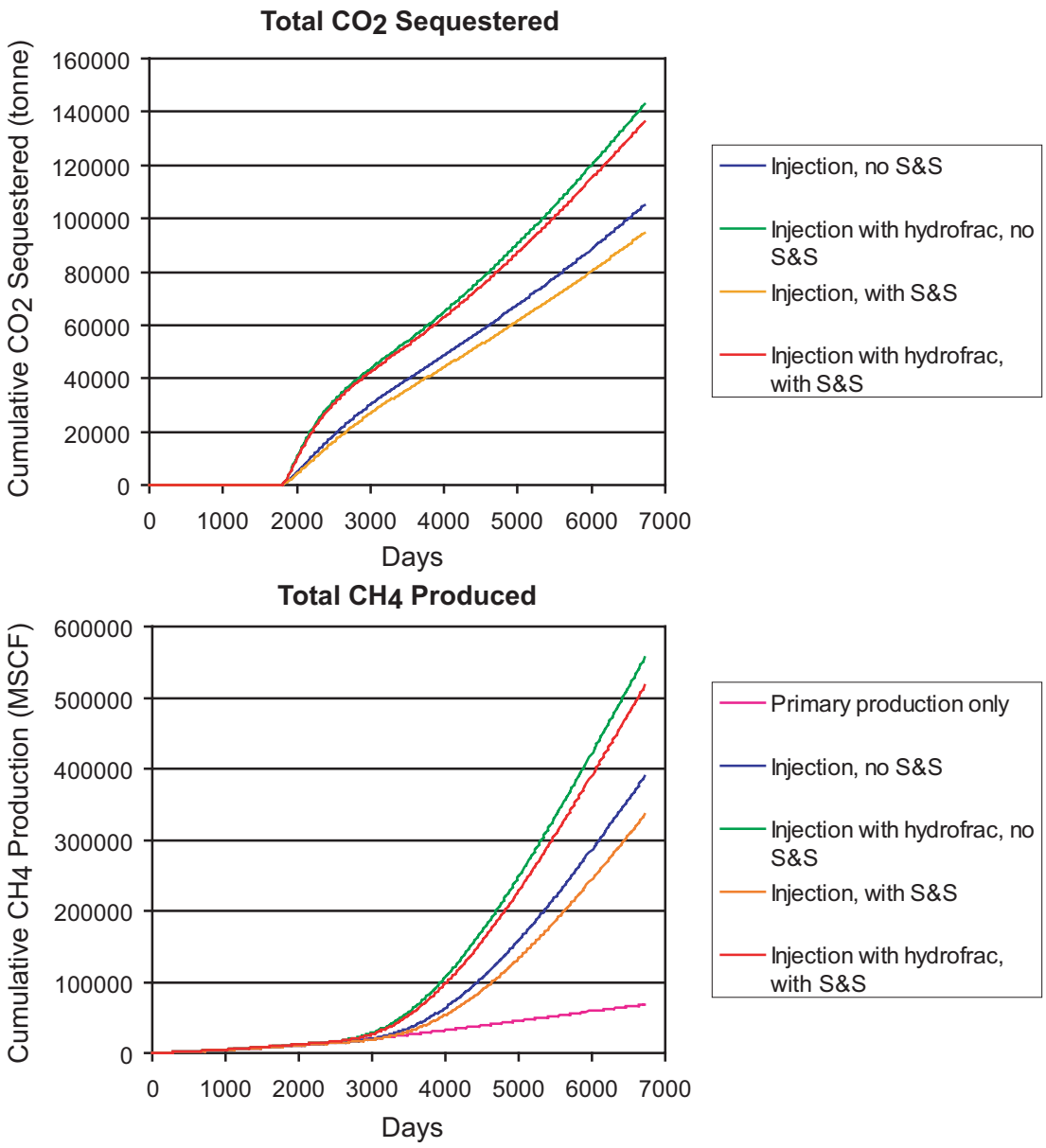

Figure 2.21: Total volume of CO_2 injected and total volume of CH_4 produced after 13 years of CO_2 injection. Hydraulically fracturing the coal at the base of the injection well increased the total volume of injected CO_2 by ~40%. With ECBM there was a ~5-8 fold increase in CH_4 production. Hydrofrac stands for hydraulic fracture and S&S stands for matrix shrinkage and swelling.

Figure 2.22 shows the yearly CO_2 gas injection rate into the Big George coal by one injection well and we find that the average gas injection rate is ~9 kt of CO_2 a year. Based on this injection rate, it would take ~7,000 injection wells (each with a lifetime of ~13 years) to sequester the current CO_2 emissions for the State of Wyoming (~63 million tonnes/yr (EIA, 2007)).

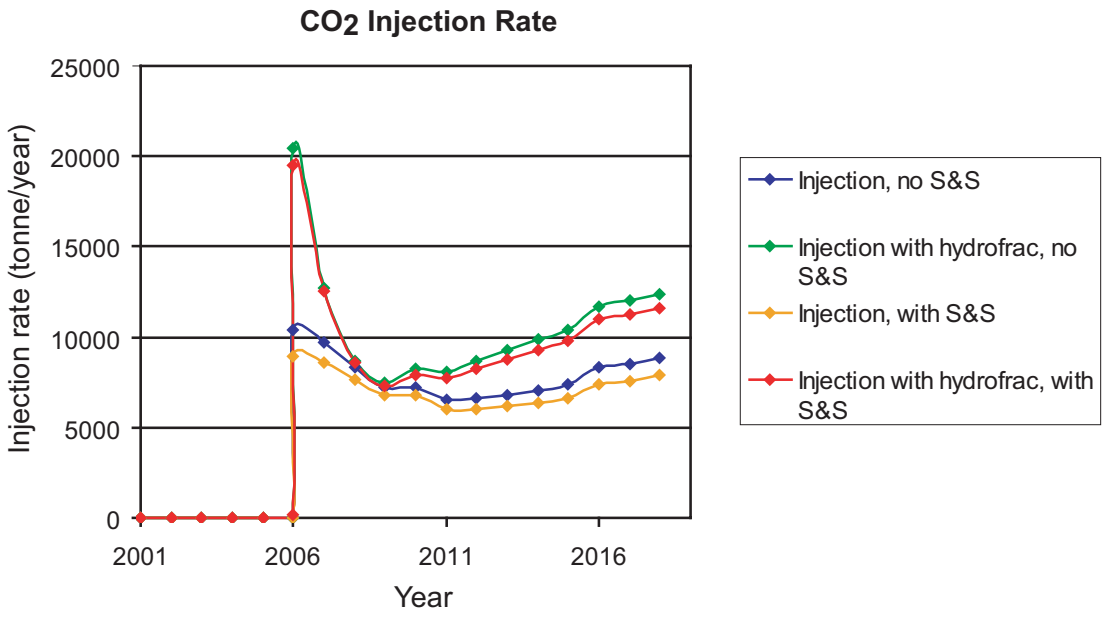

Figure 2.22: Yearly CO_2 injection rate by one injection well. Hydrofrac stands for hydraulic fracture and S&S stands for matrix shrinkage and swelling.

The volume of coal in the PRB, at depths greater than 300 m and for coalbeds greater than 3 m in thickness is 1.97×10^{11} tonnes (Nelson et al., 2006). If we assume that all the coalbeds in the PRB are overlain by impermeable caprocks, then we estimate from our simulation results that unmineable coalbeds in the PRB (at depths greater than 300 m and with thicknesses greater than 3 m) can sequester a total of 1.3 to 1.8 billion tonnes of CO_2 - depending on whether a hydraulic fracture is used for stimulation and assuming that the coal properties everywhere in the basin are the same as in our model and only horizontal hydraulic fractures will form. Therefore, at Wyoming's current CO_2 emissions rate (63 million tonnes per year); the coal resources of the PRB can sequester Wyoming's annual emissions for the next 20 to 30 years.

One caveat is that not all of the coalbeds deeper than 300 m and thicker than 3 m will be overlain by a caprock and therefore these sequestration estimates for the PRB are probably an upper bound. In addition, there are only certain parts of the basin where horizontal hydraulic fractures will form, so fracturing stimulation will not be feasible everywhere in the basin. However, we have also not taken into account the possibility of recycling produced CO_2 with optimized well placements so that more of

the coal volume in the model is contacted with CO_2 (help to overcome the negative effect of gas buoyancy on sequestration and ECBM recovery). Alternative well configurations would allow more coal to be contacted with CO_2, increasing the sequestration potential and ECBM recovery of the PRB.

To verify that the volumes we are predicting for CO_2 sequestration and ECBM in the Big George coal are consistent with actual field experiments, we have compared our volumes with those observed at the Allison pilot study in the San Juan basin. Coals in the San Juan basin are bituminous in rank, over-pressured and thinner than the Big George coal (Reeves et al., 2003). The Allison pilot involved injection into three adjacent coal seams, with a total net thickness of ~12 m (Reeves et al., 2003). Within the study area cleat permeability of the coals ranged from 100-140 mD (Reeves et al., 2003). Four injection wells and sixteen CBM wells were used in the pilot and the wells were spaced 160-acres apart (Reeves et al., 2003). Over a six year period the total CO_2 injected into the San Juan coals was 335,600 tonnes, an average of ~83,900 tonnes per injection well (Reeves, 2004). This corresponds to an average injection rate of ~14 kt/year. As expected, this rate is higher than we have predicted for the Big George coal (~9 kt/year; Figure 2.22) because of the higher reservoir pressure and cleat permeability in the San Juan coals. The relative value of these observations gives us confidence that our predictions are within an acceptable range.

In addition, we have compared our primary production recovery factor with that reported in the DOE/NETL (2003) report on multi-seam completion technology in the PRB. The DOE/NETL (2003) study determined that the total gas in place in the PRB is 75 TCF, with 2.7 TCF economically recoverable today using single-seam well completions, which are currently used in the PRB. This economically recoverable volume gives a recovery factor of 3.6%, which is close to the 2% recovery we get from our primary production simulation after 18 years of production. In contrast, the recovery factor from ECBM is 8% and when we add a horizontal hydraulic fracture at the base of the injection well it increases to 13%. However, because of the gas buoyancy effect, which causes the CO_2 to rise immediately to the top of the coalbed

and sweep only a limited, vertical portion of the coal, all of these recovery factors are low. If we were to use various well configurations to force the CO_2 to migrate into areas of the model that have not been previously contacted by CO_2, the recovery factors would increase substantially. In addition, using alternative well placements would be an ideal way of recycling CO_2 and increasing the sequestration volumes.

2.6.3 Permeability and porosity realizations

In order to model the uncertainty in our matrix and cleat permeability and porosity fields we created 15 realizations of each property distribution. As an example, Figure 2.23 shows four of the 15 face cleat permeability realizations that we generated.

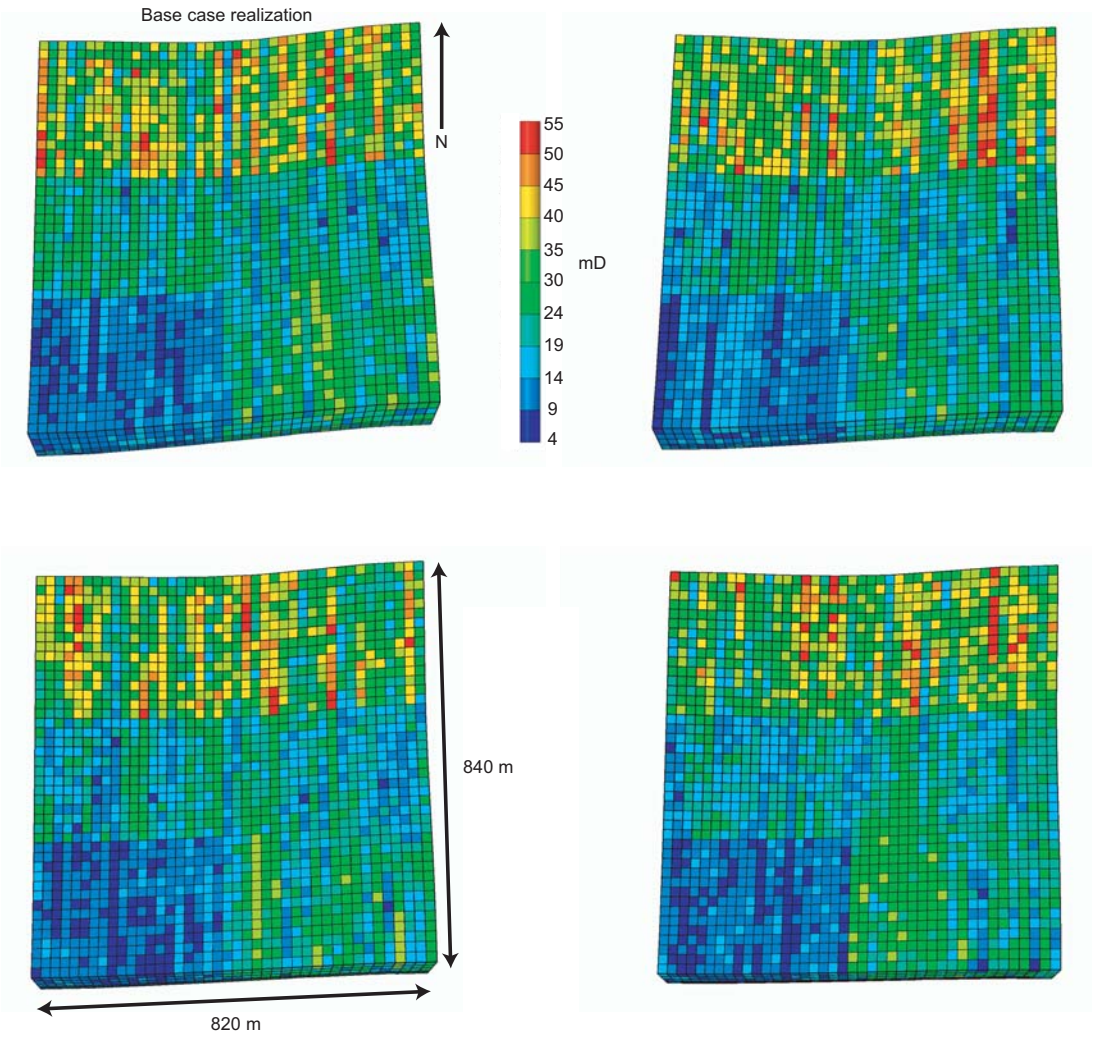

Figure 2.23: Four of the 15 face cleat permeability realizations that we generated. The top left realization is the face cleat permeability distribution we have used in all our base case simulations (Figure 2.11).

Figure 2.24 displays the possible range in total CO_2 injected and CH_4 produced from variations in the cleat and matrix permeability and porosity distributions within the Big George coal; using the base case simulation that models matrix shrinkage and swelling but contains no hydraulic fracture.

As can be seen from Figure 2.24, our base case volumes provide a minimum bound on total volumes of CO_2 that can be sequestered and CH_4 that can be produced. The percent difference between the lowest and highest cases is 12% for total CO_2

sequestered and 18% for total CH_4 produced. Additional realization runs would help constrain the uncertainty further.

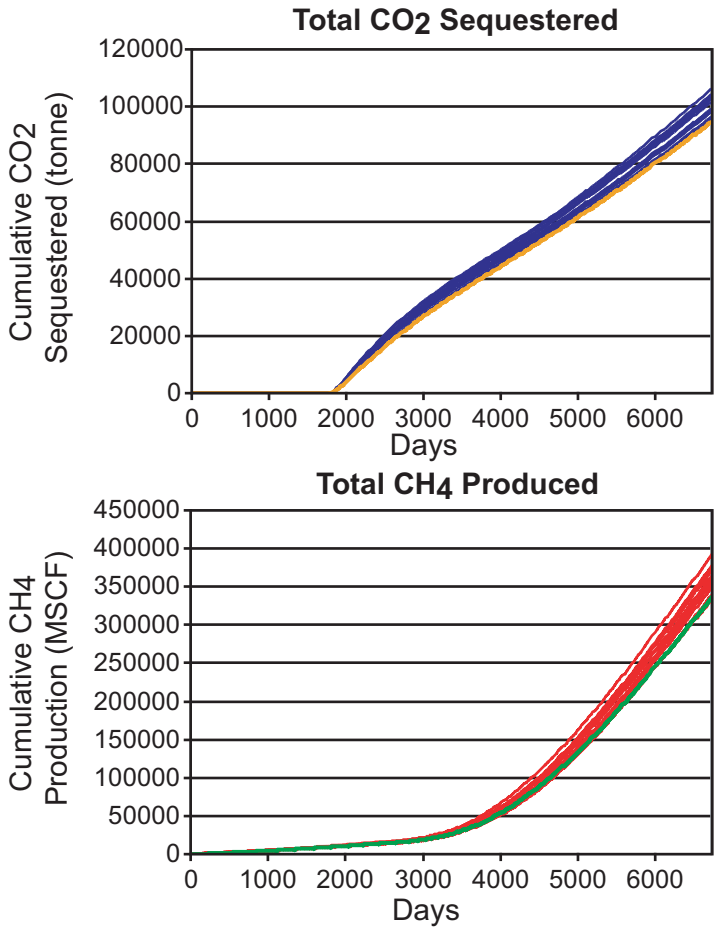

Figure 2.24: Cumulative CO_2 sequestered and CH_4 produced after 13 years of CO_2 injection for each realization. This figure represents the uncertainty in our results due to uncertainty in the coal cleat and matrix permeability and porosity distributions. The orange and green lines correspond to results from realization 1, which is the realization we have used as our base case. For all realizations shown here, matrix shrinkage and swelling was modeled but no hydraulic fracture was present in the model.

2.7 Complicating factors

2.7.1 Modeling matrix shrinkage and swelling

As mentioned earlier, GEM 2005 uses an extended Palmer and Mansoori equation (equation 1). Previous to using GEM 2005, we were restricted to the original Palmer and Mansoori equation (GEM, 2004; Palmer and Mansoori, 1996; 1998) (equation 2). We found that the matrix swelling term in the original Palmer and Mansoori equation had no effect on injectivity and that the CO_2 injection rate actually increased with CO_2 injection. After running a sensitivity analysis on the original equation we concluded that the equation is dominated by the linear-elastic effective stress term (Ross and Zoback, 2006a; Palmer et al., 2006), which incorporates cleat compressibility. We further found that the matrix shrinkage and swelling term, which incorporates matrix volumetric strain, has negligible influence on the calculated porosity changes. Hence, when the pressure increased in the reservoir because of CO_2 injection, the equation predicted that the porosity and permeability would increase since the cleats would be kept open by the pressure (decrease in the effective horizontal stress), despite the adsorption of CO_2 into the coal matrix which should cause matrix swelling and therefore a closure of the cleats.

In contrast, when we use GEM 2005, the extended Palmer and Mansoori equation predicts decreases in CO_2 injectivity due to a reduction in cleat permeability (equation 1 and Figure 2.25). This is because the matrix shrinkage and swelling term now has a greater influence on the calculated permeability changes due to the introduction of the generalized multi component Langmuir concept to the Palmer and Mansoori equation. All gas species are now used in the permeability calculations and since the CO_2 matrix volumetric strain parameter is larger than CH_4 strain values, matrix swelling dominates (Mavor and Gunter, 2004; Harpalani, 2005).

When we run only primary production simulations the extended Palmer and Mansoori equation does not predict matrix shrinkage and therefore an increase in cleat permeability. Instead, the linear-elastic effective stress term dominates the equation

and the cleat permeability decreases because of increasing effective horizontal stresses resulting from the desorption of methane (Figure 2.25). This is because the CH_4 volumetric strain value is so small that the matrix shrinkage that is calculated by the equation is smaller than the decrease in permeability caused by the increasing effective horizontal stresses. For matrix shrinkage to dominate throughout the modeling, we would need to use larger CH_4 volumetric strain values than have been observed in laboratory experiments (Harpalani, 2005) (Chapter 3, section 3.4.5).

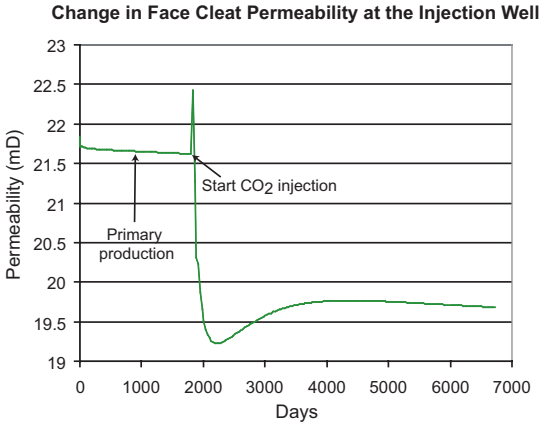

Figure 2.25: Change in the face cleat permeability at the injection well over time. Note that during the primary production stage the extended Palmer and Mansoori equation (GEM 2005) predicts a decrease in permeability. The initial increase in permeability at the point of CO_2 injection is from the increase in pressure around the well, which forces the cleats open. This is followed by matrix swelling, which causes the cleats to close. There is no hydraulic fracture modeled in this simulation example.

2.7.2 Gas buoyancy

As mentioned earlier, gravity and buoyancy are the major driving forces behind gas migration in water saturated coalbeds. Figure 2.18 shows CO_2 gas at the injection well migrating to the top of the coal and then flowing along the top towards the production wells. We find that only ~25% of the coal actually comes in contact with the migrating CO_2 which has important implications for screening models that use the total volume of coal in a basin and CO_2:CH_4 replacement ratios to determine the CO_2 sequestration capacity of coal-bearing basins. Our simulations show that not all of the coal volume will store CO_2, so many of the current sequestration volume estimates are possibly larger than what can be sequestered in reality.

The gas buoyancy effect is also important for fluid flow simulations that are used for pilot study screening and prediction. Single layer models will not show the buoyancy effect between water and gas and therefore they underestimate the time to breakthrough and overestimate the total volumes that can be sequestered and produced. We carried out simulations[2] on a single layer model and compared the results against a 6 layer model, using homogenous coal properties for simplicity (Table 2.7). We observe that after 6720 days the model with one layer in the z direction is able to sequester more CO_2 (~10%) and produce slightly more CH_4 (~5%) than the model with 6 layers. However, the largest discrepancy is observed in the breakthrough times between the two models, where breakthrough for the one layer model is at 5420 days compared to 2460 days for the model with 6 layers. If CO_2 sequestration was terminated at the time of breakthrough, the one layer model would predict significantly greater total volumes for sequestration and ECBM than the 6 layer model (325% and 450% respectively) (Figure 2.26).

Table 2.7: Coal cleat and matrix permeability and porosity values used in our single layer and 6 layer models (in the z direction).

Property	Value
Horizontal face cleat permeability	100 mD
Horizontal butt cleat permeability	50 mD
Vertical face cleat permeability	50 mD
Total cleat porosity per grid cell	0.07
Matrix permeability	0.41 mD
Matrix porosity	0.05

[2] We ran the simulations with matrix shrinkage and swelling modeling but with no horizontal hydraulic fracture.

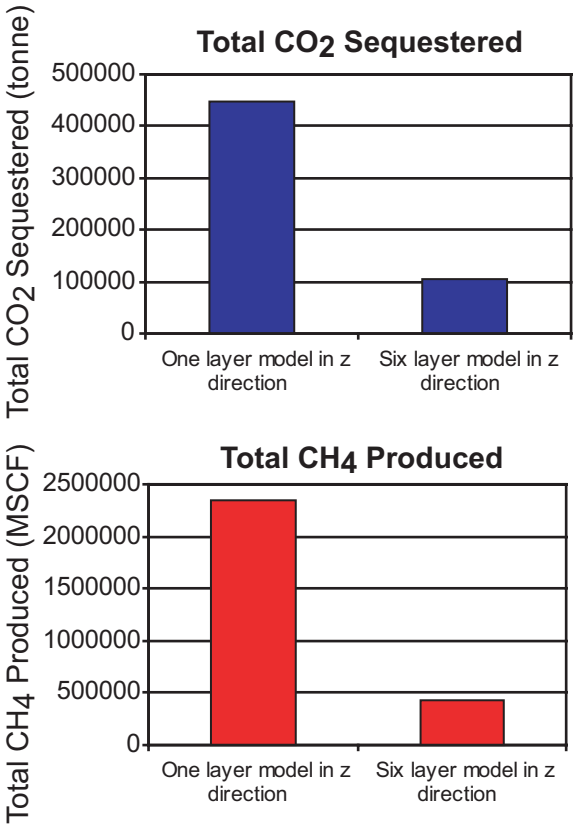

Figure 2.26: Total CO_2 sequestered and CH_4 produced at time of CO_2 breakthrough for the model with one layer in the z direction and the model with 6 layers in the z direction. Both simulations were run with matrix shrinkage and swelling modeling but no hydraulic fracture. Note that the model with one layer in the z direction over predicts the sequestration and ECBM potential of the coalbed because the one layer model is unable to capture the buoyancy effect between the gas and water in the coal.

In terms of the broad scale, the 6 layer model gives a good estimate of when breakthrough should occur in the field. However, if breakthrough time is needed precisely, the grid must be refined further in the vertical direction. We ran a simulation with 24 layers in the vertical direction to predict the breakthrough time more accurately. When we used constant cleat values in the 24 layer model (Table 2.7) the CO_2 breakthrough was actually 360 days earlier than in the 6 layer model with constant cleat values.

We also ran simulations with heterogeneous permeabilities in the 6 and 24 layer models using a constant CO_2 injection rate of 4 tonnes/day (we used the same face, butt and vertical cleat permeability distributions as in our base case simulations). We started injection and production at time zero, but had to use a low injection rate to

keep pressures low in the 24 layer model (hence our production volumes are also small). However, we are not interested in the absolute CO_2 volumes injected and produced, but in the relative volumes produced between the two models in order to highlight the importance of capturing the gravity gas tongue during simulations, so to obtain accurate CO_2 breakthrough predictions.

Figure 2.27 shows gas saturation in both the 6 and 24 layer models with heterogeneous cleat permeabilities after ten years of CO_2 injection. The model with 24 layers gives a much sharper image of the gas migration and gas front; especially it shows that at the very top of the coal the gas saturation is close to 100% which is not obvious in the 6 layer model. With the 24 layer model we are able to resolve the gravity tongue and can therefore predict a more accurate breakthrough time than given by the 6 layer model. Figure 2.28 shows that breakthrough is faster in the 24 layer model, because we capture the gravity tongue, where initial CO_2 breakthrough is at ~4000 days in the 24 layer model compared with ~5800 days in the 6 layer model.

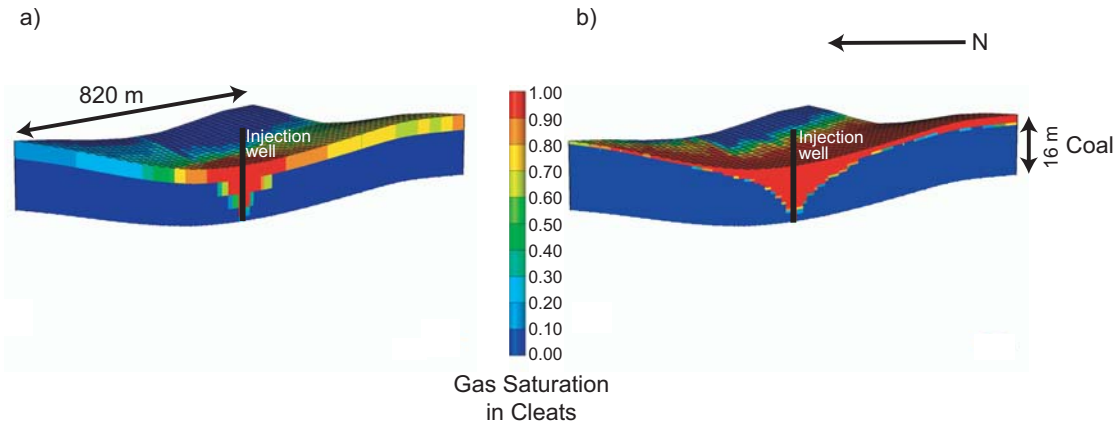

Figure 2.27: Cross section through our simulation model showing gas saturation in the cleats after 10 years of CO_2 injection a) model with 6 layers and b) model with 24 layers (cross section is from the SE to NW corners of the model). Note that the gas rises to the top of the coal before migrating laterally. We are showing results from our base case simulation that includes matrix shrinkage and swelling modeling but no hydraulic fracture.

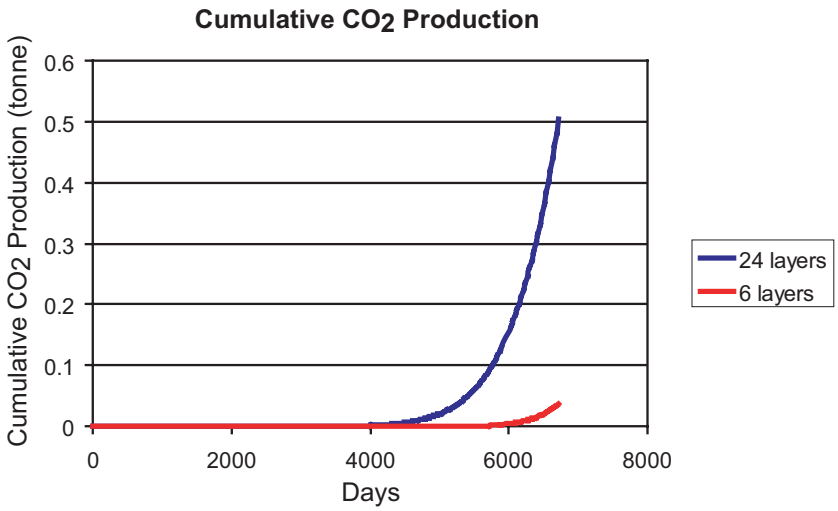

Figure 2.28: Cumulative CO_2 production for the model with 6 layers (red curve) and the model with 24 layers (blue curve). Note that breakthrough is significantly earlier in the 24 layer model than in the 6 layer model.

Therefore, we recommend that CO_2 sequestration simulation models contain more than a single layer so that sequestration and ECBM volumes are not overestimated and so that breakthrough is more accurately predicted. If precise predictions of breakthrough times are required for field studies, rather than a general breakthrough time, it is imperative that the gravity tongue is resolved in the simulations, which means that models with fine gridding in the vertical direction should be used. An example of this problem was seen at RECOPOL, where in the field breakthrough was faster than had been modeled because the simulation model contained only a single layer even though the coals were water saturated (van Wageningen, 2006).

2.7.3 Heterogeneous versus homogeneous cleat permeability fields

We looked at the effect of using a heterogeneous cleat permeability field compared to a homogeneous field on total gas volumes injected and produced. Many ECBM simulation studies use a constant cleat permeability (for example, Reeves and Taillefert, 2002; Taillefert and Reeves, 2003; Reeves et al., 2004; Harpalani, 2005; Wong et al., 2006; Jackson, 2006; Shi and Durucan, 2006), which does not capture the

heterogeneous nature of cleat permeabilities in the field. Our simulations[3] show that if we used a homogenous cleat permeability field (Table 2.8; using the average values from our history matched face, butt and vertical cleat permeability distributions) we would over predict the amount of CO_2 that can be sequestered by ~35% (Figure 2.29) and the amount of CH_4 that can be produced by ~60% (Figure 2.29) compared to volumes resulting from using a model with a heterogeneous permeability field (where we used our history matched cleat permeability distributions shown in Table 2.4 and Figure 2.11). This suggests that it is beneficial to capture the heterogeneity of the coal cleat permeability in the reservoir model to more accurately predict the coal's CO_2 sequestration potential.

Table 2.8: Cleat permeabilities used in our homogenous model.

Property	Value
Horizontal face cleat permeability	24 mD
Horizontal butt cleat permeability	7 mD
Vertical face cleat permeability	7 mD

[3] We ran the simulations with matrix shrinkage and swelling modeling but with no horizontal hydraulic fracture.

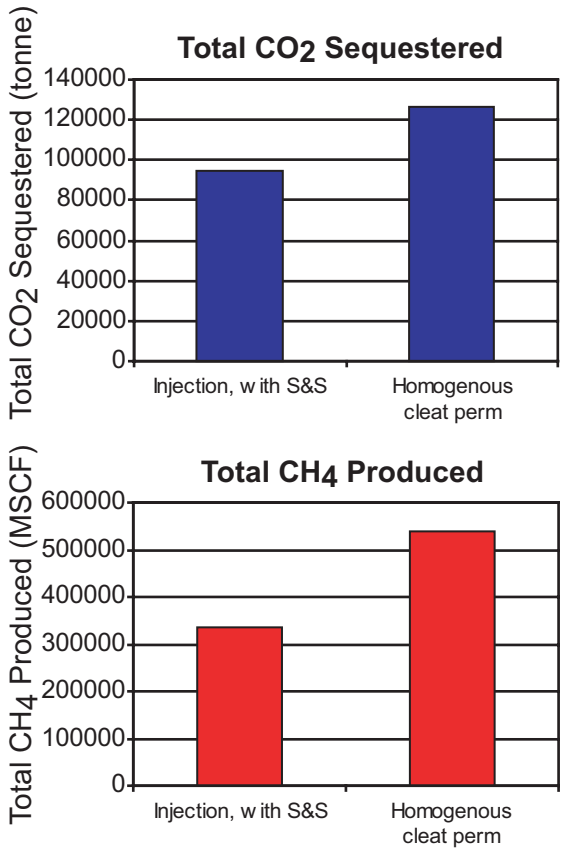

Figure 2.29: Total CO_2 sequestered and CH_4 produced after 13 years of CO_2 injection for our base case (heterogeneous cleat permeability) and homogenous cleat model. Both cases were modeled with matrix shrinkage and swelling but with no hydraulic fracture in the model. S&S stands for shrinkage and swelling.

2.8 Cap rock seal

Coalbeds are an appealing option for geologic storage of CO_2 because the CO_2 is adsorbed onto the coal matrix surfaces and effectively "locked" into the coalbed. However, as we have shown above, buoyancy forces between the gas and inherent water cause the injected CO_2 to rise to the top of the coal and flow along the top to the production wells (Figure 2.18). CO_2 leakage will not occur if the coal is overlain by a laterally extensive cap rock, but if the cap rock pinches out so that the coal is overlain by sand or if sand has scoured a coal body, the gas may migrate into the overlying sand unit. In the PRB, the coalbeds are typically overlain by a confining unit but they can come into direct contact with sandstone bodies (J. Wheaton, personal

communication, 2007; Applied Hydrology Associates and Greystone Environmental Consultants, 2002; Bartos and Ogle, 2002). Therefore, we have simulated the potential leakage of CO_2 into overlying sand units (Shimada and Funahashi (2006) investigated CO_2 leakage using a generalized 2D coal-mud-siltstone model). Our leakage simulation cases include a sand-sand sequence (4 m and 12 m thick respectively) overlying a coalbed (16 m thick) and a shale-sand sequence (4 m and 12 m thick respectively) overlying the coalbed.

We have varied the permeability and porosity of the sands and shale to see what effect these properties may have on gas migration into overlying units (we have used constant values rather than geostatistical distributions for simplicity) (Table 2.9).[4]

For the cleat and matrix permeability and porosity distributions for the coalbed (Table 2.10) we have used values similar to our history matched distributions detailed in Table 2.4 and illustrated in Figure 2.11. We have used comparable values because our leakage model is based on the same five CBM wells used to build our 3D stochastic model described previously.

[4] We have used sand and shale porosity and permeability values from Applied Hydrology Associates and Greystone Environmental Consultants (2002). The sands contained in the Wasatch and Fort Union formations are fine to medium grained (Flores, 2004; Applied Hydrology Associates and Greystone Environmental Consultants, 2002).

Table 2.9: Sand and shale permeability and porosity values used in each of our leakage scenarios.

Scenario	Stratigraphy	Property	Sand	Shale
1	sand- sand	Permeability (mD)	300	
		Porosity	0.1	
2	sand- sand	Permeability (mD)	70	
		Porosity	0.1	
3	shale-sand	Permeability (mD)	300	0.009
		Porosity	0.1	0.1
4	shale-sand	Permeability (mD)	70	0.009
		Porosity	0.1	0.1
5	shale-sand	Permeability (mD)	70 in x-y; 7 in z	0.009 in x-y; 0.002 in z
		Porosity	0.1	0.1

Table 2.10: Triangular distribution values for the coal unit matrix and cleat permeability and porosity.

Property	Minimum and Maximum Value	Mode
Horizontal face cleat permeability	10-50 mD	30 mD
Horizontal butt cleat permeability	1-16 mD	9 mD
Vertical face cleat permeability	1-16 mD	9 mD
Total cleat porosity per grid cell	0.02	
Matrix permeability	0.04-0.7 mD	0.5 mD
Matrix porosity	0.011-0.1	0.05

Because we use dual porosity settings in the simulator to model ECBM in the coal, when dual porosity is "turned on", GEM requires that all rock units are modeled as dual porosity rock types. This means that no matrix to matrix flow is allowed in any of the rock units, forcing us to model the sand and clay matrices as the actual sand and clay grains and the fractures as the pathways between clay and sand particles. We therefore set the sand and shale matrix permeability and porosity to zero. We also made the cleat spacing very small to capture the effective properties of the fine to medium grained PRB sandstones (Flores, 2004). This is obviously a conceptualized

model of the sands and shale because of the dual porosity limitation and the results should be interpreted as such.

In addition, even though it has been found that some adsorption does occur in shales we have not allowed adsorption in the shale unit (or the sand) to keep the simulation time to a minimum (Nuttall et al., 2005). If we allowed adsorption to take place in the shale units then the shales would act as traps for CO_2 and gas migration into overlying units should be impeded. Furthermore, we did not model matrix shrinkage and swelling in these simulations for simplicity.

The simulation grid used in this analysis contains 14256 grid cells, with 36 in the x direction, 33 in the y direction and 12 in the z direction. The grid dimensions are outlined in Table 2.11 and Figure 2.30. We used a 5-spot well pattern (4 production wells surrounding one injection well) with 80-acre well spacing and injected CO_2 for 18 years, as soon as production began. The production wells were perforated within the coalbed only, there is no horizontal hydraulic fracture at the base of the injection well and no-flow boundaries have been used at the boundaries of the model.

Table 2.11: Grid dimensions for cap rock seal model.

	nx, dx	**ny, dy**	**nz, dz**
Top unit (unit 2)	36, 30 m	33, 30 m	3, 4 m
Unit directly above coal (unit 1)	36, 30 m	33, 30 m	4, 1 m
Coal	36, 30 m	33, 30 m	5, 4 m

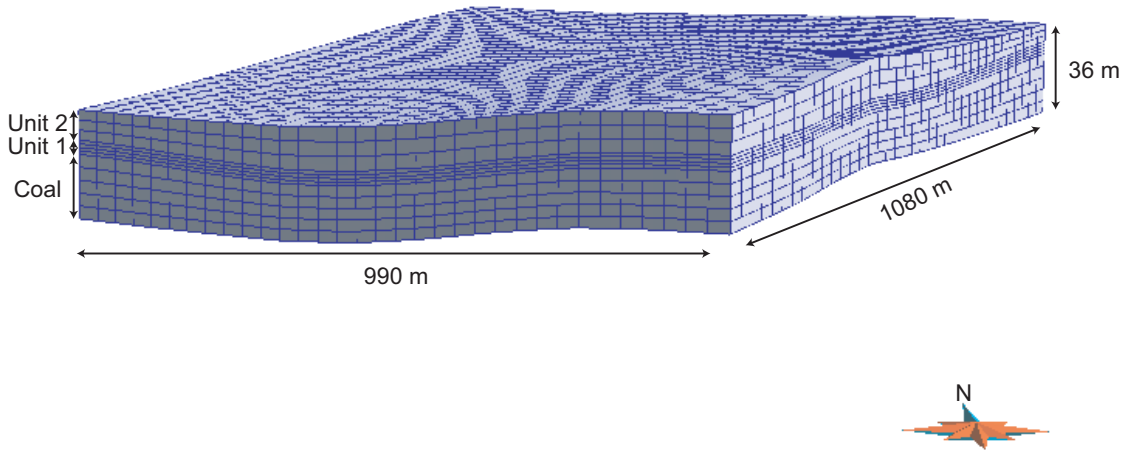

Figure 2.30: 3D simulation grid for modeling CO_2 gas migration from coal into overlying units (Table 2.9).

We found that for all our leakage scenarios the gas migrated into the overlying units, rather than being trapped within the coal (Figure 2.31). For scenarios 1 and 2, almost all of the CO_2 migrated straight into the overlying sands and went to the top of the sand body (Figures 2.31a and b). For the lower sand permeability scenario (2), migration was slower through the sand units, so lower sand layers have higher gas saturations than in scenario 1 (Figure 2.31b). For scenarios 3 and 4, the shale acts as a confining unit and gas is able to migrate further away from the injection well within the coal than in scenarios 1 and 2 (Figures 2.31c and d). However, even after one year of CO_2 injection gas has migrated into the confining unit and up into the top layer of the sand unit (~30-40% gas saturation in the shale unit and top layer of the sand unit directly above the injection well) (Figures 2.31c and d). After 18 years of CO_2 injection the top layer of the sand in both scenarios has gas saturations of 70-90%. In scenario 5 we have reduced the vertical permeability in both the sand and shale units to values given by Applied Hydrology Associates and Greystone Environmental Consultants for vertical conductivities (2002) (they calculated vertical hydraulic conductivities for sands in the Wasatch Formation and we have converted those values to permeability in mD). The lower vertical permeability in both units means that gas migration into the shale and sand is more limited than in the other scenarios, so that after one year of CO_2 injection the shale has gas saturations of only ~20%

immediately above the injection well and no gas has migrated into the overlying sand (Figure 2.31e). After 18 years of injection a small volume of gas has managed to migrate into the overlying sand and the top layer of the sand unit has gas saturations of ~10% immediately above the injection well.

These simulation cases actually show the lower bound on gas migration and saturation in overlying units, as PRB coals in some areas can have permeabilities close to 1000 mD (Flores, 2004; Mavor et al., 2003), which would mean that gas migration into the overlying units would be even faster than our simulations show.

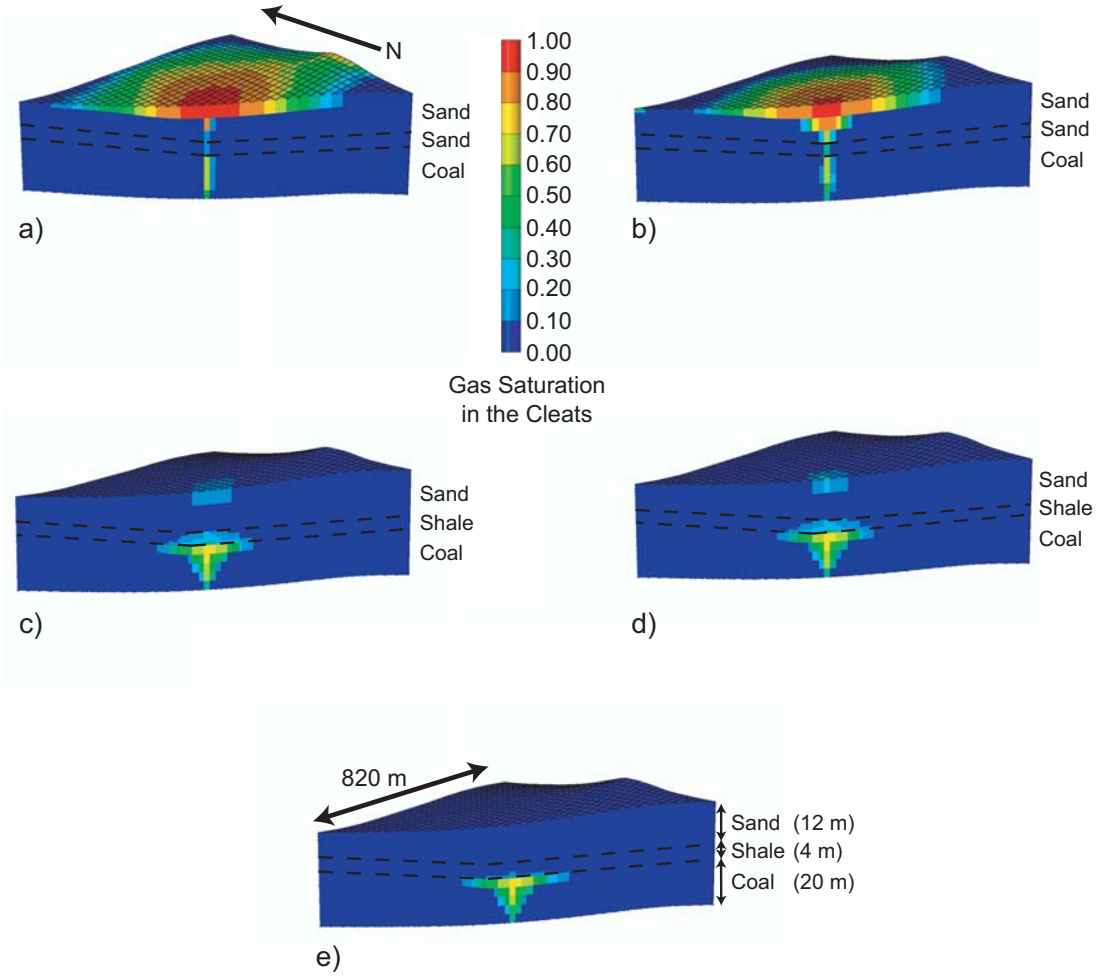

Figure 2.31: Gas saturation in the cleats after 1 year of CO_2 injection. Cross section through the model, from the SE corner to the NW corner. a) Scenario 1 in Table 2.9. b) Scenario 2 in Table 2.9. c) Scenario 3 in Table 2.9. d) Scenario 4 in Table 2.9. e) Scenario 5 in Table 2.9.

A much finer simulation grid would reveal a clearer picture of gas migration through the coal and into the shale and/or sand. However, our coarse simulations do show that it is imperative that coalbeds are overlain by cap rocks with permeabilities lower than ~0.002 mD in the vertical direction, or gas migration into overlying sands will occur (gas diffusion and adsorption in coal occurs at a much slower rate than gas flow through the cleats and therefore most of the gas is able to migrate into overlying units, rather than being adsorbed, if there is no cap rock to stop migration and keep the gas within the coal).

It could be possible to move the production wells closer to the injection well to try and force the gas to move laterally toward the producers, rather than migrating upward into overlying units. However, this would cause a trade-off between CO_2 breakthrough at the production wells and having the production wells close enough that the gas will feel the influence of the pressure gradient around the production wells and flow toward the wells rather than upward. In the following chapter (Chapter 3) we look at the influence of well spacing on sequestration and ECBM.

A present day example of gas migration from coalbeds to overlying sand units is in the eastern PRB, where overlying sand bodies have been found to contain CBM gas. It is thought that some of the gas was released during coalification and migrated up into the overlying units (Oldham, 1997). Additional gas was added to the sandstone reservoirs during glacial times, when the water table was lowered, causing CBM gas to desorb from the coal and migrate up into the overlying sands (Flores, 2004).

In terms of other potential leakage scenarios, a large drop in reservoir pressure could cause the sequestered CO_2 to desorb and migrate into overlying units as occurred in glacial times in the eastern PRB. Also, faults may cut the coalbed and if the faults are optimally orientated they could be reactivated by the pressure increase in the cleats from CO_2 injection; or if the fault is permeable the gas could migrate up the fault. Additional leakage scenarios include vertical hydraulic fractures that may penetrate the overlying strata, well bore failure and damage to overlying units from

coal matrix shrinkage and swelling during the adsorption of CO_2. All of these scenarios could lead to CO_2 leakage and should be considered in any screening studies for CO_2 sequestration in coalbeds, as well as at other potential geologic sequestration sites.

2.9 Conclusions

To determine the feasibility of sequestering CO_2 in unmineable coalbeds of the PRB we have carried out a reservoir characterization study and fluid flow simulations. We used geophysical and geological data from the PRB to develop a 3D model of the Big George coal, and used geostatistical techniques and history-matching to populate our model with numerous coal cleat and matrix permeability and porosity realizations. Results from fluid flow simulations show that gravity and buoyancy drive gas migration, and matrix swelling reduces gas injectivity. However, placing a horizontal hydraulic fracture at the base of the injection well helps to overcome the negative effect of matrix swelling on injection rates. Our simulations suggest that after 13 years of injection we can sequester ~99% of the total CO_2 injected into the Big George coal, that CH_4 production will be ~5-8 times greater with CO_2 injection than without, and that one injection well will be able to sequester ~9 kt of CO_2 a year. Based on this injection rate, it would take ~7,000 injection wells (each with a lifetime of ~13 years) to sequester the current CO_2 emissions for the State of Wyoming. In addition, our simulation results suggest that the CO_2 sequestration potential of the PRB (for coal at depths greater than 300 m) is ~1.3 to 1.8 billion tonnes, and at the current CO_2 emissions rate for the State of Wyoming the coal resources of the PRB can sequester Wyoming's annual CO_2 emissions for the next 20 to 30 years.

Finally, with regard to CO_2 sequestration feasibility and screening studies in coal-bearing basins around the world, it is important that the heterogeneous nature of the coal is captured in the simulation models, that models contain more than one layer in the vertical direction to account for gas buoyancy when water is present, and that potential coalbed sequestration sites are overlain by low permeability cap rocks. If the

simulation models do not contain multiple layers in the vertical direction and heterogeneous permeability and porosity fields, then the CO_2 sequestration potential of coal-bearing basins will be over-estimated. In addition, the absence of a cap rock will lead to CO_2 migration into overlying formations and eventual leakage to the surface.

2.10 Appendix 1 – Geostatistics

To incorporate the spatial variability of the cleat and matrix permeability and porosity distributions into the SGS algorithm, in order to populate the 3D stochastic reservoir model, we used semivariograms, one for each of the face cleat, butt cleat and matrix distributions. However, because of the lack of data, our choice of semivariograms was highly subjective. A typical spherical semivariogram model is shown in Figure 2.32. The magnitude of spatial correlation decreases with separation distance until a distance at which no spatial correlation exists. This distance is known as the range. The sill of the semivariogram is the total variance of the data set and is the semivariogram value that corresponds to zero correlation. The nugget is the short-range variability due to heterogeneities at small distances (Gringarten and Deutsch, 2001).

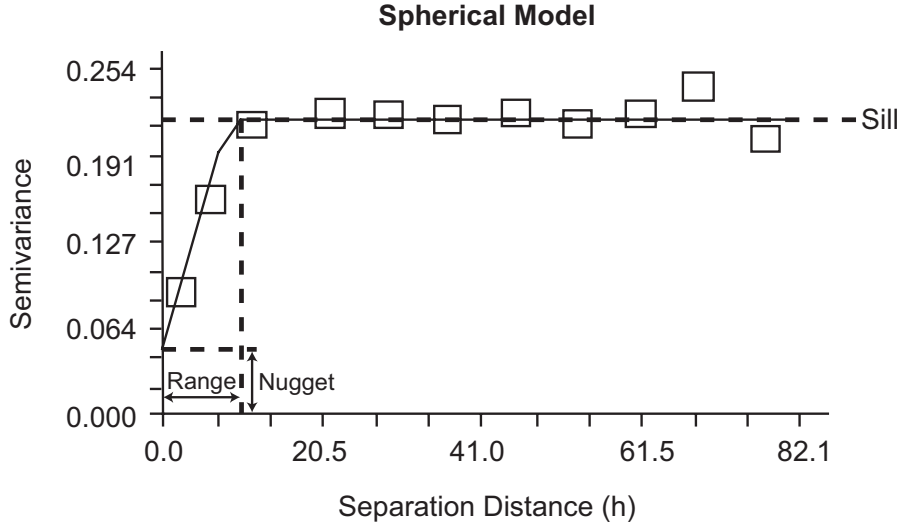

Figure 2.32: Spherical semivariogram model (modified from http://www.geostatistics.com/GSWinHelp/images/schematic_variogram_spherical60_.gif).

For the face cleat permeability, we used a semivariogram that captured the high correlation in permeability and long length of the face cleats in the face cleat direction. We chose a spherical semivariogram model with a 0.2 nugget effect and a range in the x direction (face cleat direction, which is north) of 500 m and less than 10 m in the y and z directions. The butt cleat semivariogram was used to capture the high correlation in permeability but small length of the butt cleats in the butt cleat direction. We chose a spherical semivariogram model with a 0.2 nugget effect and a range in the y direction (butt cleat direction) of 50 m and less than 10 m in the x and z directions. For the matrix permeability and porosity distributions we used a semivariogram model with a range in the x direction of 1 m and less than 1 m in the y and z directions. We also used a correlation coefficient of 0.7 between the matrix permeability and porosity.

2.11 Appendix 2 – History-matching

As mentioned in section 2.5.3, we have no hard data to help constrain our cleat and matrix permeability and porosity distributions in our 3D stochastic reservoir model. Instead we began by populating our model with permeability and porosity values reported in the literature and then used history-matching to constrain the initial cleat permeability and porosity distributions further. For the history-matching process we had both water and gas production histories from the five active CBM wells we used to build our model (WOGCC, 2006). BHP data for those wells were not available so we matched the cumulative water production for each well. We carried out the history-matching by using the average daily gas production rate for each well as a constraint and allowed the water production to vary. We followed a very simple trial and error method, where we broke the reservoir up into blocks surrounding each production well and then modified the cleat permeability and porosity values by a different constant in each block until we matched the total water production for each well over a five year period (Table 2.3 and Figure 2.11).

Chapter 3

CO_2 SEQUESTRATION AND ENHANCED COALBED METHANE RECOVERY: FLUID FLOW SIMULATION SENSITIVITY ANALYSIS OF THE POWDER RIVER BASIN, WYOMING

3.1 Abstract

In this study we have carried out a sensitivity analysis on coalbed properties and fluid flow simulation parameters used to determine the carbon dioxide (CO_2) sequestration and enhanced coalbed methane (ECBM) recovery potential of unmineable coalbeds in the Powder River Basin (PRB), Wyoming. We have focused our study on the Big George coal, part of the Wyodak-Anderson coal zone of the Tertiary Fort Union Formation. Our sensitivity analysis reveals that the CO_2 sequestration and ECBM potential of the Big George coal is sensitive to cleat permeability, the injection bottom hole pressure (BHP) constraint, slow diffusion times, coal thickness, high cleat compressibility, large volumetric strains for CO_2,

adsorption isotherms, relative permeability and injection well orientation. In addition, the ECBM recovery volume is also sensitive to cleat porosity, well spacing, the initial reservoir pressure and the injected gas composition.

3.2 Introduction

As discussed in Chapter 2, we built a 3D stochastic reservoir model of the Big George coal, Powder River Basin (PRB), Wyoming, and ran fluid flow simulations to examine the feasibility of sequestering carbon dioxide (CO_2) in unmineable coalbeds of the PRB. Both the 3D model and fluid flow simulations require a large number of parameters and coal properties to model flow and adsorption/desorption in a coalbed. Many of these parameters and properties are not known for the Big George coal, let alone for other PRB coals. In order to capture the affect of uncertainty in these values we have carried out a sensitivity study of the following input parameters: cleat permeability and porosity, cleat spacing, cleat compressibility, gas diffusion time, the Palmer and Mansoori parameters (1996; 1998; GEM, 2005), adsorption isotherms and relative permeability curves. In addition, we also used our 3D stochastic model to look at what effect bottom hole pressure (BHP) injector constraints, reservoir pressure, coal thickness, well spacing, well orientation and flue gas have on total volumes injected and produced.

In this chapter we begin by outlining the method we follow to carry out the sensitivity analysis and describe in detail the base case simulation that we compare all our sensitivity results to (section 3.3). In section 3.4 we report on the results from our sensitivity tests, beginning with cleat permeability, then cleat porosity, cleat spacing, gas diffusion coefficient, Palmer and Mansoori parameters, relative permeability curves, adsorption isotherms, maximum BHP constraint, coal thickness, well spacing, horizontal wells and finally flue gas. We discuss each of the sensitivity results in section 3.5 and then conclude by summarizing our findings from this chapter and Chapter 2 (Section 3.6).

3.3 Method

The parameters and properties used in our base case simulations in Chapter 2 came from the literature and when we had no information on a particular parameter for PRB coals we used values from other low rank coal-bearing basins (Table 3.1). Because we found a large range of published values for parameters and coal properties, we have taken values from the literature that encompass the ranges seen for each parameter and property and run simulations to determine what effect these parameters and properties have on total volumes of CO_2 sequestered and methane (CH_4) produced. Table 3.2 outlines the values we used in our sensitivity analysis. For our sensitivity simulations we varied one parameter at a time, keeping all other parameters equal to the values outlined in Table 3.1. In this chapter we compare our sensitivity results with those obtained for the base case simulation that included matrix shrinkage and swelling modeling but no hydraulic fracture (Chapter 2, section 2.6).

Table 3.1: Input parameters for our base case fluid flow simulations.

Input Parameters	Values	References
Reservoir pressure gradient, kPa/m	7.12 (0.315 psi/ft)	Advanced Resources International, Inc. (2002)
Coal gas composition	90% CH_4, 0% CO_2, 10% N_2	
Water saturation	99% in cleats, 0% in matrix	Advanced Resources International, Inc. (2002)
Injector BHP constraint, kPa	4000	Less than the fracture pressure in study area, 6200 kPa (Colmenares and Zoback, 2007)
Producer BHP constraint, kPa	1700	History-matching
Cleat spacing, cm	10	Flores (2004), Ayers (2002)
Matrix permeability, mD	0.04-0.7	Flores (2004)
Matrix porosity	0.011-0.1	Advanced Resources International, Inc. (2002)
Cleat permeability, mD	Horizontal face cleat direction, 4-55, horizontal butt cleat direction, 0.5-18 and vertical direction, 0.5-18	Literature (Flores, 2004; Twombly, et al., 2004; Mavor et al., 2003; Ayers, 2002; Laubach et al., 1998; USGS, 1995), and history-matching
Total cleat porosity per grid cell	0.017-0.63	Literature (Twombly, et al., 2004; Mavor et al., 2003; Advanced Resources International, Inc., 2002; USGS, 1995) and history-matching
Adsorption/desorption parameters for PRB coal samples (dry coal desorption for CH_4 and N_2 and moist coal adsorption for CO_2)	Langmuir volume: 0.577 gmole/kg for CH_4, 1.67 gmole/kg for CO_2 and 0.262 gmole/kg for N_2	Tang et al. (2005)
	Inverse Langmuir pressure, 1.7E-3/kPa for CH_4, 8.5E-4/kPa for CO_2 and 8.3E-4/kPa for N_2	
Diffusion coefficient, cm^2/s	0.000001 (100 days) for CH_4, CO_2 and N_2	Seto in Kovscek and Orr (2004)
Rock compressibility	Rock compressibility, 1.45E-7/kPa for matrix and 2.9E-5/kPa for cleats	Law et al. (2003) for matrix and USGS (1995) for cleats
	Reference pressure, 2246 kPa for matrix and cleats	
Shrinkage/swelling for modified Palmer and Mansoori equation in GEM 2005	Strain Langmuir pressure for CH_4, 2069 kPa, CO_2, 345 kPa and N_2, 344 kPa	Harpalani (2005),
	Young's modulus, 0.413E7 kPa	Jones et al. (1988),
	Poisson's ratio, 0.39	Jones et al. (1988),
	Strain at infinite pressure for CH_4, 0.007, CO_2, 0.013 and N_2, 0.004	Harpalani (2005),
	Exponent, 3	Palmer and Mansoori (1996; 1998)
S_3, kPa	6200	Colmenares and Zoback (2007)

Table 3.2: The range of values used in our sensitivity analysis for each parameter and coal property investigated.

Sensitivity Analysis Input Parameters	Values	References
Injector BHP constraint, kPa	3000 and 5000	Values are less than the fracture pressure in study area, 6200 kPa (Colmenares and Zoback, 2007)
Coal thickness, m	8	Half of base case (Table 3.1)
Reservoir pressure gradient, kPa/m	9.95 (0.44 psi/ft)	Hydrostatic pressure gradient
Cleat spacing, cm	0.1, 1, 5 and 200 in the k direction	Flores (2004), Ayers (2002)
Cleat permeability, mD	Double the base, half the base and increase in vertical direction	Flores (2004); Twombly, et al. (2004); Mavor et al. (2003); Ayers (2002); Laubrach et al. (1998); USGS (1995)
	Permeability before history-matching (Table 3.4)	
Cleat porosity	Double the base and half the base	
Diffusion coefficient, cm^2/s	0.1, 1E-4 and 1E-8	Seto in Kovscek and Orr (2004); USGS (1995)
Cleat compressibility, 1/kPa	6.5E-6, 1.45E-5, 5.8E-5, 8.7E-5, 1.1E-4	Harpalani (1999; 2005)
Shrinkage/swelling for extended Palmer and Mansoori equation in GEM 2005	Young's modulus, 0.138E7 and 0.551E7 kPa	Jones et al. (1988)
	Poisson's ratio, 0.23, 0.3 and 0.43	Jones et al. (1988)
	Strain at infinite pressure for CH_4, 0.001, 0.01, 0.05 and 0.1	Have used a range close to the values measured by Harpalani (2005)
	Strain at infinite pressure for CO_2, 0.007, 0.01, 0.05 and 0.1	
	Exponent, 1, 2 and 4	Have used a range close to the "typical" value of 3 (GEM, 2005)
Adsorption isotherms	Langmuir volume: 0.25475 gmole/kg for CH_4, Inverse Langmuir pressure: 2.4E-4/kPa for CH_4	Stricker et al. (2006)
Relative permeability curves		Chaturvedi (2006)
Horizontal well orientation	Perpendicular to face cleat direction	
	Parallel to face cleat direction	
Well spacing, acre	160	WOGCC (2006)
Flue gas ($N2:CO_2$)	20:80, 50:50, 80:20, 100:0	

3.3.1 Base case simulation

In this section we outline the reservoir characterization and fluid flow simulation set-up carried out for our base case simulation and subsequently for our sensitivity

simulations. We have focused our study on the sub-bituminous Big George coal, which is located in the central part of the PRB, is an amalgamation of five coalbeds and is part of the Wyodak-Anderson coal zone of the Tongue River Member (Flores and Bader, 1999). Our 3D stochastic reservoir model was built using information (gamma ray logs) from five active coalbed methane (CBM) wells in our study area, located SW of Gillette (Figure 3.1).

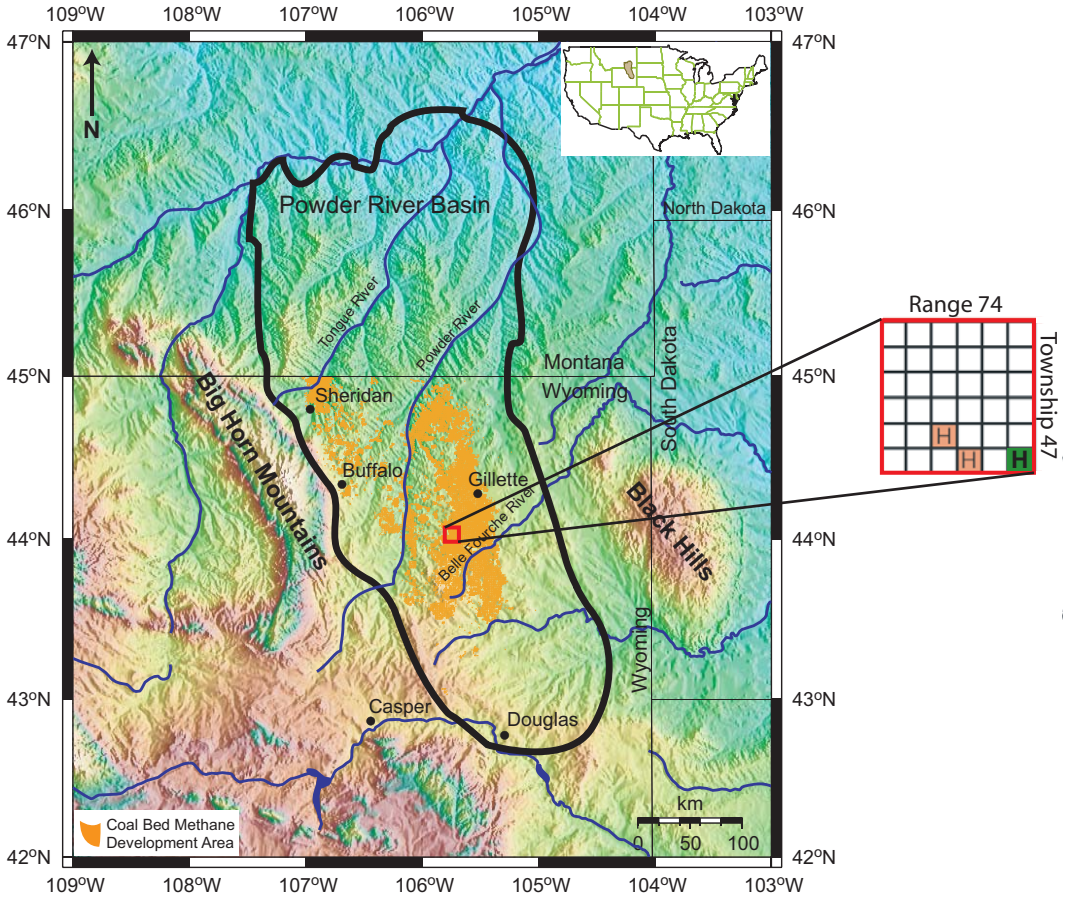

Figure 3.1: Location map of our study area. The red box corresponds to the township and range location of our study area. The green square corresponds to the section in which our 3D stochastic reservoir model was built and is in a section where Colmenares and Zoback (2007) identified horizontal fracture growth from water-enhancement (H stands for horizontal hydraulic fracture).

In the region we studied, the Big George coal is approximately 16 m thick and ranges in depth (to the top) from 315-361 m, with a slight dip to the west (Figure 3.2). The number of grid blocks in our model is 10332 (42 x 41 x 6) (Table 3.3). The grid

spacing outlined in Table 3.3 was chosen because it optimizes running time and helps maintain numerical stability with a minimal loss of detail.

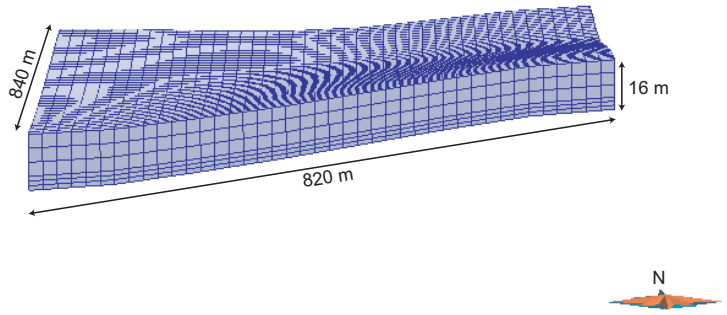

Figure 3.2: 3D simulation grid of the Big George coal. The bottom three layers are at a finer scale so that we can model a horizontal hydraulic fracture at the base of the injection well.

Table 3.3: The dimensions of our 3D simulation grid.

nx	42	dx	20 m
ny	41	dy	20 m
nz	6	dz	Top 3 layers at 4 m Bottom 3 layers at 1.3 m

We used triangular distributions, simple kriging and sequential Gaussian simulation (SGS) to populate our 3D model with equally probable cleat and matrix permeability and porosity realizations (Deutsch, 2002) and our initial permeability and porosity values came from literature on PRB coal (Table 3.4) (Flores, 2004; Twombly, et al., 2004; Mavor et al., 2003; Ayers, 2002; USGS, 1995). In addition, Laubach et al. (1998) conducted a study on coal cleat properties and observed that face cleat permeabilities can be three to ten times greater than butt cleat or vertical permeabilities. To capture this anisotropy in cleat permeability we forced the butt cleat and vertical permeabilities to be less than the horizontal face cleat permeability (Table 3.4). For the total cleat porosity per grid block we used constant values,

initially set at 0.02, because the simulator does not allow matrix shrinkage and swelling modeling with a variable cleat porosity field.

Table 3.4: Triangular distribution values for matrix and cleat permeability and porosity.

Property	Minimum and Maximum Value	Mode
Horizontal face cleat permeability	100-500 mD	300 mD
Horizontal butt cleat permeability	10-160 mD	100 mD
Vertical face cleat permeability	10-160 mD	100 mD
Matrix permeability	0.04-0.7 mD	0.5 mD
Matrix porosity	0.011-0.1	0.05

We constrained the cleat permeability and porosity values further through history-matching water production data from the active CBM wells used to build our 3D model (keeping gas production fixed) (WOGCC, 2006). The results of our history-match are detailed in Table 3.5 and the final cleat permeability values are outlined in Table 3.6 and illustrated in Figure 3.3.

Table 3.5: Results from history-matching water production data from active CBM wells used to build our 3D model.

Production Wells	True Water Production per Month (bbl/month) (WOGCC, 2006)	History-matched Water Production per Month (bbl/month)
Well 1	1768	1699
Well 2	2844	2750
Well 3	1696	1683
Well 4	3153	3198
Well 5	937	1111

Table 3.6: Final cleat permeability and porosity distributions derived from history-matching water production.

Property	Minimum and Maximum Value
Horizontal face cleat permeability	4-55 mD
Horizontal butt cleat permeability	0.5-18 mD
Vertical face cleat permeability	0.5-18 mD
Total cleat porosity per grid cell	0.017-0.63

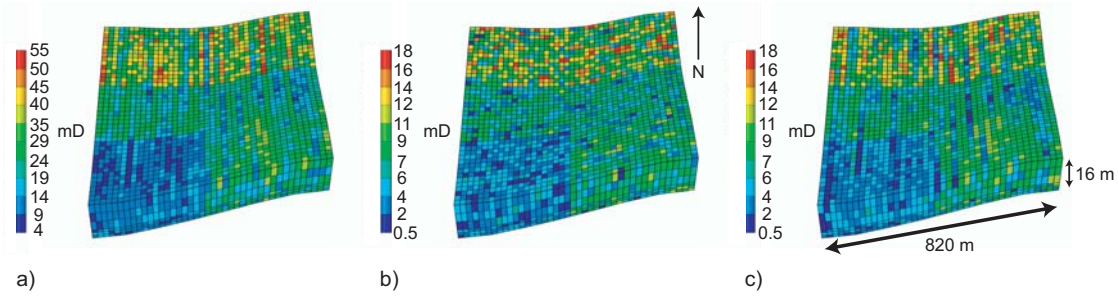

Figure 3.3: a) Horizontal face cleat permeability. b) Horizontal butt cleat permeability. c) Vertical face cleat permeability. This figure shows our 3D model populated with cleat permeability values for one realization. The heterogeneity and anisotropy in coal cleat permeability is modeled using geostatistical techniques. The horizontal face cleat permeability is higher than in the butt cleat and vertical directions (Laubach et al., 1998).

The base case and sensitivity simulations were run on a 5-spot well pattern (four production wells at each corner and one injection well in the center) with 80-acre well spacing using the Computer Modelling Group's ECBM simulator GEM. We ran both our base case and sensitivity simulations with pure CO_2 gas injection, with coal matrix shrinkage and swelling, and without a horizontal hydraulic fracture placed at the base of the injection well. To prevent accidental hydraulic fracturing of the coal near the injection well, we set the maximum value of the bottom hole pressure (BHP) less than 6200 kPa (900 psi), the fracture pressure in this area (Colmenares and Zoback, 2007).

We assumed that the coalbed is overlain by a thick confining unit by using no-flow boundaries in our simulations and coal matrix shrinkage and swelling was modeled by the extended Palmer and Mansoori equation (equation 1) included in GEM 2005 (1996; 1998; GEM 2005). The extended equation incorporates the generalized multi component Langmuir model,

$$\frac{\Phi}{\Phi_{ref}} = 1 + c_f (p - p_{ref}) + \frac{1}{\Phi_{ref}} \left(1 - \frac{K}{M}\right) \left(\sum_{j=1}^{j=n} \frac{\varepsilon_{Lj} y_{ref,j} \, p_{ref} / p_{Lj}}{1 + p_{ref} \sum_{k=1}^{k=n} y_{ref,k} / p_{Lk}} - \sum_{j=1}^{j=n} \frac{\varepsilon_{Lj} y_j \, p / p_{Lj}}{1 + p \sum_{k=1}^{k=n} y_k / p_{Lk}} \right), \quad (1)$$

where Φ_{ref} is the reference state (initial) natural fracture porosity, Φ is the fracture porosity at pressure p, c_f is the fracture pore volume compressibility (1/kPa), p_{ref} is

the reference state (initial) pressure (kPa), p is pressure (kPa), ε_{Lj} and ε_{Lk} are the volumetric strains at infinite pressure for components j and k, p_{Lj} and p_{Lk} are the Langmuir pressures for the volumetric strain at infinite pressure for components j and k, K is the bulk modulus, M is the axial modulus, $y_{ref,j}$ and $y_{ref,k}$ are the composition of components j and k at reference state (initial) and y_j and y_k are the compositions of components j and k at pressure p.

Finally, the coals in the PRB are under-pressured, so we have used the regional pressure gradient reported by Advanced Resources International, Inc. (2002) of 7.12 kPa/m (0.315 psi/ft).

3.4 Results

Both the base case and sensitivity simulations were run with 5 years of primary production and an additional 13 years of CO_2 injection (total simulation time of 18 years). Figure 3.4 shows the total volumes of CO_2 sequestered and CH_4 produced for our base case simulation. Our base case predicts that it is possible to sequester ~94,500 tonnes of CO_2 with one injection well and produce ~335,000 MSCF of CH_4 from a 160 acre area of the Big George coal (~326,000 MSCF from ECBM recovery only).

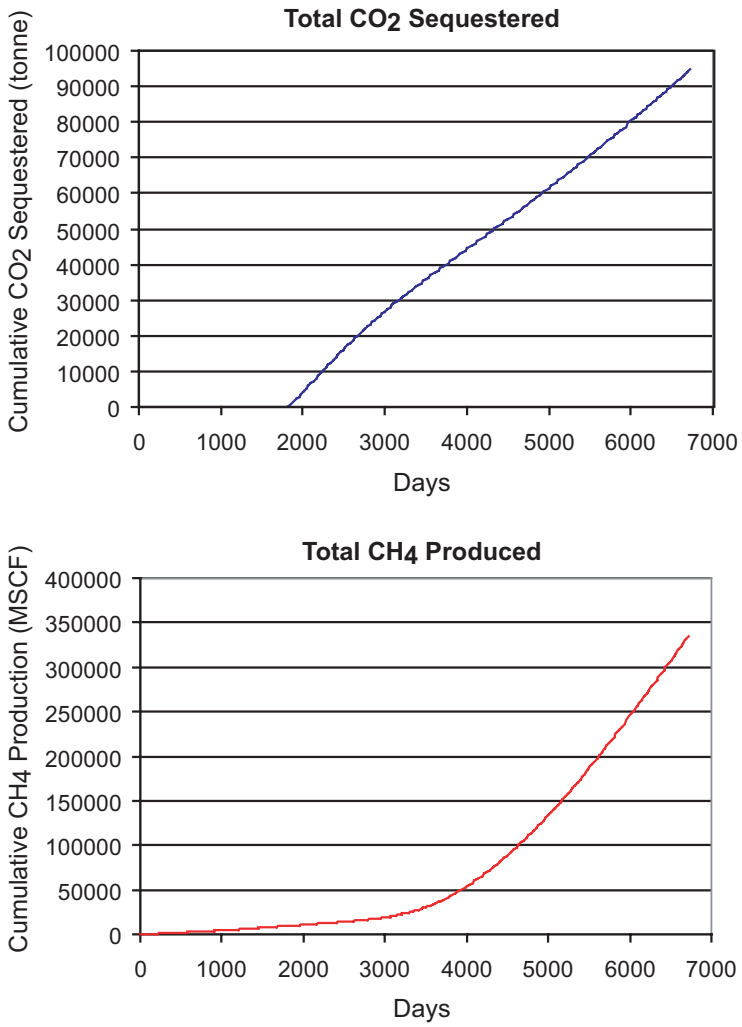

Figure 3.4: Base case simulation results: cumulative volumes of CO_2 sequestered by one injection well and CH_4 produced from an 160 acre area, after 5 years of primary production and 13 years of CO_2 injection (base case includes matrix shrinkage and swelling modeling but no hydraulic fracture).

In this chapter, we present our sensitivity results in terms of a percent increase or decrease in the total volumes of CO_2 sequestered and ECBM produced compared to the base case volumes shown in Figure 3.4. Note: in this chapter, as in Chapter 2, we define CO_2 breakthrough as the time at which 1% of the total CO_2 injected is produced. We are interested in maximizing CO_2 sequestration, so do not allow recycling of the produced CO_2. However, recycling of CO_2 could be used in conjunction with different well configurations so that more of the coal volume is contacted with CO_2, increasing CH_4 recovery and sequestration.

In addition, when reporting CH_4 production volumes we only discuss the ECBM potential of the sensitivity runs and have removed the primary production volumes (first five years of the simulation run) from the total CH_4 produced.

3.4.1 Cleat permeability

Doubling the cleat permeability increased CH_4 production (ECBM) by ~205% and CO_2 sequestration by ~110%. However, CO_2 breakthrough occurred earlier than in the base case (at 5180 days compared to no breakthrough in the base case) and a larger volume of CO_2 was produced (a 4000% increase after 6720 days). In contrast, halving the permeability reduced CH_4 production by ~85% and CO_2 sequestration by ~50%, but meant that there was no CO_2 breakthrough after 13 years of injection (Figure 3.5). By increasing the permeability we increased the total gas flow through the cleats which meant more CO_2 could be injected and CH_4 produced. However, because of the higher permeability the CO_2 was able to move through the cleats at a faster rate, decreasing the breakthrough time. If CO_2 injection was terminated at the first sign of breakthrough there would be only a ~45% increase in the total CO_2 sequestered and a ~80% increase in ECBM (Figure 3.5).

We also looked at the effect of having higher permeability in the vertical direction than in the face cleat direction, but found that there was only a slight increase in the total volume of CO_2 sequestered (6%) and CH_4 produced (17%) (Figure 3.5). Higher vertical permeability did allow for faster upward gas migration, but since sequestration and production did not increase significantly, it appears that the high permeability in the face cleat direction dominates gas flow to the production wells.

In addition, we also ran a sensitivity analysis using the initial cleat permeability input before history-matching (Table 3.4). We did this to examine the effect of having very high permeability in the cleats, as observed in other areas of the PRB (Flores, 2004; Twombly, et al., 2004; Mavor et al., 2003; Ayers, 2002; USGS, 1995). With very high permeability, breakthrough occurred at 1920 days, only 120 days after CO_2 injection began. At the point of breakthrough, ~60% less ECBM was produced than

in the base case and ~55% less CO_2 was sequestered (Figure 3.5). It seems that for coals with very high cleat permeability, >300 mD, the well spacing will need to be larger than 80 acres to reduce breakthrough times and maximize sequestration and ECBM. Alternatively, a much lower injection rate (or BHP constraint) could be used.

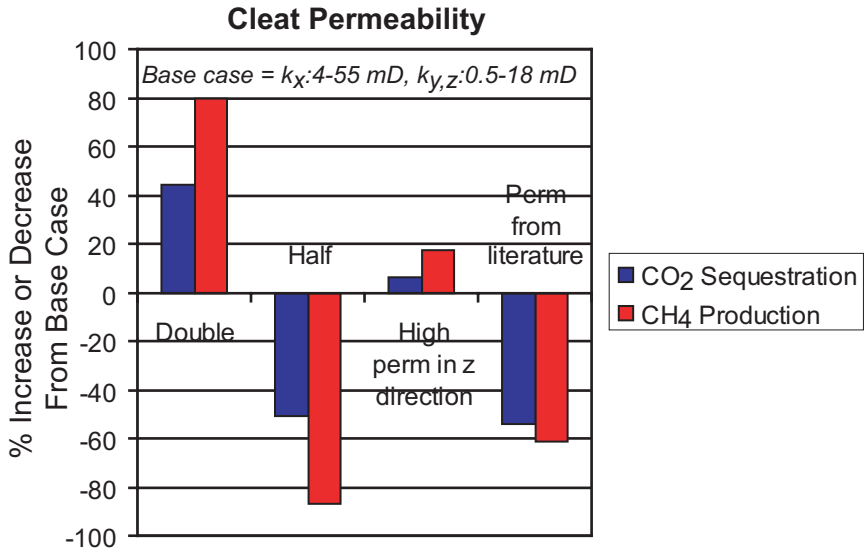

Figure 3.5: Percent increase and decrease in total volumes of CO_2 sequestered and ECBM produced at time of breakthrough compared to the base case for various changes in cleat permeability (Table 3.2).

3.4.2 Cleat porosity

Halving the cleat porosity increased CH_4 production by ~50% and CO_2 sequestration by ~15%, whereas doubling the porosity decreased CH_4 production by ~18% and total CO_2 sequestered by ~50% (Figure 3.6). By doubling the cleat porosity we introduced more water into the cleats (since we specify that the cleats are 100% water saturated), making it harder for the gas to flow through the cleats (reducing injection and production) and requiring additional water to be produced.

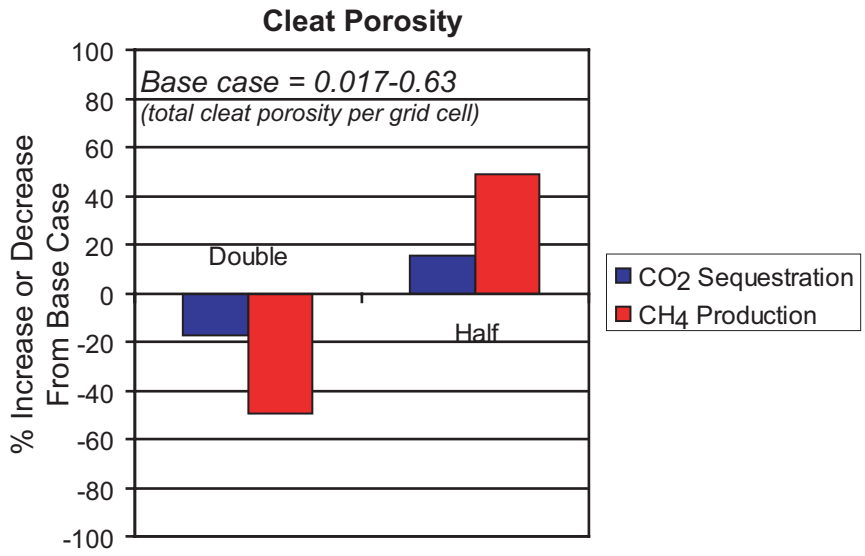

Figure 3.6: Percent increase and decrease in total volumes of CO_2 sequestered and ECBM produced at time of breakthrough compared to the base case for various changes in cleat porosity (Table 3.2).

3.4.3 Cleat spacing

Cleat spacing ranges from <1 cm to 12 cm in the PRB, as reported by Flores (2004) and Ayers (2002). Our base case used a spacing of 10 cm and we found that decreasing the cleat spacing produced slight increases in both the total CO_2 sequestered and CH_4 produced compared to the base case (Figure 3.7); CO_2 sequestration increased by ~3% and CH_4 production by ~5%. The higher number of cleats decreased the diffusion time, which is why more CH_4 could be produced (the faster the diffusion, the faster CH_4 can diffuse through the matrix and into the cleats), which in turn reduced the reservoir pressure slightly (compared to the base case) and allowed more CO_2 to be injected.

It is interesting to note that removing some of the horizontally orientated cleats did not have much of an effect on CO_2 sequestration or CH_4 production volumes (only 1% increase in total volumes). As mentioned earlier, it seems that the most important pathways to the producer are the long, vertical face cleats.

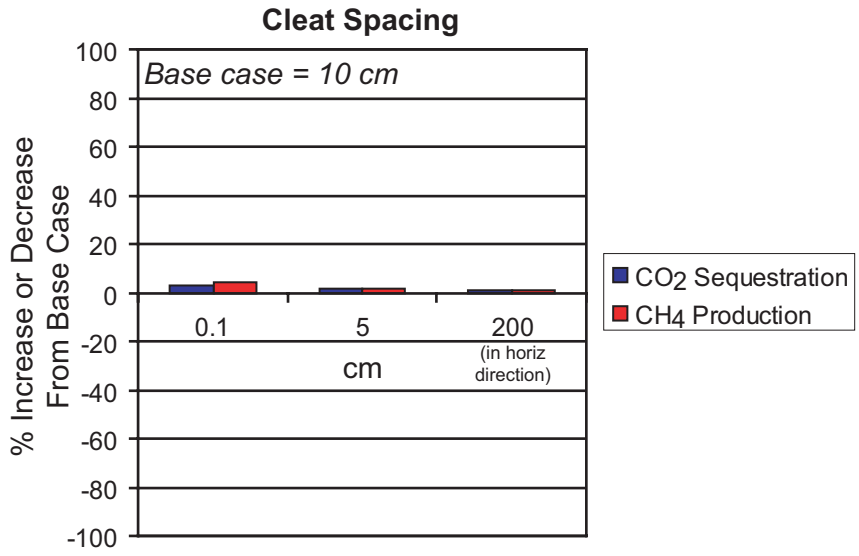

Figure 3.7: Percent increase and decrease in total volumes of CO_2 sequestered and ECBM produced at time of breakthrough compared to the base case for various changes in cleat spacing (Table 3.2).

3.4.4 Gas diffusion coefficient

In our base case model we used a diffusion coefficient that corresponded to ~100 days (1.0E-6 cm^2/s) and this was derived from calculations carried out by Seto (in Kovscek and Orr, 2004) for a cleat spacing of 10 cm. The USGS (1995) reported diffusion times of three days for coals in the PRB, so we have run a sensitivity analysis on diffusion times on the order of a day. Increasing the gas diffusion coefficient from 1.0E-6 cm^2/s (100 days) to 0.1 cm^2/s (little less than a day) only slightly increased both the total volume of CO_2 injected and the total volume of CH_4 produced; by ~3% and ~5% respectively, compared to the base case (Figure 3.8). Increasing the diffusion coefficient meant that gas diffusion through the matrix was faster, so more CH_4 was produced, lowering the reservoir pressure and allowing slightly more CO_2 to be injected and sequestered (faster diffusion) than in the base case.

However, decreasing the gas diffusion coefficient to 1.0E-8 cm^2/s (greater than 1000 days) had a significant negative effect on CO_2 sequestration and ECBM (~45% and ~50% decrease respectively from the base case). Such a low diffusion rate meant

that over the lifetime of the simulation, diffusion was too slow to allow for much of the desorbed CH_4 to move through the matrix to the cleats and for the CO_2 to diffuse into the matrix. Therefore, close to 20% of the total CO_2 injected into the coal was never adsorbed and instead flowed through the cleats to the production wells. It appears that because of the slow diffusion rate, pressures around the injection well were ~200 kPa higher at the start of CO_2 injection than in the base case (less CH_4 production during primary production, so less pressure drawdown in the coal), and then with CO_2 injection the pressure rose at a faster rate within the coalbed, to be ~300 kPa above the base case. The high reservoir pressure at the time of CO_2 injection caused the injection rate to be much lower than in the base case (because we use a BHP constraint) and therefore less CO_2 was injected into the coal. Breakthrough occurred at 2730 days, 930 days after the start of CO_2 injection, and at the time of breakthrough the volume of CO_2 sequestered was 85% less than the volume sequestered in the base case, and ECBM was ~98% less than in the base case (Figure 3.8).

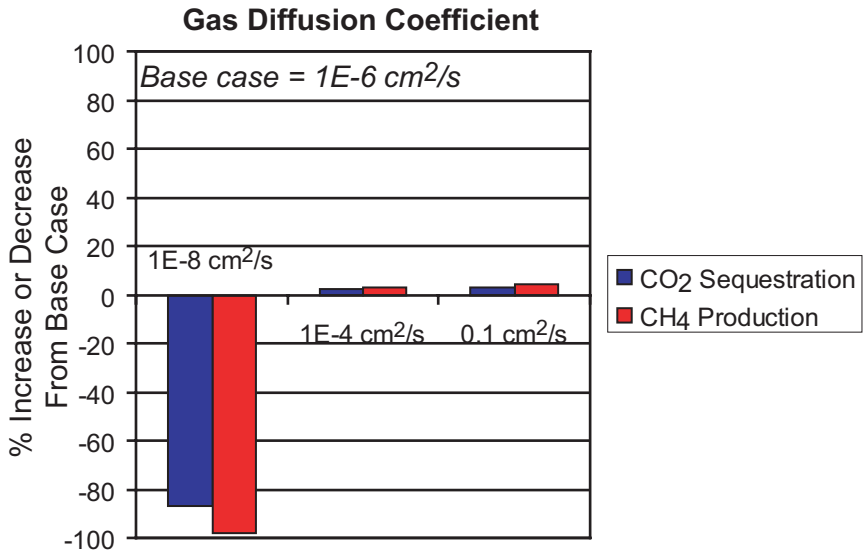

Figure 3.8: Percent increase and decrease in total volumes of CO_2 sequestered and ECBM produced at time of breakthrough compared to the base case for various changes in the gas diffusion coefficient (Table 3.2).

3.4.5 Palmer and Mansoori parameters

As discussed in section 3.3.1, GEM 2005 uses an extended Palmer and Mansoori equation (equation 1) to calculate cleat permeability changes due to desorption and adsorption of gases in the coal matrix and changes in effective horizontal stress (Palmer and Mansoori, 1996; 1998; GEM, 2005).

Cleat compressibility and volumetric strain at infinite pressure are included in the extended Palmer and Mansoori equation. Cleat compressibility is part of the linear effective stress term in the Palmer and Mansoori equation, whereas volumetric strain at infinite pressure is incorporated in the shrinkage and swelling term. Cleat compressibility values come from Harpalani (1999; 2005) who used values reported from CBM producing fields and the Illinois State Geological Survey. We found that by decreasing the cleat compressibility we decreased both the total volume of CO_2 sequestered (~15%) and the total volume of CH_4 produced (~20%) because it became harder to open the cleats (they became stiffer) and increase permeability (permeability close to the injector decreased by 2 mD) (Figure 3.9). At higher cleat compressibilities the cleats are more compliable, and therefore easier to open and keep open with a pressure increase from CO_2 injection (permeability close to the injector increased by 4 mD). Therefore, at a compressibility of 1.1E-4 /kPa the total CO_2 sequestered increased by ~60% and ECBM by ~80% compared to the base case (Figure 3.9).

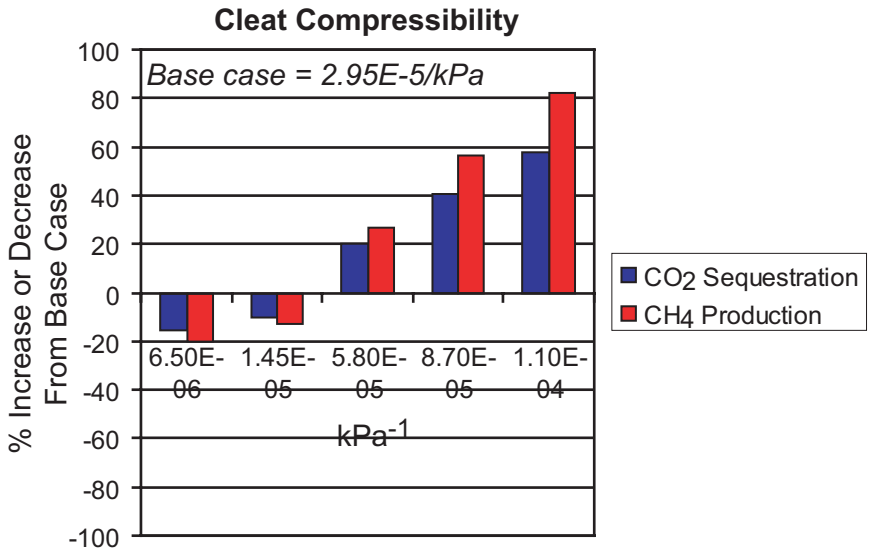

Figure 3.9: Percent increase and decrease in total volumes of CO_2 sequestered and ECBM produced at time of breakthrough compared to the base case for various changes in cleat compressibility (Table 3.2).

Volumetric strain at infinite pressure is a measure of the volume change in the coal matrix due to the adsorption and desorption of gases, and can be fit by a Langmuir curve (Harpalani, 2005). We have varied the matrix volumetric strain for CO_2 and CH_4 around the values given by Harpalani (2005) for Illinois coal. A higher strain means that there is a greater change in matrix volume, and if that change is an increase in volume, then the permeability reduction will be large, reducing injectivity and production. This is what we observed when we increased the volumetric strain for CO_2. For a large CO_2 strain the total CO_2 sequestered and CH_4 produced dropped by almost 100% and we saw a decrease in cleat permeability close to the injector from 12 mD to 0.2 mD (Figure 3.10). However, when we increased the volumetric strain for CH_4 we saw an increase in both CO_2 injection and CH_4 production, which means that there had been a large, negative change in the matrix volume because of desorbing CH_4 (decrease in volume), so matrix shrinkage dominated in this case and cleat permeability increased (Figure 3.10). For large CH_4 strain we saw a ~50% increase in total sequestered CO_2 and ~70% increase in produced CH_4 compared to the base case and an increase in cleat permeability close to the injector from 12 mD to 31 mD. However, breakthrough of CO_2 was observed at 5780 days.

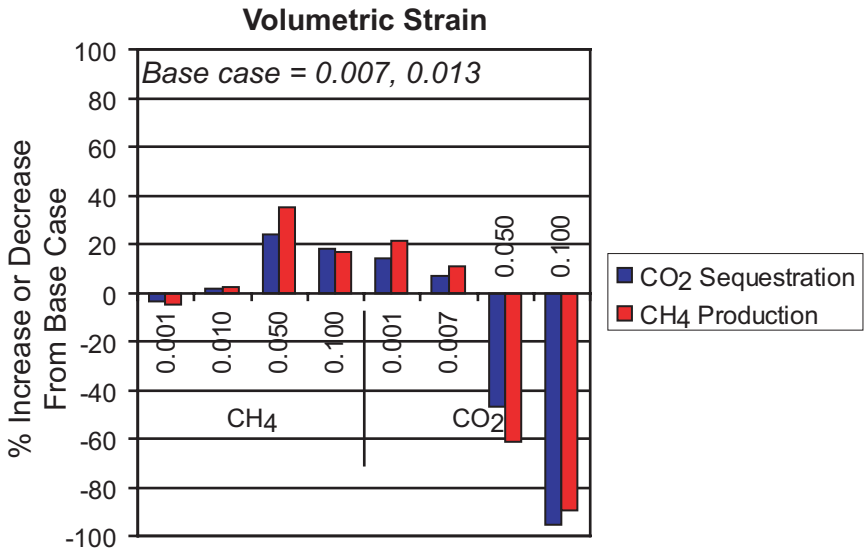

Figure 3.10: Percent increase and decrease in total volumes of CO_2 sequestered and ECBM produced at time of breakthrough compared to the base case for various changes in CH_4 and CO_2 volumetric strains at infinite pressure (Table 3.2).

Poisson's ratio and the exponent used to relate cleat porosity and permeability are also included in the Palmer and Mansoori equation, but from Figure 3.11 we can see that CO_2 injection and CH_4 production are not very sensitive to the exponent. However, by decreasing Poisson's ratio we saw a decrease in total CO_2 sequestered of ~10% and in ECBM of ~15%, whereas increasing the ratio caused the totals to increase by ~3% and ~5% respectively. The effect of Poisson's ratio on volumes sequestered and produced is a function of the extended Palmer and Mansoori equation (GEM, 2005). In the equation, Poisson's ratio is used as a scalar in front of the matrix shrinkage and swelling term. Increasing Poisson's ratio reduces the effect of the shrinkage and swelling term on overall changes in permeability, whereas decreasing Poisson's ratio increases the effect of shrinkage and swelling. These results are non-intuitive because the derivation of the Palmer and Mansoori equation assumes uniaxial strain.

From our results it appears that the extended Palmer and Mansoori equation is largely driven by cleat compressibility and matrix volumetric strain.

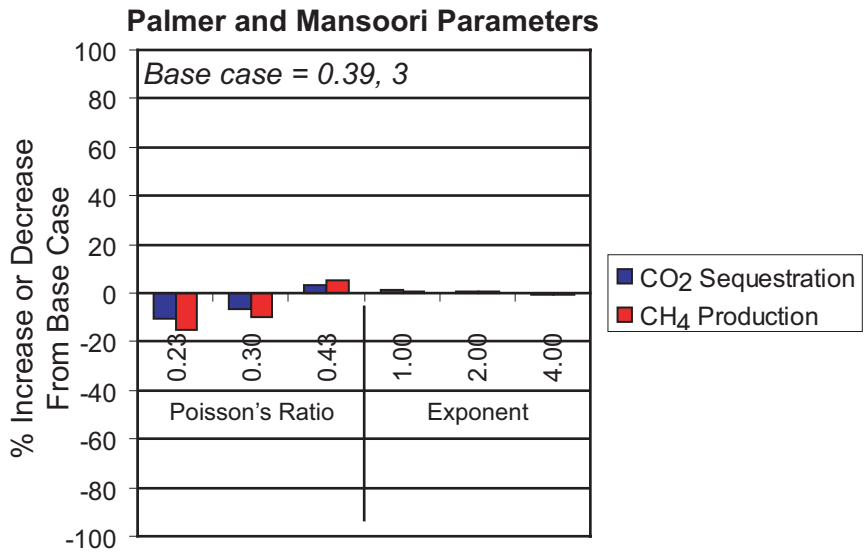

Figure 3.11: Percent increase and decrease in total volumes of CO_2 sequestered and ECBM produced at time of breakthrough compared to the base case for various changes in Poisson's ratio and the exponent that relates porosity and permeability (Table 3.2).

3.4.6 Relative permeability curves

Relative permeability measurements in coal are scarce and in some simulation studies the relative permeability curves are varied during history-matching to determine the curves that should be used in further simulation predictions (Reeves et al., 2003; Reeves and Taillefert, 2002). Alternatively, Hower et al. (2003) found that relative permeability curves had no effect on results during history-matching and instead used linear relative permeability curves. For coal in the PRB there are no generally accepted relative permeability curves, so in our base case simulations we have used relative permeability curves derived from measurements on San Juan coal by Gash (1991) (Figure 3.12). However, preliminary estimates for relative permeability of air-water flow in PRB coal were obtained by Chaturvedi (2006) and we have used his relative permeability curves (Figure 3.12) to look at what effect relative permeability has on CO_2 sequestration and ECBM volumes.

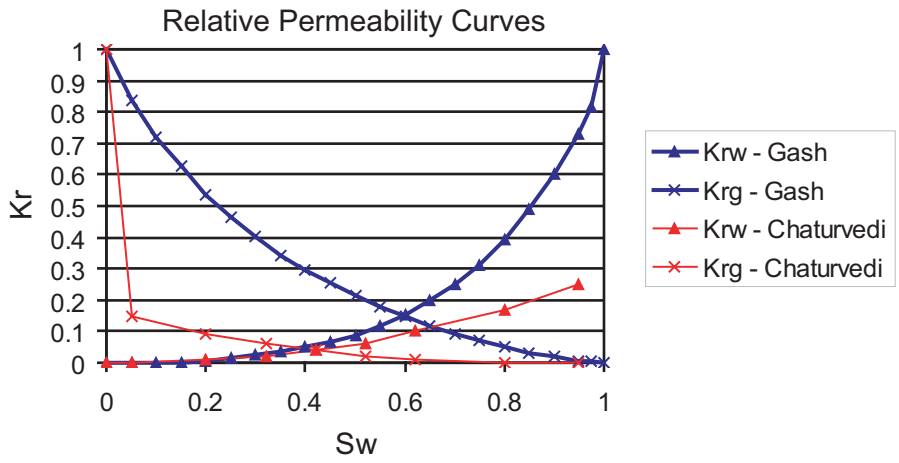

Figure 3.12: Relative permeability curves from Gash (1991) (blue curves) and Chaturvedi (2006) (red curves). The Gash (1991) curves were used in our base case and the Chaturvedi (2006) curves were used to see what effect relative permeability has on total volumes sequestered and produced.

Our simulations showed that when using Chaturvedi's (2006) relative permeability curves the total CO_2 sequestered decreased by ~55% and ECBM by ~100% (Figure 3.13). This is because the effective permeability, which is used in the fluid flow equation, at both high water and gas saturations for Chaturvedi's (2006) curves is much lower than when the Gash (1991) curves are used. Therefore, from our results it seems that relative permeability curves have a significant effect on history-matched cleat permeability fields and simulation predictions.

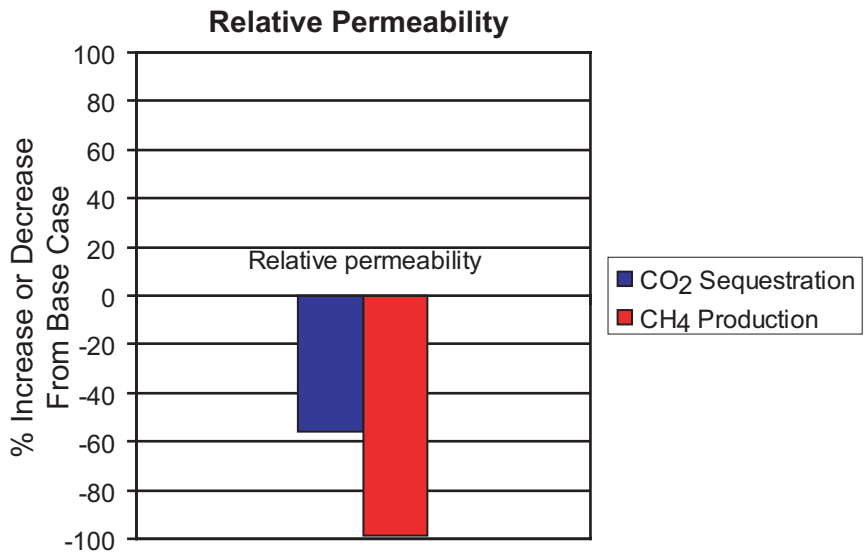

Figure 3.13: Percent increase and decrease in total volumes of CO_2 sequestered and ECBM produced at time of breakthrough compared to the base case through changing the relative permeability curves (Chaturvedi, 2006) (Figure 3.12).

3.4.7 Adsorption isotherms

In 2006 the U.S. Geological Survey (USGS) completed a study looking at adsorption isotherms and gas desorption for coals in the PRB and adjacent coal-bearing basins (Stricker et al., 2006). The CH_4 adsorption isotherms published by the USGS for PRB coal are lower than those measured by Tang et al. (2005). We believe this is because the crushed coal grains used by the USGS were slightly larger than those used by Tang et al. (2005), which means that the surface area for adsorption would have been reduced in the USGS adsorption measurements, lowering the adsorption isotherms. Table 3.7 outlines the USGS (Stricker et al., 2006) and Tang et al. (2005) adsorption parameters. The USGS (Stricker et al., 2006) did not make adsorption measurements for CO_2, so we used those of Tang et al. (2005). We believe that it is acceptable to use Tang et al.'s (2005) CO_2 isotherm because of the large adsorption ratio observed between CO_2 and CH_4 for low rank coals (Stanton et al., 2001; Gluskoter et al., 2002). The USGS (Stricker et al., 2006) measured multiple CH_4 adsorption isotherms for the Big George coal and we used an average as received adsorption isotherm from core hole 1.

Table 3.7: USGS (Stricker et al., 2006) and Tang et al. (2005) adsorption isotherm parameters.

	USGS (Stricker et al., 2006)	**Tang et al. (2005)**
Langmuir Volume	0.25475 gmole/kg for CH_4	0.577 gmole/kg for CH_4, 1.67 gmole/kg for CO_2
Inverse Langmuir pressure	2.4E-4/kPa for CH_4	1.7E-3/kPa for CH_4, 8.5E-4/kPa for CO_2

Using the USGS (Stricker et al., 2006) CH_4 isotherm we found that CO_2 sequestration would increase by ~40%, because of the larger ratio between CO_2:CH_4 adsorption, but that ECBM would decrease by ~65% because of the lower CH_4 adsorption isotherm, which decreases total initial gas in place and total volumes of CH_4 being desorbed through CO_2 displacement (Figure 3.14). If we were to use the USGS (Stricker et al., 2006) isotherms in prediction simulations, we would need to re-history-match, which would increase the cleat permeabilities and therefore we may not observe such a large decrease in CH_4 production.

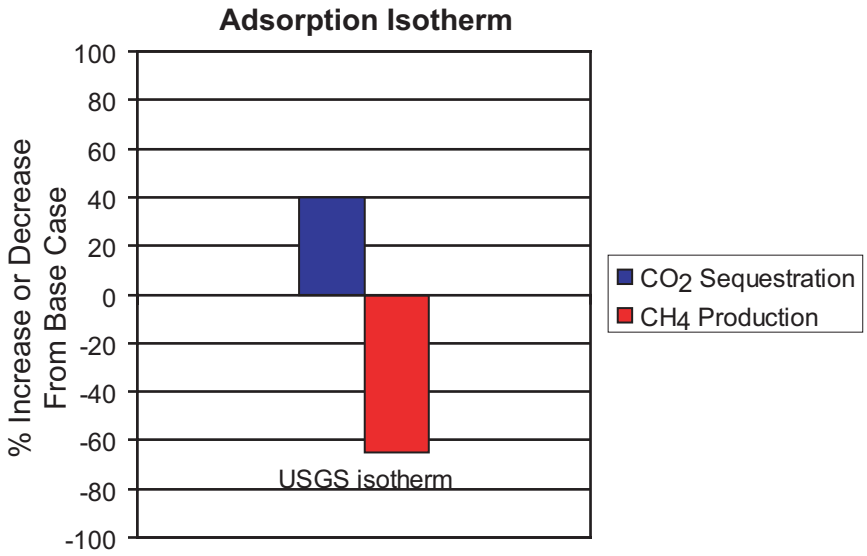

Figure 3.14: Percent increase and decrease in total volumes of CO_2 sequestered and ECBM produced at time of breakthrough compared to the base case through using the USGS (Stricker et al., 2006) CH_4 adsorption isotherm for Big George coal (Table 3.7).

3.4.8 Maximum bottom hole pressure injector constraint

A BHP constraint for the injector determines the injection rate for CO_2. A higher constraint means that the injection rate can go higher without violating the constraint. We were interested in what effect changing the BHP injector constraint would have on total volumes sequestered and produced.

We found that the BHP constraint for the injector had a significant effect on the total volumes of CO_2 sequestered and CH_4 produced. Both the total CO_2 sequestered and CH_4 produced increased by ~105% and ~140% respectively for a BHP injector constraint of 5000 kPa compared to the base case. Increasing the constraint meant that more CO_2 was injected, causing more CH_4 to be desorbed from the matrix in exchange for CO_2 (Figure 3.15). However, because of the higher CO_2 injection rate, breakthrough occurred at 5900 days. But even if injection was terminated at time of breakthrough, the total CO_2 sequestered and CH_4 produced would still be higher than in the base case (~70% and ~75% respectively) (Figure 3.15).

Lowering the BHP constraint had a negative effect on CO_2 sequestration volumes and ECBM (Figure 3.15). At 6720 days CO_2 sequestration was ~65% less than in the base case and ECBM was ~75% less. However, CO_2 breakthrough was not observed.

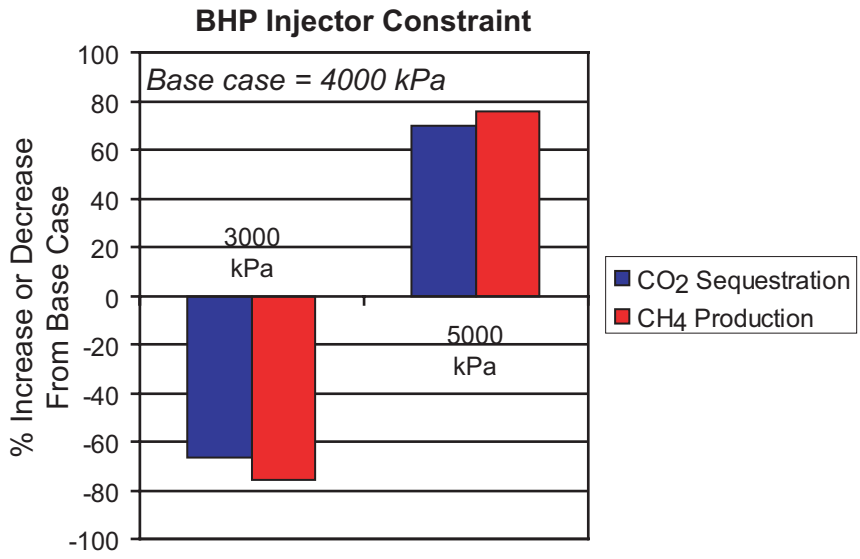

Figure 3.15: Percent increase and decrease in total volumes of CO_2 sequestered and ECBM produced at time of breakthrough compared to the base case for various changes in the BHP injector constraint (Table 3.2).

3.4.9 Coal thickness

The Big George coal varies in thickness from 14 m to 62 m, but in many other coal-bearing basins coal thickness is much smaller, for example the coal seams that the RECOPOL CO_2 sequestration pilot study injected CO_2 into were only ~1-3 m in thickness (van Bergen et al., 2006). Hence, we wanted to see what effect coal thickness would have on our results, especially a reduced thickness.

Halving the coal thickness had the effect of decreasing the total volume of CO_2 sequestered (~52% compared to the base case) and CH_4 produced (~75%), because of the lower initial CH_4 in place and shorter well length over which to inject CO_2 (the injection well was perforated over a length of 8 m compared with 16 m in the base case) (Figure 3.16).

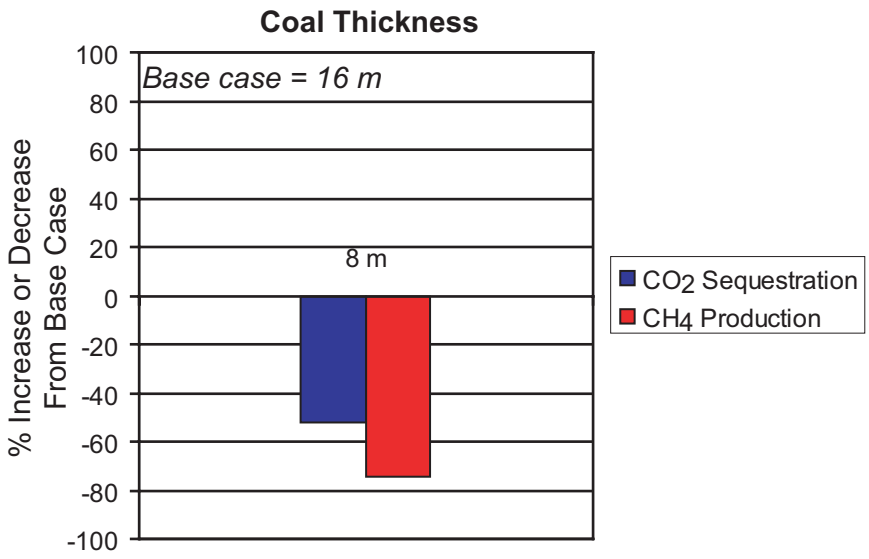

Figure 3.16: Percent increase and decrease in total volumes of CO_2 sequestered and ECBM produced at time of breakthrough compared to the base case from halving the coalbed thickness (Table 3.2).

3.4.10 Reservoir pressure

The coals in the Powder River Basin are under-pressured (Advanced Resource International, Inc., 2002; Ross and Zoback, 2006b), but this is not the case in other coal-bearing basins such as the San Juan basin, where the pressure gradient is ~12 kPa/m (Young, 2006; Reeves et al., 2003) and the basin in the RECOPOL pilot study, where the gradient is 10.6 kPa/m (Reeves and Taillefert, 2002). Hence, we wanted to see what effect a higher reservoir pressure would have on our simulation results and used a value equal to hydrostatic pressure at the model depth (~ 9.95 kPa/m).

Increasing the reservoir pressure caused no change in the total CO_2 sequestered, whereas the total CH_4 produced increased by ~40% (Figure 3.17). We believe the increase in CH_4 production is because there is more initial CH_4 adsorbed due to the higher initial reservoir pressure. In terms of the total CO_2 sequestered, even though cumulatively there was no difference in the total CO_2 sequestered between the base case and having a higher reservoir pressure, initially the CO_2 injection rate was lower for the higher reservoir pressure case than in the base case, because it was harder to inject CO_2. However, because the base case initially injected CO_2 at a higher rate, the

reservoir pressure rose more quickly and to a higher value than in the high reservoir pressure case, so the injection rate then decreased to a much lower rate than in the high reservoir pressure case to maintain the BHP. Hence, overall the total amount of CO_2 injected and sequestered was the same for the two cases.

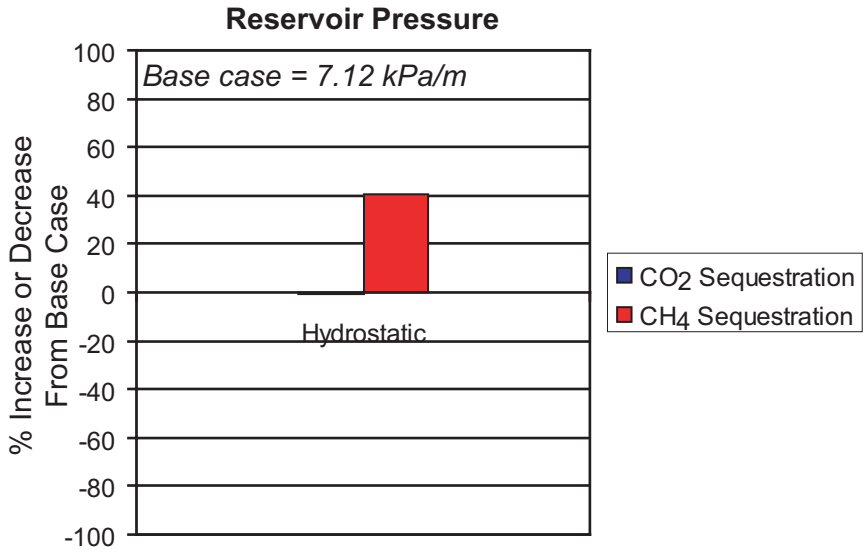

Figure 3.17: Percent increase and decrease in total volumes of CO_2 sequestered and ECBM produced at time of breakthrough compared to the base case from changing the initial reservoir pressure to hydrostatic (Table 3.2).

3.4.11 Well spacing and horizontal wells

3.4.11.1 Well spacing

In the PRB, most CBM wells are placed on an 80-acre well spacing, but in other coal-bearing basins CBM wells are required to be on 160 or even 320-acre spacing. We increased the well spacing to 160 acres (the simulations were run on a ¼ of a 5-spot, 160-acre spacing model and we multiplied the results by 4 to get the volumes for a full 5-spot on 160-acre spacing) and found that CO_2 breakthrough is prolonged, enabling the injection well to stay on line for a longer period before needing to be shut in due to CO_2 production. From a sequestration stand point, 160-acre spacing is optimal, but because of the larger area between the injection and production wells, ECBM production does not exceed the volume of CH_4 produced from primary production when the CBM wells are placed on an 80-acre well spacing, as is the case

in the PRB. The 80-acre spacing for CBM wells means that there are more production wells within the 160-acre area, and therefore more CH_4 can be produced by primary production. In addition, because the injection and production wells are further apart on 160-acre spacing, it takes much longer for them to communicate with one another. In the 80-acre spacing simulations, the pressure around the injection well only decreased once CO_2 reached the production wells. At the same time, the pressure around the production wells stopped increasing. In contrast, in the 160-acre spacing simulations the pressure around both the injection well and production well never decreased because the CO_2 did not reach the production wells (within the simulation time). The higher pressure around all the wells meant that sequestration and ECBM were reduced in the 160-acre scenario compared to the base case (~29% and ~84% respectively) (Figure 3.18). However, if we had run the simulations for a much longer time the wells would have finally come into communication with one another and ECBM would have been produced.

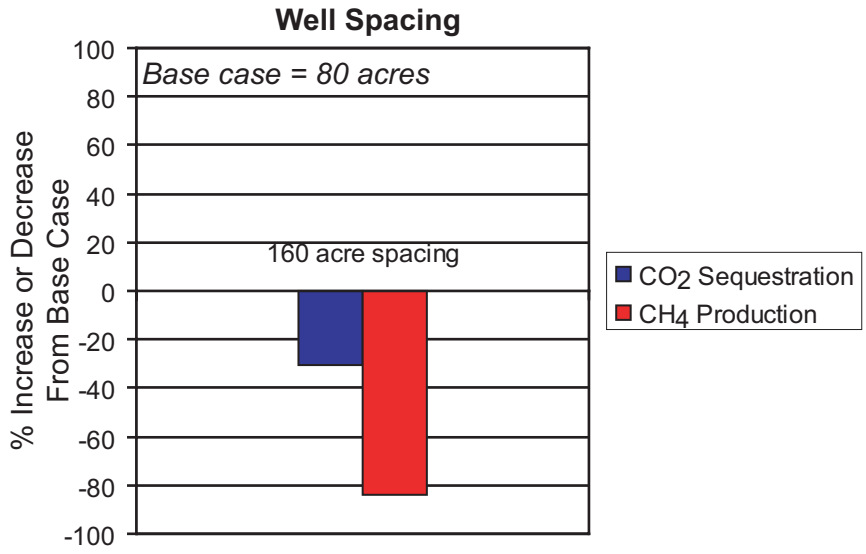

Figure 3.18: Percent increase and decrease in total volumes of CO_2 sequestered and ECBM produced at time of breakthrough compared to the base case through increasing the well spacing to 160-acres.

160-acre well spacing is probably more ideal for coals with very high cleat permeability, as the injection and production wells will come into communication much faster, but breakthrough will be at later times than when using 80-acre spacing.

We ran the 160-acre well spacing simulation using the "original" cleat permeability before history-matching (Table 3.4) and found that breakthrough occurred at 4100 days, compared to 1920 days for the 80-acre well spacing case with the "original" permeability. At the time of breakthrough, CO_2 sequestration was ~270% greater than in the base case (80-acre spacing and history matched permeabilities and porosities) and ECBM increased by ~350%. If we had used a lower BHP constraint than 4000 kPa, breakthrough would have been prolonged.

3.4.11.2 Horizontal wells

Horizontal wells are an injection option that is being investigated by a number of researchers (Smith et al., 2005; Winschel and Douglas, 2006; Shi and Durucan, 2006) and we were interested to see what effect they would have on total volumes sequestered and produced compared to both our base and hydraulic fracture cases. GEM allows for the input of horizontal wells, so we did not need to model a horizontal well as we did for the horizontal hydraulic fractures (Chapter 2, section 2.5). We specified a well length of 200 m and carried out two runs. The first had a well oriented perpendicular to the face cleat direction and the second had a well oriented parallel to the face cleat direction. In both instances, the horizontal well was placed in the bottom layer of the model to take advantage of the vertical upward sweep of gas (buoyancy effect). There was only a slight difference in total volumes between the two well orientations, where total CO_2 sequestered for the well perpendicular to the face cleats increased by ~60% and ECBM by ~80%, compared to ~55% and ~75% for the well orientated parallel to the face cleat direction (Figure 3.19). This increase in total volumes is greater than the case with a hydraulic fracture, where CO_2 sequestration and ECBM only increased by ~45% and 55% respectively compared to the base case. The higher volumes for the cases with horizontal wells are not surprising, since we are able to inject CO_2 from along the entire length of the well (which is 200 m and therefore longer than the vertical well (16 m)), whereas in the horizontal hydraulic fracture case we are only injecting into the fracture, which still limits the volume of CO_2 that can be injected. The horizontal wells also provide a

more efficient CO_2 gas sweep as the gas rises to the top of the coal, compared to the sweep from the vertical well in the base case (Figure 3.20).

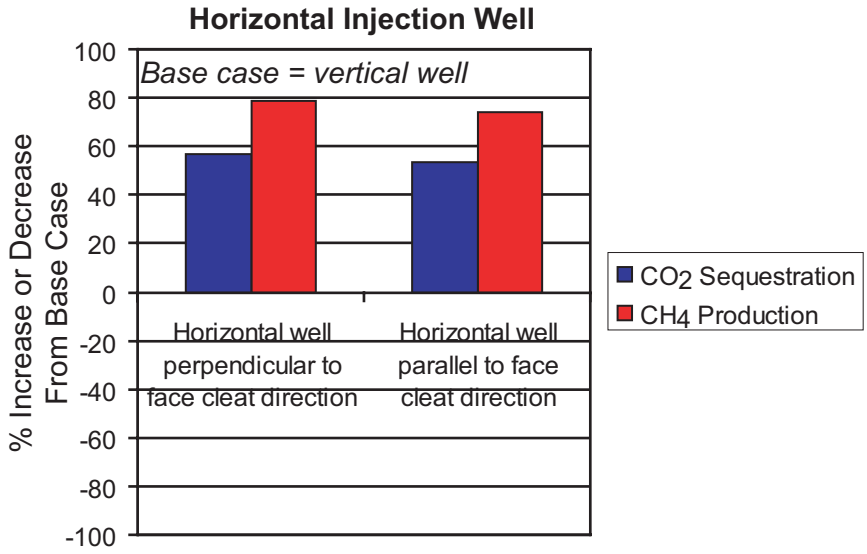

Figure 3.19: Percent increase and decrease in total volumes of CO_2 sequestered and ECBM produced at time of breakthrough compared to the base case if horizontal wells are utilized.

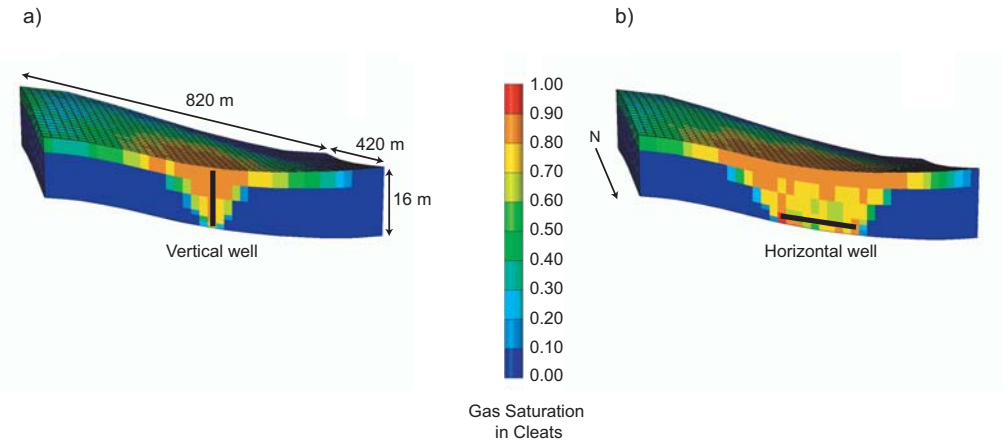

Figure 3.20: Gas saturation in the coal cleats after 1 year of CO_2 injection. a) Map of gas saturation in the coal cleats when using a vertical injection well versus b) when using a horizontal well. Note that a horizontal well helps obtain a more efficient vertical gas sweep.

3.4.12 Flue gas

Kovscek et al. (2005) carried out laboratory experiments on gas mixtures (flue gas) composed of varying concentrations of N_2 and CO_2. They found "that a small

fraction of nitrogen in the injection gas serves to preserve coal pack permeability". We ran simulations to investigate the effect of flue gas composition on CO_2 sequestration and ECBM at the reservoir scale in Big George coal. In addition, an actual field pilot study of N_2 injection for ECBM purposes was carried out in coal in the San Juan basin and this project is known as the Tiffany Unit. N_2 was injected from 1998 to 2002 through 12 injection wells, surrounded by 34 CBM producers. Almost immediately, the total CBM production rate rose from 5 MMcfd to 27 MMcfd and N_2 breakthrough was fast (Reeves and Oudinot, 2004).

We ran four different flue gas scenarios with N_2:CO_2 mixtures of 20:80, 50:50, 80:20 and 100:0. We found that in all four cases the total ECBM increased from 9% to 23% to 32% to 40% respectively compared to the base case (0:100) (Figure 3.21). Like Kovscek et al., (2005) we observed a positive effect on cleat permeability due to the presence of N_2. For the 20:80, 50:50 and 80:20 cases the permeability still decreased because of matrix swelling, but not as much as in the base case (decrease by 1.9 mD, 1.4 mD and 0.2 mD respectively at the injection well, compared to 2.2 mD in the base case), and for the 100:0 case, the permeability actually increased by 3 mD at the injection well. It appears that when less than 20% CO_2 is present in the injection stream, stress dependent permeability dominates in the extended Palmer and Mansoori equation (GEM, 2005), rather than matrix swelling, and the cleats are pushed open and kept open by the higher pressure in the reservoir due to the gas injection (the effective horizontal stress decreases). It seems that ECBM increases with N_2 content, not only because of the observed permeability increases but because the N_2 migrates through the coal at a faster rate than CO_2 and therefore contacts more of the coal, helping to desorb more CH_4 (Figure 3.22). However, breakthrough of N_2 occurred much earlier than in the base case, ~2 years after the start of injection compared with no breakthrough during the simulation period for the base case.

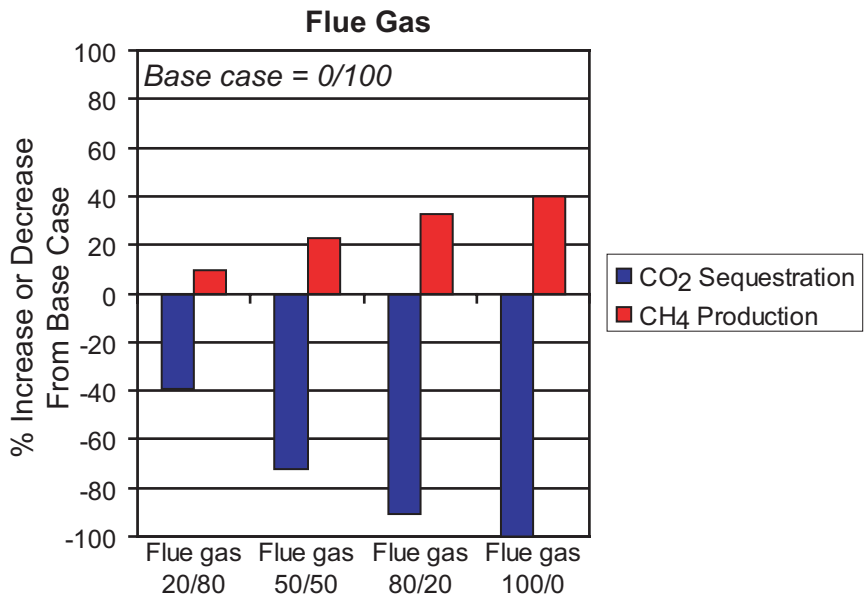

Figure 3.21: Percent increase and decrease in total volumes of CO_2 sequestered and ECBM produced at time of breakthrough compared to the base case for various compositions of flue gas (Table 3.2).

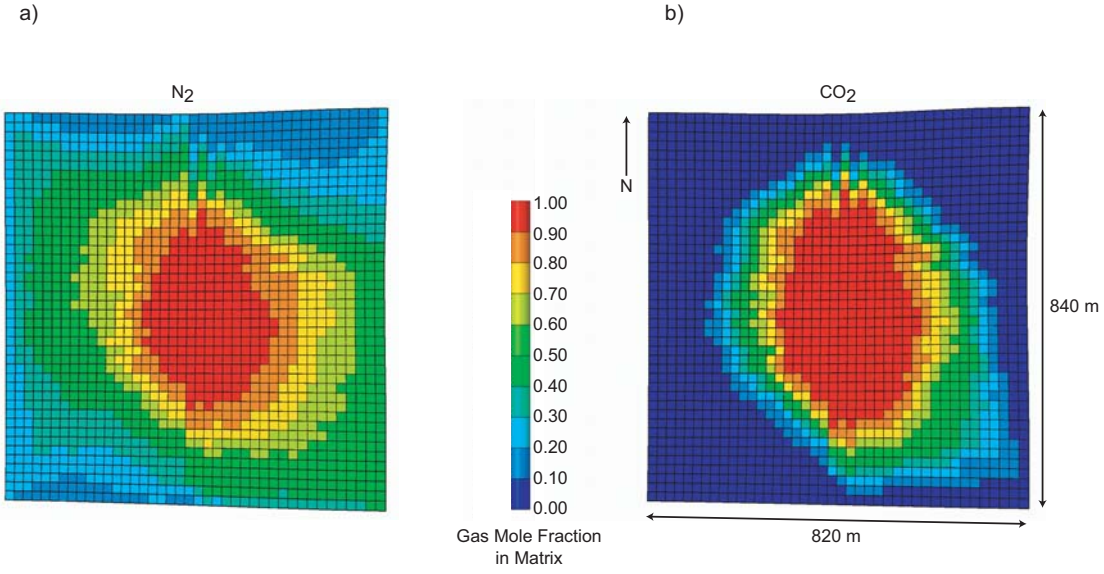

Figure 3.22: a) N_2 gas mole fraction in the coal matrix versus b) the CO_2 gas mole fraction in the coal matrix after 13 years of injection. Figure a is for the case with 100% N_2 injection and b is for the base case. Note that the N_2 has migrated further away from the injection well than the CO_2 in the base case and therefore the N_2 has contacted a larger volume of the matrix, causing more CH_4 to desorb than in the base case.

3.5 Discussion

Our sensitivity study of coal properties and simulation model parameters reveals that cleat permeability and porosity, fracture pressure, gas diffusion times, cleat compressibility, matrix volumetric strains for gas species in the reservoir, relative permeability curves and the adsorption isotherms for gas species have large effects on total volumes of sequestered CO_2 and ECBM recovery predicted by fluid flow simulations. We believe that it is imperative that accurate values of these parameters are used in simulations for screening and pilot studies to obtain realistic predictions of the sequestration potential of a coal-bearing basin and for determining the best operating designs and constraints for field projects.

In terms of the Big George coal, we find that if the cleat permeability is truly hundreds of mD in magnitude, as reported by some publications (Flores, 2004; Mavor, 2003), then an 80-acre well spacing for CO_2 sequestration is too small, causing breakthrough to be too fast for any significant sequestration or ECBM. However, when the wells are spaced 160 acres apart, breakthrough is minimized. In the Allison ECBM pilot study the wells were placed on 160-acre spacing and the cleat permeability was estimated to be between 100 and 140 mD in the study area (Reeves et al., 2003). After 5 years of CO_2 injection no CO_2 breakthrough was reported (Reeves, 2001). In contrast, our simulations show that if the cleat permeability is closer to tens of mD then an 80-acre well spacing is ideal (160-acre well spacing is too large on time scales that we are interested in). Measured cleat porosity values are also important so that correct water volumes within the coalbed can be calculated by the simulator. If values are higher than is realistic the simulator will predict lower volumes of ECBM recovery than would be true in the field.

The fracture pressure of the coal and overlying units should determine the BHP injection constraint, which needs to be set at a value that does not allow the pressure in the reservoir to exceed the fracture pressure. Setting a BHP injector constraint of 5000 kPa for the Big George coal did not cause the reservoir pressure to exceed the fracture pressure. But there was a trade-off, in that breakthrough occurred earlier than when

using a constraint of 4000 kPa, causing sequestration to be terminated at an earlier time. However, as we saw in our simulations, the higher constraint meant that more CO_2 could still be sequestered and greater volumes of ECBM were still produced despite having to terminate sequestration sooner than when using the lower constraint. In other coal-bearing basins this trade-off will need to be taken into consideration when determining the BHP injection constraint or injection pressure. In the Japan and Allison (USA) pilot studies, BHP has been used as the injection constraint (Yamaguchi et al., 2006; Reeves et al., 2002), whereas in the China and Poland (RECOPOL) pilot studies, injection pressure was used and BHP was monitored (Wong et al., 2006; van Bergen et al., 2006). All of the pilot studies seem to have taken into account the fracture pressure of the coalbeds.

Cleat compressibility and matrix volumetric strains for CO_2 and CH_4 are both included in calculations of cleat permeability changes due to matrix shrinkage and swelling and changes in effective horizontal stress (GEM, 2005; Palmer and Mansoori, 1996; 1998). Both of these properties are unknown for the Big George coal, but from sensitivity runs we find that high cleat compressibility would be a positive property for CO_2 sequestration and ECBM in the PRB, whereas high CO_2 volumetric strain would have a negative effect on sequestration and ECBM volumes. We also observe that if the Big George coal had very slow gas diffusion times, then that would also be a negative property for CO_2 sequestration and ECBM in the PRB.

Finally, from our sensitivity study we have found that CO_2 sequestration and ECBM predictions are greatly affected by the adsorption isotherms used in simulations. We believe that adsorption isotherms measured on intact coal samples may yield isotherms with values closer to the magnitude of adsorption that occurs on the reservoir scale. In addition, we have shown that relative permeability curves play a significant role when history-matching to determine the true cleat permeability and porosity values of the coal. Ideally, accurate relative permeability curves for the coal being modeled need to be measured in the laboratory and used in the history-matching simulations.

Our sensitivity study also revealed the effect of more general coal characteristics and engineering practices on CO_2 sequestration and ECBM feasibility, such as coal thickness, initial reservoir pressure, well orientations and injected gas composition. We saw that thinner coals have a smaller capacity for CO_2 and contain less initial CH_4 in place for ECBM production. However, the volumes of CO_2 sequestered and ECBM produced could be greater in these thinner coals if the initial reservoir pressure is higher and/or if horizontal wells are utilized. Shi and Durucan (2006) carried out a simulation study looking specifically at the effect of horizontal wells on ECBM in thin coal seams (1.3 m) and found that horizontal wells increased ECBM volumes by a factor of five compared to vertical wells on a 5-spot pattern. For coal-bearing basins with high initial reservoir pressures (close to hydrostatic), it appears that hydraulically fracturing the coal will help with CO_2 injectivity, as was seen at RECOPOL (van Bergen et al., 2006).

In addition, it seems that when horizontal wells can be utilized (depending on stress conditions and well bore stability), they greatly improve CO_2 sequestration and ECBM. Not only can you inject more CO_2, but the gas sweep is a lot more efficient in water saturated coals than when vertical wells are employed.

Lastly, we do see great improvements in ECBM when N_2 is employed to enhance production; however, N_2 is used at the expense of CO_2, decreasing the volume of greenhouse gas that might be sequestered. Perhaps adding a small percent of N_2 to the CO_2 injection stream would be wise, as suggested by Kovscek et al. (2005), to help reduce some of the effect of matrix swelling on injectivity and production.

To quantify the uncertainty in the total volume of CO_2 that can be sequestered in unmineable coalbeds of the PRB we have taken the maximum and minimum volumes from our sensitivity simulation results (at time of breakthrough) and calculated the range in total volume of CO_2 that can be sequestered in coalbeds at depths greater than 300 m and with bed thicknesses of greater than 3 m (assuming the coal properties are the same as our models throughout the basin and that the coalbeds are overlain by

impermeable caprocks). If we were to use a BHP constraint of 5000 kPa, this would permit us to sequester the most CO_2 out of all of our sensitivity runs. Using the total coal volume calculated by Nelson (2006) for the PRB, for coal deeper than 300 m and with thicknesses greater than 3 m, a BHP constraint of 5000 kPa would allow us to sequester ~2.17 billion tonnes of CO_2. In contrast, if coal everywhere in the PRB had a CO_2 matrix volumetric strain of 0.1, we could only sequester ~59 million tonnes of CO_2. It appears from our sensitivity analysis that coal resources of the PRB, at depths greater than 300 m and with thicknesses greater than 3 m, could sequester from ~59 million tonnes to ~2.17 billion tonnes of CO_2, where ~63 million tonnes of CO_2 is produced per year in the State of Wyoming (EIA, 2007).

3.6 Summary (Chapters 2 and 3)

As a result of our CO_2 sequestration and ECBM feasibility and sensitivity study on unmineable coalbeds in the PRB, we have noted a number of model parameters and coal properties that we believe are important for obtaining accurate results when carrying out predictive fluid flow simulations for pilot and full-field CO_2 sequestration projects in coal-bearing basins. In terms of making sure that CO_2 sequestration estimates for coal-bearing basins are accurate and rates and breakthrough times from simulations used to develop a pilot project are precise; realistic, heterogeneous permeability fields need to be incorporated into fluid flow models and model grids need to contain more than one layer in the vertical direction, especially if the coals are water saturated. In addition, if history-matching is undertaken to constrain the permeability field, laboratory derived relative permeability curves for the coal in question should be used. Likewise, measurements of cleat compressibility and matrix volumetric strain at infinite pressure need to be obtained, particularly if the simulation software uses the Palmer and Mansoori equation, or a variant on the equation, to model matrix shrinkage and swelling. Ideally, matrix shrinkage and swelling equations derived specifically for the coal being modeled would give better estimates on the reduction in permeability with CO_2 injection than a general equation. As has been observed with coal in both Japan and Canada, no reduction in injectivity

occurred during CO_2 sequestration pilot projects (Yamaguchi et al., 2006; Mavor et al., 2004). This suggests that shrinkage and swelling cannot be modeled by a single equation and that the process is different in different coals.

It is also critical that correct adsorption isotherms are used within the simulator and intact coal samples should be used where possible to obtain adsorption curves representative of adsorption on the reservoir scale. In addition, the fracture pressures for the coalbed and overlying geologic units need to be determined so that pressures do not exceed the fracture pressure and cause fracturing. It is important that the limit in pressure is incorporated into simulations or sequestration estimates will be larger than is realistic and if a pilot project is carried out based on results from fluid flow simulations, the coal could be accidentally fractured. With this in mind, it is also imperative that target coalbeds are overlain by low permeability confining units so that CO_2 does not migrate into overlying sand bodies and then to the surface.

We have also identified coalbeds that are not ideal for CO_2 sequestration sites. These include coals with no confining units, coals with very slow diffusion times and coals with large matrix volumetric changes due to CO_2 adsorption and/or low cleat compressibility. The last two factors would mean that the coal was very susceptible to matrix swelling with the adsorption of CO_2, which would limit sequestration. Slow diffusion times will mean that on time scales required to mitigate the effects of global warming, the CO_2 will not be adsorbed and a large volume of it will by-pass the matrix and flow to the production wells (to stabilize CO_2 concentrations in the atmosphere at 550 ppm, ~22 $GtCO_2$/year over the remaining century will need to be sequestered (Wigley et al., 1996)). However, to reduce global warming it may come to the point that all coal-bearing basins need to be considered for CO_2 storage and ways around sequestration limitations should be investigated, such as utilizing horizontal wells and hydraulic fractures, injecting N_2 enriched gas and recycling CO_2 to obtain incremental sequestration.

Our study has shown that it should be feasible to sequester CO_2 in unmineable coalbeds of the PRB, so long as target beds are overlain by impermeable confining

units. It also appears that sequestration in the PRB will play only a small role in helping to mitigate global greenhouse gas emissions and it seems from our sensitivity analysis that this will be true of other coal-bearing basins. Therefore, it is going to take many different geologic sequestration sites to sequester global CO_2 emissions.

3.7 Appendix 1 – Using GEM to match laboratory gas flow experiments

We were interested in determining the detail to which GEM could model fluid flow through coalbeds and have used GEM to match laboratory experiments on gas flow through a 25 cm long coalpack. Tang et al. (2005) carried out several experiments in the laboratory looking at gas displacement through a coalpack, 25 cm in length and 4.25 cm in diameter, composed of crushed PRB coal with a mean particle size of 25 mm. In the laboratory experiment, the coalpack was saturated with CH_4 and pressurized to 4137 kPa (600 psi). Pure CO_2 was then injected at the inlet, at an injection rate of 0.5 cm^3/min, and gas composition and flow rate were measured at the outlet to determine the CH_4 displacement.

The 1D model we built of the laboratory coalpack utilized GEM's slimtube capabilities. The number of grid cells was 200, with dimensions of 200x1x1 and grid spacing of 0.00125 m x 0.03767 m x 0.03767 m. Dual porosity was turned on in GEM and the cleats and matrix were assigned a permeability of 31 mD, the permeability of the coalpack measured by Tang et al. (2005). In order to match the production profiles from the laboratory experiment we varied the cleat and matrix porosities. Since the coal pack was composed of crushed coal we assigned the matrix porosity to the particles and the cleat porosity to the void space between particles. Tang et al. (2005) measured the total porosity of the coal pack to be 37%. The cleat spacing was 0.00025 m, the mean coal particle size. In addition, we used the CH_4 desorption curve measured at a starting pressure of 4137 kPa (600 psi) and the CO_2 adsorption isotherm measured by Tang et al. (2005) on dry, crushed PRB coal.

We ran our simulations by injecting pure CO_2 into one end of the slimtube, at a constant injection rate of 0.5 cm^3/min. We set the reservoir pressure at 4137 kPa and used a production BHP constraint of 4100 kPa. Furthermore, we have assumed that adsorption is instantaneous (the diffusion time is 0), as suggested by Tang et al. (2005). Figure 3.23 shows the best match we could obtain with the laboratory production profiles using GEM. The final cleat and matrix porosities we used were 0.3 and 0.07 respectively. This is similar to the results from Tang et al.'s (2005) numerical match to the laboratory data, where they found that the matrix porosity was 0.074 and the cleat porosity was 0.296. However, when using GEM we found that the production profiles were not greatly affected by changes in the cleat and matrix porosities.

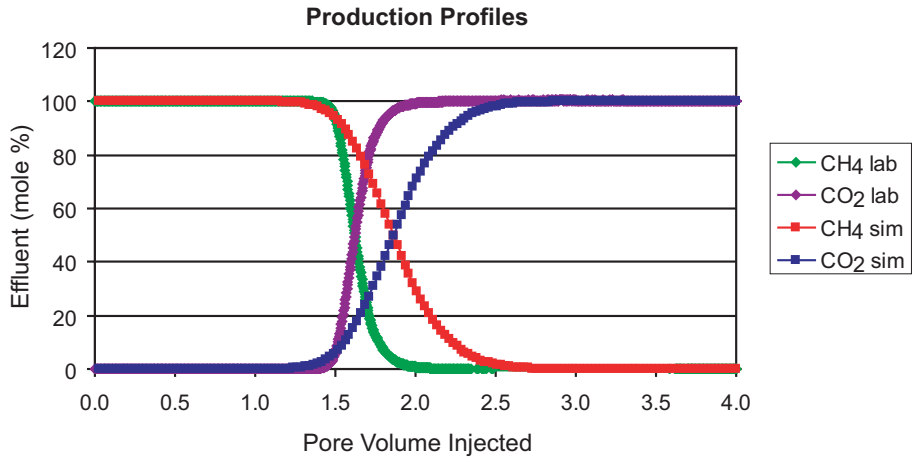

Figure 3.23: CO_2 and CH_4 production profiles from the gas displacement laboratory experiment and the fluid flow simulations. CH_4 and CO_2 lab stands for the CH_4 and CO_2 production profiles from the laboratory experiment by Tang et al. (2005). CH_4 and CO_2 sim stands for the production profiles from the fluid flow simulations, where we tried to use GEM to match the laboratory results.

As can be seen from Figure 3.23, we were unable to match the steep shape of the laboratory production profiles or the exact time of CO_2 breakthrough; although the match is still fairly good for the CO_2 breakthrough time and the crossover point of our curves is only ~0.5 injected pore volumes after the cross over point of the laboratory production curves. At present we have been unable to determine why the production curves from the simulation are not steep like those in the laboratory experiment. We

do find that if we make the diffusion time significantly long, so that effectively no adsorption is taking place in the coal, the production curves steepen, but breakthrough is observed several pore volumes earlier than in the laboratory results. Making the simulation grid finer also did not help to steepen the curves. It is possible that the extended multicomponent Langmuir model used by GEM to model adsorption is not able to capture the detail required for laboratory scale models. We do find that changing the CH_4 adsorption parameters to those for the desorption isotherm measured with the pressure starting at 2900 kPa (475 psi) (Figure 3.24) causes the production profiles to steepen, but we are still unable to match the laboratory results (Tang et al., 2005) (Figure 3.25). Additional work is required to fully understand why GEM is unable to match the laboratory flow displacement results.

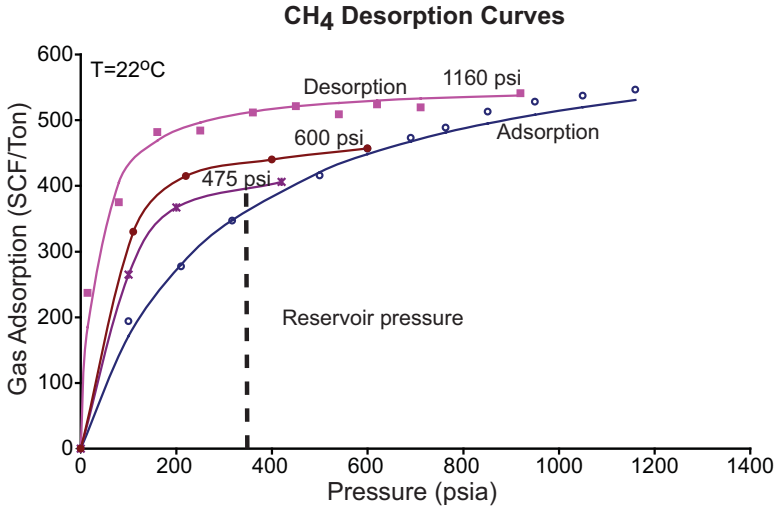

Figure 3.24: Desorption isotherms for CH_4 from dry, crushed, PRB coal samples. The desorption curve starting at a pressure of 2900 kPa (475 psi) is shown in purple. The reservoir pressure line marks the reservoir pressure used in our sensitivity fluid flow simulations (Table 3.1). Modified from Tang et al. (2005).

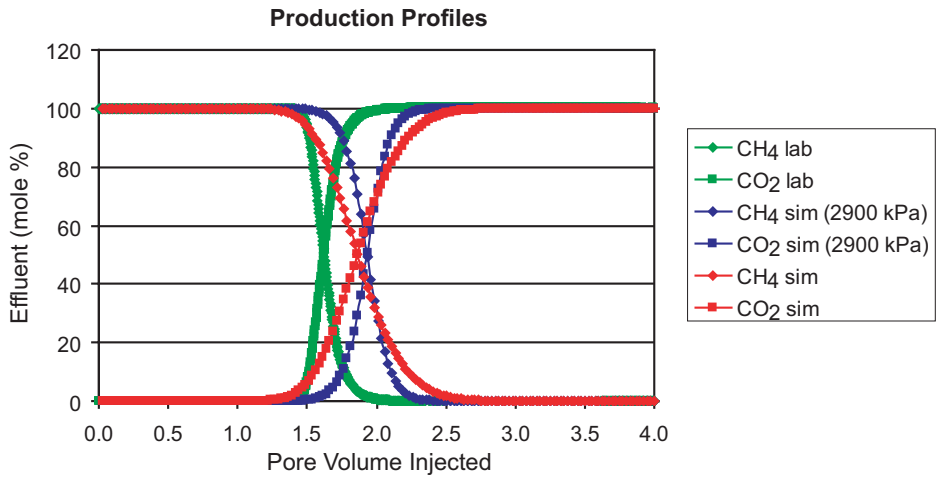

Figure 3.25: CO_2 and CH_4 production profiles from the gas displacement laboratory experiment and the fluid flow simulations using the CH_4 desorption curve at 2900 kPa (475 psi) (Figure 3.24). CH_4 and CO_2 lab stands for the CH_4 and CO_2 production profiles from the laboratory experiment by Tang et al. (2005). CH_4 and CO_2 sim stands for the production profiles from the fluid flow simulations, where we tried to use GEM to match the laboratory results. The blue curves are the production profiles resulting from using the CH_4 desorption curve at 2900 kPa (475 psi) (Figure 3.24).

Chapter 4

SUB-HYDROSTATIC PORE PRESSURE IN COALBED AND SAND AQUIFERS OF THE POWDER RIVER BASIN, WYOMING, AND IMPLICATIONS FOR DISPOSAL OF COALBED METHANE WATER THROUGH INJECTION

4.1 Abstract

Coalbed methane (CBM) production in the Powder River Basin (PRB), Wyoming, is associated with the production of large volumes of CBM water. In some places, CBM water from the PRB has high saline and sodium contents, making it unsuitable for agricultural use and potentially environmentally damaging if discharged at the surface. One option for the disposal of CBM water is injection into aquifers, but for injection to be feasible the porosity and permeability of the sands needs to be high, the pore pressure would ideally be sub-hydrostatic, and the aquifer cannot be in

hydraulic communication with coalbeds or aquifers used for irrigation or domestic use.

In order to determine if pore pressures in the aquifers are low enough to allow for significant CBM water injection and to determine whether the coals and sands are in hydraulic communication with each other we have determined pore pressures in 250 wells that monitor water levels in coalbeds and adjacent sands within the PRB. All 250 wells have pore pressures below hydrostatic pressure, suggesting that injection of CBM water should be feasible from that perspective. However, by analyzing pore pressure changes with time for both the coals and their overlying/underlying sands, we find after 8 to 13 years of water level monitoring that ~60% of the sands less than 200 ft from producing coals appear to be in hydraulic communication with the coalbeds. In contrast, sands further than 200 ft from producing coalbeds show no changes in pore pressure over the 8 to 13 year time period. Therefore, we recommend that injection of CBM water should be carried out in sands further than at least 200 ft from adjacent coalbeds to be sure that the disposed water does not migrate into producing coalbeds over time.

In addition, we ran fluid flow simulations to determine the rates at which CBM water can be injected into shallow (~300 ft) and deep (~1000 ft) aquifers. We find that for the shallow sand model we can inject water at a rate of ~160 bbl/day, whereas for the deeper sand, whose pore pressures are lower than the shallow sand, the rate is ~435 bbl/day. Both these rates are higher than the average water production rate from CBM wells in the PRB, which is ~100 bbl/day. This implies that for deep aquifer injection sites, it would take only one injection well to dispose of the water production from approximately four CBM wells.

4.2 Introduction

Coalbed methane (CBM) production in the Powder River Basin (PRB) began in the early 1980s and by 1989 there were 22 CBM wells (De Bruin et al., 2004; Wyoming Oil and Gas Conservation Commission (WOGCC), 2007). Following this limited early success, production expanded rapidly and today there are ~17,000 wells (WOGCC, 2007), with another 34,000 expected to be drilled over the next 5 to 10 years (Environmental News Network, 2001) (Figure 4.1a). CBM gas from the PRB accounts for ~17% of the total gas produced in Wyoming (WOGCC, 2007). However, CBM production in the PRB is associated with the production of large volumes of CBM water. In 2006 ~590 million barrels (bbl) of CBM water were produced, at an average rate of ~100 bbl/well/day (WOGCC, 2006). Even though the water quality is generally sufficient for drinking water and livestock use, its saline and sodium contents are too high for agricultural use in many places (Wheaton and Donato, 2004; Bartos and Ogle, 2002; The Ruckelshaus Institute of Environment and Natural Resources, 2005). CBM in the PRB is produced through de-watering of the coalbeds (pumping water out of the coalbeds), which reduces the reservoir pressure and causes methane (CH_4) to desorb and flow to the production wells. Because the volumes of CBM water being produced are very large, there is far too much for immediate human and livestock consumption, so most of it is discharged into evaporation/infiltration ponds or streams (Advanced Resources International, 2002; The Ruckelshaus Institute of Environment and Natural Resources, 2005). However, the high saline and sodium contents mean that when the CBM water comes into contact with soil, the ions precipitate out of solution and lower the permeability of the soil, thus reducing the productivity of the soil (Wheaton and Donato, 2004). This in turn can cause soil erosion and ultimately damage to wildlife habitats.

One option for the disposal of CBM water is injection into aquifers, but for injection to be feasible both the porosity and permeability of the aquifer need to be high (for capacity and injectivity), the pore pressure needs to be low (for capacity and injectivity) and the aquifer cannot be in hydraulic communication with coalbeds or

other aquifers (for containment). High porosity and permeability and low pore pressures in the aquifer result in a large capacity for water and increased injectivity. In addition, the water quality of the CBM water should be comparable to that of the aquifer water, so that the CBM water does not degrade the aquifer (Chapter 4, section 5 of the Rules and Statures set out by the WOGCC, 2007). In order to determine if pore pressures in the aquifers are low enough to allow for significant CBM water injection and whether the coals and sands are in hydraulic communication with each other, we have determined pore pressures as a function of time in ~250 wells that monitor water levels in coalbeds and adjacent sands within the PRB. In this study we assumed that an aquifer with sufficient pore pressure below hydrostatic would have storage capacity and ran fluid flow simulations to determine the feasibility of injecting CBM water into those aquifers.

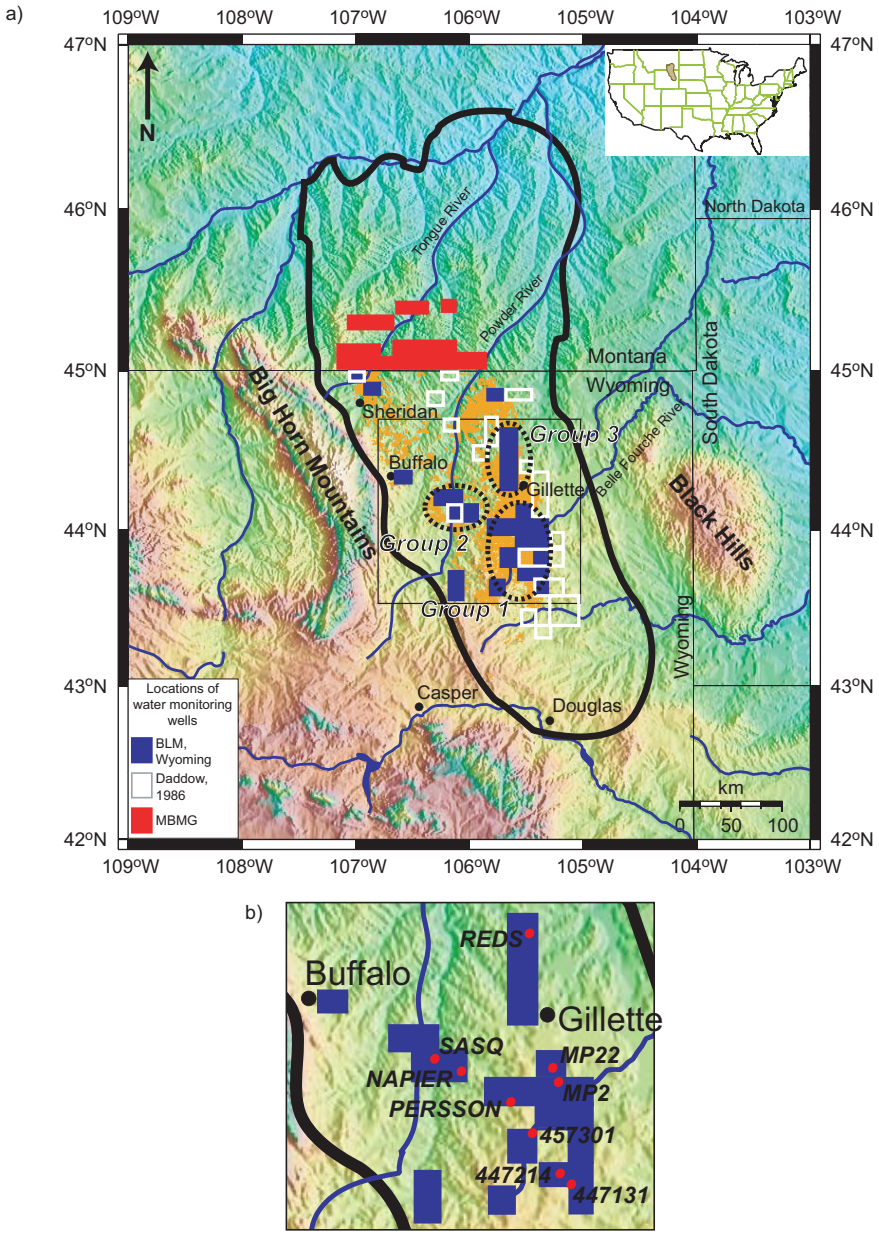

Figure 4.1: a) Location map of the Powder River Basin, WY and MT, and of the water monitoring wells used in this study (modified from Colmenares and Zoback, 2007). The orange dots correspond to CBM wells. The red squares correspond to the township and range location of water monitoring wells maintained by the Montana Bureau of Mines and Geology (MBMG) and Montana Tech of the University of Montana. Blue squares correspond to the township and range location of water monitoring wells maintained by the Wyoming Bureau of Land Management (BLM). White squares correspond to the township and range location of historic water monitoring wells from Daddow (1986). Dotted ovals surrounding the water monitoring wells correspond to groups 1, 2 and 3 mentioned in the text. b) Location map of individual water monitoring wells mentioned in the text. The black box in Figure 1a outlines the area encompassed by this map.

4.2.1 Powder River Basin hydrogeology

A number of studies have been carried out on the hydrogeology of the PRB and many of these are summarized in Lindner-Lunsford and Wilson (1992). More recent studies have focused on water drawdown from CBM production (Wheaton and Metesh, 2002; Bartos and Ogle, 2002; Applied Hydrology Associates and Greystone Environmental Consultants, 2002), water quality (Bartos and Ogle, 2002; The Ruckelshaus Institute of Environment and Natural Resources, 2005) and groundwater systems in the basin (Bartos and Ogle, 2002; Applied Hydrology Associates and Greystone Environmental Consultants, 2002). Bartos and Ogle (2002) used 23 water-level monitoring wells in the Wyoming part of the PRB to look at the hydraulic potential for vertical water flow and the ground water quality at each of these well sites. They found that there was a strong drive for vertical water flow in all but one well site. In addition, they used water chemistry to distinguish isolated ground water systems present in the PRB. The water chemistry revealed the potential for two different aquifer systems in the PRB, a shallow system dominated by a mixed cation composition, with either sulfate or bicarbonate as the dominant anion, and a deeper system composed of sodium-bicarbonate-type waters. They proposed that either there are two ground water systems within the PRB, one shallow and the other deeper (with no vertical flow between them), or that there is one system, where water migrates downward from shallow levels and its composition is changed through chemical interactions and mixing to become sodium-bicarbonate rich.

Applied Hydrology Associates and Greystone Environmental Consultants (2002) also used water level monitoring data in the Wyoming part of the PRB to look at the effect of CBM production on sand and coal aquifers in the basin. They were interested in the volume of recoverable groundwater from these aquifers and what the rate of recharge to the aquifers would be, based on various water management strategies. They proposed that water production from CBM production could induce water “leakage” into the coalbeds from overlying and underlying sand units that occur within 100 ft of the coal, but that leakage would be minimized because most of the coals are isolated from these sand units by fine grained silts/shales that vary in

thickness from 11 to 363 ft. To test this they analyzed hydraulic heads in two sets of paired Bureau of Land Management (BLM) monitoring wells (where one well in the pair is perforated in coal and the other in overlying sandstone) and observed a water level decline over time of ~250 ft in the coals and a ~20 ft decline in the overlying sands. The coals and sands are ~40 ft apart, so they concluded that the water from the sand had migrated into the underlying coal, but that the confining unit between the sand and coal limited their hydraulic communication. We have carried out a similar study, but have used changes in pore pressure with time to infer hydraulic communication between the sands and underlying/overlying coals.

4.2.2 Powder River Basin geology

Coals in the Tongue River Member of the Paleocene Fort Union Formation are the targets for CBM production in the PRB. Figure 4.2 is a cross-section through the central part of the basin, from W-E. The Fort Union Formation is overlain by the Eocene Wasatch Formation, which is exposed at the surface over much of the Wyoming part of the basin (Bartos and Ogle, 2002). Both the Fort Union and Wasatch Formations were deposited in fluvial, lacustrine and swamp environments. The Wasatch Formation is composed of lenticular, discontinuous, fine to medium grained sandstones that are interbedded with siltstones, shales and coals (Applied Hydrology Associates and Greystone Environmental Consultants, 2002; Bartos and Ogle, 2002). The formation varies in thickness from 0 ft at outcrop to ~3000 ft in the central part of the basin (Applied Hydrology Associates and Greystone Environmental Consultants, 2002).

The Fort Union Formation is also composed of interbedded sandstones, siltstones, shales and coals. The Wyodak-Anderson coal zone, part of the Tongue River Member, is the coal zone of interest for CBM production. The coal zone ranges in thickness from less than an inch to 200 ft, and the coals merge and split into as many as 11 beds (Flores and Bader, 1999; Flores, 2004). The coal zone is considered an aquifer and represents the most continuous hydrologic unit in the lower Tertiary part of the PRB (Bartos and Ogle, 2002). The Tongue River Member comprises the

upper part of the Fort Union Formation, and the Wyodak-Anderson coal zone is separated from overlying sands in the Wasatch Formation by low permeability siltstones and shales which act as a confining unit (Applied Hydrology Associates and Greystone Environmental Consultants, 2002; Bartos and Ogle, 2002). Applied Hydrology Associates and Greystone Environmental Consultants (2002) report that the permeability of the confining unit ranges from 0.009 mD to 2 mD in the horizontal directions and 0.002 mD to 0.02 mD in the vertical direction. It is thought that this confining unit ranges in thickness from 11 to 363 ft, but averages ~30 ft across the basin (Applied Hydrology Associates and Greystone Environmental Consultants, 2002).

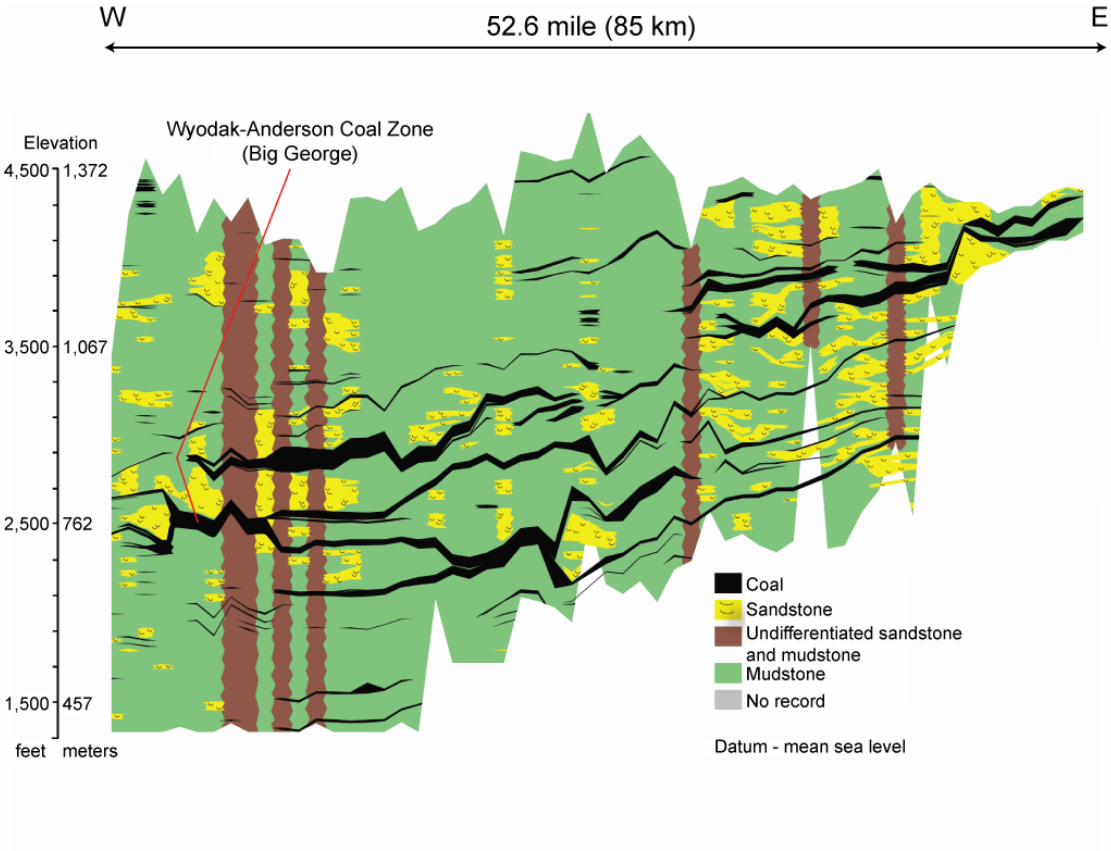

Figure 4.2: Cross section of the upper part of the Fort Union Formation, across the central part of the PRB, from W to E (modified from Flores, 2004).

4.3 Water level data

We obtained water level data from active and historic water monitoring wells across the PRB that monitor water levels in both sand and coalbed units of the Wasatch and Fort Union Formations respectively. In the Montana part of the basin, 219 water monitoring wells are currently operated by the Montana Bureau of Mines (MBMG) and Geology and Montana Tech of the University of Montana; and in the Wyoming part of the basin the Wyoming BLM operates 134 water monitoring wells. We also obtained water level data from 62 historic water monitoring wells in Wyoming, which were in operation before CBM production began in the PRB (Daddow, 1986).

The water monitoring databases contain information on the location, ground elevation, well completion, depth, geologic unit and water level for the wells. However, information for some of the monitoring wells is incomplete, so for the Montana part of the basin we used 144 wells in our analysis, and for the Wyoming part of the basin we used 69 wells from the BLM database and 40 of the historic wells. The locations of all the monitoring wells used in this study are shown in Figure 4.1.

Records for the Montana water monitoring wells go as far back as 1974 and monitoring has been continuous from 1974 to the present. In contrast, the BLM monitoring began much later, in 1993, after CBM production had begun in the basin. Hence, the historic wells (Daddow, 1986) were used to establish water levels before CBM production in the Wyoming part of the basin.

Both the Montana and BLM monitoring databases contain paired wells/well clusters, which are a series of wells located close to one another, where each well is completed at successively shallower depths. Paired wells can be used to determine the potential for vertical fluid flow and whether overlying units are in hydraulic communication with underlying units. In the Wyoming part of the PRB there are 23 well pairs, while in Montana there are 11.

4.4 Calculating pore pressure

We used water level data from monitoring wells to calculate pore pressures for coals and sands in the PRB. The pore pressure (P_p) (fluid pressure) at a position P in the monitoring well is found as follows:

$$P_p = \psi g \rho , \tag{1}$$

where ψ is the height of the water column above P (Figure 4.3), ρ is the water density and g is gravity (Freeze and Cherry, 1979).

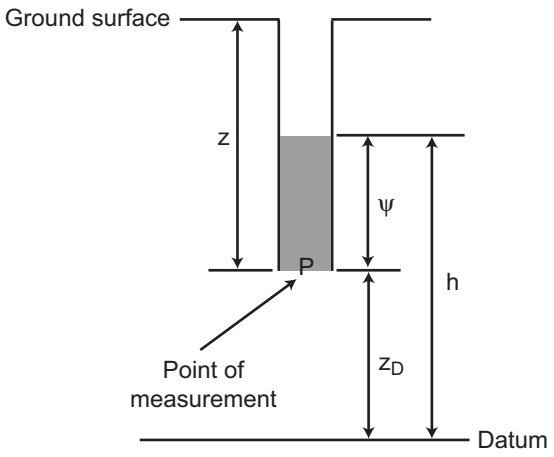

Figure 4.3: Hydraulic head, h, height of the water column above P, ψ, and elevation head, z_D, for a piezometer (modified from Freeze and Cherry, 1979). The datum, where $z_D = 0$, is usually defined to be sea level.

Additional pressure gradients that we will be referring to in the following sections are the hydrostatic and overburden pressure gradients. Hydrostatic pressure is the pressure exerted by a column of water from the ground surface to point P. The gradient is taken as ~0.44 psi/ft. To calculate the overburden pressure, S_v, rock densities are integrated from the surface to the depth of interest, z, where

$$S_v = \int \rho(z) g dz \cong \overline{\rho} g z , \tag{2}$$

and $\rho(z)$ is the density as a function of depth, g is the gravitational acceleration and $\overline{\rho}$ is the mean overburden density. Because density logs are not available for any of

the monitoring wells analyzed we used a mean overburden density of 2.3 g/cc, which is a reasonable average for the lithological units above the coal in the PRB (interbedded shales and sands).

4.5 Pore pressure analysis

4.5.1 Present day sand and coal pore pressure magnitudes in the Powder River Basin

We calculated present day (2005) pore pressures for sands and coals in both the Montana and Wyoming parts of the PRB and found that they are sub-hydrostatic everywhere that data is available (Figure 4.4). Figure 4.4 shows that the pore pressure magnitudes for both coals and sands in Montana and Wyoming plot below the hydrostatic pore pressure line, indicating that pore pressures are sub-hydrostatic. Pore pressures for the coalbeds are much lower than for overlying sands because of CBM production, which has reduced pore pressures in the coalbeds through water extraction.

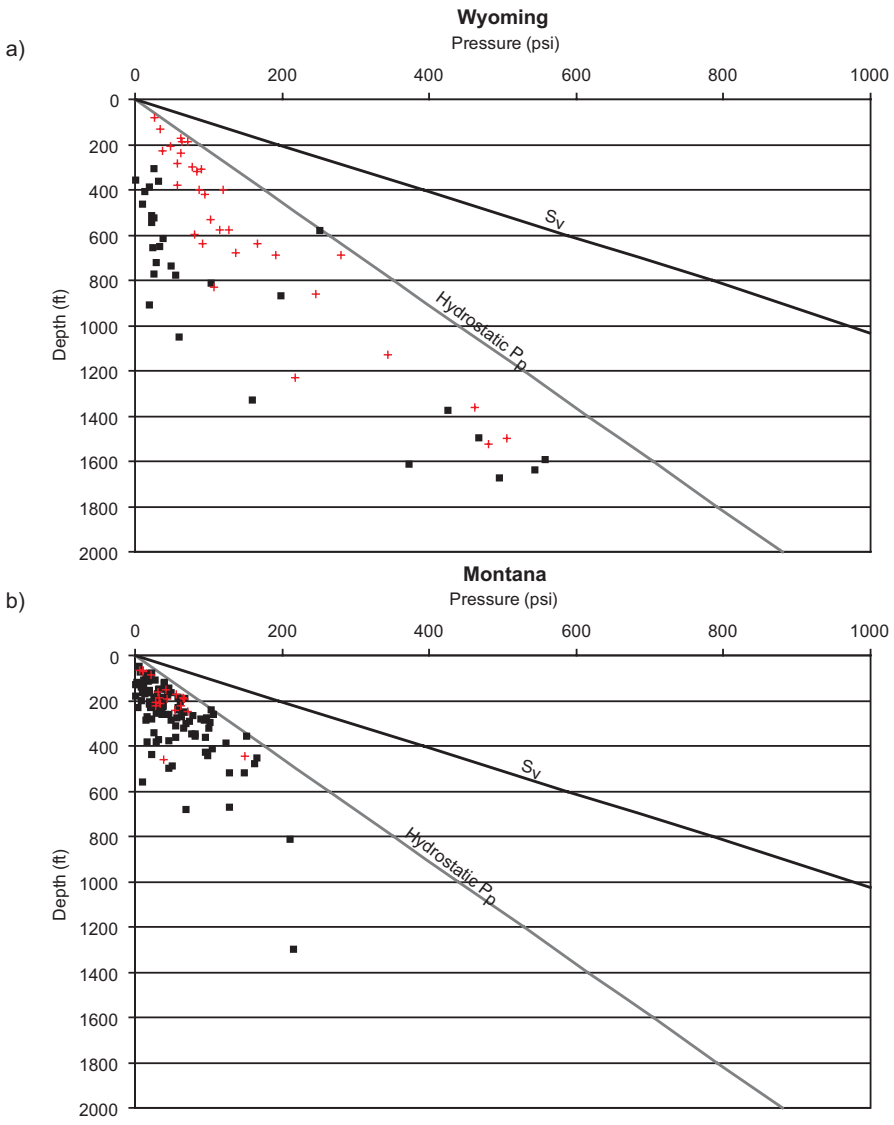

Figure 4.4: Present day pore pressure in a) Wyoming and b) Montana. S_v corresponds to the overburden pressure and the black line is the overburden pressure gradient. The grey line corresponds to the hydrostatic pore pressure gradient (~0.44 psi/ft). Black squares correspond to pore pressures in coal and red crosses to pore pressures in sand.

4.5.2 Groundwater system before CBM production in the Powder River Basin

Taking water level data from 1972 to 1984 from both the Montana and Wyoming parts (Daddow, 1986) of the PRB, we calculated sand and coal pore pressure magnitudes across the basin before CBM production began in the basin. We find that pore pressures in both the sands and coals plot below hydrostatic where we

have historic data (Figure 4.5), indicating that pore pressures were sub-hydrostatic before CBM production in the basin.

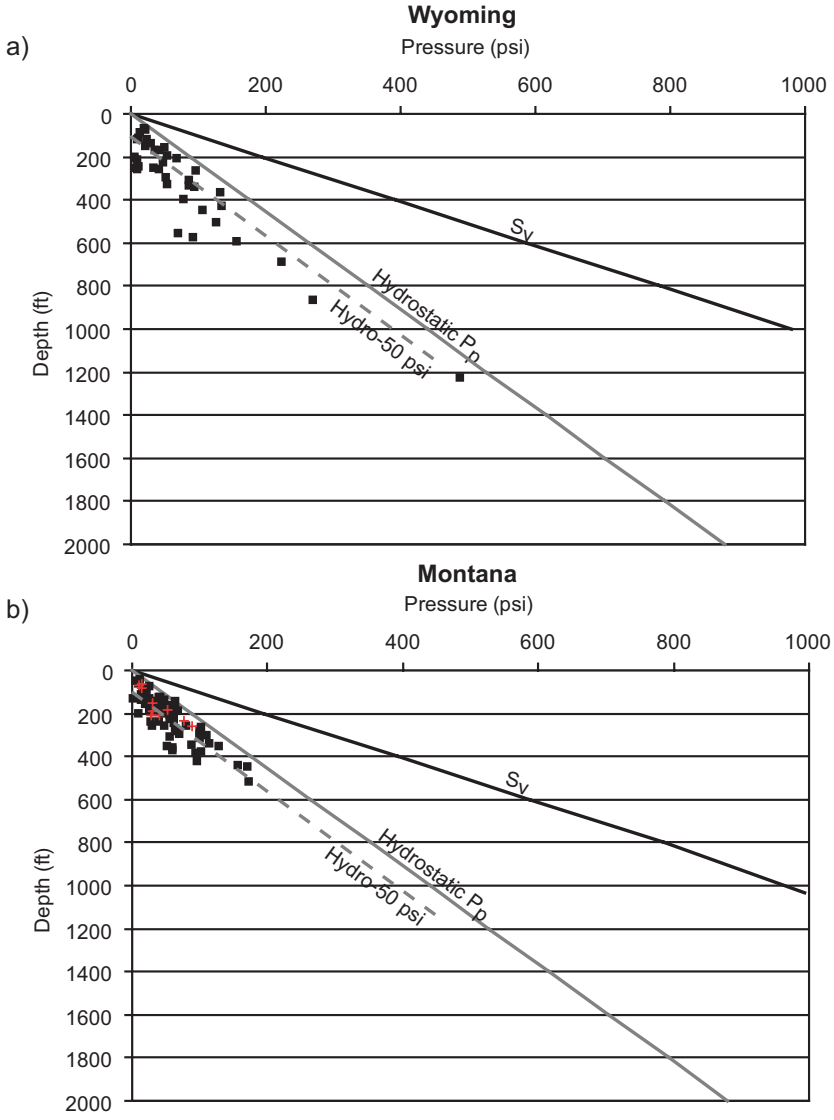

Figure 4.5: Pore pressure in a) Wyoming and b) Montana before CBM production (1972-1984) in the PRB. S_v corresponds to the overburden pressure and the black line is the overburden pressure gradient. The grey line corresponds to the hydrostatic pore pressure gradient (~0.44 psi/ft). The dashed grey lines correspond to the coal and sand pore pressure gradient, where hydro-50 psi means that the gradient is 50 psi less than hydrostatic pressure. Black squares correspond to pore pressures in coal and red crosses to pore pressures in sand.

By plotting the fluid elevation measured in each well versus ground level elevation (both in feet above sea level), we observe a linear trend between these two parameters, but the linear trend lies ~100 ft above the hydrostatic water level line

(Figure 4.6). This suggests that the water level in sands and coals before CBM production in the basin followed topography, but was ~100 ft below the ground surface (Figure 4.7).

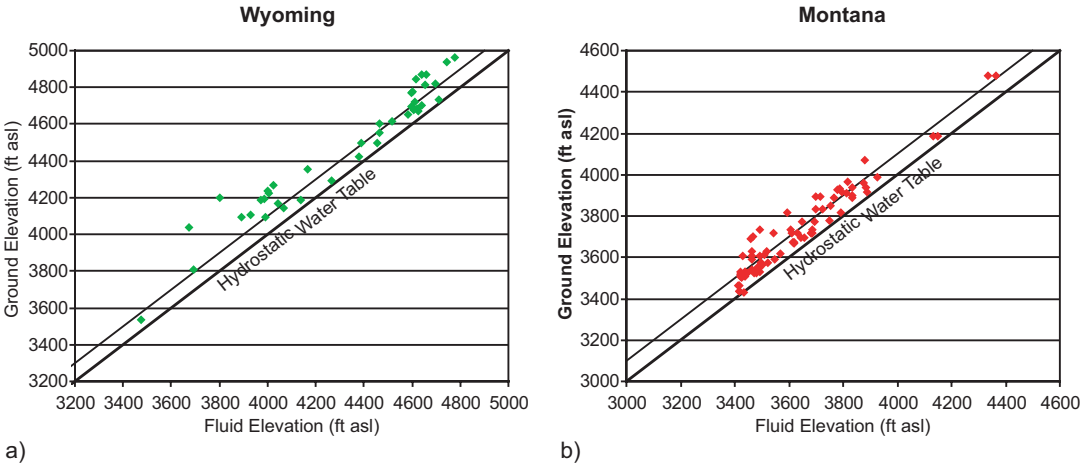

Figure 4.6: Ground elevation versus fluid elevation in feet above sea level for a) Wyoming and b) Montana.

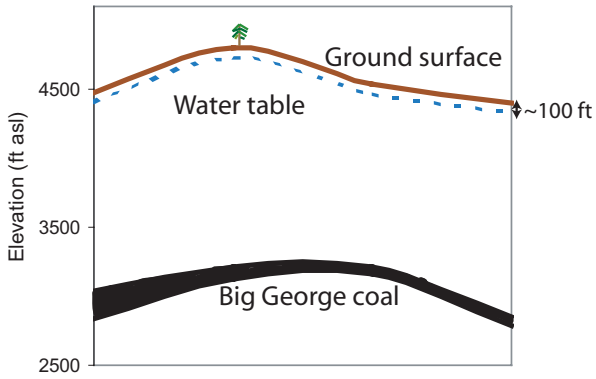

Figure 4.7: Schematic cross section showing the water table in the PRB before CBM production, where it followed topography but was ~100 ft below the ground surface.

4.5.3 Initial pore pressure magnitudes from the BLM database

Before analyzing initial pore pressures from the BLM data, we filtered the data by removing all wells whose first water level measurements appear to have been affected by prior CBM production. Wells were removed if we observed changes in pore pressure with time immediately after monitoring began. After filtering out CBM

production effects we observe in Figure 4.8 that the shallower coals and sands have slightly higher pore pressures than the deeper coals and sands. The shallower coals and sands have pore pressures ~50 psi less than hydrostatic, whereas the deeper coals and sands have pore pressures ~150 psi less than hydrostatic. The observed difference in pore pressures between coals and sands at different depths could be because the deeper coals and sands are part of a confined aquifer, rather than being connected to the water table (Applied Hydrology Associates and Greystone Environmental Consultants, 2002; Bartos and Ogle, 2002).

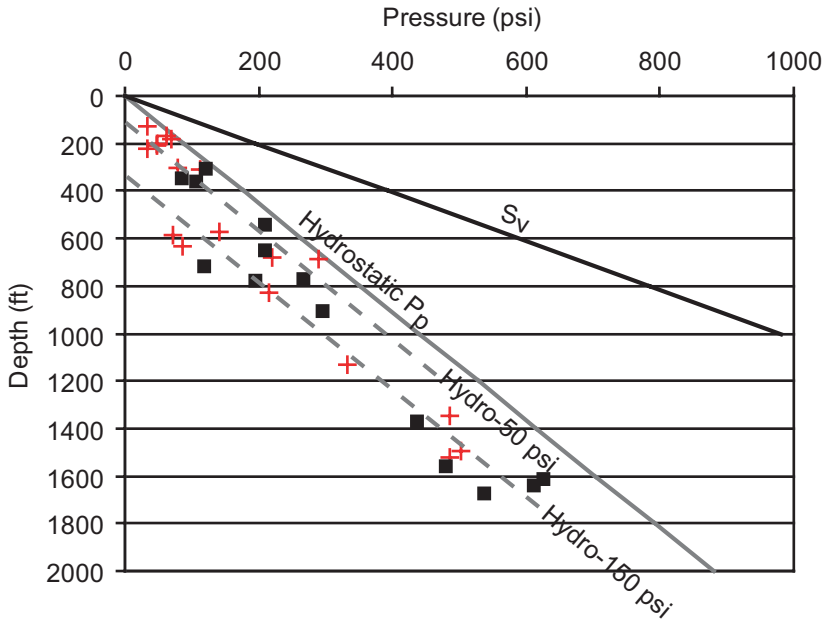

Figure 4.8: Pore pressures for sands and coals monitored by the BLM after removing those wells in the database whose initial water levels appear to have been affected by CBM production. Note that the pore pressures for the deeper coals and sands are much lower than hydrostatic compared to the shallower sands and coals. S_v corresponds to the overburden pressure and the black line is the overburden pressure gradient. The grey line corresponds to the hydrostatic pore pressure gradient (~0.44 psi/ft). The dashed grey lines correspond to the coal and sand pore pressure gradients, where hydro-50 psi means that the gradient is 50 psi less than hydrostatic pressure and hydro-150 psi means that the gradient is 150 psi less than hydrostatic pressure. Black squares correspond to pore pressures in coal and red crosses to pore pressures in sand.

4.6 Hydraulic communication between sands and coalbeds in the Powder River Basin

4.6.1 Wyoming

Because water levels have been continuously monitored over time in almost all of the BLM water level monitoring wells in the PRB, we were able to calculate pore pressure changes with time for the monitored sand aquifers. Using paired wells, we find that after 8 to 13 years of water level monitoring that ~60% of sands less than ~200 ft from underlying/overlying coalbeds show the greatest change in pore pressure with time (Figure 4.9).

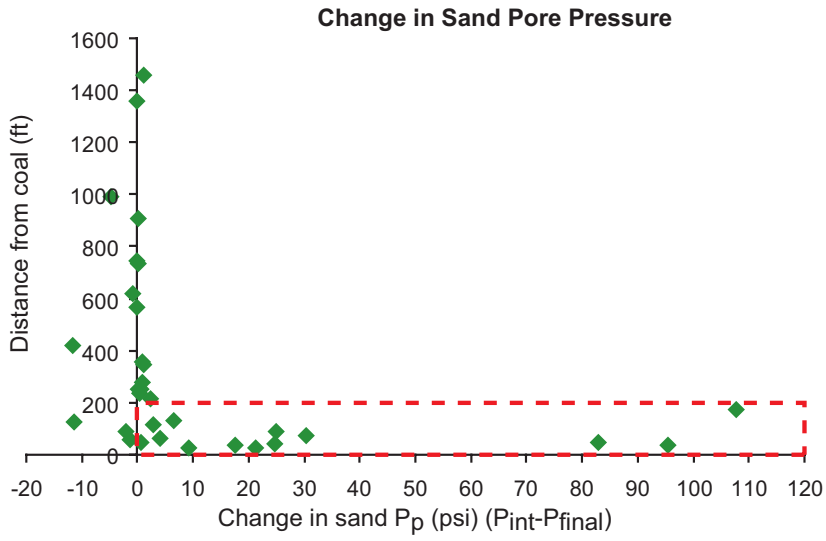

Figure 4.9: Separation between sand and coal pairs (in feet) versus change in pore pressure (P_p) with time for monitored sands in Wyoming. Red box highlights the sands with the greatest change in pore pressure, which are all within 200 ft of a producing coalbed. P_{int} stands for initial pressure and P_{final} stands for final pressure. A positive change in pore pressure corresponds to a decrease in pore pressure with time.

To determine if the large changes in pore pressure for the overlying/underlying sands are due to hydraulic communication with the coalbeds, we looked at pore pressure changes with time for each coalbed and its overlying/underlying paired sand. We grouped the BLM data into three groups based on CBM production areas (Figure

4.1a). For each well in each group we determined the pore pressure with respect to a datum, using the deepest coalbed in each area as the datum. We plotted pore pressure against time for all paired wells, investigating the possibility that overlying/underlying sands had similar pore pressure depletion histories to their underlying/overlying coalbeds.

We found that 10 out of 16 monitored sands within ~200 ft of their paired coalbed had similar pore pressure trends as their paired coal, implying that the sands are in hydraulic communication with the coalbeds. Using Figure 4.10 as an example, we see that pore pressures for the coals decrease with time and the pore pressure curves for the overlying sands follow similar pore pressure paths as the underlying coal. In some cases (7 out of the 10 pairs with similar pore pressure trends) pore pressures in the sands do not start to decline until several years after pore pressures in the coals start to decline (e.g. well MP2, well 447131 (Figure 4.1b for well locations)). We also found that several (6 pairs) of the sands within ~200 ft of an underlying coal show no change in pore pressure with time even though pore pressures in the underlying coals have decreased significantly (Figure 4.11, the NAPIER well, and Figure 4.12, the REDS well (Figure 4.1b well for locations)). It appears that most of the coal and sand pairs that show similar pore pressure depletion trends are located in group 1, south of Gillette, where CBM production and coal mining first began in the Wyoming part of the PRB (Figure 4.1a) (Ayers, 2002; Hower et al., 2003).

Water monitoring in the Wyoming part of the basin started approximately 13 years ago, so our observations are based on a limited data set. However, at present, the water monitoring data show that ~60% of the sands within ~200 ft of a producing coalbed are in hydraulic communication with that coalbed. Therefore, sand aquifers closer than ~200 ft to a coalbed should not be used as water disposal sites as there is a strong possibility that the disposed water will migrate from the aquifer into the producing coalbeds. In contrast, sand aquifers further than 200 ft from producing coalbeds show no change in pore pressure after 8 to 13 years of water level monitoring and could be potential sites for CBM water disposal. Additional investigations will

need to be carried out to make sure that sand aquifers further than ~200 ft from a coalbed are not in hydraulic communication with the coalbed and will not communicate with the coalbed at a future date.

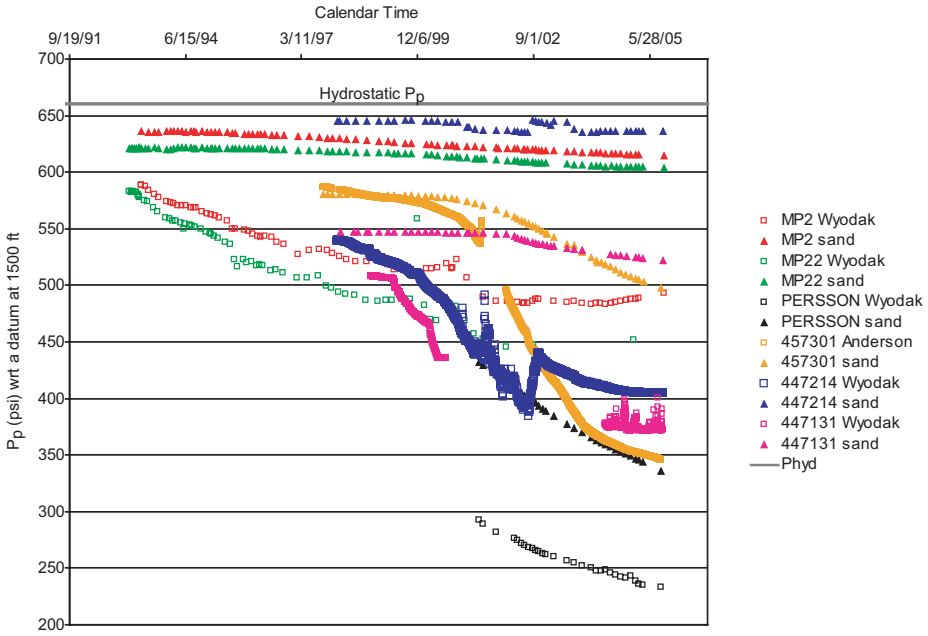

Figure 4.10: Pore pressure changes with time for water monitoring wells with sand and coal pairs less than 200 ft from one another in group 1. The names in capital letters in the key are the names given for the water monitoring wells and their locations are marked on Figure 4.1b. Wyodak stands for the Wyodak coal and Anderson, the Anderson coal.

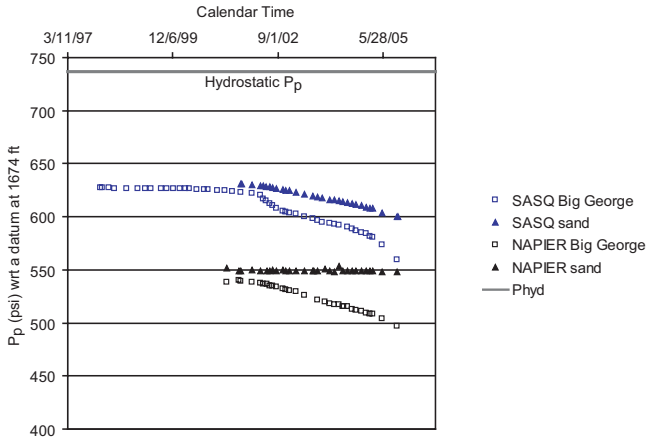

Figure 4.11: Pore pressure changes with time for water monitoring wells with sand and coal pairs less than 200 ft from one another in group 2. The names in capital letters in the key are the names given for the water monitoring wells and their locations are marked on Figure 4.1b. Big George stands for the Big George coal.

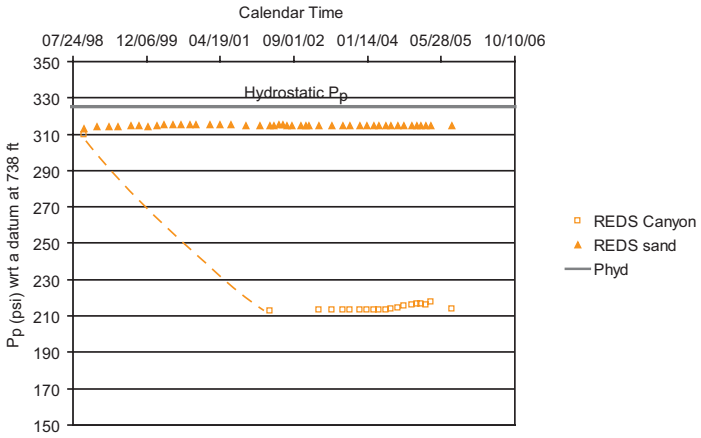

Figure 4.12: Pore pressure changes with time for water monitoring wells with sand and coal pairs less than 200 ft from one another in group 3. The name in capital letters in the key is the name given o the water monitoring well and its location is marked on Figure 4.1b. Canyon stands for the Canyon coal.

We also investigated the potential for vertical flow between paired sand and coalbed wells to help support our observation that some sands and coals are in hydraulic communication with each other. The potential for vertical flow is determined by using the water head elevation for each well in the well pairs (Bartos and Ogle, 2002). If the shallower unit has a higher head than the underlying unit, the potential for vertical flow is downward. We find that the vertical flow potential is in

the downward direction in all but one of the well pairs. In addition, one of the monitoring wells monitors water levels in sand that is below its paired coalbed and we find that the potential for vertical flow is upward from the sand to the overlying coalbed. The direction for vertical flow is consistent with the large decrease in pore pressure observed over time for the underlying sand, implying that CBM production is removing water from the underlying sand aquifer.

4.6.2 Montana

CBM production in Montana is on a much smaller scale than in the Wyoming part of the PRB. In 1990 there were 3 drilling permits issued in Montana and as of the end of 2006 there have been only ~1500 issued (MBOGC, 2007). Because of the limited CBM activities in the Montana part of the basin we have observed much smaller ground water drawdown than in the Wyoming part of the basin. Hence, when analyzing pore pressure changes with time for the 11 paired wells in Montana, only 5 of the 11 coals had significant decreases in pore pressure with time (between 50 and 90 psi). From our limited dataset it appears that at present overlying sand aquifers are not being drained through CBM production. The greatest pore pressure decrease observed in overlying sands is ~5 psi (Figure 4.13), compared with over 100 psi in the Wyoming part of the basin. Even if we analyze pore pressure changes with time for overlying sands not part of well pairs, the greatest decrease in pore pressure is only 2 psi.

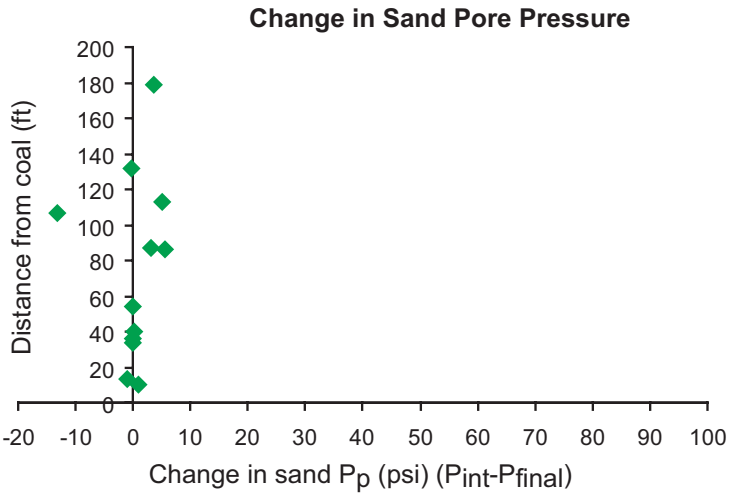

Figure 4.13: Separation between sand and coal pairs (in feet) versus change in pore pressure (P_p) with time for sand and coal pairs in Montana. P_{int} stands for initial pressure and P_{final} stands for final pressure. A positive change in pore pressure corresponds to a decrease in pore pressure with time.

4.7 Implications for injection of CBM water into sand aquifers

4.7.1 Modeling CBM water injection into sand aquifers

From our pore pressure analysis it appears that most sand and coal units in the PRB have sub-hydrostatic pore pressures, which means that injection of CBM water into sand aquifers should be feasible, as there should be no initial pressure resistance to injection. However, based on 8 to 13 years of water monitoring data, we believe it is important that potential sand aquifers for disposal sites are further than ~200 ft from producing coalbeds and are vertically confined so that water does not migrate into adjacent coals.

With this in mind, we have constructed two 3D stochastic reservoir models of conceptualized sand units in the PRB (using geostatistics to populate our models with sand permeability and porosity data) and have run fluid flow simulations to determine the rate at which CBM water can be injected into the aquifers. The first model is of a shallow sand unit with depth to the top ranging from 166-316 ft, and the second model is of a deeper sand body, with depth to the top ranging from 1034-1184 ft. We modeled water injection into both shallow and deep sands because our pore pressure

analysis showed that deeper sands and coals have lower initial pore pressures than the shallower sands and coals (Figure 4.8), suggesting that we should be able to inject a larger volume of CBM water into the deeper sands. In order to be able to compare our results between the two sand units we kept the thickness the same for both, ~40 ft (average thickness of sands being monitored by the BLM monitoring wells), and populated the models with permeability and porosity values using the same property distributions and variograms.

Each 3D model grid contains 16830 grid cells, 55 in the x direction, 51 in the y direction and 6 in the z direction. Each grid cell is 67ft by 67 ft by 7 ft and the total area of the model is ~160 acres (Figure 4.14).

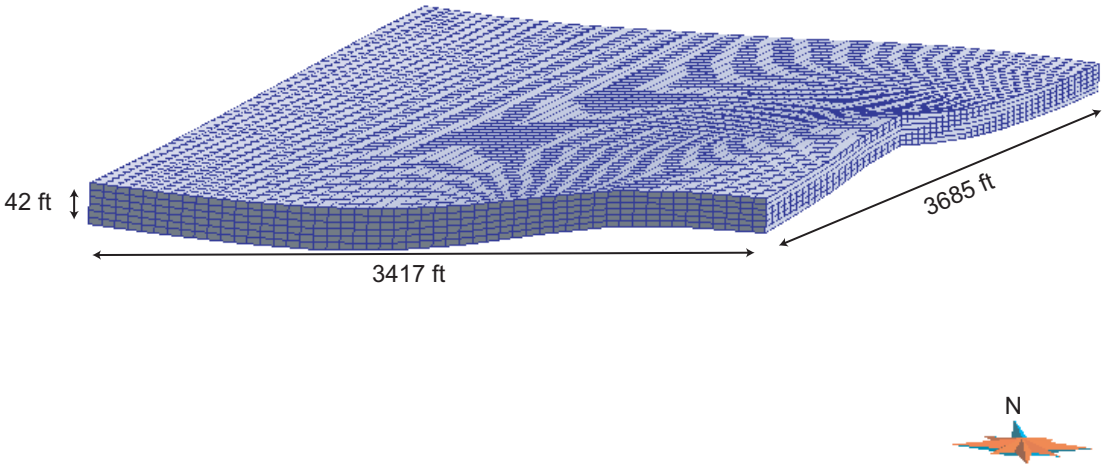

Figure 4.14: Simulation grid for general 3D sand model.

We obtained permeability and porosity distributions from Applied Hydrology Associates and Greystone Environmental Consultants (2002), who reported hydraulic conductivity values for sand units and determined porosity values from their modeling of recharge into the Wasatch and Fort Union formations. We calculated permeability from hydraulic conductivity using the following equation,

$$K = \frac{k\rho g}{\mu}, \tag{3}$$

where k is permeability in Darcies, K is hydraulic conductivity in ft/s, ρ is the fluid density, μ is the dynamic viscosity of the fluid and g is gravity.

Applied Hydrology Associates and Greystone Environmental Consultants (2002) report measured hydraulic conductivity values representative of fine to medium grained sand, which is the sand grain-size given by Flores (2004) for sandstone reservoirs in the Wasatch and Fort Union Formations. Applied Hydrology Associates and Greystone Environmental Consultants (2002) give an average hydraulic conductivity of 2E-6 ft/s (70 mD) for the sands, with an upper limit of 1E-5 ft/s (350 mD), and in their model they use a porosity of 10% for the sand units.

In our geostatistical modeling we used triangular property distributions to represent the range in permeability and porosity values reported by Applied Hydrology Associates and Greystone Environmental Consultants (2002) for sandstone reservoirs in the Wasatch and Fort Union Formations. Table 4.1 shows the maximum, minimum and mode values of our distributions.

Table 4.1: Triangular distribution parameters for sand permeability and porosity.

Property	Minimum and Maximum Value	Mode
Permeability	30-350 mD	70 mD
Porosity	0.08-0.15	0.1

To populate our 3D stochastic models we used simple Kriging and sequential Gaussian simulation (SGS) to generate 20 equally probable permeability and porosity realizations (Deutsch, 2002). To incorporate the spatial variability of the permeability and porosity distributions into the SGS algorithm we used a spherical semivariogram (Deutsch, 2002). However, because we have no hard data, our choice of semivariogram is highly subjective. Since the sands are fine to medium grained, contain ~30% clay particles and are moderately sorted (Flores, 2004), we used a correlation coefficient of 0.7 between the porosity and permeability. Also, the sands were deposited be meandering rivers (Flores,2004), so we created a semivariogram that captured the channelized nature of the sands and which also reduced the

permeability correlation in the vertical direction to mimic both bedding and the lower vertical hydraulic conductivities found in the sands (Applied Hydrology Associates and Greystone Environmental Consultants, 2002). Our spherical semivariogram model had a nugget of 0.2 and a range in the north direction of 16,400 ft, in the east direction of 1640 ft and in the vertical direction of 1.6 ft. Figure 4.15 shows one realization of our sand model with its associated permeability and porosity distributions.

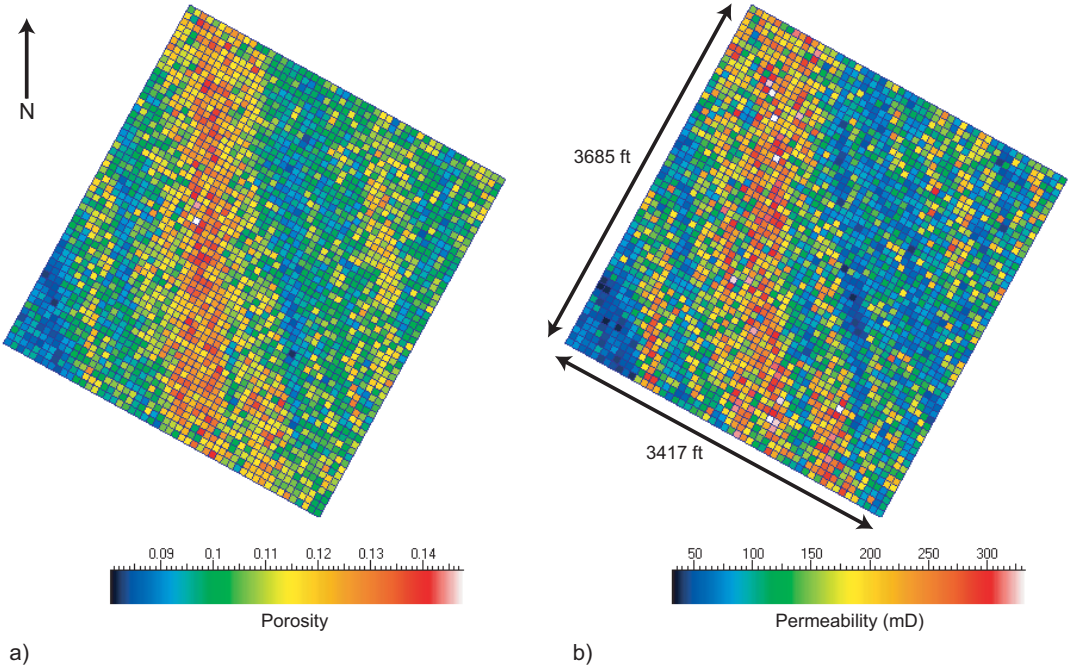

Figure 4.15: a) Porosity and b) permeability distributions for one realization of our general sand model.

We used the Computer Modeling Group's Generalized Equation-of-State Model Compositional Reservoir Simulator (GEM) and the fluid flow simulations were carried out by injecting water through an injection well located in the middle of the simulation grid (the well is perforated for the entire thickness of the sand). We used a higher reservoir pressure gradient for the shallower sand (60 psi less than hydrostatic) than for the deeper sand (150 psi less than hydrostatic) (Figure 4.8), but all other parameters required by the simulator were set the same. The sands were modeled as semi-infinite in the horizontal direction, with constant-pressure boundaries, but confined vertically.

We injected water until the injection well bottom hole pressure (BHP) reached hydrostatic pressure, which means that the reservoir pressure of the aquifer is close to hydrostatic. At this point, rather than the water flowing under gravity into the aquifer when reservoir pressures are below hydrostatic, the operators would need to pump the water down the injection well at a higher pressure than hydrostatic for it to flow into the aquifer and away from the well (need a pressure gradient). Water could be injected into the sand aquifer until the reservoir pressure reaches the fracture pressure of the aquifer, but we do not know the fracture pressure of the sands in the Wasatch and Fort Union formations so the hydrostatic BHP is a good cutoff, since injection costs would increase with the need to start pumping.

Our simulations show that for the shallower sand, water can be injected at a rate of ~160 bbl/day for ~4000 days before the BHP reaches hydrostatic (Figure 4.16, 4.17a). In contrast, for the deeper sand, water can be injected at a rate of ~435 bbl/day for ~4000 days (Figure 4.16, 4.17b). At present the average water production rate per CBM well in the PRB is ~100 bbl/day (WOGCC, 2007) and the average lifetime of a CBM well is ~7 to 15 years (2555 to 5500 days) (Ayers, 2002; De Bruin et al., 2004). Therefore, if operators were to inject CBM water into shallow sands they will be able to dispose of the water production from one and a half CBM wells every 160 acres using one disposal well (assuming the sand properties throughout the basin are similar to those in our model). If injection takes places in deeper sands, operators will be able to dispose of the water production from four CBM wells every 160 acres using one disposal well.

In Figure 4.16 we have marked the water injection rate achievable in our two different sand models and have also plotted the average water production in bbl/day for CBM wells analyzed by Colmenares and Zoback (2007) and Ross (Chapter 5 of this thesis). Colmenares and Zoback (2007) looked at over 500 water-enhancement tests that are used by CBM operators in the PRB to connect the natural coal fracture network to their CBM wells. The procedure involves pumping water down the CBM wells at a rate of ~60 bpm for ~15 min. Through their analysis, Colmenares and

Zoback (2007) showed that water-enhancement actually hydraulically fractures the coal and in some areas the fractures grow horizontally (because the least principal stress is equal to the overburden stress) and in other areas they propagate vertically (because the least principle stress is equal to the minimum horizontal stress). Interestingly, they found a correlation between fracture orientation and water and gas production from CBM wells. Wells with horizontal hydraulic fractures typically produce small volumes of both gas and water, whereas some wells with vertical hydraulic fractures produce manageable volumes of water, but are actually good gas producers. However, ~30% of wells with vertical hydraulic fractures produce excessive volumes of water and little to no gas. Colmenares and Zoback (2007) define excessive water production as ~230 bbl/day and higher. From Figure 4.16 we see that deeper sand aquifers will need to be used as water disposal sites for CBM wells with excessive water production. The shallower sands do not have the capacity to store water from excessive water producing wells over the lifetime of the CBM well.

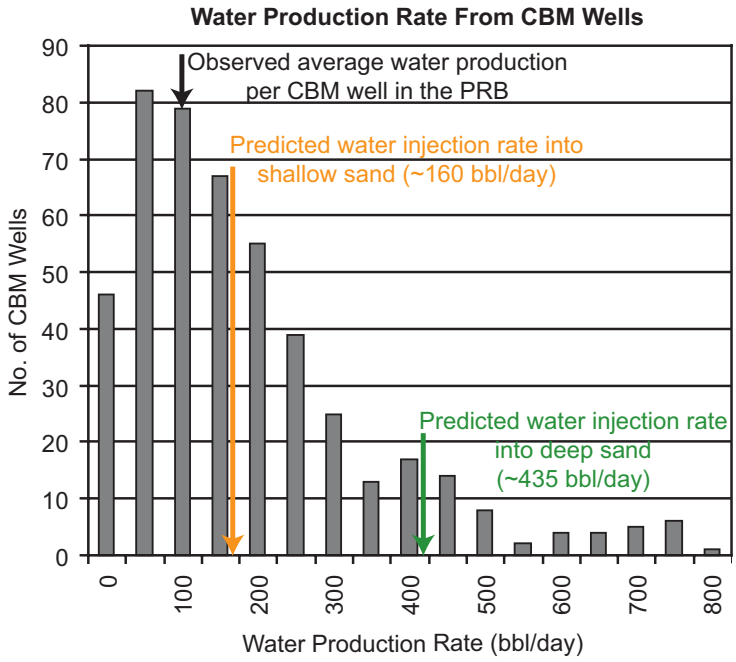

Figure 4.16: Water production rate per well for CBM wells analyzed by Colmenares and Zoback (2007) and Ross (Chapter 5 of this thesis) compared with the injection rates obtained from fluid flow simulations for our shallow (orange) and deep (green) sand models. Average CBM water production for the PRB is from the WOGCC (2007).

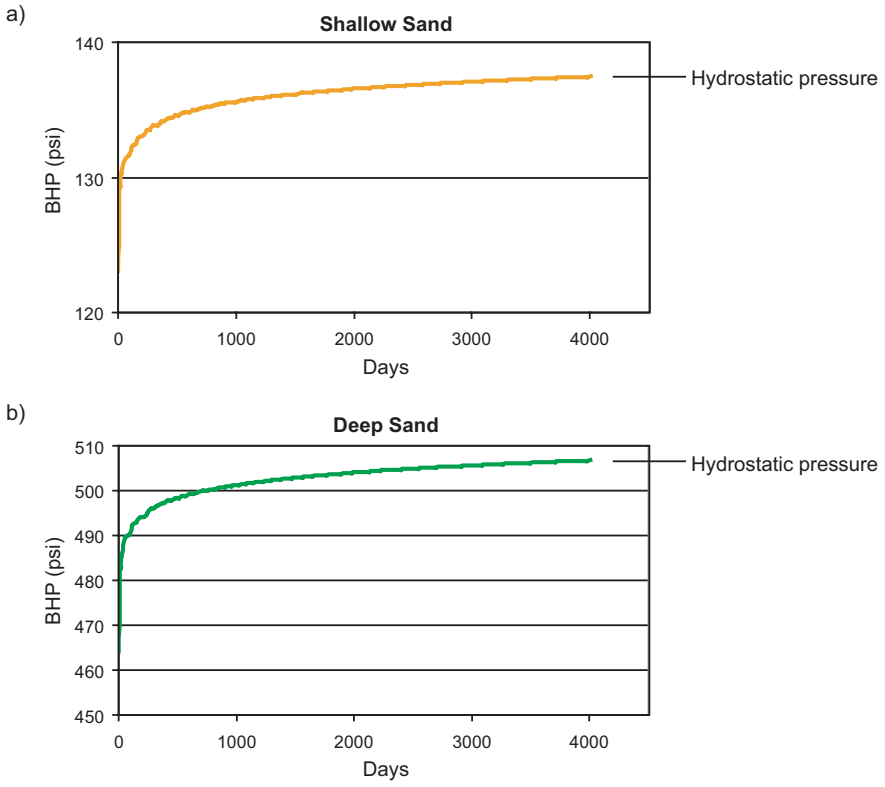

Figure 4.17: Bottom hole injection pressure (BHP) for the a) shallow (orange) and b) deep (green) sand models.

As mentioned earlier, we generated 20 sand porosity and permeability realizations to capture the uncertainty in our knowledge of the sand geology in the PRB. In Figure 4.18 we show two examples of the 20 permeability and porosity realizations generated for our injection modeling. The results from our realization runs are shown in Figure 4.19. The range in water injection rate due to uncertainty in the permeability and porosity distributions for the deep sand model is ~400 to ~510 bbl/day and the range in injection rate for the shallow sand model is ~150 to ~190 bbl/day. The red lines correspond to the base case results reported above.

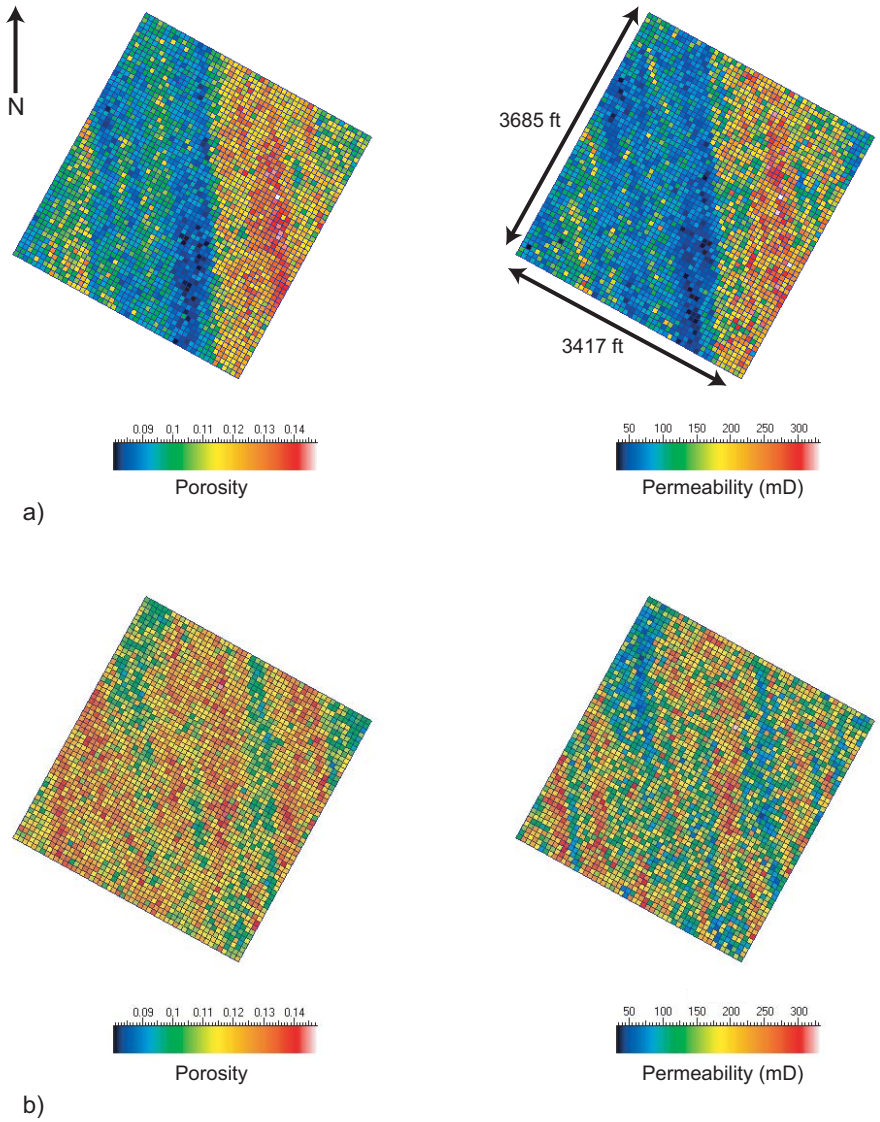

Figure 4.18: a) Porosity and permeability distribution for realization 17. b) Porosity and permeability distribution for realization 3.

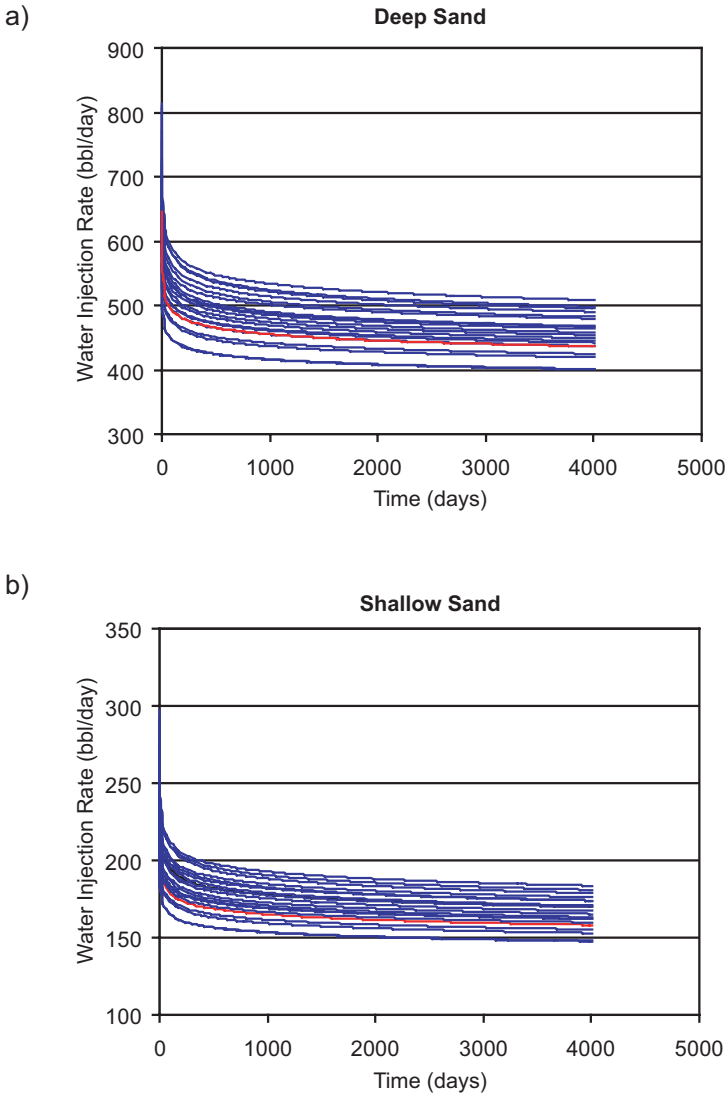

Figure 4.19: a) Water injection rate (bbl/day) results from 20 realization runs for the deep sand model. b) Water injection rate (bbl/day) results from 20 realization runs for the shallow sand model. The red lines correspond to the base case results for both models.

We have also run a sensitivity analysis on sand permeability, assuming that in general the sands have permeabilities closer to the reported average of ~70 mD and rarely have permeabilities as high as 350 mD (Applied Hydrology Associates and Greystone Environmental Consultants, 2002). We effectively modeled the sand as if it were only fine grained. Table 4.2 outlines the permeability distribution used for our fine grained sensitivity analysis and Figure 4.20 shows the water injection rates that could be obtained if water is injected into both a shallow and deep fine grained sand body in the PRB.

Table 4.2: Triangular distribution parameters for fine grained sand permeability and porosity.

Property	Minimum and Maximum Value	Mode
Permeability	10-70 mD	65 mD
Porosity	0.08-0.15	0.1

Our simulations show that for a shallow fine grained sand aquifer the water injection rate could range from ~55 to ~60 bbl/day, whereas for a deeper fine grained sand body the injection rate could range from ~150 to ~170 bbl/day (Figure 4.20).

The water injection rates estimated from our fine grained sand sensitivity analysis are significantly lower than for a sand model that includes slightly coarser grained sands found in the PRB. We show that a deep fine grained sand aquifer would only be able to hold water produced from one average CBM well, compared with four for the deep sand model with coarser grains. This implies that operators need to find the coarser grained sand bodies within the PRB for CBM water disposal to minimize disposal costs.

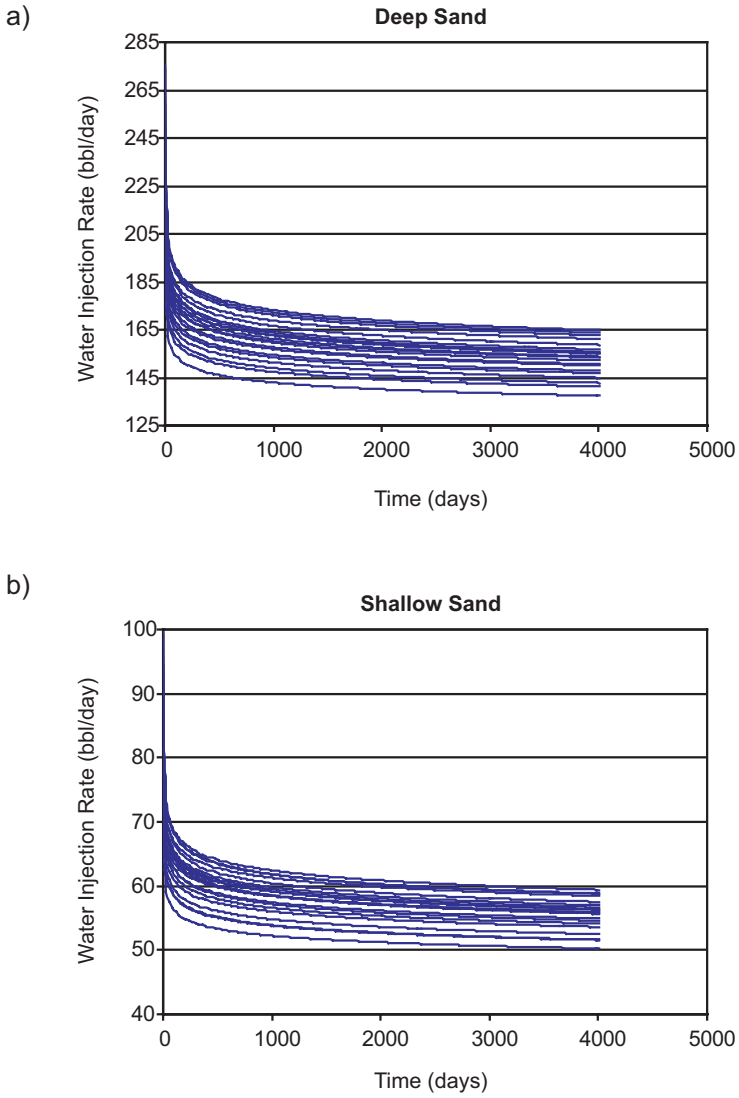

Figure 4.20: a) Water injection rate (bbl/day) results from 20 realization runs for the deep fine grained sand model. b) Water injection rate (bbl/day) results from 20 realization runs for the shallow fine grained sand model.

4.7.2 Characteristics of the confining unit between coalbeds and aquifers in the PRB

Aquifers designated for CBM water disposal not only need to have low pore pressures and adequate permeability and porosity, which we modeled in the previous section, but aquifer water has to be of similar quality to CBM water and the sands should not be in hydraulic communication with producing coalbeds. In terms of hydraulic communication, we have found that at present, ~60% of sands within ~200

ft of producing coals are probably in hydraulic communication with the coalbeds and should not be sites for CBM water disposal (section 4.6.1). However, coalbeds in the Upper Fort Union Formation are typically overlain by a confining unit and are rarely in direct contact with a sand body (J. Wheaton, personal communication, 2007; Applied Hydrology Associates and Greystone Environmental Consultants, 2002; Bartos and Ogle, 2002). So why do we observe hydraulic communication after 8 to 13 years of water level monitoring between coals and sands that are within ~200 ft of each other?

It is possible that sands that show delays in pore pressure reduction, compared with when pore pressure decline in the coalbeds started, are separated from the coal by a thicker confining unit than in areas where we see declines in sand pore pressures almost immediately after pressures in the coal start to decline (Figures 4.10, 4.1b). Areas where pore pressures in both the coals and sands start decreasing at similar times may be where sand bodies immediately overlie the coalbeds or the confining unit is very thin (Figures 4.10, 4.11, 4.1b). Gamma ray logs for the monitoring wells are not available, but through analysis of gamma ray logs from CBM wells located in the same sections as the monitoring wells we see no correlation between the geologic units above the coals and timing or magnitude of pore pressure changes in the overlying monitored sands (Figure 4.21). In two sections, 1-45-73 (monitoring well 457301, Figures 4.10, 4.1b), where the pore pressure in the overlying sand has started to decrease at the same time as in the underlying coalbed, and 32-47-73 (monitoring well PERSSON, Figures 4.10, 4.1b), where the sand pore pressure change is large, the coals are overlain by ~4 ft and ~36 ft of shale respectively (Figure 4.21). In contrast, in sections where there is a delay between the start in decline of the coal pore pressure and the start in decline of the sand pore pressure, the shale units overlying the coals are only ~10 ft thick (monitoring wells MP2 and MP22, Figures 4.21, 4.10, 4.1b).

It seems that hydraulic communication may be more of a function of the properties of the shale and the rate at which the CBM well is pumping water, rather than just thickness alone. A “leaky” confining unit will allow water to flow from the

sand, through the confining unit, and into the coalbed. In addition, a "leaky" confining unit will contain water itself and some of the initial water entering the coal may be from the confining unit. Sands that have delays in pore pressure decline could be separated from the coalbeds by confining units with very low permeability, limiting the migration of water to the coalbed.

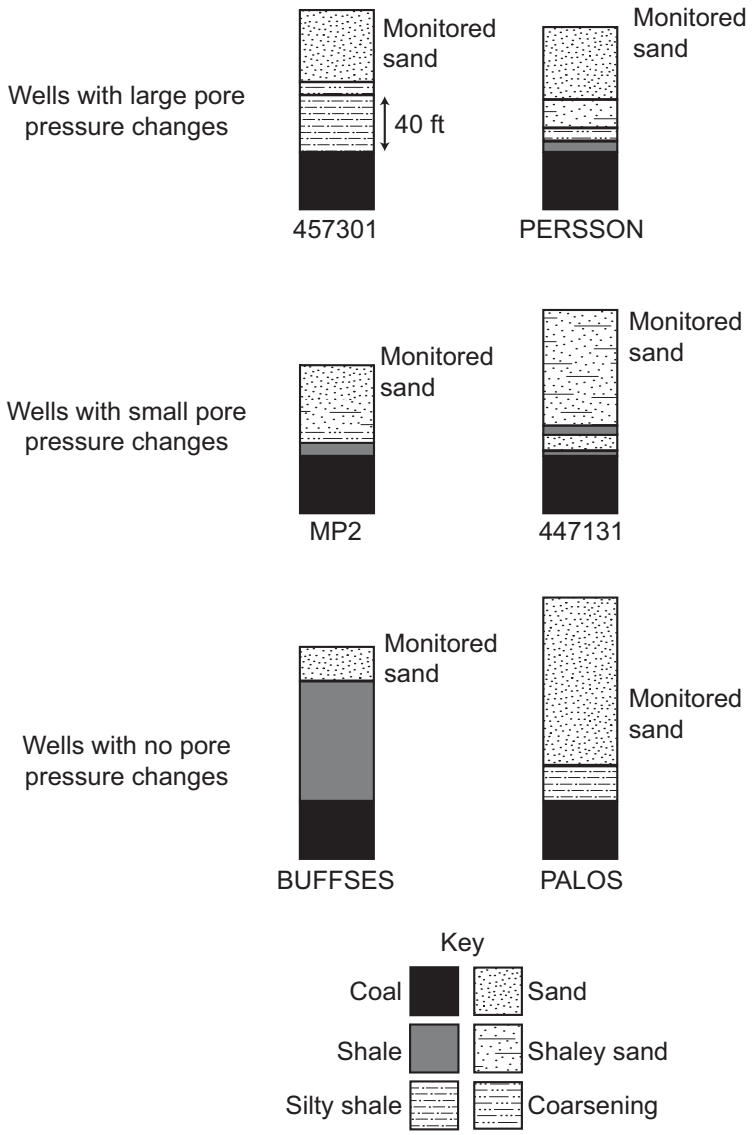

Figure 4.21: Examples of the lithology found directly above coalbeds in the PRB. These examples are from water monitoring wells 457301, PERSSON, MP2, 447131, BUFFSES and PALOS (the well locations are marked on Figure 4.1b). The lithology comes from gamma logs from CBM wells in the same sections as the monitoring wells. Large pore pressure changes are on the order of ~100 psi, whereas small pore pressure changes are ~20 psi.

4.8 Conclusions

Through the analysis of water level data from water monitoring wells located in both Montana and Wyoming, we have determined that sands and coals in the PRB have sub-hydrostatic pore pressures. In addition, pore pressure changes with time reveal that at present ~60% of sands less than 200 ft from underlying/overlying coals appear to be in hydraulic communication with the coalbeds. In contrast, sand aquifers further than 200 ft from producing coalbeds show no change in pore pressure after 8 to 13 years of water level monitoring. These findings have important implications for the disposal of CBM water through injection into sand aquifers. The occurrence of sub-hydrostatic pore pressures means that the sands have the capacity to store water, but to insure that the disposed water does not reach producing coalbeds in the future; we recommend that sands closer than ~200 ft to producing coals should not be used as disposal sites because they may be in hydraulic communication with the coalbeds.

Furthermore, we ran fluid flow simulations to determine the rates at which CBM water could be injected into shallow (~300 ft) and deep (~1000 ft) aquifers. We found that for the shallow sand model an injection water rate of ~160 bbl/day could be achieved, whereas for the deeper sand, whose pore pressures are lower than the shallow sand, the rate was ~435 bbl/day. Both these rates are higher than the average water production rate from CBM wells in the PRB, which is ~100 bbl/day. This implies that for deep aquifer injection sites, only one injection well would be required to dispose of the water produced from four CBM wells, reducing the cost of CBM water disposal.

Chapter 5

HYDRAULIC FRACTURE GROWTH FROM COALBED METHANE OPERATIONS IN THE POWDER RIVER BASIN, WYOMING: IMPLICATIONS FOR COALBED METHANE WATER MANAGEMENT

5.1 Abstract

Large quantities of water are associated with the production of coalbed methane (CBM) in the Powder River Basin (PRB), Wyoming, and this water has high saline and sodium contents, making it unsuitable for agricultural use and environmentally damaging. In order to determine if there are ways for CBM operators to produce less CBM water we have evaluated CBM wellbore completion methods in the PRB. We have found that CBM operators in the PRB routinely carry out water-enhancement on their wells, where water-enhancement procedures are used to connect the coal cleats to

the wellbore to increase gas production. Operators in the PRB are routinely fracturing the coal through this water-enhancement process (Colmenares and Zoback, 2007). We analyzed ~200 water-enhancement tests from CBM wells in the PRB in order to determine the magnitude of the least principal stress and the orientation of hydraulic fracture growth. We find that both horizontal and vertical hydraulic fractures are created and that some wells with vertical hydraulic fractures produce excessive volumes of CBM water.

The creation of both vertical and horizontal hydraulic fractures implies that the magnitude of the least principal stress is varying throughout the basin and this has lead us to define three different stress states in the PRB: areas that have active normal faults, areas that are slightly more compressive (either normal or strike-slip stress regimes) and finally, areas with reverse faulting regimes. We observe that for the Big George coal, wells with excessive water production are within normal faulting areas, suggesting that vertical hydraulic fractures in communication with normal faults may play a role in the water production.

5.2 Introduction

Coalbed methane (CBM) production in the Powder River Basin (PRB) is accompanied by the production of large volumes of CBM water (Figure 5.1). In 2006, ~590 million barrels (bbl) of CBM water were produced (an average of ~100 bbl/well/day) (WOGCC, 2006). The water quality is generally sufficient for drinking and livestock use, however the saline and sodium contents are too high for agricultural use (Wheaton and Donato, 2004; Bartos and Ogle, 2002; The Ruckelshaus Institute of Environment and Natural Resources, 2005). The high saline and sodium content of the CBM water causes a reduction in soil permeability because the ions precipitate out of solution and are deposited within the soil. This in turn reduces the productivity of the soil and can cause soil erosion and ultimately damage to wildlife habitats (Wheaton and Donato, 2004). At present, most of the produced water is discharged into evaporation/infiltration ponds or reservoirs (The Ruckelshaus Institute of

Environment and Natural Resources, 2005). However, in the eastern part of the PRB, where water quality is reasonably high, CBM water is used for irrigation or discharged directly into streams (The Ruckelshaus Institute of Environment and Natural Resources, 2005).

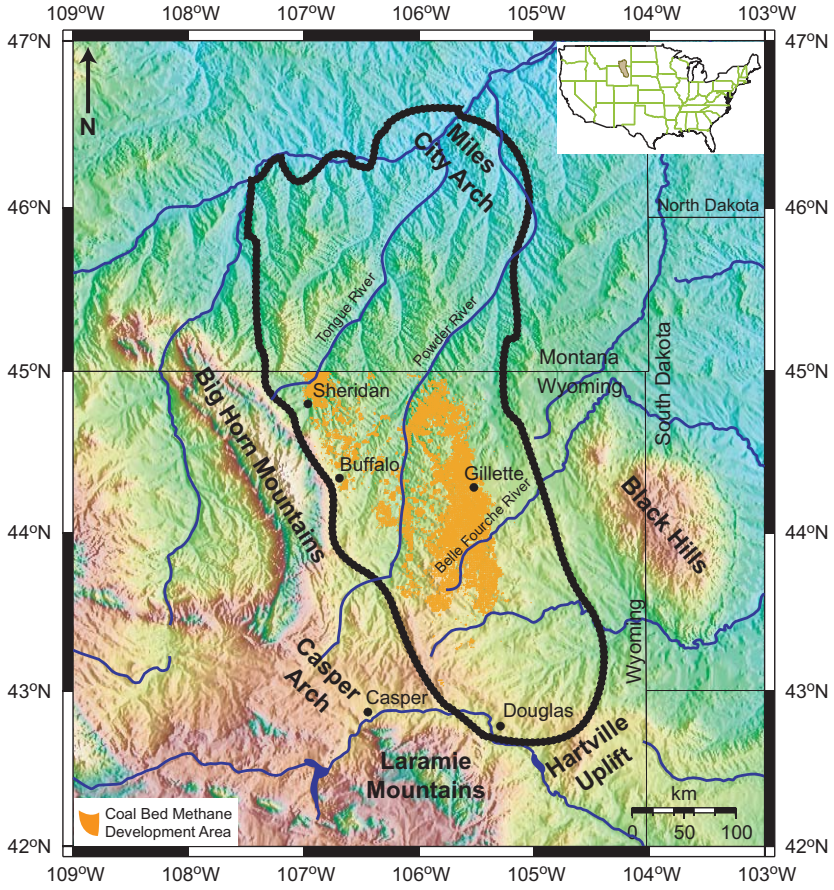

Figure 5.1: Location map of the Powder River Basin, Wyoming (modified from Colmenares and Zoback, 2007). Orange dots correspond to CBM wells.

The goals of this study are to evaluate CBM wellbore completion methods in the PRB to determine if there are ways to produce less CBM water, while still achieving adequate coal depressurization for CBM production. To achieve these goals we have extended the study conducted by Colmenares and Zoback (2007), using water-enhancement tests to map stress across the basin and to understand why water production from some wells is excessive (>7,000 bbl/month), whereas in other parts of the basin water production is manageable.

Colmenares and Zoback (2007) found that CBM operators in the PRB routinely carry out water-enhancement on their wells. Water-enhancement procedures are used to connect the coal cleats to the wellbore to increase gas production, as well as to wash away any drilling fines generated during drilling that may block gas flow to the well. As it turns out, CBM operators in the PRB routinely fracture the coal through water-enhancement. Colmenares and Zoback (2007) analyzed water-enhancement tests from CBM wells to determine which wells had been hydraulically fractured. Using the flow rate and wellhead pressure recorded during water-enhancement they were able to calculate the magnitude of the least principal stress (S_3) in 372 CBM wells and determine the orientation of hydraulic fracture propagation.

Colmenares and Zoback (2007) found that in some areas the hydraulic fractures were propagating horizontally, whereas in other areas the fractures were propagating vertically. In addition, they found that many of the wells with vertical fractures produced excessive volumes of CBM water (~7,000 bbl/month) and little to no methane (CH_4). In the Big George coal, ~70% of all the water produced is from only one third of the total number of wells, all of which are characterized by vertical hydraulic fractures. In contrast, some of the wells with vertical hydraulic fracture propagation produce small volumes of water (<7000 bbl/month) and are very good gas producers (with some delay in gas production). Wells with horizontal hydraulic fractures typically produce small volumes of water but are poor gas producers. Colmenares and Zoback (2007) hypothesize that the vertical fractures associated with the production of large volumes of water actually penetrate overlying sand aquifers. Hence, the operators are draining the aquifers rather than the coals and are unable to efficiently depressurize the coal for CH_4 production.

Colmenares and Zoback (2007) investigated reasons for the apparent correlation between hydraulic fracture orientation and water production. They looked at stratigraphy, coal thickness and coal depth, but found no correlation with any of these factors. Colmenares and Zoback (2007) also tried to understand why S_3 varies throughout the basin (Figure 5 in Colmenares and Zoback (2007)) and concluded that

perhaps coal thickness plays a role, as the ratio of S_3 to the overburden stress (S_v) appears to be smaller in thicker coals than in thinner coalbeds. However, this correlation seems to be only truly apparent in the Big George coal, which incidentally contains the largest water producing wells (greater than 20,000 bbl/month) analyzed by Colmenares and Zoback (2007).

We have obtained additional water-enhancement tests from CBM wells in the PRB, to supplement those analyzed by Colmenares and Zoback (2007), in order to better understand why the stress varies throughout the basin and why some wells produce excessive volumes of CBM water (Figure 5.2). In this chapter we outline the method used to determine the orientation of hydraulic fracture propagation and then report on the fracture orientations obtained from our water-enhancement tests (section 5.3). In section 5.4, we look at the relationship between fracture orientation and gas and water production, where we observe a similar correlation as Colmenares and Zoback (2007). Following this, we define three stress states that we observe to exist in the PRB (section 5.5) and show that active normal faults may play a role in fluid migration.

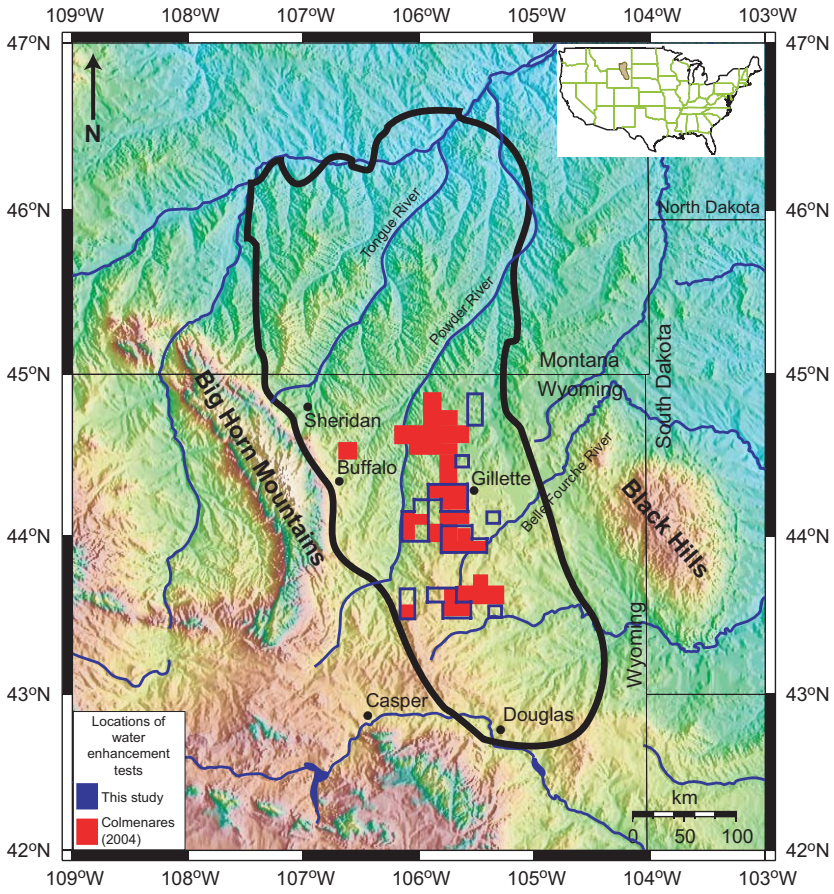

Figure 5.2: Township and range locations of wells with water-enhancements tests analyzed for both this study, in blue, and by Colmenares (2004) and Colmenares and Zoback (2007), in red.

5.3 Calculating the least principal stress and hydraulic fracture orientation from water-enhancement tests

During water-enhancement the operators typically pump water into the well at a rate of ~60 barrels per minute (bpm) for approximately 15 minutes. The flow rate and wellhead pressure are measured during the procedure and if the wellhead pressure stays at a constant value, even though a constant rate of water is being pumped into the coal, this indicates that a hydraulic fracture has formed (Figure 5.3a) (Colmenares and Zoback, 2007).

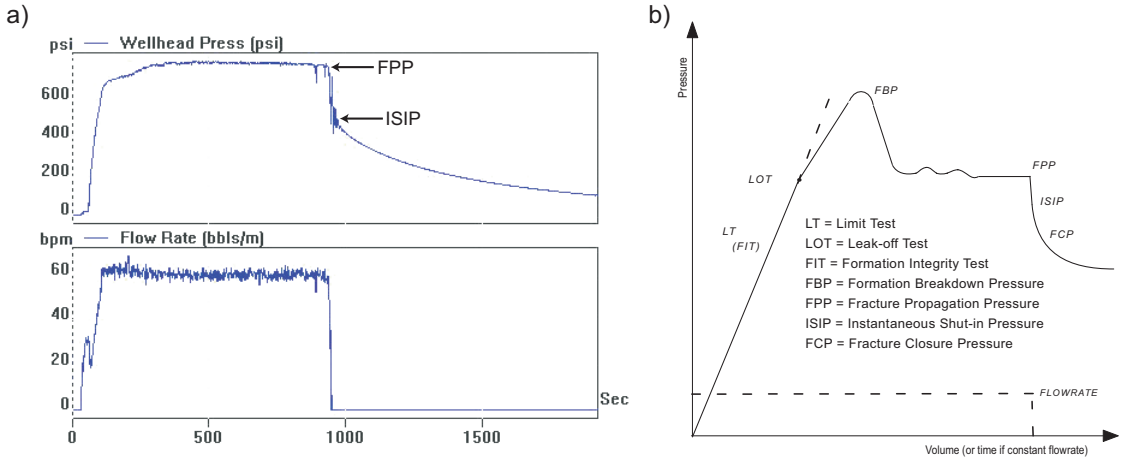

Figure 5.3: a) Water-enhancement test from a CBM well in the PRB. b) Schematic diagram of an extended leakoff test (Zoback et al., 2003). The dashed line diverging from the leakoff test would be the pressure path if no fracture is created. Modified from Colmenares and Zoback, 2007.

Water-enhancement tests from the PRB have similar pressure-time history as extended leak-off tests (Zoback et al., 2003), which means that we can calculate the magnitude of S_3 using the same principals applied to extended leak-off tests. To calculate the magnitude of the least principal stress (S_3) at depth, we take the instantaneous shut-in pressure at the surface and add the pressure from the weight of the column of fluid in the wellbore (Figure 5.3b) (Zoback et al., 2003). After obtaining the magnitude of S_3, we can then determine the orientation of fracture propagation. Hydraulic fractures will open in the direction of S_3 and propagate perpendicular to the orientation of S_3 (Hubbert and Willis, 1957). If S_3 corresponds to the minimum horizontal stress (S_{hmin}) then the fracture will propagate in the vertical plane. However, if S_3 is equal to the overburden stress (S_v), the fracture will propagate in the horizontal direction. To calculate the magnitude of S_v, rock densities are integrated from the surface to the depth of interest, z, where

$$S_v = \int \rho(z) g dz \cong \overline{\rho} g z \,, \qquad (1)$$

and $\rho(z)$ is the density as a function of depth, g is the gravitational acceleration and $\overline{\rho}$ is the mean overburden density. Because density logs are not available for any of the CBM wells analyzed we used a mean overburden density of 2.3 g/cc, which is a

reasonable average for the lithological units above the coal in the PRB (interbedded shales and sands).

To determine whether S_3 corresponds to S_v we compare the magnitude of S_3 with the magnitude of the expected overburden stress for the depth of the coal interval in question. In Figure 5.4 we show the overburden stress gradient and the hydrostatic pore pressure gradient as black and grey lines respectively. If S_3 plots on the overburden line it means that S_3 is equal in magnitude to S_v and horizontal hydraulic fractures have formed. If S_3 plots below the overburden line then the magnitude of S_3 is equal to S_{hmin} and vertical hydraulic fractures have formed. For the wells shown in Figure 5.4, vertical hydraulic fractures were created through water-enhancement tests.

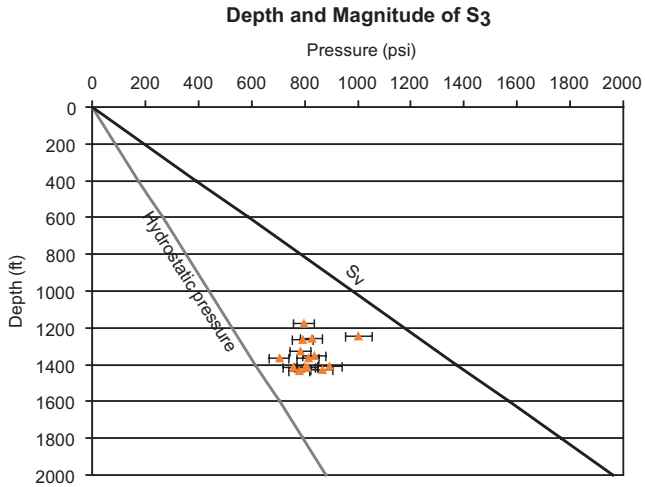

Figure 5.4: Depth versus pressure plot showing the magnitude of S_3 (orange triangles) for the Big George coal. Note that S_3 is less than the overburden stress (S_v) implying that hydraulic fractures created through water-enhancement are vertical. The hydrostatic pore pressure gradient is ~0.44 psi/ft.

5.3.1 Water-enhancement tests from Cordilleran Compliance Services

We obtained 198 water-enhancement tests from Cordilleran Compliance Services that supplement tests previously available to Colmenares and Zoback (2007) (Figure 5.2). An analysis of the 198 wells suggests that 87 were hydraulically fractured during the water-enhancement process and of those 87 wells, 89% have vertical fractures and 11% horizontal fractures (Figure 5.5).

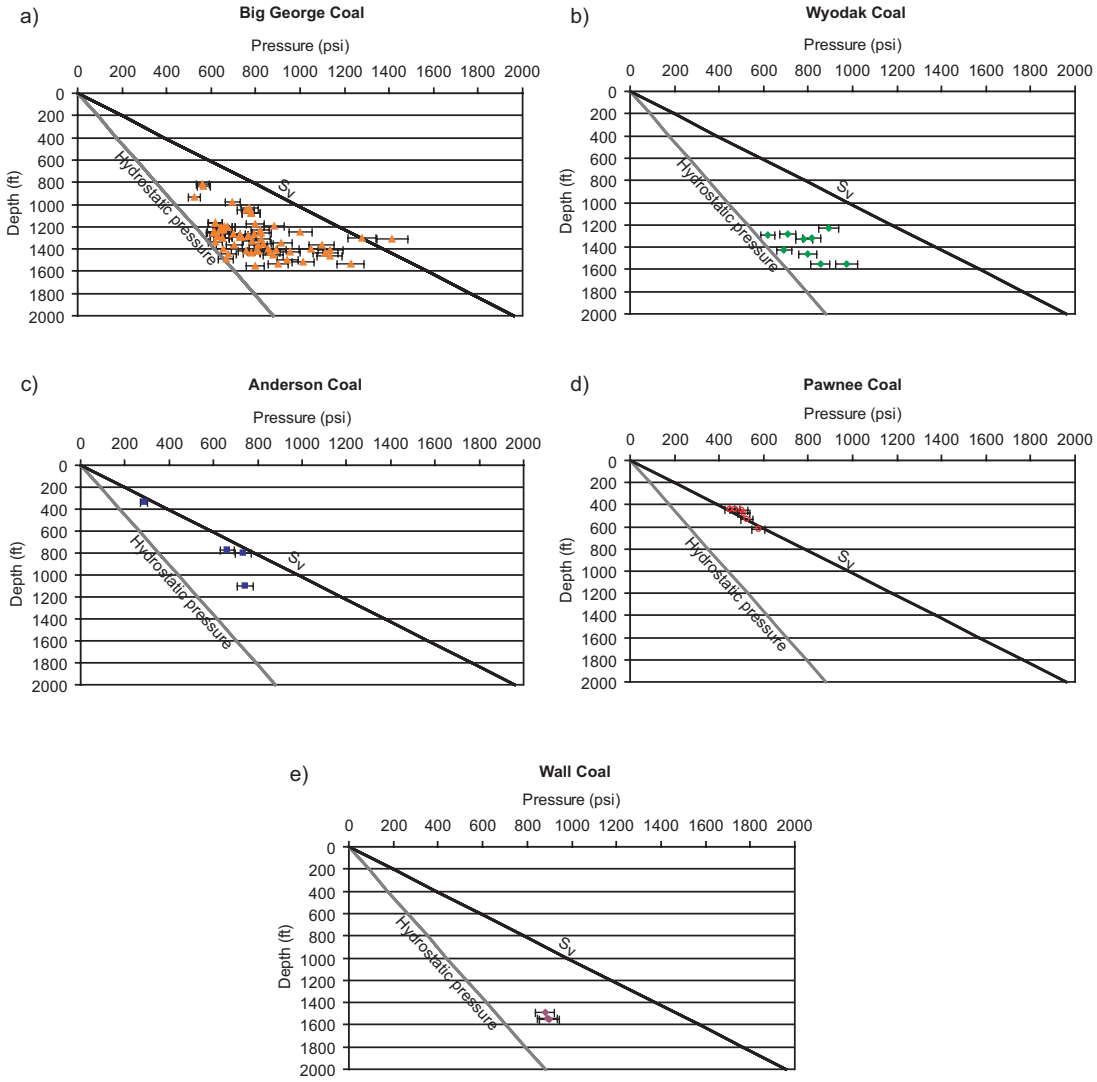

Figure 5.5: Magnitude of S_3 plotted on pressure versus depth profiles for the a) Big George, b) Wyodak, c) Anderson, d) Pawnee and e) Wall coals. The black line corresponds to the overburden stress (S_v) and the dark grey line corresponds to the hydrostatic pore pressure gradient.

5.4 Relationship between water production and orientation of hydraulic fractures

We carried out a similar analysis as Colmenares and Zoback (2007) to see if hydraulic fracture orientation was correlated with CBM water and gas production. We obtained gas and water production data from the Wyoming Oil and Gas Conservation Commission (WOGCC, 2006) for the same CBM wells that we analyzed water-enhancement tests. Our conclusions are similar to Colmenares and Zoback (2007) (Figure 5.6), where they found that some CBM wells with vertical fractures produced large volumes of CBM water (~7,000 bbl/month) and little to no gas, whereas CBM wells with horizontal hydraulic fractures produced small volumes of both water and gas. They also found that some CBM wells with vertical fractures produced large volumes of gas with manageable volumes of water. Our analysis supports their findings, although we do find that three wells with horizontal hydraulic fractures in our data set produce over 7,000 bbl/month (Figure 5.6a and c). In addition, one of our wells producing from the Big George coal has excessive water production (~9,000 bbl/month), but also produces extremely large volumes of gas (~35,500 mcf/month) (Figure 5.6a).

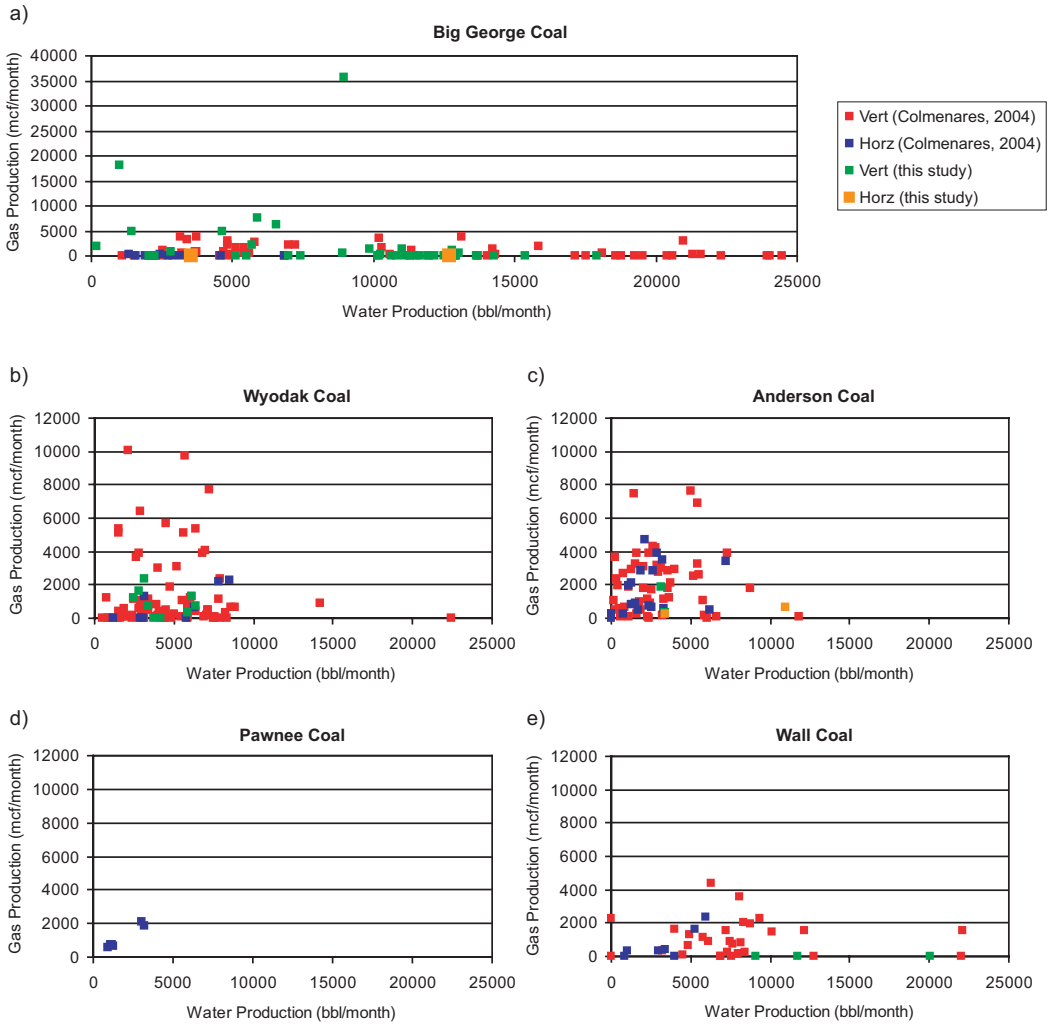

Figure 5.6: Gas production versus water production for the a) Big George, b) Wyodak, c) Anderson, d) Pawnee and e) Wall coals. Vert corresponds to wells with vertical hydraulic fractures and horz corresponds to wells with horizontal hydraulic fractures. Points in blue and red come from Colmenares (2004) and Colmenares and Zoback (2007). Points in green and orange are from this study.

5.5 Relationship between water production and normal faults

We have used Anderson, Coulomb and Byerlee faulting theory (Zoback, in press) to look at the magnitude of S_3 in relation to the critical magnitude of S_{hmin} required for normal faults to slip. Horizontal hydraulic fractures tell us that S_3 is equal to the overburden stress and according to Anderson faulting theory; we are in a reverse faulting stress regime wherever we have determined that horizontal fractures have

formed in the PRB. However, vertical hydraulic fractures tell us that S_3 is less than S_v and therefore we are in either a strike-slip or normal faulting regime. We can use Coulomb faulting theory and Byerlee's law to calculate the magnitude of S_{hmin} that will cause normal faults to slip. The following equation is used in the calculation:

$$\frac{S_v - P_p}{S_{h\min} - P_p} \leq \left[\sqrt{\mu^2 + 1} + \mu\right]^2, \tag{2}$$

where μ is the coefficient of friction, S_v is the overburden stress, S_{hmin} is the minimum horizontal stress and P_p is the pore pressure.

We calculated S_v using equation 1 and determined the P_p from our pore pressure analysis of coals in the PRB in Chapter 4. Figures 5.7a-e show S_3 plotted against depth for the Big George, Wyodak, Anderson, Wall and Canyon coals. We can see that for the Big George, Wyodak and Wall coals, some of the wells have least principal stresses that fall within the critical S_{hmin} lines, indicating that normal faults are present and likely to slip in the areas where these wells are located. However, for wells with least principal stresses that fall between the critical $0.6S_{hmin}$ and S_v lines, they could be part of either normal or strike-slip faulting regimes. For the Canyon and Anderson coals there are no normal faults likely to slip in the areas analyzed (Figure 5.7c and e).

This has lead us to define three different stress states in the PRB, areas that have active normal faults, areas that are slightly more compressive (either normal or strike-slip stress regimes) and finally, areas with reverse faulting regimes. Figure 5.8 is a location map showing the stress state and the coalbed for which this stress state has been determined. We can see from Figure 5.8 that normal, compressive and reverse stress regimes exist very close to each other within the lower half of the study area, but to the north we see only compressive and reverse regimes. It appears that the magnitudes of the horizontal stresses are changing within coalbeds in the PRB, and that in general the horizontal stresses are decreasing toward the south and west.

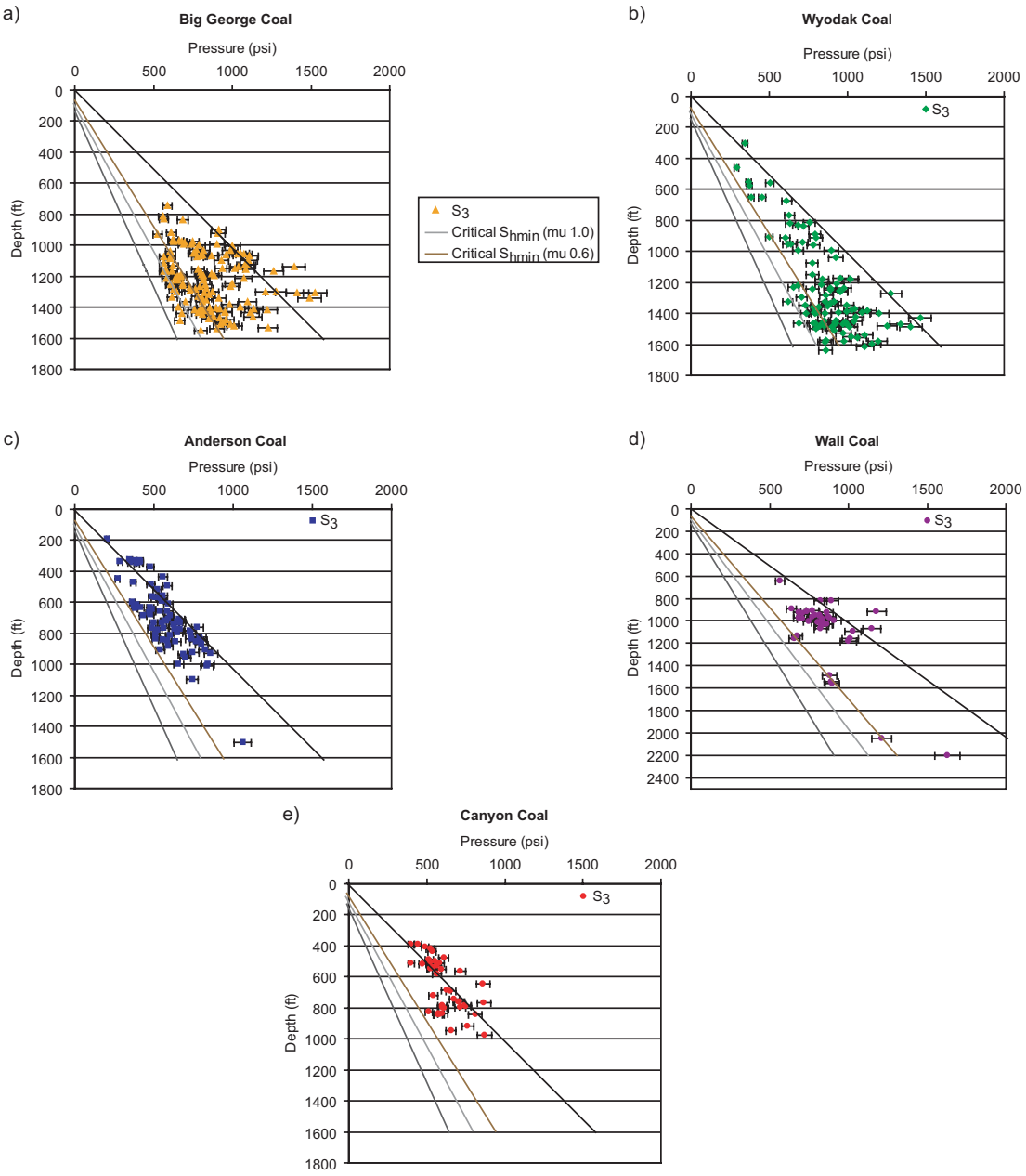

Figure 5.7: Magnitude of S_3 plotted on pressure versus depth profiles for the a) Big George, b) Wyodak, c) Anderson, d) Pawnee and e) Wall coals. The black line corresponds to the overburden stress (S_v), the dark grey line corresponds to the pore pressure gradient, the light grey line corresponds to the critical normal faulting line using a coefficient of friction of 1.0 and the brown line corresponds to the critical normal faulting line using a coefficient of friction of 0.6. When S_3 falls between the critical normal faulting lines it means that those wells are in active normal faulting areas.

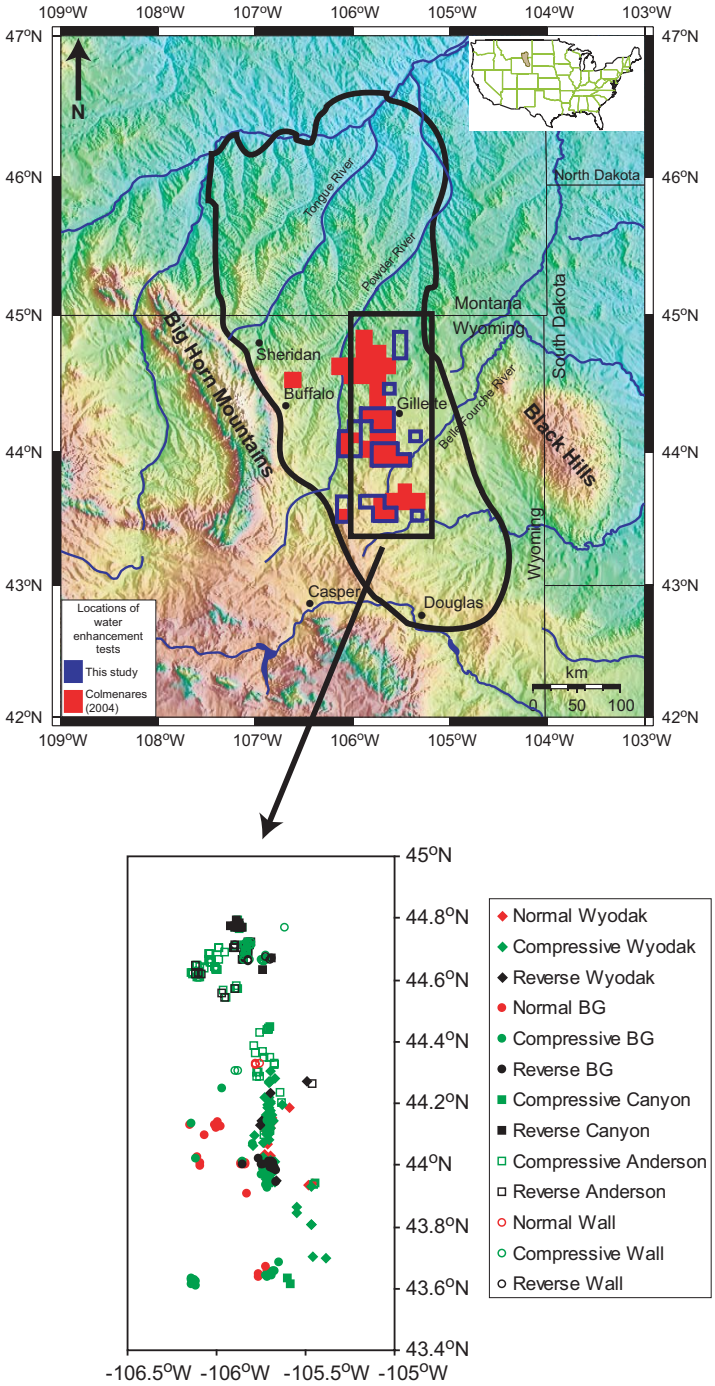

Figure 5.8: Location map showing the stress state and the coalbed for which this stress state has been determined. Points in red correspond to wells in active normal faulting areas, green, to wells in compressive areas (normal/strike-slip) and black, to wells in reverse faulting areas. Wyodak stands for the Wyodak coal, BG for Big George coal, Canyon for Canyon coal, Anderson for Anderson coal and Wall for Wall coal.

When we compare S_3/S_v with water production for wells from Colmenares and Zoback's (2007) study, as well as the current study, we find a correlation in the Big George coal between active normal faulting areas and wells with vertical hydraulic fractures that produce very large volumes of water (> 25,000 bbl/month) (Figure 5.9). Water production from other coalbeds does not reach 25,000 bbl/month, so we do not observe the same relationship as in the Big George coal.

Figure 5.9 implies that active normal faults in communication with vertical hydraulic fractures may play a role in CBM wells with very large water production, where the faults may act as permeable conduits for fluid migration to the producing coalbed.

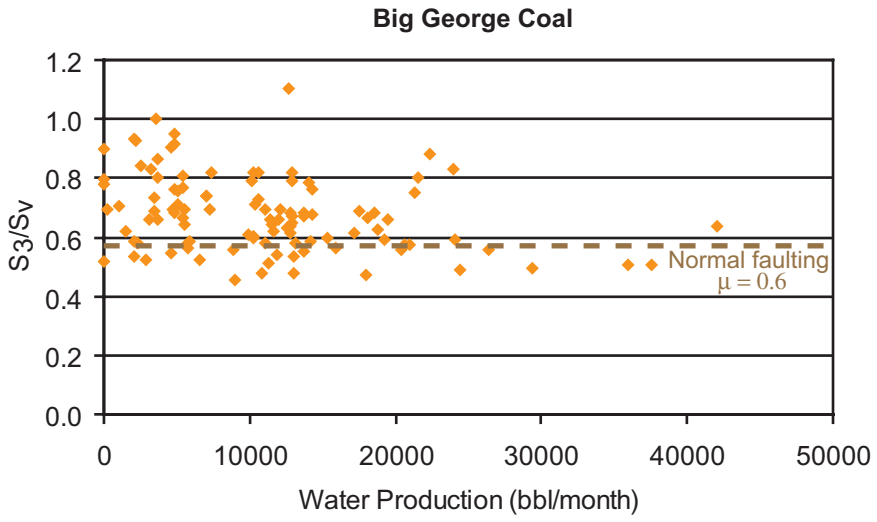

Figure 5.9: The ratio of S_3:S_v plotted against water production for the Big George coal. S_3/S_v < 0.58 means that the well is in an active normal faulting regime.

5.6 Implications for CBM water disposal and CBM wellbore completion practices in the Powder River Basin

In this study we have analyzed 198 water-enhancement tests in order to extend the research carried out by Colmenares and Zoback (2007), who analyzed ~500 tests to understand CBM operating procedures in the PRB. Like Colmenares and Zoback (2007), we find that in some areas of the basin the operators are creating vertical hydraulic fractures through water-enhancement, whereas in other areas they are creating horizontal hydraulic fractures. In addition, we find that some of the wells with vertical hydraulic fractures produce excessive volumes of CBM water, >7,000 bbl/month, and when the Big George coal is located in areas of active normal faulting, water production from CBM wells can be in excess of ~25,000 bbl/month. We hypothesize that active normal faults in communication with vertical hydraulic fractures may act as permeable conduits for water migration and give rise to production rates in excess of 25,000 bbl/month.

We also recommend that operators follow the procedures outlined in Colmenares and Zoback (2007) to help minimize CBM water production. Colmenares and Zoback recommended that operators create minifracs (~2 bbl/min for ~ 2 min) to determine the magnitude of S_3 before carrying out normal water-enhancement procedures. The minifrac will allow the operator to determine if they are in an area where horizontal hydraulic fractures will form or in an area where vertical fractures will form. If they are in an area where horizontal hydraulic fracture will form the operators can then water enhance at any rate and duration they choose. However, if they are in an area where vertical fractures will form, it is best if water-enhancement is kept to a minimum to ensure that the fractures do not propagate into overlying aquifers or come into communication with active normal faults.

Chapter 6

TESTING THE USE OF AEROMAGNETIC DATA FOR THE DETERMINATION OF CURIE DEPTH IN CALIFORNIA*

6.1 Abstract

Using California as a test region, we have examined the feasibility of using Curie-isotherm depths, estimated from magnetic anomalies, as a proxy for lithospheric thermal structure. Our method follows previous studies by dividing a regional aeromagnetic database into overlapping sub-regions and analyzing the power-density spectrum of each sub-region, but we have improved on previous studies in two important ways: We increase sub-region dimensions in a stepwise manner until long-wavelength anomalies are appropriately sampled, and each sub-region spectrum determined from the magnetic anomalies is manually fit with a theoretical expression

* This chapter was previously published in Geophysics: Ross, H. E., R. J. Blakely, and M. D. Zoback, 2006, Testing the use of aeromagnetic data for the determination of Curie depth in California: Geophysics, **71**, L51-L59.

that directly yields the depth to the bottom of the magnetic layer. Using this method, we have obtained Curie-isotherm depths for California that show a general inverse correlation with measured heat flow, as expected. The Coast Ranges of California are characterized by high heat flow (80-85 mW/m^2) and shallow Curie depths (20-30 km), whereas the Great Valley has low heat flow (less than 50 mW/m^2) and deeper Curie depths (30-45 km).

6.2 Introduction

Adequate knowledge of the thermal structure of the lithosphere is required for a wide variety of geodynamic investigations, including rock deformation, mineral phase boundaries, rates of chemical reactions, electrical conductivity, magnetic susceptibility, seismic velocity, and mass density (Chapman and Furlong, 1992). Lithospheric thermal gradients are often estimated from near-surface heat-flow measurements, but high-quality heat-flow measurements are not available globally, are rarely distributed uniformly, and are sometimes contaminated by local thermal anomalies. In places where heat-flow information is inadequate, the depth to the Curie-temperature isotherm may provide a proxy for temperature at depth.

This paper presents a spectral analysis method applied to magnetic anomalies from the state of California in order to estimate the depth of the Curie-isotherm throughout the state. We selected California as the study area because of its large number of well-documented surface heat-flow measurements (USGS Heat Flow Database for California, 2003) (Figure 6.1a) and statewide aeromagnetic coverage of adequate quality (Roberts and Jachens, 1999) (Figure 6.1b). California also has distinct zones of high (Coast Ranges and Mojave Desert) and low heat flow (Great Valley and Sierra Nevada) that correspond reasonably well with geologic provinces (Figure 6.1a). These aspects make California a good region to test whether the spectral analysis method can be transported to other regions with fewer heat-flow measurements, such as intraplate regions of the conterminous United States, in order to resolve areas with anomalously high temperatures in the lower crust.

So far as we know, our study is the first to determine the Curie-temperature isotherm for California. Using an improved methodology to estimate the depth to the Curie-isotherm, we find an inverse relationship between estimated Curie depths and heat-flow measurements across California. Specifically, the Coast Ranges geologic province is characterized by high heat flow and shallow Curie depths, whereas the Great Valley province is characterized by low heat flow and deep Curie depths.

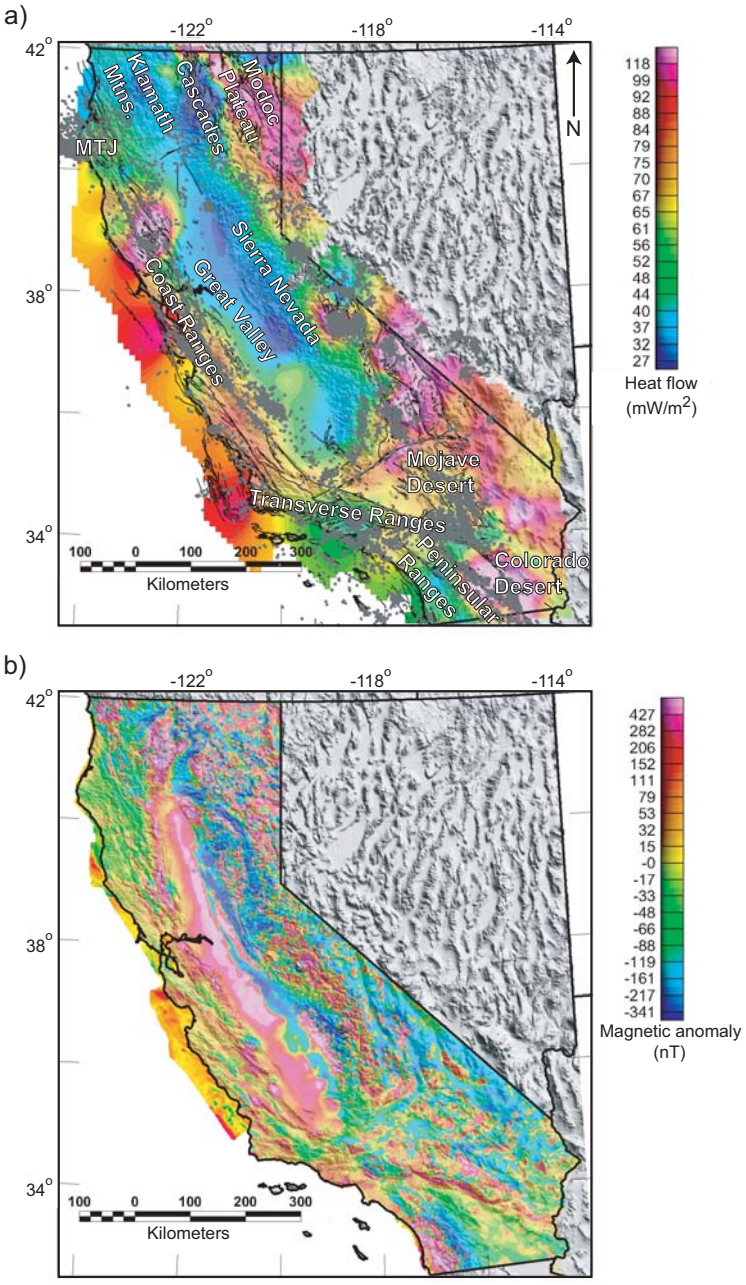

Figure 6.1: a) Heat-flow map for the state of California, USA, on the topographic relief map (USGS Heat Flow Database for California, 2003). Gray dots are earthquakes of magnitude >2, occurring from 1973 to 2003 (National Earthquake Information Center). Black lines indicate known faults (Jennings, 1994). Note that the seismicity is concentrated in areas with high heat flow, such as the Coast Ranges. Geomorphic provinces (shown in white letters) are modified from Norris and Webb (1990). MTJ, Mendocino Triple Junction. b) Aeromagnetic anomaly map for the state of California, from Roberts and Jachens (1999).

The Curie-temperature isotherm corresponds to the temperature at which magnetic minerals lose their ferromagnetism (approximately 580°C for magnetite at atmospheric pressure). Magnetic minerals warmer than their Curie-temperature are paramagnetic and, from the perspective of the earth's surface, are essentially nonmagnetic. Thus, the Curie-temperature isotherm corresponds to the basal surface of magnetic crust and can be calculated from the lowest wavenumbers of magnetic anomalies (after removing the appropriate International Geomagnetic Reference Field (IGRF) from the aeromagnetic data) (e.g., Bhattacharyya and Morley, 1965; Spector and Grant, 1970; Mishra and Naidu, 1974; Byerly and Stolt, 1977; Connard et al., 1983; Hamdy et al., 1984; Blakely, 1988; Tanaka et al., 1999; Salem et al., 2000).

A number of assumptions and problems are associated with estimations of the Curie-temperature isotherm. Uncertainties about the nature of magnetization at depth affect assumed Curie temperatures, and the basal depth itself may be caused by a lithologic contact rather than a thermal boundary. Trade-offs also exist between accuracy and spatial resolution of Curie depth determinations.

Nevertheless, various studies have shown correlations between Curie-temperature depths and average crustal temperatures, leading to viable conclusions regarding lithospheric thermal conditions in a number of regions around the world. Byerly and Stolt (1977) estimated Curie-temperature isotherms across northern and central Arizona. They determined an average Curie depth of 20 km and identified a narrow (~60 km) region of shallower depths (~10 km) corresponding with low P-wave velocities in the upper mantle. They attributed the shallow Curie depths and low velocities to a zone of elevated crustal temperature. Connard et al. (1983) conducted a similar study of the Cascade Range of central Oregon, which is part of the volcanic arc associated with the Cascadia subduction zone. They found a narrow zone of shallow Curie depths consistent with thermal models of the area. Similarly, Blakely (1988) calculated basal depths for the state of Nevada and noted several areas where shallow basal depths corresponded with high heat flow, historic faulting, high seismicity, and P- and S-wave attenuation, which he interpreted as regions of shallow Curie-

temperature isotherms. Likewise, Tanaka et al. (1999) used aeromagnetic data from east and southeast Asia to estimate depths to Curie isotherm. They identified shallow basal depths across back-arc regions and deeper basal depths along the trench axis as expected from heat-flow values, showing relatively high temperatures in arc environments and relatively low temperatures at trenches.

Tanaka et al. (1999) also noted an inverse correlation between estimated Curie depths and heat-flow measurements; specifically, Curie depths calculated from magnetic anomalies generally agreed with Curie depths derived from the one-dimensional heat conductive transport model. The one-dimensional heat conductive transport equation

$$D_c = \frac{\kappa \theta_c}{q} \tag{1}$$

(Tanaka et al., 1999) shows that any given depth to a thermal isotherm is inversely related to heat flow, where D_c is the depth to the isotherm, κ is the coefficient of thermal conductivity, θ_c is isotherm temperature, and q is heat flux. This equation implies that regions of high heat flow are associated with shallower isotherms, whereas regions of lower heat flow are associated with deeper isotherms.

Our study of California was motivated by a broader interest in recent studies of intraplate seismicity. Following Liu and Zoback (1997), we hypothesize that one possible mechanism for strain localization in intraplate seismic zones is elevated temperatures at depth, which weakens the lower crust in those areas (Zoback et al., 2002). Unfortunately, most intraplate regions lack heat-flow data (Pollack et al., 1993), and this led us to investigate whether the depth to the Curie-temperature isotherm might serve as a proxy for crustal temperature in those areas. We focused on the nominal resolution of the spectral analysis method, in the hope that we could detect a correlation between areas with high rates of seismicity and areas with elevated crustal temperature.

Present-day deformation in California nicely illustrates our hypothesis for intraplate seismicity. The Pacific/North America plate boundary in western California accommodates both right-lateral shear along the San Andreas fault (48 mm/yr, Kreemer et al., 2003), and transverse compression over a broad (~100 km) zone (1 mm/yr, Page et al., 1998). During the past 3.5 m.y. the compressional component of the plate boundary has produced 400-1200 m of vertical uplift in the Coast Ranges through concomitant folding and reverse faulting (Page et al., 1998).

This compressional deformation ceases at the boundary between the Coast Ranges and the Great Valley, despite a uniform stress field across the region oriented at a high angle to the San Andreas Fault (Zoback, et al., 2002). In addition, the Great Valley is characterized by low seismicity in comparison to the seismically active San Andreas Fault and associated faults cutting through the Coast Ranges (Figure 6.1a).

The differing patterns of seismicity beneath the Coast Ranges and the Great Valley suggest a fundamental difference in lithospheric rheology in the two provinces; this difference may be controlled by the thermal structure of the lithosphere. The Coast Ranges exhibit high heat flow, with an average of 85 mW/m^2, whereas heat-flow values in the Great Valley and Sierra Nevada average 40-50 mW/m^2 (Figure 6.1a). Roy et al. (1972) postulated that the Sierra Nevada and Great Valley have low heat-flow signatures because they have been "chilled" by the subducted oceanic plate lying beneath them. The Coast Ranges also have subducted oceanic crust below them, but asthenospheric upwelling from the northward-migrating Mendocino Triple Junction (Lachenbruch and Sass, 1980) or a broad shear zone at depth (Lachenbruch and Sass, 1973; Thatcher and England, 1998) may have generated the anomalously high temperatures beneath these ranges.

The geomorphic boundary between the Coast Ranges and the Great Valley, which marks the edge of the transpressional deformation, coincides with this abrupt change from high heat flow in the Coast Ranges to low heat flow in the Great Valley (Page et al., 1998). From what we have observed of the Pacific/North America plate boundary, it does seem that elevated temperatures at depth may be the mechanism that

is weakening the upper mantle and/or lower crust in the vicinity of the Coast Ranges and San Andreas Fault system. The presence of this zone of high heat flow may explain the formation of the Coast Ranges and San Andreas Fault (high temperatures at depth weakening the lithosphere) and why compressional deformation and the Pacific/North America plate boundary have remained within this narrow region.

6.3 Databases

6.3.1 Heat-flow database for California

In our study, we have compared heat-flow values with our estimated Curie-temperature isotherm depths for each geological province of California, to determine if we can use Curie depth as a proxy for heat flow. The heat flow database of California currently contains 542 heat-flow measurements, compiled from scientific publications that reported heat-flow values from across California (USGS Heat Flow Database for California, 2003) (Figure 6.1a).

In general, measured heat-flow values from California reflect crustal thermal conditions at depth, but several regions of California may be exceptions to this general rule. Heat flow varies significantly in the Cascade Range of northern California (Figure 6.1a), for example, from less than 50 mW/m^2 to 100 mW/m^2. The Cascade Range forms the present day active magmatic arc, with oldest volcanic units of Pliocene age (Norris and Webb, 1990). In California, this province has a relatively low heat-flow signature (Figure 6.1a), although directly north of California, in the state of Oregon, the Cascade Range has high heat flow consistent with its magmatic arc setting. The low heat-flow values of the California Cascades have been attributed to convective heat transfer by ground-water flow, masking the high conductive heat flow expected for a magmatic arc (Mase et al., 1982).

In the Sierra Nevada province, heat-flow measurements are also low (less than 50 mW/m^2), but Brady and Ducea (2000) and Saltus and Lachenbruch (1991) found that surface heat-flow measurements for the Sierra Nevada do not reflect modeled

temperatures at depth. Specifically, modeled temperatures are high and predict surface heat-flow measurements of 49 to 120 mW/m^2 (Brady and Ducea, 2000); these values exceed observed heat-flow values in the Sierra Nevada by approximately 15 to 100 mW/m^2 (e.g. Figure 6.1a). Saltus and Lachenbruch (1991) suggest that asthenospheric upwelling generated by the northward-migrating Mendocino Triple Junction reached the southern Sierra Nevada at 20 Ma, at the beginning of its uplift, but this heat pulse has not yet reached the surface. Therefore, in the Sierra Nevada, surface heat-flow measurements may not accurately indicate thermal conditions at depth.

Despite these specific discrepancies between heat-flow measurements and thermal conditions at depth in the California Cascades and Sierra Nevada, most heat-flow measurements from the Coast Ranges, Great Valley, Mojave Desert, and Transverse Ranges probably do reflect the crustal thermal gradient.

6.3.2 Aeromagnetic anomaly map for California

We estimated Curie-temperature isotherm depths using the magnetic anomaly map of California (Roberts and Jachens, 1999) (Figure 6.1b). The magnetic anomaly map was compiled by Roberts and Jachens (1999) from numerous individual aeromagnetic surveys conducted at various times and with different flight elevations and line spacings. Individual surveys were gridded to a common projection and sample interval (1 km), converted to anomaly values by subtraction of the appropriate IGRF, analytically continued to a surface (305 m above terrain), and smoothly merged with neighboring surveys (Roberts and Jachens, 1999).

6.4 Curie-temperature isotherm depth estimates

6.4.1 Method

Our method to estimate the depth to the Curie-temperature isotherm relies on previous methodologies that analyzed spectral information within sub-regions of a magnetic data set (Smith et al., 1974; Shuey et al., 1977; Boler, 1978; Connard et al., 1983; Blakely, 1988). Within each sub-region, we assume that magnetization, $M(x,y)$, has a high degree of randomness and is confined between two horizontal surfaces at depths z_t and z_b (depth to the top and depth to the bottom, respectively). The power-density spectrum of the observed magnetic field is given by

$$\Phi_h\left(k_x,k_y\right)=A\left(k_x,k_y\right)\Phi_M\left(k_x,k_y\right)\left(e^{-kz_t}-e^{-kz_b}\right)^2 \tag{2}$$

where $\Phi_M\left(k_x,k_y\right)$ is the power-density spectrum of the magnetization, $A\left(k_x,k_y\right)$ is a function that depends on the vector directions of magnetization and ambient field (Blakely, 1995, p.301), k_x and k_y are wavenumbers in the x and y directions respectively, and

$$k=\left(k_x{}^2+k_y{}^2\right)^{1/2} \tag{3}$$

The two-dimensional power-density spectrum is averaged within concentric rings about the origin, transforming equation 2 into a one-dimensional spectrum:

$$\Phi_h\left(k\right)=A\Phi_M\left(k\right)\left(e^{-kz_t}-e^{-kz_b}\right)^2 \tag{4}$$

where A is a constant. This averaging around the origin is valid only if we assume that the statistical properties of $M(x,y)$ are not directionally dependent. We can calculate an estimate of $\Phi_M\left(k\right)$ without actually knowing the details of $M(x,y)$ because of the assumption that the statistical properties of the magnetization are random (Spector and Grant, 1970). Thus z_t and z_b are the only unknowns in equation 4.

Our method has evolved from published methods in several ways. Rather than dividing the aeromagnetic data into overlapping sub-regions of equal dimensions on a uniform grid, we distribute sub-regions across California and systematically vary the dimension, *W,* of each sub-region. Sub-regions are increased in dimension until a peak in the power spectrum is observed at $k > k_f$, where

$$k_f = \frac{2\pi}{W} \tag{5}$$

is the fundamental wavenumber (Figure 6.2). The presence of a peak at $k > k_f$ indicates that the bottom of the magnetic layer is being resolved; i.e., the dimensions of the sub-region are large enough to include long wavelength signal caused by sources at the bottom of the magnetic layer.

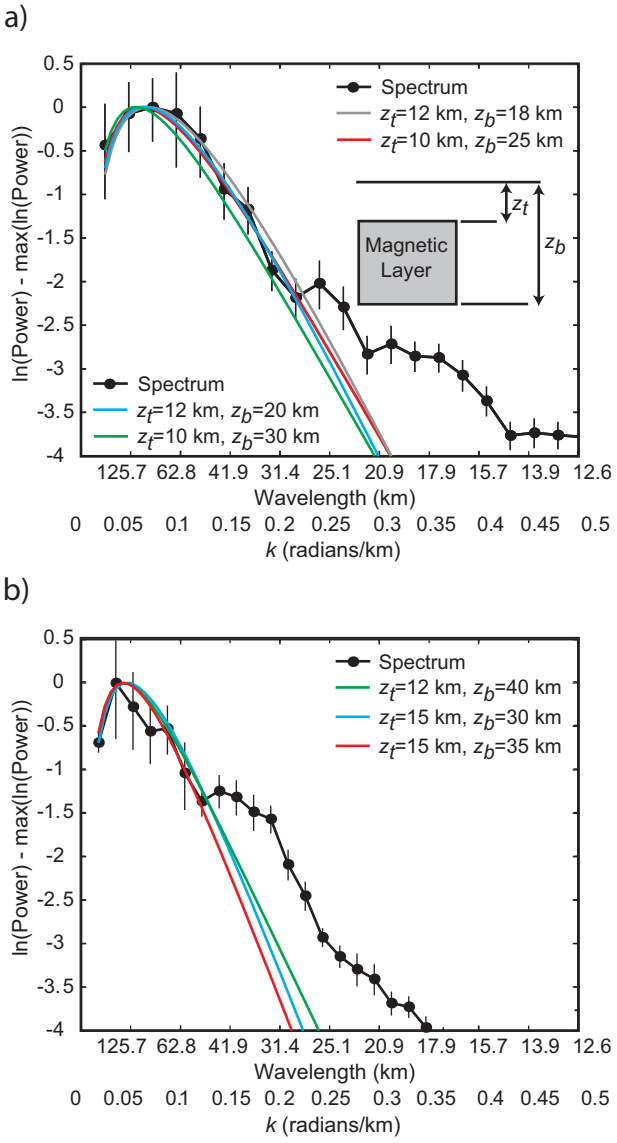

Figure 6.2: Normalized radial power spectrums for a) sub-region with W = 130 km, and b) sub-region with W = 180 km. The black solid-dot curves are the power-density spectrums for each sub-region, and the solid colored curves are the "best" fit curves from equation 4 to the low-wavenumber portion of the spectrums. Error bars are the 95% confidence limits calculated from the spectral values within each ring used in the calculation of the one-dimensional radial spectrum $\Phi_M(k)$. The Nyquist wavenumber is π.

Increasing the dimension of each sub-region in this fashion was necessary because of the complexity of California geology. Geologic provinces vary markedly in terms of thermal properties and lateral dimensions. For example, the Coast Ranges geologic province is associated with high heat flow (80-85 mW/m^2) and is approximately 120 km wide in the east-west direction. Thus, sub-regions with

$W > 120$ km incorporate anomalies from the neighboring Great Valley province, a "contamination" that affects the estimation of basal depth within the Coast Ranges. On the other hand, the Great Valley is characterized by low heat flow (less than 50 mW/m^2), suggesting that the Curie-isotherm for this province will be deep. Sub-regions in the Great Valley province must be sufficiently large to capture the longest wavelengths of magnetic anomalies associated with this deep Curie isotherm (Shuey et al., 1977).

To alleviate the problems of contamination, we placed center points for sub-regions within geologic provinces in order to capture and emphasize aeromagnetic anomalies associated with each province. This is in contrast to previous methods that used uniform grids of overlapping sub-regions, forcing center points to follow a secondary uniform grid. A uniform grid of center points would ultimately capture magnetic anomalies from neighboring geological provinces with contrasting crustal thermal conditions.

We note that sub-regions for the Great Valley, because of their large dimensions ($W = 240$ km), will include magnetic anomalies from the Coast Ranges, Sierra Nevada, and Cascade Range provinces. However, as noted earlier, these neighboring provinces all have crustal temperatures higher than the Great Valley. We have made the Great Valley sub-regions large enough to resolve the peak in the power-density spectrum from the longest wavelengths associated with the Great Valley, rather than the shorter wavelengths from the warmer geological provinces.

Another variation on previous methodologies regards the manner in which we analyze the spectra. Most previous methods (e.g., Connard et al., 1983; Blakely, 1988; Okubo and Tsu, 1992; Tanaka et al., 1999) used a two-step process to estimate basal depth: First the position of the spectral peak relative to k was determined, then straight lines were fit to a specific part of the spectrum. Here we use a one-step procedure by actually fitting equation 4 to observed power-density spectra in order to estimate z_b (a suggestion made to us by G. Connard, personal communication, 2004) (Figure 6.2). We believe that by reducing this process to a single step, we introduce

less error in the final estimation. Determining the correct straight-line portion of the spectrum is often ambiguous and estimates of z_b are very sensitive to the length of this straight line. Our one-step method requires that we look at the entire shape of the spectral peak, which Shuey et al. (1977) state is an essential requirement for "good resolution of z_b".

Our method proceeds as follows:

1. We designate sub-region centers within geological provinces and divide the aeromagnetic data into square sub-regions of dimension W centered over each sub-region center. An average value for each sub-region is removed from the aeromagnetic data for that sub-region.

2. A two-dimensional Fourier transform is applied to each sub-region, using the method of Ricard and Blakely (1988) to minimize edge effects.

3. Each two-dimensional Fourier transform is reduced to a one-dimensional radial spectrum $\Phi_h(k)$ by averaging amplitude values within overlapping rings that are concentric about the spectral origin (equation 4).

4. If a peak occurs at $k > k_f$, we manually fit equation 4 to the low-wavenumber portion of the power spectrum, thus obtaining z_b (Figure 6.2).

If a peak does not occur, we increase W and repeat steps 2 through 4, continuing in this fashion until a peak is observed. W was initially set at 90 km and increased to 250 km, in increments of 10 km.

We fit equation 4 to the low-wavenumber end of the power-density spectrum through trial and error, varying z_t and z_b to determine the best fit to the spectral peak. Because most of the information on the depth to the base of the magnetic layer is

contained in the low-wavenumber, peaked portion of the spectrum, our fits concentrated on this part of the spectrum, typically at wavenumbers less than 0.5 radians/km. We found that manually fitting the theoretical curve provided better results than using a non-linear least-squares method, because the non-linear least-squares method gave geologically unrealistic depths to the base of the magnetic crust (depths between 80-100 km). By manually fitting equation 4 we found the best fit curves within geologically realistic bounds (z_b no greater than the Moho for each geological province). Although we cannot prove the uniqueness of our method, on the basis of numerous trials we believe the repeatability of our results to be within ±5 km for both z_t and z_b.

To quantify the error in the estimated basal depths, we fitted multiple curves to the peak of the spectrum and considered the minimum and maximum z_b values determined from the theoretical curves to define a range of acceptable basal depths. The theoretical curves were kept within the 95% confidence bounds for each power-density spectrum. Figure 6.2 shows two power-density spectra from different sub-regions, with a number of theoretical curves that fit each spectrum. Estimated basal depth is most sensitive to the shape of the spectral peak. If z_t is held constant, a broad peak tends to give shallow basal depths, whereas steeper peaks give deeper depths.

As a verification of our methodology, we also applied the method of Okubo and Tsu (1992) to the same sub-regions. Curie depths estimated using Okubo and Tsu's method are in good agreement with our estimates (see Appendix 1 for more details).

6.4.2 Assumptions and caveats

A number of assumptions and potential problems are associated with these Curie-depth calculations. Deep magnetic sources have long wavelengths and low amplitudes, which makes them difficult to distinguish from anomalies caused by shallow sources. The dimension W of the sub-region must be sufficiently large to capture these long wavelengths, which forces a tradeoff between accurately determining z_b within each sub-region and resolving small changes in z_b across sub-

regions. Further, regional-scale magnetic-anomaly databases are usually a mosaic of individual aeromagnetic surveys. Subtle discontinuities can occur along survey boundaries owing to differences in survey specifications (flight-line spacing and flight altitude, for example), regional-field removal, and quality of data acquisition. These discontinuities can contribute long-wavelength noise to the regional compilation and may contaminate long-wavelength signal caused by deep magnetic sources (Grauch, 1993). Roberts and Jachens (1999) did not quantitatively estimate errors associated with the merging of California aeromagnetic surveys but did note the potential for errors introduced by continuing the data to a common reference level (305 m above terrain) and from variability of survey specifications and quality.

Our method assumes that magnetic measurements are made on a horizontal surface, whereas the California aeromagnetic compilation has been analytically continued to a surface with constant terrain clearance (305 m above terrain). We have investigated the implications of this decision by analytically continuing specific sub-regions of the California data to uniform altitudes (for example, the highest elevation in a sub-region and midway between the highest and lowest elevation in a sub-region) and recalculating the depth extent for those sub-regions. Our tests indicate that using a draped surface introduces only small differences (less than ±2 km) (see Appendix 2 for more details).

The assumption of random magnetization is critical to this spectral analysis method in order that the power-density spectrum ($\Phi_M\left(k_x, k_y\right)$) in equation 2 be a constant. The degree of randomness, however, depends on the geology of the region. The magnetization of an extrusive volcanic layer, for example, may have different statistical properties from plutonic rocks (Blakely, 1988). Fedi et al. (1997) and Pilkington et al. (1994) have shown that magnetization actually has a degree of correlation and have suggested power-law decay rates to correct for this correlation. There is no agreement on the decay rates that should be used, however, so we have assumed a purely uncorrelated magnetization in our investigation.

Disagreement also remains over the actual Curie temperature to be assumed in Curie-temperature isotherm studies. The Curie temperature of titanomagnetite at atmospheric pressure varies with titanium content, from 580°C for pure magnetite (Fe_3O_4) to –100°C for ulvöspinel (Fe_2TiO_4) (Stacey and Banerjee, 1974). Moreover, Haggerty (1978) argued that magnetic anomalies may arise from alloys of iron within the crust, resulting in Curie temperatures ranging from 600°C to 1100°C. Other rock-magnetic studies, however, have concluded that deep crustal rocks should have Curie temperatures ranging from 550°C to 600°C. Schlinger (1985) tested 40 rock samples representative of all lithologies from Lofoten and Vesterålen, Norway, and each had a Curie temperature between 550°C and 575°C. Frost and Shive (1986) studied the magnetic mineral compositions of xenoliths derived from deep continental crust that were exposed at the surface in plutonic and high-grade metamorphic terrains. They concluded that magnetite is the dominant magnetic mineral contributing to long-wavelength magnetic anomalies in continental crust, and hence 580°C is a reasonable Curie temperature for deep crustal rocks. We concur with Schlinger (1985) and Frost and Shive (1986) and have assumed 580ºC to be the Curie temperature in continental crust.

Finally, the depth to the base of all magnetic sources is not necessarily the Curie-temperature isotherm. The estimated basal depth may correspond to a vertical change in lithology, such as a sub-horizontal detachment fault or unconformity. For example, the spectral analysis method may find z_b at a contact between young volcanic rocks overlying a thick section of weakly magnetic sedimentary rocks, even though the Curie temperature lies at greater depth. In very low-heat-flow regions, the Curie-isotherm may lie deeper than the Moho, and because mantle rocks are typically nonmagnetic (e.g., Saad, 1969), z_b in such regions would correspond to Moho rather than the actual Curie depth. Thus, the deepest z_b that should be calculated with this method is the depth to Moho. The depths to Moho for the geological provinces of California are 28-30 km for the southern Coast Ranges (Page et al., 1999; Godfrey et al., 1997), 35-40 km for the Great Valley (Godfrey et al., 1997; Fliender et al., 2000), 40-42 km for the Sierra Nevada (Fliender et al., 2000; Surpless et al., 2002), 27-30 km

for the Mojave Desert (Zhu and Kanamori, 2000), and 30-37 km for the Transverse Ranges (Zhu and Kanamori, 2000).

6.5 Results

Estimated depths to the base of the magnetic crust are detailed in Table 6.1, shown relative to the elevation of the magnetic anomaly map (305 m above terrain). We have attempted to assign subjective quality values to each depth estimate based on the contamination within each sub-region from adjacent geological provinces, the magnitude of the error bars on each power-density spectrum, and the magnitude of the range in basal depths estimated for each sub-region. A is excellent, B is good and C is fair. As discussed subsequently, comparison of Table 6.1 with heat-flow values and the thickness of the seismogenic crust provides additional confidence in our basal depth determinations.

The map in Figure 6.3 shows the depth to the Curie-temperature isotherm in California, determined by applying a minimum-curvature algorithm to the basal depth values in Table 6.1. Figure 6.3 shows a general inverse relation between heat flow and depth to the Curie-isotherm, as expected from equation 1. In particular, depths to the base of magnetic crust determined from sub-regions centered over the Great Valley (Figure 6.3; points 1, 2, 3, 4, 7 and 9) are generally deeper than those determined for the Coast Ranges and Mojave Desert.

Table 6.1: Minimum and maximum z_b estimates for each sub-region, with a quality value assigned to the estimates (A is excellent, B is good and C is fair). Refer to Figure 3 for the geographical location of each sub-region.

Sub-regions	**1**	**2**	**3**	**4**	**5**	**6**	**7**	**8**	**9**
Geological province	GV/ SN	GV/ SN	GV/ SN	GV/ SN	GV/ SN	CR	GV/ SN	CR	GV/ SN
Z_b min (km)	40	30	30	25	18	25	35	20	30
Z_b max (km)	45	45	45	40	30	28	40	30	40
Quality	B	C	C	C	B	A	B	A	B

Table 6.1 contd.: Minimum and maximum z_b estimates for each sub-region, with a quality value assigned to the estimates (A is excellent, B is good and C is fair). Refer to Figure 3 for the geographical location of each sub-region.

Sub-regions	**10**	**11**	**12**	**13**	**14**	**15**	**16**	**17**	**18**
Geological province	GV/ SN	M	TR	M	M	TR	TR	M	M
Z_b min (km)	16	28	18	18	18	25	28	16	20
Z_b max (km)	30	35	20	30	30	35	32	20	30
Quality	B	B	B	B	B	B	B	A	B

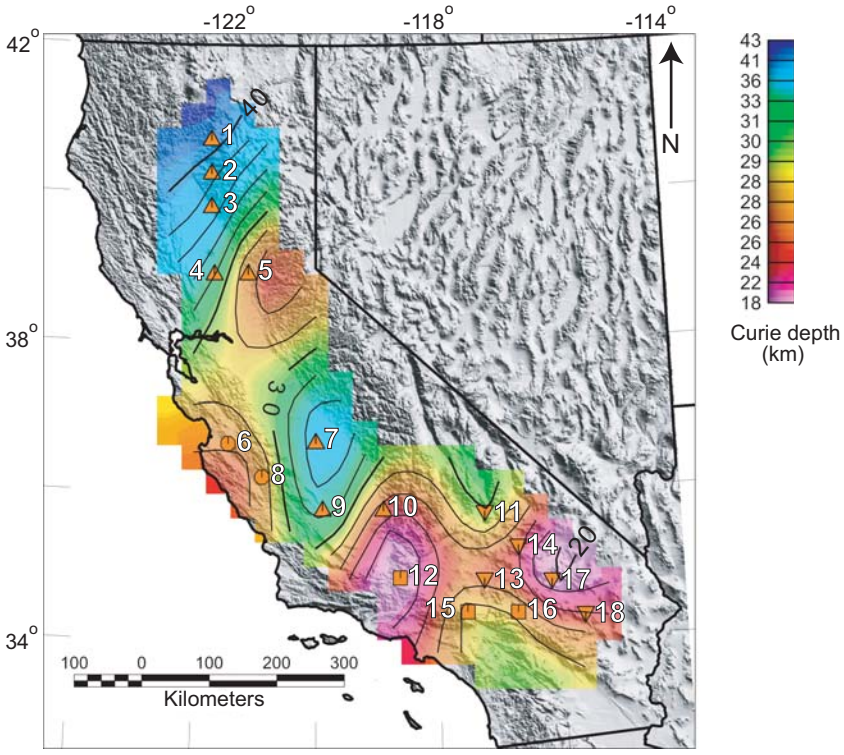

Figure 6.3: Interpolated map of 18 estimated Curie depths for the state of California. Contour interval is 2 km. Orange triangles, inverted triangles, circles, and squares mark the center points of the sub-regions described below. Triangles denote Great Valley/Sierra Nevada sub-regions, inverted triangles denote Mojave Desert sub-regions, circles denote Coast Ranges sub-regions, and squares denote Transverse Ranges sub-regions. White numbers are used as identifiers for the 18 sub-regions.

As with any interpolation algorithm, contours are only truly accurate near observational points, and contours far from observational points should be interpreted with caution. For example, the shallow basal depths interpolated between points 5 and 6 (Figure 6.3) over the Great Valley are probably too shallow; they should be similar to values at points 4 and 7 (Figure 6.3), in accordance with the heat flow for that part of the Great Valley (Figure 6.1a: less than 40 mW/m^2). In addition, interpolated depths southwest of point 12 (Figure 6.3) are shallower than expected from the heat-flow values for that region (45-60 mW/m^2), and points 5 and 10, sub-regions centered over the Great Valley/Sierra Nevada, also have shallower Curie depths than expected from the heat-flow values in each of those regions (less than 50 mW/m^2).

Figure 6.4 shows average heat flow versus estimated basal depth for each sub-region. Average heat-flow values in Figure 6.4 were calculated using all heat-flow

measurements within each sub-region, with two exceptions: heat-flow values greater than 100 mW/m^2 or less than 20 mW/m^2 were rejected, and heat-flow measurements were restricted to the geologic province appropriate for each sub-region.

The theoretical curves in Figure 6.4 follow from equation 1 for various values of thermal conductivity typical of crustal rocks (Sass et al., 1971). The average thermal conductivity for the crust in California is 2.5 W/m°K (C. Williams, personal communication, 2004), and calculated basal depths generally follow this curve in Figure 6.4. However, a spread of conductivities ranging from 1.3 W/m°K to 3.6 W/m°K also explains the data.

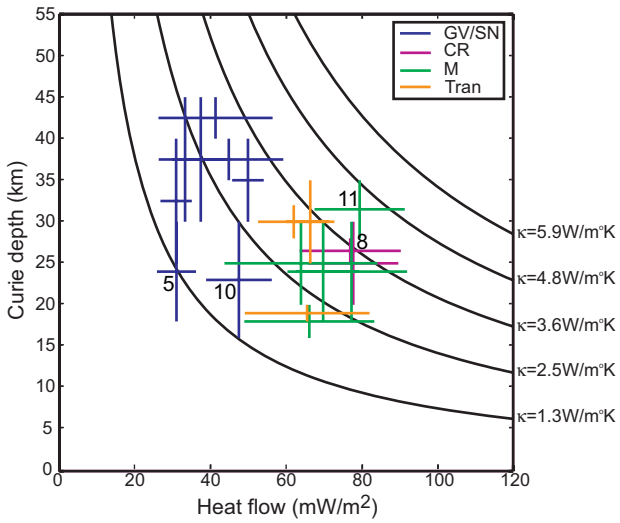

Figure 6.4: The relationship between estimated Curie depths and average heat flow for 18 sub-regions of California. GV/SN corresponds to sub-regions within the Great Valley and Sierra Nevada, CR from the Coast Ranges, M from the Mojave Desert, and Tran from the Transverse Ranges. Error bars on the heat flow are ±1σ from the mean. Error bars on Curie depths are determined by fitting a number of curves to the spectra for each sub-region. Also shown on this figure are theoretical curves for the one-dimensional heat conductive model (equation 1) using a reasonable magnitude range in values for the coefficient of thermal conductivity (κ). The theoretical curves come from equation 1, where κ was varied from 1.3 to 5.9 W/m°K (Sass et al., 1971), θ_c=580°C, and q ranged from 0 to 120 mW/m^2. Points 5, 8 10 and 11 are discussed in the Results and Discussion sections of the paper, and their geographical locations are shown in Figure 6.3.

Figure 6.4 shows a general inverse correlation between heat flow and estimated basal depth, as predicted by equation 1, indicating that spectral analysis of magnetic anomalies provides useful information regarding thermal conditions in the crust. On

the other hand, the large scatter of points in Figure 6.4 implies that using Curie-depth estimates as a proxy for heat-flow measurements would be problematic. In particular, shallow estimates of basal depths, between approximately 20-35 km, are spread over a particularly wide range of heat-flow values (30-80 mW/m^2).

6.6 Discussion

Within the scatter of our results, we interpret basal depths in Figures 6.3 and 6.4 to generally reflect depths to the Curie-temperature isotherm rather than lithologic contacts. Across California there are several known contacts in vertical section between highly magnetic and weakly magnetic crust (Franciscan rocks beneath ophiolites, for example) that could produce "false bottoms" in our calculations of basal depths (Page et al., 1998). These contacts occur mainly beneath the eastern Coast Ranges and western and central Great Valley at depths below 20 km (Godfrey et al. 1997; Page et al., 1998; Fliedner et al., 2000; Constenius et al., 2000), which is shallower than our calculated basal depths for these provinces (the shallowest estimated basal depths for both provinces in these areas are 20 km and 30 km, respectively). In addition, we observe that areas with highest heat flow generally have shallowest basal depths, namely the Coast Ranges and Mojave Desert (Figures 6.3 and 6.4), which also supports our assumption that the estimated basal depths correspond with depth to the Curie-temperature isotherm. The geology of California is very complicated, however, and we may have overlooked a structural or lithological contact at depth. It is also possible that the statistical properties of $M(x,y)$ vary from province to province, rather than remaining random as assumed.

The large scatter in Figure 6.4 derives from several factors, including non-conductive heat transport and poor resolution of Curie depths. Convection may be an important heat-transfer mechanism in California, making the one-dimensional conductive heat transport model (equation 1) inappropriate for representing thermal structure, as well as causing heat-flow measurements to inaccurately reflect conductive temperatures at depth. In addition, as pointed out by Shuey et al. (1977),

an accurate representation of the shape of the low-wavenumber spectral peak is an essential requirement for resolution of z_b. The only way to increase the resolution of the low-wavenumber peak is to increase the sub-region dimensions, but the sizes of our sub-regions are limited by the lateral extent of geologic provinces. In relatively small geologic provinces, like the Coast Ranges, window dimensions may be insufficient to properly sample the low-wavenumber part of the spectrum. Moreover, areas with low heat flow, like the Great Valley, require particularly large sub-regions because of the expected deep Curie isotherm, and large sub-regions may extend into neighboring geologic provinces with higher heat flow. A related problem involves the derivation of equation 4 from equation 2. Because of the geometry of the two-dimensional power spectrum, radial averages at low wavenumbers involve only a few points, thus limiting the resolution of the low-wavenumber peak.

In summary, our calculated Curie depths for California show the expected pattern: shallow depths correspond to areas with high heat flow, while deeper depths correspond to areas with low heat flow. On the other hand, the resolution of our calculation (Figure 6.4) is insufficient to distinguish areas with high temperatures in the lower crust without independent knowledge of the geology and abundant heat-flow measurements. As noted in the Results section, calculated Curie depths of 20-35 km correspond to a wide range of measured heat-flow values. Relying strictly on Figure 6.4 and ignoring heat flow, as we would be forced to do in an area with sparse heat-flow measurements, we would probably classify the deepest Coast Range and Mojave Desert Curie depths (points 8 and 11 in Figures 6.3 and 6.4) as areas with moderate temperatures in the lower crust, even though these regions are characterized by high heat flow.

In contrast, when using only heat-flow values to independently verify our estimated Curie depths, we would probably reject the Curie depths estimated for sub-regions 5 and 10 (Figures 6.3 and 6.4). Both of these sub-regions straddle the Sierra Nevada and Great Valley geologic provinces and appear to have Curie depths shallower than predicted by their heat-flow values. However, according to Brady and

Ducea (2000) and Saltus and Lachenbruch (1991), the thermal gradient of the lower crust beneath the Sierra Nevada is actually much higher than expected from heat-flow measurements for this geological province. Therefore, crustal thermal conditions predicted by our Curie depth estimates may be more reliable than those predicted from heat-flow measurements, at least for sub-regions 5 and 10.

Another proxy for temperature at depth is the depth extent of the seismogenic zone. Earthquakes rarely occur at depths greater than the brittle-ductile transition, which is strongly temperature-dependent (300±50°C) but can also be affected by lithology, stress type, and strain rate (Sibson, 1982, 1983; Bonner et al., 2003). Since both Curie depth and the depth above which earthquakes nucleate are temperature-dependent, these measurements should be linearly related.

Figure 6.5 shows the depth of the seismogenic zone, D_{90}, plotted against our calculated Curie depths. We have considered the seismogenic zone to be the region of the crust above which 90% of all earthquakes occur, a definition that should exclude deep, mislocated outliers. We also rejected earthquake locations with depth and horizontal location errors greater than ±5 km. The earthquake data used in this study are from the Northern and Southern California Earthquake Data Centers and span a 10-year period, from August 27, 1993, to August 27, 2003 (NCEDC, Berkeley Seismological Laboratory, University of California, Berkeley; SCEDC).

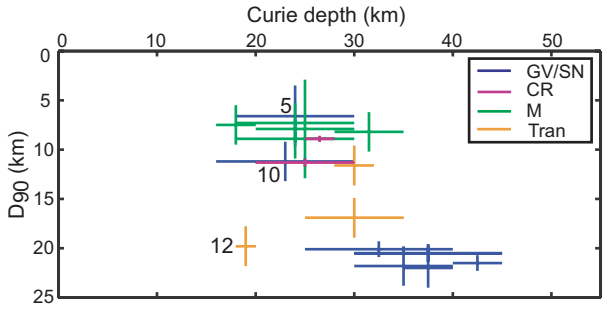

Figure 6.5: D_{90} (depth above which 90% of earthquakes nucleate) versus estimated Curie depths for each sub-region of California. Error bars for D_{90} come from the NCEDC and SCEDC earthquake catalogs. Explanations about GV/SN, CR, M and Tran are the same as Figure 4. Points 5, 10 and 12 are discussed in the Results and Discussion sections of the paper, and their geographical locations are shown in Figure 6.3.

In general, we see a linear relationship between D_{90} and calculated Curie depths (Figure 6.5), which gives us confidence that our calculated Curie depths reflect average thermal conditions for the crust of California.

Sub-regions 5 and 10 (discussed above and shown in Figures 6.3, 6.4 and 6.5) have shallow D_{90} depths despite having low heat flow, which suggests that both of these areas have elevated thermal gradients at depth. Again, this finding agrees with those of Brady and Ducea (2000) and Saltus and Lachenbruch (1991), who suggested that the thermal gradient at depth for the Sierra Nevada is higher than predicted from surface heat-flow measurements because of asthenospheric upwelling. The D_{90} depths for both of these sub-regions agree with our estimated Curie depths. Thus, at least in these specific areas, Curie depths more accurately represent crustal thermal conditions than heat-heat flow measurements.

In contrast, the Curie depth calculated for sub-region 12, centered over the Transverse Ranges, is shallower than predicted by its D_{90} depth (Figures 6.3 and 6.5). Sibson (1982, 1983) proposed that deep seismicity observed for the Western Transverse Ranges may arise from the depression of the thermal gradient at depth owing to high rates of imbricate thrust stacking that have uplifted the ranges. This thickening and thrusting may have placed highly magnetic material over more weakly magnetized rocks, causing the calculation of a shallower Curie depth than expected

from the D_{90} value for this sub-region. Alternatively, since this sub-region encompasses magnetic anomalies from the Mojave Desert, the estimated Curie depth for this sub-region may be an average of the Curie depths for the Mojave Desert and Transverse Ranges geologic provinces.

Thus it appears that much of the complexity implied by the scatter in Figure 6.4 results from the tectonic and thermal complexities of California. This gives us some confidence that our methodology can be translated to intraplate areas with fewer heat-flow measurements if sufficient geologic and thermal information is available to validate the estimated depths to Curie-temperature isotherm.

6.7 Conclusions

We have applied spectral analysis to aeromagnetic anomalies in order to estimate depths to the Curie-temperature isotherm beneath California, a region with an abundance of heat-flow measurements. We found a general inverse correlation between calculated Curie depths and heat flow in California, with high heat-flow regions (Coast Ranges and Mojave Desert) characterized by shallow Curie depths and low heat-flow regions (Great Valley) corresponding to deeper Curie depths. In addition, our calculated Curie depths agree generally with locations of deepest earthquakes across California, providing confidence that our method is sampling the Curie-temperature isotherm and assessing reasonable average thermal conditions for the crust of California.

6.8 Appendix 1 - Results from an alternative spectral analysis method

Figure 6.6 shows average heat flow versus calculated Curie depth for each sub-region following the method of Okubo and Tsu (1992). This method gave a much greater range in calculated Curie depth for each sub-region compared to our method (compare figures 6.4 and 6.6).

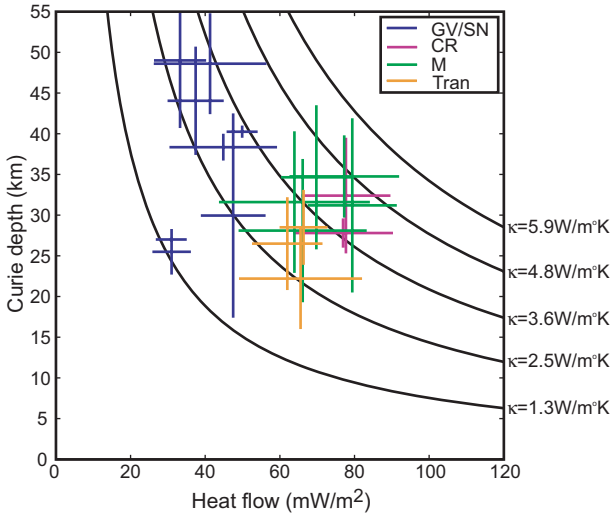

Figure 6.6: Curie depths, calculated using the method of Okubo and Tsu (1992), versus average heat flow for all 18 sub-regions of California. GV/SN corresponds to sub-regions within the Great Valley and Sierra Nevada, CR from the Coast Ranges, M from the Mojave Desert, and Tran from the Transverse Ranges. Error bars on the heat flow are ±1σ from the mean. Error bars on Curie depths are determined by fitting a number of straight lines to the spectra for each sub-region. Also shown on this figure are theoretical curves for the one-dimensional heat conductive model (equation 1) using a reasonable magnitude range in values for the coefficient of thermal conductivity (κ). The theoretical curves come from equation 1, where κ was varied from 1.3 to 5.9 W/m°K (Sass et al., 1971), θ_c=580°C, and q ranged from 0 to 120 mW/m^2.

Okubo and Tsu (1992) estimate depths to the top and centroid of a magnetic body by fitting straight lines to the low wavenumber end of the spectra. The depth to the bottom is then calculated using the following equation:

$$z_b = 2z_0 - z_t\,, \tag{6}$$

where, z_b is depth to the bottom, z_t, depth to the top and z_0, depth to the centroid.

However, we found that z_b was very sensitive to the length of the straight line used to fit the linear part of the spectra. In some cases it was hard to discern the correct linear part of the spectra to fit a straight line to and hence, when we tested the method using different lengths of a straight line to fit the spectra, we found large variances in the calculated depth to the bottom.

6.9 Appendix 2 - Analytically continuing aeromagnetic data to uniform altitudes

As mentioned in section 6.2.4, our method assumes that magnetic measurements are made on a horizontal surface, whereas the California aeromagnetic compilation has been analytically continued to a surface with constant terrain clearance (305 m above terrain). We carried out a test to see whether using draped magnetic data instead of data set at a horizontal surface affected our Curie depth estimates. Figure 6.7 shows the results from one of our tests, where we obtained power-density spectrums from magnetic data continued to various uniform altitudes (for example, the highest elevation in a sub-region and midway between the highest and lowest elevation in a sub-region) and compared our original spectra with those obtained from the magnetic data at constant altitudes.

As can be seen from Figure 6.7, there is only a slight difference between the different power-density spectrums, especially at the low-wavenumber end of the spectrums where we are interested. Therefore, we believe that using the draped California magnetic data introduced negligible error in our Curie depth estimates.

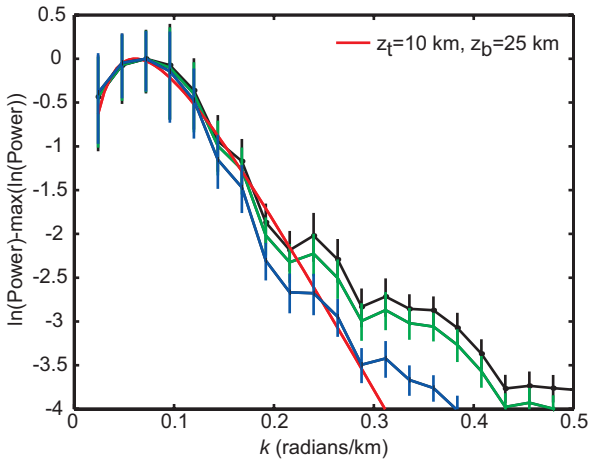

Figure 6.7: Normalized radial power spectrums for a sub-region with W = 130 km. The black curve corresponds to our original power-density spectrum shown in Figure 6.2a. The green curve is derived from the magnetic data in the sub-region being continued to an altitude midway between the highest and lowest elevation in the sub-region. The blue curve is derived from the magnetic data being continued to the highest elevation in the sub-region. The solid red curve is the "best" fit curve we used to estimate the Curie depth for this sub-region. Error bars are the 95% confidence limits calculated from the spectral values within each ring used in the calculation of the one-dimensional radial spectrum $\Phi_M(k)$. The Nyquist wavenumber is π.

REFERENCES

Abass, H. H., M. L. Van Domelen, and W. M. El Rabaa, 1990, Experimental observations of hydraulic fracture propagation through coal blocks: SPE **21289**, presented at the SPE Eastern Regional Meeting, Columbus, Ohio, October 31-November 2.

Advanced Resources International, Inc., 2002, Powder River Basin coalbed methane development and produced water management: **DOE/NETL-2003/1184**.

Anderson, J., M. Simpson, P. Basinski, A. Beaton, C. Boyer, D. Bulat, S. Ray, D. Reinheimer, G. Schlachter, L. Colson, T. Olsen, Z. John, R. Khan, N. Low, B. Ryan, and D. Schoderbek, 2003, Producing natural gas from coal: Oilfield Review, **15**, 8-31.

Applied Hydrology Associates, Inc. and Greystone Environmental Consultants, Inc., 2002, Groundwater modeling of impacts associated with mining coal bed methane development in the Powder River Basin: Technical Report Powder River Basin Oil and Gas Environmental Impact Statement, U.S. Bureau of Land Management, Buffalo Field Office, <http://www.blm.gov/wy/st/en/info/NEPA/bfodocs/prb_eis/prb-feis.html>.

Ayers, W., 2002, Coalbed gas systems, resources, and production and a review of contrasting cases from the San Juan and Powder River basins: AAPG Bulletin, **86**, 1853-1890.

Bartos, T. T., and K. M. Ogle, 2002, Water quality and environmental isotopic analyses of ground-water samples collected from the Wasatch and Fort Union Formations in areas of coalbed methane development — implications to recharge and ground-water flow, Eastern Powder River Basin, Wyoming: U.S. Geological Survey Water-Resources Investigations Report **02-4045**.

Bhattacharyya, B. K., and L. W. Morley, 1965, The delineation of deep crustal magnetic bodies from total field aeromagnetic anomalies: Journal of Geomagnetism and Geoelectricity, **17**, 237-252.

Blakely, R. J., 1988, Curie temperature isotherm analysis and tectonic implications of aeromagnetic data from Nevada: Journal of Geophysical Research, **93**, 11817-11832.

Blakely, R.J., 1995, Potential Theory in gravity and magnetic applications: Cambridge University Press.

Boler, F. M., 1978, Aeromagnetic measurements, magnetic source depths, and the Curie-point isotherm in the Vale-Owyhee, Oregon, geothermal area: M.S. thesis, Oregon State University.

Bonner, J. L., D. D. Blackwell, and E. T. Herrin, 2003, Thermal constraints on earthquake depths in California: Bulletin of the Seismological Society of America, **93**, 2333-2354.

Brady, R. J., and M. N. Ducea, 2000, Large integrated crustal heat production vs. low measured heat flow from the Sierra Nevada, California: Abstracts with programs – Geological Society of America, **32**, 43.

Byerly, P. E., and R. H. Stolt, 1977, An attempt to define the Curie-temperature isotherm in Northern and Central Arizona: Geophysics, **42**, 1394-1400.

Chapman, D. S., and K. P. Furlong, 1992, The thermal state of the lower crust, in D. M. Fountain, R. J. Arculus, and R. M. Kay, eds., Continental Lower Crust: Development in Geotectonics, **23**, 179-199.

Chaturvedi, T., 2006, Spontaneous imbibition and wettability characteristics of Powder River Basin coal: unpublished MS Thesis, Stanford University, Stanford, California.

Colmenares, L. B., 2004, Rock strength under true triaxial loading, seismotectonics of Northern South America and geomechanics and Coal Bed Methane Production in the Powder River Basin: unpublished PhD Thesis, Stanford University, Stanford, California.

Colmenares, L. B., and M. D. Zoback, 2007, Hydraulic Fracturing and Wellbore Completion of Coalbed Methane (CBM) Wells in the Powder River Basin, Wyoming: Implications for Water and Gas Production: AAPG Bulletin, **91**, 51-67.

Connard, G., R. Couch, and M. Gemperle, 1983, Analysis of aeromagnetic measurements from the Cascade Range in central Oregon: Geophysics, **48**, 376-390.

Constenius, K. N., R. A. Johnson, W. R. Dickinson, and T. A. Williams, 2000, Tectonic evolution of the Jurassic-Cretaceous Great Valley forearc, California: Implications for the Franciscan thrust-wedge hypothesis: Geological Society of America Bulletin, **112**, 1703-1723.

Daddow, P. B., 1986, Potentiometric-surface map of the Wyodak-Anderson coal bed, Powder River structural basin, Wyoming, 1973-84: U.S. Geological Survey Water-Resources Investigations Report **85-4305**, 1 sheet, Scale 1:250,000.

De Bruin, R. H., and R. M. Lyman, 1999, Coalbed Methane in Wyoming: in W. R., Miller, ed., Coalbed Methane and the Tertiary Geology of the Powder River Basin, Wyoming and Montana: Wyoming Geological Association Guidebook, **50**, 61-72.

De Bruin, R. H., R. M. Lyman, R. W. Jones, and L. W. Cook, 2004, Coalbed Methane in Wyoming: State of Wyoming Geological Survey Information Pamphlet 7, Laramie, Wyoming.

Deutsch, C. V., 2002, Geostatistical reservoir modeling: Oxford University Press.

Diamond, W. P., J. C. LaScola, and D. M. Hyman, 1986, Results of direct-method determination of the gas content of U.S. coalbeds: U.S. Department of the Interior, Bureau of Mines Information Circular **9067**.

Ellis, M. S., 2002, Quality of economically extractable coal beds in the Gillette coal field as compared with other Tertiary coal beds in the Powder River Basin, Wyoming and Montana: U. S. Geological Survey Open-File Report, **02-174**.

Energy Information Administration, 2006, Energy-Related Carbon Dioxide Emissions: International Energy Outlook 2006, **DOE/EIA-0484(2006)**, chapter 7, accessed February 2007.

Energy Information Administration, 2007, State carbon dioxide emissions: <http://www.eia.doe.gov/environment.html>, accessed April 2007.

Environmental News Network, 2001, Coalbed methane boom in Wyoming's Powder River Basin: <http://www.enn.com/archive.html?id=25012&cat=archives>, accessed April 2007.

Flores, R. M., 2004, Coalbed methane in the Powder River Basin, Wyoming and Montana: An assessment of the Tertiary-Upper Cretaceous coalbed methane total petroleum system: U.S. Geological Survey Digital Data Series, **DDS-69-C**, chapter 2.

Flores, R. M., and L. R. Bader, 1999, Fort Union coal in the Powder River Basin, Wyoming and Montana: A synthesis: U.S. Geological Survey Professional Paper, **1625-A**, PS8-PS29.

Freeze, R. A., and J. A. Cherry, 1979, Groundwater: Prentice-Hall.

Frost, B. R., and P. N. Shive, 1986, Magnetic mineralogy of the lower continental crust: Journal of Geophysical Research, **91**, 6513-6521.

Gale, J., and P. Freund, 2001, Coal-bed methane enhancement with CO_2 sequestration worldwide potential: Environmental Geosciences, **8**, 210-217.

Gale, J., 2003, Going Underground CO_2 Storage and Emissions Reduction: Power Engineer, **17**, 15-17.

Gash, B. W., 1991, Measurement of "rock properties" in coal for coalbed methane production: SPE 22909, presented at the SPE 66th Annual Technical Conference and Exhibition, Dallas, Texas, October 6-9.

GEM, 2004, GEM 2004.10 User's Guide: Computer Modelling Group Ltd., Calgary, Alberta, Canada.

GEM, 2005, GEM 2005.15 User's Guide: Computer Modelling Group Ltd., Calgary, Alberta, Canada.

Gluskoter, H. J., R. W. Stanton, R. M. Flores, and P. D. Warwick, 2002, Adsorption of carbon dioxide and methane in low-rank coals and the potential for sequestration of carbon dioxide: Environmental Geosciences, **9**, 160-161.

Godfrey, N. J., B. C., Beaudoin, S. L., Klemperer, and Mendocino Working Group, 1997, Ophiolitic basement to the Great Valley forearc basin, California, from seismic and gravity data: Implications for crustal growth at the North American continental margin: Geological Society of America Bulletin, **109**, 1536-1562.

Grauch, V. J. S., 1993, Limitations on digital filtering of the DNAG magnetic data set for the conterminous U.S.: Geophysics, **58**, 1281-1296.

Gringarten, E., and C. V. Deutsch, 2001, Teacher's aide variogram interpretation and modeling: Mathematical Geology, **33**, 507-534.

Gu, F., and R. J. Chalaturnyk, 2005, Analysis of coalbed methane production by reservoir and geomechanical coupling simulation: Journal of Canadian Petroleum Technology, **44**, 33-42.

Haggerty, S. E., 1978, Mineralogical constraints on Curie isotherms in deep crustal magnetic anomalies: Geophysical Research Letters, **5**, 105-108.

Hamdy, S. S., S. M. Rashad, and H. R. Blank, 1984, Spectral analysis of aeromagnetic profiles for depth estimation principles, software, and practical application: USGS Open-File Report, **84-0849**.

Harpalani, S., and G. Chen, 1997, Influence of gas production induced volumetric strain on permeability of coal: Geotechnical and Geological Engineering, **15**, 303-325.

Harpalani, S., and R. A. Schraufnagel, 1990, Shrinkage of coal matrix with release of gas and its impact on permeability of coal: Fuel, **69**, 551-556.

Harpalani, S., 1999, Compressibility of Coal and its Impact on Gas Production from Coalbed Methane Reservoirs: Proceedings of the 37th U.S. Rock Mechanics Symposium, Vail, Colorado, 301-308.

Harpalani, S., 2005, Gas flow characterization of Illinois coal: Final technical report, ICCI project number **03-1/7.1B-2**.

Holditch, S. A., J. W. Ely, M. E. Semmelback, R. H. Carter, J. Hinkel, and R. G. Jeffery, 1988, Enhanced Recovery of Coalbed Methane through Hydraulic Fracturing: SPE **18250**, presented at the 63rd Annual Technical Conference and Exhibition of the Society of Petroleum Engineers, Houston, Texas, October 2-5.

Hower, T. L, J. E. Jones, D. M. Goldstein, and W. Harbridge, 2003, Development of the Wyodak coalbed methane resource in the Powder River Basin: SPE **84428**, presented at the SPE Annual Technical Conference and Exhibition, Denver, Colorado, October 5-8.

Hubbert, M. K., and D. G. Willis, 1957, Mechanics of hydraulic fracturing: Petroleum Transactions of the American Institute of Mining Metallurgical and Petroleum Engineers, **210**, 153–163.

Intergovernmental Panel on Climate Change, 2007, Contribution of Working Group I to the Fourth Assessment Report of the Intergovernmental Panel on Climate Change, Summary for policymakers: < http://www.ipcc.ch/>, accessed April 2007.

Jackson, G., 2006, CO_2 enhanced methane and reduced water production in high permeability, under-saturated coal seams – a modelling study: Proceedings of the 8th International Conference on Greenhouse Gas Control Technologies, Trondheim, Norway, June 19-22.

Jones, A. H., G. J. Bell, and R. A. Schraufngel, 1988, A review of the physical and mechanical properties of coal with implications for coalbed methane well completion and production: Coal-bed Methane, San Juan Basin, Rocky Mountain Association of Geologists, 169-181.

Journel, A. G., 1994, Geostatistics and reservoir geology: *in* J. M., Yarus and R. L. Chambers, eds., Computer Applications 3: Modeling and Geostatistics, AAPG, 19-20.

Kovscek, A. R., and F. M Orr, 2004, Rapid prediction of CO_2 movement in aquifers, coal beds, and oil and gas reservoirs: Stanford University Global Climate and Energy Project (GCEP) Technical Report 2003-2004, 115-147, <http://gcep.stanford.edu/research/technical_report/2004.html>.

Kovscek, A. R., F. M. Orr, K. Jessen, G. Q. Tang, T. Chaturvedi, M. Hesse, T. Ide, W. Lin, and C. J. Seto, 2005, Rapid Prediction of CO_2 Movement in Aquifers, Coal Beds, and Oil and Gas Reservoirs: in the CO_2 Storage section of the Stanford University Global Climate and Energy Project (GCEP) Technical Report 2004-2005, <http://gcep.stanford.edu/research/technical_report/2005.html>.

Kreemer, C., W. E. Holt, and A. J. Haines, 2003, An integrated global model of present-day motion and plate boundary deformation: Geophysical Journal International, **154**, 8-34.

Jennings, C. W., 1994, Fault activity map of California and adjacent areas, with locations and ages of recent volcanic eruptions, scale 1:750,000: California Geologic Data Map Series 6, California Division of Mines and Geology.

Lachenbruch, A. H., and J. H. Sass, 1973, Thermo-mechanical aspects of the San Andreas, in R. Kovach and A. Nur, eds., Tectonic Problems of the San Andreas Fault System: School of Earth Sciences, Stanford University, **13**, 192-205.

Lachenbruch, A. H., and J. H. Sass, 1980, Heat flow and energetics of the San Andreas fault zone: Journal of Geophysical Research, **85**, 6185-6222.

Laubach, S. E., R. A. Marrett, J. E. Olson, and A. R. Scott, 1998, Characteristics and origins of coal cleat: A Review: International Journal of Coal Geology, **35**, 175-207.

Law, D. H. –S., L. G. H. van der Meer, and W. D. Gunter, 2002, Numerical simulator comparison study for enhanced coalbed methane recovery processes, Part I: Pure carbon dioxide injection: SPE **75669**, presented at the SPE Gas Technology Symposium, Calgary, Alberta, Canada, April 30-May 2.

Law, D. H. –S., L. G. H. van der Meer, and W. D. Gunter, 2003, Comparison simulators for greenhouse gas sequestration in coalbeds, part III: More complex problems: 2nd Annual Conference on Carbon Sequestration, May 5-8.

Law, D. H. –S., L. G. H. van der Meer, and W. D. Gunter, 2004, Comparison of numerical simulators for greenhouse gas sequestration in coalbeds, part IV: History match of field micro-pilot test data: presented at the 7th International Conference on Greenhouse Gas Technologies, Vancouver, B. C., Canada.

Linder-Lunsford, J. B., and J. F. Wilson, 1992, Shallow ground water in the Powder River basin, northeastern Wyoming-Description of selected publications, 1950-91, and indications for further study: U.S. Geological Survey Water-Resources Investigations Report **91-4067**.

Liu, L., and M. D. Zoback, 1997, Lithospheric strength and intraplate seismicity in the New Madrid seismic zone: Tectonics, **16**, 585-595.

Mann, M., R. S. Bradley, and M. K. Hughes, 1998, Global-scale temperature patterns and climate forcing over the past six centuries: Nature, **392**, 779-787.

Mase, C. W., J. H., Sass, A. H., Lachenbruch, and R. J., Munroe, 1982, Preliminary heat-flow investigations of the California Cascades: USGS Open-File Report, **82-150**.

Mavor, M. J., B. Russell, and T. J. Pratt, 2003, Powder River Basin Ft. Union coal reservoir properties and production decline analysis: SPE **84427**, presented at the SPE Annual Technical Conference and Exhibition, Denver, Colorado, October 5-8.

Mavor, M. J., and W. D. Gunter, 2004, Secondary porosity and permeability of coal vs. gas composition and pressure: SPE **90255**, presented at the SPE Annual Technical Conference and Exhibition, Houston, Texas, September 26-29.

Mavor, M. J., W. D. Gunter, and J. R. Robinson, 2004, Alberta Multiwell Micro-Pilot Testing for CBM Properties, Enhanced Methane Recovery and CO_2 Storage Potential: SPE **90256**, presented at the SPE Annual Technical Conference and Exhibition, Houston, Texas, September 26-29.

Meissner, F. F., 1984, Cretaceous and lower Tertiary coals as sources for gas accumulations in the Rocky Mountain area: *in* J. Woodward, F. F. Meissner, and J. L. Clayton, eds., Hydrocarbon source rocks of the greater Rocky Mountain Region: Rocky Mountain Association of Geologists 1984 symposium, 401-431.

Mishra, D. C., and P. S. Naidu, 1974, Two-dimensional power spectral analysis of aeromagnetic fields: Geophysical Prospecting, **22**, 345-353.

Montana Board of Oil and Gas Conservation (MBOGC), 2007, <http://bogc.dnrc.state.mt.us/>, accessed March 2007.

National Earthquake Information Center, 1973-2003, <http://neic.usgs.gov/>, 20 August, 2004.

Nelson, C. R., 2006, Geologic Suitability of Coal Deposits in the Northern Great Plains Region of the United States for CO_2 Sequestration: Proceedings of the 8th International Conference on Greenhouse Gas Control Technologies, Trondheim, Norway, June 19-22.

Norris, R. M. and Webb, R. W., 1990, Geology of California: John Wiley & Sons, Inc.

Northern California Earthquake Data Center, Berkeley Seismological Laboratories, University of California, Berkeley, earthquake catalog from 27 August, 1993, to 27 August, 2003, <http://quake.geo.berkeley.edu/>, 4 January, 2005.

Nuccio, V., 2000, Coal-bed methane: Potential and concerns: USGS Fact Sheet, **FS-123-00**.

Nummedal, D., B. Towler, C. Mason, and M. Allen, 2003, Enhanced oil recovery in Wyoming: Prospects and challenges: prepared for Governor Dave Freudenthal, University of Wyoming, <http://uwadmnweb.uwyo.edu/AcadAffairs/PolicyStatements/EORfinal.pdf>, accessed February 2007.

Nuttall, B. C., F. E. Cortland, J. A. Drahoval, and R. M Bustin, 2005, Analysis of Devonian black shales in Kentucky for potential carbon dioxide sequestration and enhanced natural gas production: Final report for the U.S. Department of Energy and National Energy Technology Laboratory, **DE-FC26-02NT41442**, <http://www.uky.edu/KGS/emsweb/devsh/devshseq.html>, accessed March 2007.

Okubo, Y., and H. Tsu, 1992, Depth estimate of two-dimensional source using spectrum of one-dimensional linear trending magnetic anomaly: Butsuri-Tansa, **45**, 398-409.

Oldham, D. W., 1997, Exploration for shallow compaction-induced gas accumulations in sandstones of the Fort Union Formation, Powder River Basin, Wyoming: The Mountain Geologist, **34**, 25-38.

Page, B., G. Thompson, and R. Coleman, 1998, Late Cenozoic tectonics of the central and southern Coast Ranges of California: Geological Society of America Bulletin, **110**, 846-876.

Palmer, I., and J. Mansoori, 1996, How Permeability Depends on Stress and Pore Pressure in coalbeds: A New Model: SPE **36737**, Proceedings of the 71st Annual Technical Conference, Denver, CO.

Palmer, I., and J. Mansoori, 1998, How Permeability Depends on Stress and Pore Pressure in Coalbeds: A New Model: SPE Reservoir Evaluation & Engineering, **52607**, 539-544.

Palmer, I. D., and H. Vaziri, 2004, Permeability changes in CBM reservoir during production: An update and implications for CO_2 injection: The 2004 International Coalbed Methane Symposium Technical Sessions, Tuscaloosa, Alabama, May 3-7.

Palmer, I., 2004: SPE Applied Technology Workshop, Enhanced Coalbed-Methane Recovery and CO_2 Sequestration, Denver, Colorado, October 27-29 <http://www.spe.org/spe/jpt/jsp/jptmonthlysection/0,2440,1104_1585_0_3627982,00.html>, accessed March 2005.

Palmer, I., M. Mavor, and W. Gunter, 2006, Permeability Changes in Coal Seams during Production and Injection: presented at the fifth International Forum on Geologic Sequestration of CO_2 in Deep, Unmineable Coalseams (Coal-Seq V), Houston, Texas, November 8-9.

Parson E. A., and D. W. Keith, 1998, Climate change: Fossil fuels without CO_2 emissions: Science, **282**, 1053-1054.

Pekot, L. J., and S. R. Reeves, 2002, Modeling coal matrix shrinkage and differential swelling with CO_2 injection for enhanced coalbed methane recovery and carbon sequestration applications: U. S. Department of Energy, **DE-FC26-00NT40924**.

Pilkington, M., M. E. Gregotski, and J. P. Todoeschuck, 1994, Using fractal crustal magnetization models in magnetic interpretation: Geophysical Prospecting, **42**, 677-692.

Pollack, H. N., S. J. Hurter, and J. R. Johnson, 1993, Heat flow from the earth's interior: analysis of the global data set: Reviews of Geophysics, **31**, 267-280.

Puri, R., G. E. King, and I. D. Palmer, 1991, Damage to coal permeability during hydraulic fracturing: SPE **21813**, presented at the Rocky Mountain Regional Meeting and Low-Permeability Reservoirs Symposium, Denver, Colorado, April 15-17.

Reeves, S. R., 2001, Geologic Sequestration of CO_2 in Deep, Unmineable Coalbeds: An Integrated Research and Commercial-Scale Field Demonstration Project: SPE **71749**, Proceedings of the SPE Annual Technical Conference and Exhibition, New Orleans, September 30-October 3.

Reeves, S. R., and L. Pekot, 2001, Advanced reservoir modeling in desorption-controlled reservoirs: SPE **71090,** presented at the SPE Rocky Mountain Petroleum Technology Conference, Keystone, Colorado, May 21-23.

Reeves, S. R., and A. Taillefert, 2002, Reservoir Modeling for the Design of the RECOPOL CO_2 Sequestration Project, Poland: Topical report, U.S. Department of Energy, **DE-FC26-00NT40924**.

Reeves, S., C. Clarkson, and D. Erickson, 2002, Selected Field Practices for ECBM Recovery and CO_2 Sequestration in Coals based on Experience Gained at the Allison and Tiffany Units, San Juan Basin: Topical report, U.S. Department of Energy, **DE-FC26-00NT40924**.

Reeves, S. R., 2003, Assessment of CO_2 sequestration and ECBM potential of U.S. coalbeds: Topical report, U.S. Department of Energy, **DE-FC26-00NT40924**.

Reeves, S. R., A. Taillefert, L. Pekot, and C. Clarckson, 2003, The Allison Unit CO_2 – ECBM Pilot: A Reservoir Modeling Study: Topical Report, U.S. Department of Energy, **DE-FC26-0NT40924**.

Reeves, S. R., 2004, The Coal-Seq Project: Key Results from Field, Laboratory, and Modeling Studies: Proceedings of the 7th International Conference on Greenhouse Gas Control Technologies (GHGT-7), Vancouver, BC, Canada, September 5-9.

Reeves, S. R., and A. Oudinot, 2004, A Tiffany Unit N_2 - ECBM Pilot: A Reservoir Modeling Study: Topical Report, U.S. Department of Energy, **DE-FC26-00NT40924**.

Reeves, S. R., D. A. Davis, and A. Y. Oudinot, 2004, A technical and economic sensitivity study of enhanced coalbed methane recovery and carbon sequestration in coal: Topical Report, U.S. Department of Energy, **DE-FC26-0NT40924**.

Ricard, Y., and R. J. Blakely, 1988, Short note: A method to minimize edge effects in two-dimensional discrete Fourier transforms: Geophysics, **53**, 1113-1117.

Rice, D. D., 1997, Coalbed methane - An untapped energy resource and an environmental concern: U.S. Geological Survey Fact Sheet, **FS–019–97**.

Roberts, C. W., and R. C. Jachens, 1999, Preliminary aeromagnetic anomaly map of California: USGS Open-File Report **99-0440**.

[a]Ross, H. E., and M. D. Zoback, 2006, Reservoir characterization of coals in the Powder River Basin, Wyoming, USA, for CO_2 sequestration feasibility studies: Proceedings of the 8th International Conference on Greenhouse Gas Control Technologies, Trondheim, Norway, June 19-22.

[b]Ross, H. E., and M. D. Zoback, 2006, Hydraulic communication between coalbeds and overlying sands in the Powder River Basin, Wyoming and Montana: Implications for re-injection of coalbed methane water: presented at the AGU 2006 Fall Meeting, San Francisco, California, December 11-15.

Roy, R. F., D. D. Blackwell, and E. R. Decker, 1972, Continental heat flow, in E. C. Robertson, ed., Nature of the solid earth: McGraw-Hill, 506-543.

The Ruckelshaus Institute of Environment and Natural Resources, 2005, Water production from coalbed methane development in Wyoming: A summary of quantity, quality and management options: Final report prepared for the Office of the Governor, State of Wyoming, <http://www.uwyo.edu/enr/ienr/cbm.asp>, accessed February 2007.

Saad, A. F., 1969, Magnetic properties of ultramafic rocks from Red Mountain, California: Geophysics, **34**, 974-987.

Salem, A., K. Ushijima, A. Elsiraft, and H. Mizunaga, 2000, Spectral analysis of aeromagnetic data for geothermal reconnaissance of Quseir Area, northern Red Sea, Egypt: Proceedings World Geothermal Congress, Kyushu – Tohoku, Japan, May 28 – June 10, 1669-1674.

Saltus, R. W., and A. H. Lauchenbruch, 1991, Thermal evolution of the Sierra Nevada: tectonic implications of new heat flow data: Tectonics, **10**, 325-344.

Sass, J. H., A. H. Lachenbruch, and R. J. Munroe, 1971, Thermal conductivity of rocks from measurements on fragments and its application to heat-flow determinations: Journal of Geophysical Research, **76**, 3391-3401.

Sass, J. H., C. F. Williams, A. H. Lachenbruch, S. P. Jr. Galanis, and F. V. Grubb, 1997, Thermal regime of the San Andreas Fault near Parkfield, California: Journal of Geophysical Research, **102**, 27575-27585.

Schlinger, C. M., 1985, Magnetization of lower crust and interpretation of regional crustal anomalies: example from Lofoten and Vesterålen, Norway: Journal of Geophysical Research, **90**, 11484-11504.

Shi, J-Q., and S. Durucan, 2004, A numerical simulation study of the Allison unit CO_2-ECBM pilot: The impact of matrix shrinkage and swelling on ECBM production and CO_2 injectivity: presented at the 7th International Conference on Greenhouse Gas Control Technologies, Vancouver, Canada, September 5-9.

Shi, J-Q., and S. Durucan, 2006, The assessment of horizontal well option for CO_2 storage and ECBM recovery in unmineable thin seams: Pure CO_2 vs CO_2 enriched flue gas: Proceedings of the 8th International Conference on Greenhouse Gas Control Technologies, Trondheim, Norway, June 19-22.

Shimada, S., and Y. Funahashi, 2006, CO_2 leakage assessment in enhanced coalbed methane recovery: Proceedings of the 8th International Conference on Greenhouse Gas Control Technologies, Trondheim, Norway, June 19-22.

Shuey, R. T., D. K. Schellinger, A. C. Tripp, and L. B. Alley, 1977, Curie depth determination from aeromagnetic spectra: Geophysical Journal of the Royal Astrological Society, **50**, 75-101.

Sibson, R. H., 1982, Fault zone models, heat flow, and the depth distribution of earthquakes in the continental crust of the United States: Bulletin of the Seismological Society of America, **72**, 151-163.

Sibson, R. H., 1983, Continental fault structure and the shallow earthquake source: Geological Society of London, **140**, 741-767.

Smith, R. B., R. T. Shuey, R. O. Freidline, R. M. Otis, and L. B. Alley, 1974, Yellowstone hot spot: New magnetic and seismic evidence: Geology, **2**, 451-455.

Smith, D. H, G. Bromhal, W. N. Sams, S. Jikich, and T. Ertkin, 2005, Simulating carbon dioxide sequestration/ECBM production in coal seams: Effects of permeability anisotropies and the diffusion-time constant: SPE Reservoir Evaluation & Engineering, SPE **84423**, 156-163.

Southern California Earthquake Data Center, earthquake catalog from 27 August, 1993, to 27 August, 2003, <http://www.data.scec.org/catalog_search/>, 4 January, 2005.

Spector, A., and F. S. Grant, 1970, Statistical models for interpreting aeromagnetic data: Geophysics, **25**, 293-302.

Srivastava, R. M., 1994, An overview of stochastic methods for reservoir characterization: *in* J. M. Yarus and R. L. Chambers, eds., Modeling and Geostatistics, AAPG, 3-16.

Stacey, F. D., and S. K. Banerjee, 1974, The physical principles of rock magnetism: Elsevier.

Stanton, R., R. M. Flores, P. D. Warwick, H. Gluskoter, and G. D. Stricker, 2001, Coal bed sequestration of carbon dioxide: presented at the First National Conference on Carbon Sequestration, Washington DC, May 14-17.

Stevens, S. H., and D. Spector, 1998, Enhanced coalbed methane recovery and Enhanced Coalbed Methane Recovery: Worldwide Application and CO_2 Sequestration Potential: Final Report **IEA/CONS/97/27** prepared for the IEA Greenhouse Gas R&D Programme.

Stricker, G. D., R. M Flores, D. E. McGarry, D. P. Stillwell, D. J. Hoppe, C. R. Stillwell, A. M. Ochs, M. S. Ellis, K. S. Osvald, S. L. Taylor, M. C. Thorvaldson, M. H. Trippi, S. D. Grose, F. J. Crockett, and A. J. Shariff, 2006, Gas Desorption and Adsorption Isotherm Studies of Coals in the Powder River Basin, Wyoming and Adjacent Basins in Wyoming and North Dakota: U.S. Geological Survey Open-File Report 2006-1174, <http://pubs.usgs.gov/of/2006/1174/>, accessed August 2006.

Surpless, Benjamin E., D. F. Stockli, T. A. Dumitru, and E. L. Miller, 2002, Two-phase westward encroachment of Basin and Range extension into the northern Sierra Nevada: Tectonics, **21**, 2-1 to 2-13.

Taillefert, A., and S. R. Reeves, 2003, Screening model for ECBM recovery and CO_2 sequestration in Coal: Topical Report, U. S. Department of Energy, **DE-FC26-ONT40924**.

Tanaka, A., Y. Okubo, and O. Matsubayashi, 1999, Curie-temperature isotherm depth based on spectrum analysis of the magnetic anomaly data in East and Southeast Asia: Tectonophysics, **306**, 461-470.

Tang, G. -Q., K. Jessen, and A. R. Kovscek, 2005, Laboratory and simulation investigation of enhanced coalbed methane recovery by gas injection: SPE **95947**, presented at the SPE Annual Technical Conference and Exhibition, Dallas, Texas, October 8-12.

Tans, P., 2007, NOAA/ESRL: <www.esrl.noaa.gov/gmd/ccgg/trends>, accessed February 2007.

Thatcher, W., and P. England, 1998, Ductile shear zones beneath strike-slip faults: implications for the thermomechanics of the San Andreas fault zone: Journal of Geophysical Research, **103**, 891-905.

Twombly, G., S. H. Stepanek, and T. A. Moore, 2004, Coalbed methane potential in the Waikato Coalfield of New Zealand: A comparison with developed basins in the United States: 2004 New Zealand Petroleum Conference Proceedings.

U.S. Department of Energy and National Energy Technology Laboratory, 2003, Multi-seam well completion technology: Implications for Powder River Basin coalbed methane production: DOE/NETl-**2003/1193**, <www.netl.doe.gov/publications/EPreports/MSCreport.pdf>, accessed Marck 2007.

U.S. Department of Energy, 2007, Carbon Sequestration R&D Overview, <http://www.fossil.energy.gov/programs/sequestration/overview.html>, accessed April 2007.

U.S. Geological Survey National Oil and Gas Resource Assessment Team, 1995, 1995 National assessment of United States oil and gas resources: U. S. Geological Survey Circular **1118**.

U.S. Geological Survey Powder River Basin Province Assessment Team, 2004, Executive Summary: Assessment of Coalbed Gas Resources of the Powder River Basin Province, Wyoming and Montana, 2003: U. S. Geological Survey Digital Data Series, DDS-69-C, chapter 1.

U.S. Geological Survey Heat Flow Database for California, <http://quake.wr.usgs.gov/heatflow/>, 25 September, 2003.

van Bergen, F., H. Pagnier, and P. Krzystolik, 2006, Field experiment of CO_2-ECBM in the Upper Silesian Basin of Poland: Proceedings of the 8th International Conference on Greenhouse Gas Control Technologies, Trondheim, Norway, June 19-22.

van Wageningen, N., 2006, Lessons learned from RECOPOL (ECBM) pilot: presented at the fifth International Forum on Geologic Sequestration of CO_2 in Deep, Unmineable Coalseams (Coal-Seq V), Houston, Texas, November 8-9.

Wheaton, J., and J. Metesh, 2002, Potential Ground-Water Drawdown and Recovery from Coalbed Methane Development in the Powder River Basin, Montana: Project Completion Report to the U.S. Bureau of Land Management, Montana Bureau of Mines and Geology Open File Report **458**, <http://www.mt.blm.gov/mcfo/cbm/eis/CBM3DGWReport.pdf>, accessed March 2007.

Wheaton, J., and T. Donato, 2004, Coalbed-methane basics: Powder River Basin, Montana: Montana Bureau of Mines and Geology Information Pamphlet **5**, <www.mbmg.mtech.edu/pdf/ip_5.pdf>, accessed March 2007.

White, C. M., D. H. Smith, K. L. Jones, A. L. Goodman, S. A. Jikich, R. B. LaCount, S. B. DuBose, E. Ozdemir, B. I. Morsi, and K. T. Schroeder, 2005, Sequestration of Carbon Dioxide in Coal with Enhanced Coalbed Methane Recovery – A Review: Energy and Fuels, DOI **10.1021/ef040047w**, web release March 22, 2005.

Wigley, T. M. L, R. Richels, and J. A. Edmonds, 1996, Economic and environmental choices in the stabilization of atmospheric CO_2 concentrations: Nature, **379**, 240-243.

Winschel, R. A., and R. E. Douglas, 2006, Enhanced Coal Bed Methane Production and Sequestration of CO_2 in Unmineable Coal Seams: presented at the fifth International Forum on Geologic Sequestration of CO_2 in Deep, Unmineable Coalseams (Coal-Seq V), Houston, Texas, November 8-9.

Wong, S., D. Law, X. Deng, J. Robinson, B. Kadatz, W. D. Gunter, Y. Jianping, F. Sanli, and F. Zhiqiang, 2006, Enhanced Coalbed Methane – Micro-Pilot Test At South Qinshui, Shanxi, China: Proceedings of the 8th International Conference on Greenhouse Gas Control Technologies, Trondheim, Norway, June 19-22.

Wyman, R. E., 1984, Gas Resources in Elmworth Coal Seams: AAPG Memoir, **38**, 173-187.

Wyoming Oil and Gas Conservation Commission (WOGCC), <http://wogcc.state.wy.us/>, accessed between 2004 and 2007.

Yamaguchi, S., K. Ohga, M. Fujioka, M. Nako, and S. Muto, 2006, Field experiment of Japan CO_2 geosequestration in coal seams project (JCOP): Proceedings of the 8th International Conference on Greenhouse Gas Control Technologies, Trondheim, Norway, June 19-22.

Young, G., 2006, San Juan Basin ECBM Pilot Project Update: presented at the fifth International Forum on Geologic Sequestration of CO_2 in Deep, Unmineable Coalseams (Coal-Seq V), Houston, Texas, November 8-9.

Zhu, L., and H. Kanamori, 2000, Moho depth variation in southern California from teleseismic receiver functions: Journal of Geophysical Research, **105**, 2969-2980.

Zoback, M. D., J. Townend, and B. Grollimund, 2002, Steady-state failure equilibrium and deformation of intraplate lithosphere: International Geology Review, **44**, 383-401.

Zoback, M. D., C. A. Barton, M. Brudy, D. A. Castillo, T. Finkbeiner, B. Grollimund, D. B. Moos, P. Peska, C. D. Ward and D. J. Wiprut, 2003, Determination of stress orientation and magnitude in deep wells: International Journal of Rock Mechanics and Mining Sciences, **40**, 1049–1076.

Zoback, M. D., 2007, Reservoir geomechanics: Cambridge Press.